DEPARTMENT OF PHYSICS

DIRECT EVALUATION OF PARTON DISTRIBUTION FUNCTIONS OF THE NUCLEON FROM LATTICE QCD

AURORA SCAPELLATO

A dissertation submitted to the University of Cyprus in partial fulfillment of the requirements for the degree of Doctor of Philosophy and submitted to the University of Wuppertal in partial fulfillment of the requirements for the degree of Doctor Rerum Naturalium.

MAY 2019

VALIDATION PAGE

Doctoral Candidate: Aurora Scapellato

Dissertation Title: Direct evaluation of Parton Distribution Functions of the Nucleon from Lattice QCD

The present Doctoral Dissertation was submitted in partial fulfillment of the requirements for the degree of Doctor of Philosophy at the Department of Physics of the University of Cyprus and for the degree of Doctor Rerum Naturalium at the Department of Physics of the University of Wuppertal, and was approved on May 30, 2019 by the members of the Examination Committee.

Examination Committee:

Prof. Dr. Constantia Alexandrou, Research Supervisor

Prof. Dr. Francesco Knechtli, Research Supervisor

Prof. Dr. Andreas Frommer

Dr. Karl Jansen

Prof. Dr. Konstantinos Orginos

Prof. Dr. Haralambos Panagopoulos

DECLARATION OF DOCTORAL CANDIDATE

The present doctoral dissertation was submitted in partial fulfillment of the requirements for the degree of Doctor of Philosophy at the Department of Physics of the University of Cyprus and for the degree of Doctor in Rerum Naturalium at the University of Wuppertal. It is a product of original work of my own, unless otherwise mentioned through references, notes, or any other statements.

Aurora Scapellato

"Every great and deep difficulty bears in itself its own solution. It forces us to change our thinking in order to find it."

Niels Bohr

Acknowledgements

Abstract

We describe the computation of parton distribution functions (PDFs) of the nucleon from first principles. The investigation is done within the lattice formulation of Quantum Chromodynamics (QCD). The numerical calculations are performed employing a twisted mass ensemble of gauge field configurations simulated with two degenerate light quarks with mass fixed to their physical value. By using the quasi-PDF approach we extract the isovector unpolarized, helicity and transversity distributions. Within this approach, we compute quasi-distributions which are related to the physical PDFs using the framework of Large Momentum Effective Theory. As the nucleon boost increases, we observe that the renormalized lattice PDFs move towards the quark distributions extracted from global QCD analyses. The results at larger momentum boost reproduce the main features of the phenomenological fits to inclusive and semi-inclusive scattering data. We discuss future issues that need to be addressed to eliminate systematic uncertainties related to the lattice calculation. The results obtained clearly demonstrate the potential impact of non-perturbative methods in the determination of PDFs and open a most promising path to investigate quantities that require the evaluation of non-local operators on the lattice.

Περίληψη

Περιγράφουμε τον υπολογισμό των συναρτήσεων διανομής (**PDFs**) του νουκλεονίου αρχίζοντας από τη Λαγκαντζιανή των ισχυρών αλληλεπιδράσεων και χρησιμοποιώντας το φορμαλισμό Κβαντικής Χρωμοδυναμικής (ΚΧΔ) πλέγματος. Οι αριθμητικοί υπολογισμοί εκτελούνται χρησιμοποιώντας ένα σύνολο γκλουονικών πεδίων που προσομοιώνεται με δύο εκφυλισμένα ελαφρά κουάρκ (**up, down**) με μάζα ίση με τη φυσική τους τιμή. Εξάγουμε τις μη-πολωμένες, ελικοειδείς και εγκάρσιες κατανομές. Ο υπολογισμός των κατανομών σχετίζεται με τα φυσικά **PDFs** χρησιμοποιώντας το πλαίσιο της Θεωρίας Μεγάλης Ορμής. Καθώς αυξάνεται η ορμή του νουκλεονίου, παρατηρούμε ότι τα **PDFs** πλέγματος προσεγγίζουν τις κατανομές κουάρκς που εξάγονται από τις αναλύσεις των πειραματικών δεδομένων. Τα αποτελέσματα σε μεγαλύτερη ορμή αναπαράγουν τα κύρια χαρακτηριστικά των φαινομενολογικών **PDFs**. Συζητάμε τα μελλοντικά ερωτήματα που πρέπει να αντιμετωπιστούν προκειμένου να εξαλειφθούν οι συστηματικές αβεβαιότητες που σχετίζονται με τον υπολογισμό του πλέγματος. Τα αποτελέσματα που προέκυψαν δείχνουν σαφώς τον πιθανό αντίκτυπο των μη διαταρακτικών μεθόδων στον προσδιορισμό των **PDFs** και ανοίγουν μια πολύ ελπιδοφόρα πορεία για τη διερεύνηση ποσοτήτων που απαιτούν την αξιολόγηση μη τοπικών τελεστών στο πλέγμα.

Zusammenfassung

Wir beschreiben die ab-initio Berechnung von Parton Verteilungsfunktionen (PDFs) des Nukleons. Die Untersuchung wird innerhalb der Gitterformulierung der Quanten-Chromodynamik (QCD) durchgeführt. Die numerischen Berechnungen werden unter Verwendung von Ensemblen von Eichfeldkonfigurationen durchgeführt, die einen chiral verdrehten Massenterm benutzen, wobei die leichten Quarks massen-degeneriert und auf ihren physikalischen Wert fixiert sind. Mit Hilfe des Quasi-PDF-Ansatzes extrahieren wir die Isovektor-unpolarisierten Helizität und Transversalverteilungen. Innerhalb dieses Ansatzes berechnen wir zunächst Quasi-Verteilungen und verknüpfen diese mit den physikalischen PDFs im Rahmen der effektiven Theorie großer Impulse. Wir finden, dass sich die renormierten Gitter-PDFs mit zunehmenden Nukleon-Boost den Quark-Verteilungen annähern, wie sie aus globalen QCD-Analysen extrahiert werden. Insbesondere reproduzieren die Ergebnisse bei größerem Boost die Hauptmerkmale der phänomenologischen Fits an inklusive und semi-inklusive Streudaten. Wir sprechen zukünftige Probleme an, die angegangen werden müssen, um systematische Unsicherheiten im Zusammenhang mit der Gitterberechnung zu kontrollieren. Die erzielten Ergebnisse verdeutlichen klar die potenzielle Anwendung von nicht-störungstheoretischen Methoden bei der Bestimmung von PDFs und eröffnen einen vielversprechenden Weg zur Untersuchung von Größen, die die Berechnung von nicht-lokalen Operatoren auf dem Gitter erfordern.

Contents

List of Figures

List of Tables

Chapter 1

Introduction

The strong nuclear force plays an essential role in Particle Physics. It is one of the four fundamentals forces in Nature, responsible for holding *quarks* and *gluons* together to form composite states, called hadrons. Protons and neutrons are perhaps the most well known strongly interacting particles and form the essential building blocks of atomic nuclei. The theory describing the strong force is called *Quantum Chromodynamics* (QCD).

QCD has its roots in the *constituent quark picture*, formulated in the '60s by Gell-Mann and Zweig [1, 2] independently. They put forward that low energy properties, such as the spin, could be explained if hadrons were made up of elementary particles, called quarks. At the same time, there was an intensive experimental program to study the inner structure of hadrons through scattering experiments, mostly limited to scattering of electrons off a proton target. In 1969 at the Standford Linear Accelerator (SLAC) it was discovered that at large momentum transfer Q, new hadronic states were produced as final products of the collisions [3, 4]. Moreover, the structure functions that parameterize the cross sections were surprisingly found to be almost constant over a large range of Q^2 values. This behavior, which appeared clearly in contrast with the rapid decay observed for the elastic structure functions, was also predicted by Bjorken and is known as *Bjorken scaling* [5].

To explain the formation of new states in the so-called *deep inelastic scattering* regime, it was assumed that the proton had a granular structure and its point-like constituents were essentially free [6]. Within Feynman's parton model, the proton constituents were called *partons*. Later it became natural to identify the partons with the quarks of Gell-Mann and Zweig. However, in this picture there were still some inconsistencies that needed to be solved. Firstly, assuming that quarks are charged point-like particles, the measured cross sections $e^+e^- \rightarrow$ hadrons were found to be larger than expected; secondly, it was difficult to construct antisymmetric wave functions for certain hadronic states, like for the Δ^{++}. These paradoxes were overcome by associating to the quarks an extra quantum number called *color*, which exists in three variants. In addition, measurements of structure functions showed that quarks did not generate the complete momentum of the proton and almost half was missing. This suggested that there must be other constituents besides quarks, that at high energies interact very weakly so that Bjorken scaling is satisfied. These inconsistencies were finally explained with the discovery of *asymptotic freedom* of non-Abelian gauge theories [7–9].

For this discovery, Gross, Politzer and Wilczek were awarded the Nobel Prize in Physics in 2004. Thus, the experimental fundings and theoretical discoveries mentioned above led to the establishment of QCD as the theory of strong interactions. This is a non-Abelian gauge theory, based on the SU(3) color symmetry group [10]. QCD is described in terms of matter fields (*quarks* and *antiquarks*) and *gluons*, vector bosons that mediate the strong force. Quarks, antiquarks and gluons are collectively called partons. In Table 1.1, we list the six known flavors of quarks: *up*, *down*, *strange*, *charm*, *top*, *bottom*. They cover a wide range of masses, from few MeV (for *up* and *down* quarks) up to around 170 GeV for *top* quark [11].

	u	d	s	c	b	t
Q-electric charge	$+2/3$	$-1/3$	$-1/3$	$+2/3$	$-1/3$	$+2/3$
I- isospin	$+1/2$	$+1/2$	0	0	0	0
I_z- isospin z-component	$+1/2$	$-1/2$	0	0	0	0

Table 1.1 The six flavors of quarks (u, d, s, c, b, t) and their additive quantum numbers for the electric charge (Q), isospin (I) and isospin z-component (I_z) [11].

The non-Abelian structure of the theory is responsible for asymptotic freedom: at high energies (or equivalently at small distances) quarks and gluons behave as free particles, in line with the original Feynman's parton model and Bjorken's prediction. On the other hand, the constituents are only approximately free because of QCD effects, as later confirmed by deep inelastic scattering where Bjorken scaling violations were observed. However, the most puzzling feature of QCD is that quarks have never been observed isolated. This property is called *color confinement*: color-charged particles, such as quarks and gluons, cannot be isolated and are confined within hadrons. An analytic proof of color confinement has not been found up to date. The reason is that the value of the strong coupling, α_s, increases at large distances and $\alpha_s \sim O(1)$ at energies comparable to Λ_{QCD} (approximately 300 MeV [12]). The running of the coupling is qualitatively shown in Fig. 1.1. At low energies, the behavior
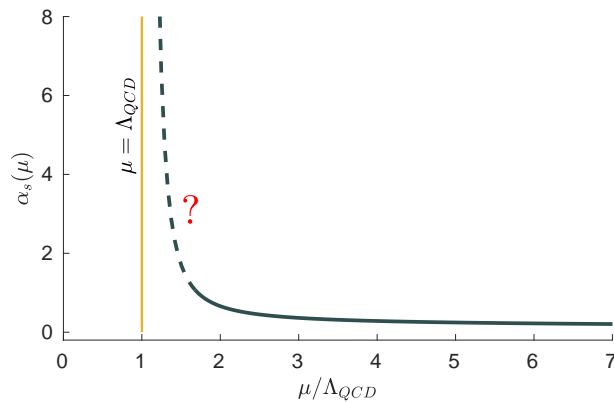
Figure 1.1 The dependence of α_s on the energy scale μ.

of α_s cannot be predicted in perturbative QCD, as perturbative methods fail in this regime.

Consequently, no hadronic property involving long-distance physics can be investigated in terms of an expansion of the coupling.

An approach to study gauge field theories in the non-perturbative regime was proposed by Wilson in 1974 [13]. Applied to the strong interactions, this method took the name of *lattice QCD*. In this approach, the theory is discretized in a hypercubic grid with Euclidean metric and is solved numerically via Monte Carlo methods.

In Euclidean space, the distance between two space-time points is defined in the usual way as $d^2 = t^2 + \vec{r}^2$, whilst in the Minkowski as $d^2 = t^2 - \vec{r}^2$. The metric used in lattice QCD poses serious limitations on the study of quantities that in Minkowski space are defined on the light-cone. An example of those are *parton distribution functions* (PDFs), which are the objects of interest in this Thesis.

Parton distribution functions are among the intangible elements of the real world, describing the momentum distributions of quarks and gluons inside hadrons. They were first introduced in Feynman's parton model, where deep inelastic cross sections lepton-proton were shown to factorize in *partonic cross sections* and PDFs. The twist-two PDFs of interest here are of three kinds: *unpolarized*, *helicity*, and *transversity* distributions. They all quantify the probability densities of finding a parton with a longitudinal momentum fraction x ($0 \leq x \leq 1$) of the total momentum of the parent hadron. The difference among them lies on how the quark helicity is aligned with respect to the helicity of the parent hadron, which can be longitudinally or transversely polarized. Much later, PDFs were generalized to functions that probe also the quark spin and the transverse momentum distributions; these include generalized parton distributions (GPDs) [14–17] and transverse-momentum dependent parton distribution functions (TMDs) [18–21].

PDFs, which are the simplest distribution functions, have been studied intensively and continuously in experimental facilities over the last few decades, most notably for the proton. The interest was, also in part, motivated by the fact that PDFs are an essential and indispensable input for collider experiments, such as the LHC. In fact, a rich experimental program at major facilities, e.g. BNL, CERN, DESY, Fermilab, JLab and SLAC, has provided a wealth of measurements with a corresponding world-wide theoretical effort to interpret the results. The method used to extract information from scattering data is called *global QCD analysis* (see e.g. [22, 23]). In general, one resorts to fits of experimental data aided by phenomenologically motivated Ansätze. However, knowledge of PDFs only from phenomenological fits cannot be considered as a direct and *ab initio* QCD prediction, as the analysis is not-unique [24]. In fact, a comparison between different extractions from global fits is shown in Fig. 1.2 for the gluon (left) and *down* quark (right) PDF within the proton. As can be seen, PDF determinations are not without ambiguities and an extraction from first principles is a valuable addition to the global fitting analyses.

The non-perturbative nature of PDFs makes lattice QCD an ideal *ab initio* formulation to study them, utilizing large-scale simulations. A direct evaluation was thought to be impossible until recently, since PDFs require light-cone dynamics, which cannot be implemented on a Euclidean lattice. Unlike PDFs, there is no theoretical difficulty in extracting the *moments* of these distributions, as they are related to matrix elements of local operators. However,
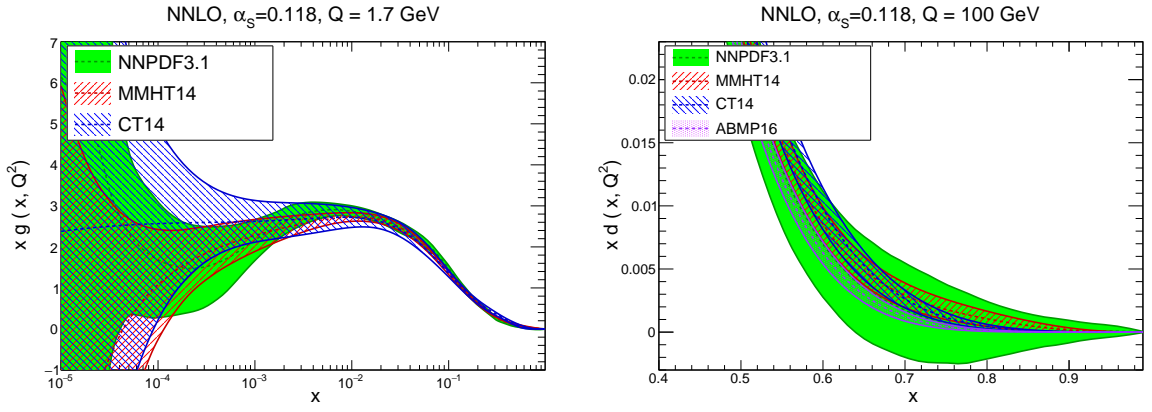
Figure 1.2 Left: The gluon PDF $xg(x, Q^2)$, at $Q = 1.7$ GeV, extracted from NNPDF3.1 [25], MMHT14 [26], CT14 [27] NNLO sets with $\alpha_s(m_Z) = 0.118$. Right: The *down* quark PDF, $xd(x, Q^2)$ at $Q = 100$ GeV, comparing the NNPDF3.1 [25], MMHT14 [26], CT14 [27], ABMP16 [28] NNLO sets. Figures from Ref. [23].

only the lowest moments can be realistically computed, due to an unavoidable large gauge noise for high moments and the presence of power-divergent mixing with lower-dimensional operators (see e.g. [29–32]). This has clearly made impossible a full reconstruction of PDFs from first principles.

A possible solution to extract parton distribution functions from lattice QCD was proposed six years ago by X.Ji [33]. Within this method, called *quasi-PDF* approach, one computes matrix elements probing purely spatial correlations, accessible in Euclidean lattice QCD. The correlation functions are then related to the physical PDFs within the framework of Large Momentum Effective Theory [34]. Soon after its introduction, this method was intensively explored with promising results presented in Ref. [35] and later in Refs. [36, 37] by the ETM (Extended Twisted Mass) Collaboration. Subsequent investigations can be found in Refs. [38, 39]. The quasi-PDF approach has renewed interest towards a direct computation of PDFs from lattice QCD and also in other approaches that were proposed earlier but not applied until recent times, such as the *hadronic tensor* [40–42]. Other recent lattice techniques for studying *x*-dependent hadron structure include the so-called *good lattice cross sections* [43, 44] and *pseudo-PDFs* [45–48]; the lattice investigations with the latter approach can be found in Refs. [49–52]. For a detail overview of the current status of lattice QCD calculations of PDFs and other partonic distributions we refer to recent reviews [53, 54].

Despite the tremendous progress in this field, the accuracy of lattice QCD computations of PDFs cannot still compete so far with the one of the moments, achieved after a long history of lattice effort. This is because the investigation of PDFs is a new research field that entails many delicate components, such as the renormalization of non-local operators that was understood only in 2017, with the first works of Refs. [55, 56].

The work presented in this Thesis is part of the effort by ETM Collaboration and is based on Refs. [57–59]. The results presented here concern distribution functions of the nucleon corresponding to the isovector flavor structure $u - d$ and are obtained by using a gauge field ensemble with two degenerate light quarks whose masses are tuned to their physical value.

Before discussing the actual research that has been done for quark distribution functions, we dedicate Chapter 2 to an overview of scattering experiments, as they played a pivotal role in understanding the inner structure of hadrons. Starting from elastic scattering we proceed to deep inelastic scattering and introduce the definition of parton distribution functions. State-of-the-art unpolarized, helicity and transversity PDFs are also presented, with focus on the light-content of the proton of interest in our work.

In Chapter 3 we give an overview of lattice QCD, describing the Wilson discretization of the QCD action and the *clover improvement*. We then introduce the twisted mass fermion action for two degenerate light quarks and subsequently explain the theoretical principles of the quasi-PDF approach.

The lattice techniques employed in our computation are described in Chapter 4. These include smearings of interpolating fields and of the gauge links, as well as the method to generate quark propagators, which are the building blocks of nucleon correlation functions in lattice QCD. The focus is only on the so-called *connected diagrams* entering our calculation.

In Chapter 5 we present our numerical setup, namely the gauge ensemble used and the tuning of different parameters in order to reduce the signal-to-noise ratio for large momenta and accumulate high statistics at reduced computational cost. Moreover, we present the unrenormalized results for the matrix elements at different source-sink time separations and our analysis on isolating the ground state matrix element. We also discuss the computational cost of our calculations and explain what the computational challenges are for such lattice investigations.

The renormalization procedure of our lattice operators is addressed in Chapter 6. In particular, we describe the types of divergences that need to be removed, the computation of the renormalization functions on the lattice and finally present the renormalized matrix elements for the unpolarized, helicity and transversity distributions. The effect of gauge link-smearing is also discussed.

In Chapter 7 we describe the extraction of the physical PDFs. From the renormalized matrix elements, we show how to compute the quasi-distributions for the three twist-two operators and apply the necessary corrections to match the quasi- to the physical PDFs. We show how the lattice results approach the phenomenological PDFs as the momentum increases, and compare our results at the highest momentum with PDFs from global analyses. We also discuss the dependence on the quark mass and demonstrate that performing the calculation at physical mass is important. Finally, we summarize the outcome and discuss future directions in Chapter 8.

Chapter 2

Parton physics

In this Chapter we present an overview of the theoretical and experimental background in which this work is embedded. Given the central role played by scattering processes in understanding hadron structure, the first two Sections are dedicated to the analyses of some of the simplest scatterings, elastic and inelastic, and to the calculation of the corresponding cross sections. The interpretation of experimental data in the inelastic scattering regime will naturally lead to the formulation of a *parton model* and to the introduction of *Parton Distribution Functions* (PDFs). In the last Section, state-of-the-art phenomenological results for PDFs are reported, with special emphasis on the light-content of the proton.

Before introducing the concept of parton distribution functions, let us first start with the basic scattering processes, and then add complications that bring us to the lepton-hadron inelastic scattering.

2.1 Elastic scattering

2.1.1 Electron-muon scattering

The simplest scattering processes exclusively involve point-like particles and have the same initial and final particle states. These processes are known as *elastic scattering*. To establish the formalism, we consider the elastic scattering of electrons off muons, $e^- \mu^- \to e^- \mu^-$. The interaction between e^- and μ^- can be mediated by a photon or Z^0 bosons, with the electroweak contribution becoming important for center-of-mass energy $E_{CM} > M_Z \simeq 90$ GeV. For simplicity, we assume that the collision occurs at low energy so that the cross section can be computed in Quantum Electrodynamics (QED) at the leading order; we also suppose that it is dominated by only one virtual photon exchange. The Feynman diagram associated to this process is shown in Fig. 2.1.

We call k_μ, k'_μ the momenta of the incoming and outgoing electron and p_μ, p'_μ the ones of the initial and final muon respectively. The particle states, with well-defined momentum and spin, are indicated by Dirac spinors, like $u(k,\sigma)$, $u(p,s)$ for the incoming electron and muon, etc. Using this notation and denoting with $q^\mu = (k - k')^\mu$ the momentum transfer carried by
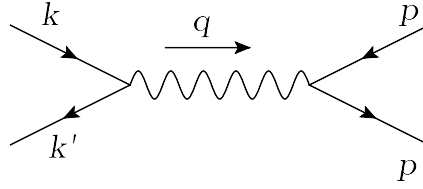
Figure 2.1 Lowest-order diagram for $e^-(k)\mu^-(p) \to e^-(k')\mu^-(p')$.

the virtual photon, the scattering amplitude of the process reads

$$iM_{fi} = \bar{u}(k',\sigma')(-ie\gamma^\mu)u(k,\sigma)\left(-i\frac{g_{\mu\nu}}{q^2}\right)u(p',s')(-ie\gamma^\nu)u(p,s)\,. \tag{2.1}$$

$g_{\mu\nu} = \text{diag}(+1,-1,-1,-1)$ is the Minkowski tensor and γ^μ are the Dirac γ-matrices (see e.g. [60] for standard conventions). The amplitude above enters the general expression for the differential cross section, $d\sigma$, in the following way

$$d\sigma = (2\pi)^4\delta^4(P_f - P_i)\frac{1}{4I}|M_{fi}|^2\prod_{i=1}^{n}\frac{d^3p_i}{(2\pi)^3 2E_i}\,, \tag{2.2}$$

where $4I$ is the flux factor [60], P_f, P_i are the quadri-momenta of the initial and final states, and p_i, E_i are the momenta and energies of the final particles, which are fixed by momentum conservation through the Dirac-delta $\delta^4(P_f - P_i)$.

To evaluate the cross section, one needs to choose a reference frame, since the scattering amplitude depends on the momenta and polarization of the particles involved in the collision. The simplest case, considered here, corresponds to the one in which the incoming particles are not polarized and the final polarizations are not measured in experiments. Thus, for $1/2$-spin particles, the conditions above lead to the following replacement at the level of the scattering amplitude:

$$|M_{fi}|^2 \to \frac{1}{4}\sum_{\sigma,\sigma',s,s'}|M_{fi}|^2\,. \tag{2.3}$$

The sum over the spins can now be carried out by using the spinor completeness relation $\sum_\sigma u(p,\sigma)\bar{u}(p,\sigma) = (\slashed{p}+m)$, which yields the following expressions for the electronic and muonic tensor

$$L_e^{\mu\nu} = \frac{1}{2}\text{Tr}[(\slashed{k}'+m_e)\gamma^\mu(\slashed{k}+m_e)\gamma^\nu]\,,\quad L_{muon}^{\mu\nu} = \frac{1}{2}\text{Tr}[(\slashed{p}'+m_\mu)\gamma^\mu(\slashed{p}+m_\mu)\gamma^\nu]\,. \tag{2.4}$$

We now have to choose a reference frame where to evaluate the expressions (2.4) and, as a consequence, the final cross section. Here we suppose that the muon is initially at rest,

which means performing the calculation in the laboratory frame (LAB). In this frame, the quadri-momenta and kinematic are indicated below:

$$p = (m_\mu, \vec{0}) \qquad k = (E, \vec{k})$$
$$k' = (E', \vec{k}') \qquad p' = p + q$$
$$q = k - k'$$
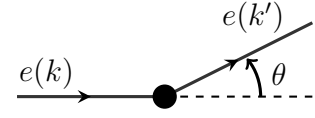
$$\Rightarrow q^2 = k^2 + k'^2 - 2k \cdot k = 2m_e - 2k \cdot k' \approx -2k \cdot k'$$
$$\approx -2EE'(1 - \cos\theta) = -4EE' \sin^2\frac{\theta}{2} \, ,$$

where θ is the scattering angle and we have assumed that the electron mass is negligible compared to its momentum, i.e. $m_e << |\vec{k}|$. From the computation above we also find that $q^2 < 0$.

Making now explicit the kinematic in Eq. (2.4) and substituting $I = m_\mu E$ for the LAB frame, one can see that the differential cross section takes the form [61]

$$\left(\frac{d\sigma}{dE'd\Omega}\right)_{LAB} = \frac{\alpha_e^2}{4E^2 \sin^4\theta/2} \left[\cos^2\frac{\theta}{2} + \frac{(E-E')}{m_\mu}\sin^2\frac{\theta}{2}\right] \delta\left(E - E' + \frac{q^2}{2m_\mu}\right), \quad (2.5)$$

where $\alpha_e^2 = e^2/4\pi$ is the fine-structure constant in natural units ($\varepsilon_0 = c = \hbar = 1$). If we integrate over the energy E' of the outgoing electron, we obtain a more compact expression [61][1]

$$\left(\frac{d\sigma}{d\Omega}\right)_{LAB} = \frac{\alpha_e^2}{4E^2 \sin^4\theta/2} \frac{E'}{E} \left[\cos^2\frac{\theta}{2} + \frac{(E-E')}{m_\mu}\sin^2\frac{\theta}{2}\right]. \quad (2.6)$$

From these results, given in Eqs. (2.5, 2.6), it thus clear that the cross section between point-like particles can be written in terms of quantities that can be really measured in experiments, which in the LAB frame are the energies of the incident and outgoing electron, and the scattering angle θ.

Moreover, a crucial observation is that the dependence on the momentum transfer q^2 appears only in the second term of Eq. (2.6), being $(E - E') = -q^2/(2m_\mu)$ in the LAB frame. Therefore, large values of q^2 lead to a decrease of the cross section, as intuitively expected. This represents a characteristic of those scattering processes where only point-like particles are involved, as discussed further along this Chapter.

2.1.2 Elastic electron-proton scattering

A slightly more sophisticated scattering than $e^-\mu^- \to e^-\mu^-$ involves a lepton and a particle which is not point-like, such as the proton N. We consider in QED the elastic scattering electron-proton

$$e^-(k) + N(p) \to e^-(k') + N(p')$$

---

[1]We use this property: $\delta\left(E - E' - \frac{4EE'\sin^2\theta/2}{2m_\mu}\right) = \frac{1}{1+\frac{4EE'\sin^2\theta/2}{2m_\mu}}\delta\left(E' - \frac{E}{1+\frac{4E\sin^2\theta/2}{2m_\mu}}\right)$, which integrated over dE' gives the factor $\frac{E'}{E}$.

for which the leading order Feynman diagram is analogous to the one of Fig. 2.1. For simplicity, we assume again that the interaction is mediated by the exchange of one virtual photon, γ. This kind of process has been extensively studied over the years, with the first experiments dating back to the '50s at the Standford linear accelerator [62]. They discovered that the cross section $e - N$ had a strong dependence on the momentum transfer q^2 and the behavior was different from the one observed for $e - \mu$ scattering. This has been theoretically formalized assuming that the interaction $\gamma - N$ is described by a matrix element of the form

$$\langle N(p')|J_{em}(0)^\mu|N(p)\rangle = \bar{u}_N(p')\Gamma_{em}^\mu u_N(p) , \tag{2.7}$$

where Γ_{em}^μ is no longer γ^μ as for $\gamma - e$ interaction, but a linear combination of all possible four-vectors on which the kinematic may depend on [63]

$$\Gamma_{em}^\mu = A_1\gamma^\mu + iA_2\sigma^{\mu\nu}(p'-p)_\nu + iA_3\sigma^{\mu\nu}(p'+p)_\nu + A_4(p-p')^\mu + A_5(p+p')^\mu , \tag{2.8}$$

where $\sigma_{\mu\nu} = i/2[\gamma_\mu, \gamma_\nu]$. The coefficients A_i must be functions of Lorentz invariants, dependent in principle on $(p'+p)^2$ and $q^2 = (p-p')^2$. Since these two quantities depend one from each other, being $q^2 = 2m_p^2 - 2p' \cdot p$ and $(p'+p)^2 = 2m_p^2 + 2p' \cdot p$, it is sufficient to consider only one of them and is customary to use q^2. By using the Gordon identity[2] [60] and the electromagnetic current conservation, which is a consequence of the gauge invariance, it is possible to rewrite Eq. (2.8) as a combination of only two terms [60], namely

$$\Gamma_{em}^\mu = F_1(q^2)\gamma^\mu + F_2(q^2)\frac{i}{2m_p}\sigma^{\mu\nu}q_\nu . \tag{2.9}$$

F_1 and F_2 are real dimensionless functions that can only depend on q^2 and are the so-called electromagnetic *elastic structure functions* or *form factors*. Through an analogous calculation to the one of the cross section $e\mu \to e\mu$, with γ^μ replaced by Γ^μ in Eq. (2.9) for the proton vertex, one obtains the well-known *Rosenbluth formula* [62]

$$\frac{d^2\sigma}{d\Omega dE'} = \frac{\alpha_e^2}{4E^2\sin^4\theta/2}\left[\left(F_1^2 - \frac{q^2}{4m_p^2}F_2^2\right)\cos^2\frac{\theta}{2} - \frac{q^2}{2m_p^2}\left(F_1^2 + F_2^2\right)\sin^2\frac{\theta}{2}\right]\delta\left(E - E' + \frac{q^2}{2m_p}\right) . \tag{2.10}$$

This result suggests that the differential cross section is modulated by two q^2-dependent quantities, F_1 and F_2, that can be directly extracted from measurements of the angular dependence at several q^2. F_1, F_2 are important observables because they correspond to the Fourier transform of the electric and magnetic charge distribution, $\rho(\vec{r})$ and $\mu(\vec{r})$, through Born approximation [64]

$$F_1(q) = \int d^3r \rho(\vec{r})e^{i\vec{q}\cdot\vec{r}}, \quad F_2(q) = \int d^3r \mu(\vec{r})e^{i\vec{q}\cdot\vec{r}} . \tag{2.11}$$

---

[2]The Gordon identity reads: $\bar{u}(p')\gamma^\mu u(p) = \frac{1}{2m_p}\bar{u}(p')[(p+p')^\mu + i\sigma^{\mu\nu}q_\nu]u(p)$. It is valid if $\bar{u}_N(p')$ and $u_N(p)$ are solutions of the Dirac equation, i.e. $(\slashed{p} - m)u(p) = 0$ and $\bar{u}(p')(\slashed{p}' - m) = 0$.

Therefore, their measurements can provide information on the inner structure of the proton. In the earliest measurement of cross sections in the '50 [65] it was observed that the two proton form factors have approximately the same dependence on the momentum transfer squared up to 0.5 GeV^2 and they drop off as

$$F(q^2) \sim \frac{1}{\left(1 - \frac{q^2}{0.71\text{GeV}^2}\right)^2} \, . \tag{2.12}$$

By consequence, from the inverse Fourier transform of such parametrization, it became clear that the proton is an extended object whose electric charge distribution decays exponentially as e^{-r/r_0}, with $r_0 \sim 1$ fm.

However, in subsequent experiments conducted at SLAC in the '60s [3, 4], it was discovered surprisingly that at energies $|q^2| > 1$ GeV^2 (above the proton mass) the analogous form factors did not decrease at large q^2. This lead to the idea that the proton is not an elementary particle and that at high energies the electron can interact with its constituents.

In addition, at energies $|q^2| > 1$ GeV^2, production of new particles was also observed in the final state of $e - p$ collisions. This discovery is the basis of a new class of scattering processes called *inelastic scattering*, for which we need a new formalism.

2.2 Inelastic scattering

2.2.1 Inelastic electron-proton scattering

The reaction of our interest is referred to as *deep inelastic scattering*. It encodes a large number of processes in which the inner structure of hadrons is probed at large values of the momentum transfer. Examples are: *inclusive* (DIS) [66], *semi-inclusive* (SIDIS) and *exclusive* scattering processes, such as deeply virtual Compton scattering (DVCS) [67]. In DIS, such as $eN \to eX$, only the energy E' of the outgoing electron and the scattering angle θ are measured by the detector and what remains of the proton is not observed; therefore, X stands for anything the proton can break up into. On the contrary, in semi-inclusive scattering (SIDIS), a hadron is also detected among the final products of the collision, and the reaction will be $eN \to ehX$. DIS and SIDIS data are nowadays the major sources of information about parton distribution functions and provide information somewhat also complementary to each other, as we will see in Section 2.4.

Here we want to study the simplest inclusive process, $eN \to eX$, sketched in Fig. 2.2. In particular, we extract the cross section in the LAB frame and then compare it to the one of a generic elastic scattering.

Let us suppose again that the weak interactions can be neglected[3] and the main contribution comes from the exchange of one photon in QED. As discussed in Section 2.1.1, the differential

---

[3]This is a good approximation for $|q| < M_W$.
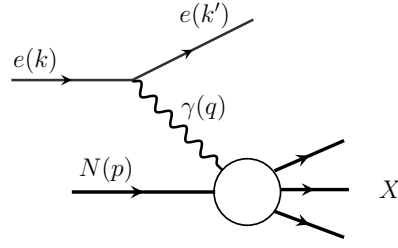
Figure 2.2 Schematic diagram of the inclusive inelastic scattering electron-proton: $eN \to eX$. X stands for all particles created in the collision.

cross section is proportional to the product of two tensors

$$\frac{d^2\sigma}{d\Omega dE'} \propto \frac{\alpha_e^2}{m_N q^4} \frac{E'}{E} L^{\mu\nu} W_{\mu\nu} \,, \tag{2.13}$$

where E, E' are the energies of the incoming and outgoing electron, m_N is the proton mass and $L^{\mu\nu}$, $W_{\mu\nu}$ are the electronic and hadronic tensor. The electronic tensor is the same as for the process $e\mu \to e\mu$ and is given in Eq. (2.4) for unpolarized scattering. What is different is the form of $W_{\mu\nu}$, which now depends on the vertex $\gamma N \to X$ and therefore on the matrix element $\langle X | J^\mu | N \rangle$, with J^μ the electromagnetic current. The hadronic tensor for unpolarized scattering is defined as [63]

$$W_{\mu\nu} = \frac{1}{2} \sum_{\substack{\text{initial} \\ \text{spins}}} \sum_X (2\pi)^3 \delta^4 (P_X - p - q) \langle N | J_\mu(0) | X \rangle \langle X | J_\nu(0) | N \rangle \,, \tag{2.14}$$

where $\sum_X$ includes the factor $\frac{d^3 p_j}{(2\pi)^3 2E_j}$ for each particle j contained in X. We note that the tensor $W_{\mu\nu}$ is Hermitian, i.e. $W_{\mu\nu} = W_{\nu\mu}^*$, and therefore it can be decomposed in a symmetric (S) and antisymmetric (A) part under exchange $\mu \leftrightarrow \nu$ [63]

$$W_{\mu\nu} = W_{\mu\nu}^S + i W_{\mu\nu}^A \,, \qquad W^S, W^A \in \mathbb{R} \,. \tag{2.15}$$

However, after contraction with the leptonic tensor of Eq. (2.4), only the symmetric part W^S will contribute to the cross section in (2.13), since $L_{\mu\nu} = L_{\nu\mu}$. By consequence, the most general form for $W_{\mu\nu}$ reads

$$W_{\mu\nu} = A_1 g_{\mu\nu} + A_2 q_\mu q_\nu + A_3 (q_\alpha p_\beta + q_\beta p_\alpha) + A_4 p_\alpha p_\beta \,, \tag{2.16}$$

where A_i are real functions that may depend on p^2, q^2, $p \cdot q$. A crucial property that $W_{\mu\nu}$ has to satisfy is the electromagnetic current conservation, which implies $q^\mu W_{\mu\nu} = 0$. This condition can be used to rewrite A_2 and A_3 in terms of A_1 and A_4, and introducing the standard notation [63]

$$W_1 = -\frac{A_1}{2m_N} \,, \quad \frac{W_2}{m_N^2} = \frac{A_4}{2m_N} \,, \tag{2.17}$$

the hadronic tensor simplifies into

$$\frac{W_{\mu\nu}}{2m_N} = W_1 \left(-g_{\mu\nu} + \frac{q_\mu q_\nu}{q^2} \right) + \frac{1}{m_N^2} W_2 \left(p_\mu - \frac{p \cdot q}{q^2} q_\mu \right) \left(p_\nu - \frac{p \cdot q}{q^2} q_\nu \right) . \qquad (2.18)$$

W_1, W_2 are real scalar functions, called *structure functions*. Finally, substituting the above expression into Eq. (2.13), the cross section in the LAB frame takes the form [63]

$$\frac{d^2\sigma}{d\Omega dE'} = \frac{\alpha_e^2}{4E^2 \sin^4 \theta/2} \left[2W_1 \sin^2 \frac{\theta}{2} + W_2 \cos^2 \frac{\theta}{2} \right] . \qquad (2.19)$$

From this result we can see that the cross section has the same angular dependence as for the elastic scattering $e\mu \to e\mu$ and $eN \to eN$, with the difference that the *structure functions* W_1, W_2 depend now on three variables (i.e. q^2, $p^2 = m_N^2$ and $p \cdot q$) instead of only on q^2, see Eq. (2.9) for the proton vertex. The Lorentz invariants used to describe DIS processes are the momentum transfer $Q^2 \equiv -q^2 > 0$ and one of the following variables

$$\nu \equiv \frac{p \cdot q}{m_N} \xlongequal{\text{LAB}} E - E', \qquad x \equiv \frac{Q^2}{2p \cdot q} = \frac{Q^2}{2m_N \nu} \quad \textbf{(Bjorken variable)} , \qquad (2.20)$$

where x is a dimensionless quantity, called *Bjorken variable*.

The Bjorken variable satisfies the relation $0 \le x \le 1$. This inequality follows from two conditions: **i)** for physical processes $Q^2 \ge 0$, since energies cannot be negative; **ii)** for the baryon number to be preserved, we must have $M_X \ge m_N$, which means that at least one baryon is produced in the final state. From the above, it follows that

$$M_X^2 = (p+q)^2 = m_N^2 + 2m_N \nu - Q^2 \ge m_N^2 \quad \Rightarrow \boxed{Q^2 \le 2m_N \nu} , \qquad (2.21)$$

and $x = 1$ in the limit of elastic scattering, where $M_X = m_N$.

The denomination "Bjorken variable" is due to the prediction by Bjorken (in 1969) that the structure functions W_1 and the combination νW_2 only depend on the variable x in the limit $Q^2 \to \infty$ and $\nu \to \infty$, at x fixed. This prediction was confirmed in experiments conducted at SLAC in the '60s, where W_1 and νW_2 (a priori function of two variables) were found to be almost independent on Q^2, at fixed x and for $Q^2 > 1 \text{ GeV}^2$. This appeared in contrast to the behavior of the elastic form factors that decay rapidly with Q^2, as indicated in Eq. (2.12).

This remarkable discovery led to the idea of the proton (and hadrons) as made of structureless objects, which are struck by the virtual photon in the DIS regime. The constituents of hadrons were called *partons* and the behavior of the inelastic structure functions at large momentum transfer was called *Bjorken scaling*.

2.3 Parton Model

Since the Q^2-independence of the structure functions could not be explained by elastic scattering, a sophisticated model was formulated to interpret the experimental results. This model was introduced by Feynman in 1969 and is called *quark parton model* (QMP) [5, 6].

The basic assumption is that, at very large momentum transfer, lepton-hadron interactions are due to interactions of partons, because the virtual photon has a sufficient small wavelength ($\lambda \sim 1/Q$) to resolve the constituents of the target. The interaction $eN \to eX$ can be then described as in Fig. 2.3.
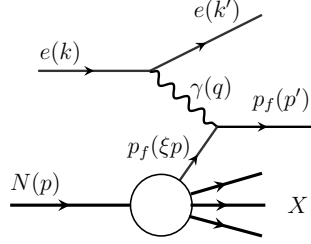
Figure 2.3 At large momentum transfer a lepton interacts with a parton.

Moreover, in the *naive* picture, partons behave as free particles. This assumption can be justified thinking that the fast-moving hadron is Lorentz contracted in the center of mass frame, where also time is dilated by relativistic effects. Therefore, lepton-parton interactions occur on a time scale which is much smaller than the typical interaction scales among partons themselves.

From the above, the parton model assumes that electron-proton cross sections can be factorized as

$$\sigma(eN \to eX) = \int_0^1 d\xi \sum_f f_f(\xi) \, \hat{\sigma}(e(k)p_f(\xi \, p) \to e(k') \, p_f(p')) \,, \qquad (2.22)$$

where the struck parton has quadri-momentum ξp^μ and $f_f(\xi)$ is the probability density that parton f carries a fraction ξ of the proton momentum and is called *parton distribution function*. In the equation above, $\hat{\sigma}$ is a partonic cross section that must have the same form as the one for $e - \mu$ scattering, see Eq. (2.5). In particular, the energy conservation in Eq. (2.5) now becomes

$$\delta \left(E - E' - \frac{Q^2}{2m_\mu} \right) \to \delta \left(\frac{Q^2}{2m_N x} - \frac{Q^2}{2\xi m_N} \right) = \delta \left[\frac{Q^2}{2m_N} \left(\frac{1}{x} - \frac{1}{\xi} \right) \right] = \frac{2m_N}{Q^2} x^2 \, \delta(\xi - x) \,, \qquad (2.23)$$

where m_μ has been replaced with the mass of a parton, i.e ξm_N. The result of Eq. (2.23) implies that the Bjorken variable $x = Q^2/(2p \cdot q)$, introduced in the previous Section, is nothing but the parton momentum. We can now use this result to rewrite the decomposed cross section in Eq. (2.22) as

$$\frac{d^2\sigma(eN \to eX)}{d\Omega \, dE'} = \sum_f f_f(x) \frac{\alpha_e^2 Q_f^2}{4E^2 \sin^4 \theta/2} \left(\frac{2m_N}{Q^2} x^2 \cos^2 \frac{\theta}{2} + \frac{1}{m_N} \sin^2 \frac{\theta}{2} \right) \,, \qquad (2.24)$$

where Q_f is the electric charge of each quark and we have assumed that the partonic cross section, $\hat{\sigma}$, is equivalent to Eq. (2.5). On the other hand, the above result must be equal to the DIS cross section (2.19) which depends on the structure functions W_1, W_2. From the comparison of Eq. (2.24) with Eq. (2.19), we get the following relations for the structure

functions

$$m_N W_1(x, Q^2) = \frac{1}{2} \sum_f Q_f^2 f_f(x) \equiv F_1(x), \quad \nu W_2(x, Q^2) = \sum_f Q_f^2 x \, f_f(x) \equiv F_2(x), \quad (2.25)$$

which are the quantitative formulation of the scaling predicted by Bjorken. The above result is also important because it relates the structure functions to parton densities $f_f(x)$.

An illustration of the Bjorken scaling is reported in Fig. 2.4 for the inelastic proton structure function F_2, obtained from unpolarized scattering. As can be seen, in the range $0.1 \lesssim$

Figure 2.4 Unpolarized proton structure function F_2, measured from electromagnetic scattering of electrons and positrons on protons (collider experiments H1 and ZEUS for $Q^2 > 2$ GeV), and for electrons (SLAC) and muons (BCDMS, E665, NMC) on a fixed target. For the purpose of plotting, F_2 is multiplied by 2^{i_x}, where i_x is the number of the x bin, ranging from $i_x = 1$ ($x = 0.85$) to $i_x = 24$ ($x = 0.00005$). Figure from Ref. [68].

$x \lesssim 0.5$, F_2 is approximately constant with Q^2, in agreement with Bjorken's prediction. On the other hand, we can also notice that there are x-regions in which F_2 is not Q^2-independent. For instance, at small x values the structure function increases with Q^2, namely when the probe has a smaller wavelength. These scaling violations were not predicted by the naive parton model and were later explained as an effect of the strong nuclear force, whose strength increases at large distances (or equivalently at low-x). Indeed, in the framework of QCD in which partons are identified by quarks and gluons, we know that quarks emit gluons with higher probability at low-x. Therefore, if Q^2 is sufficiently large, the particles produced via strong interaction can be resolved as separate objects and this leads to an increase of the structure functions, as can be seen in Fig. (2.4). As a consequence, also the parton densities $f_f(x)$ will depend on the resolving power Q^2, as illustrated in Section 2.4.

2.3.1 OPE analysis and light-cone dominance

The parton densities (or parton distribution functions), introduced within the naive parton model, emerge also naturally from the analysis of the hadronic tensor in the deep inelastic scattering. In this Section we want to briefly summarize how they can be derived in this framework, from which a fundamental property of parton distributions also arises, namely the *light-cone dominance*. The starting point is the definition of the hadronic tensor, here rewritten

$$W_{\mu\nu} = \frac{1}{2} \sum_{\substack{\text{initial} \\ \text{spins}}} \sum_X (2\pi)^3 \delta^4(P_X - p - q) \langle N|J_\mu(0)|X\rangle\langle X|J_\nu(0)|N\rangle . \qquad (2.26)$$

Applying a translation operator $\hat{P}$, which acts in the following way

$$\langle N|J_\mu(0)|X\rangle = \langle N|e^{-i\hat{P}\cdot x}J_\mu(x)e^{i\hat{P}\cdot x}|X\rangle = e^{-i(P-p_x)x}\langle N|J_\mu(x)|X\rangle , \qquad (2.27)$$

together with the completeness relation of the states and the Dirac-delta integral representation

$$\sum_X |X\rangle\langle X| = 1 , \qquad \delta^4(P + q - p_X) = \int \frac{d^4x}{(2\pi)^4} e^{i(P+q-p_X)x} , \qquad (2.28)$$

we can see that the hadronic tensor can be written in terms of commutator of the currents

$$W_{\mu\nu} = \frac{1}{4\pi} \int d^4x \, e^{iqx} \langle N|[J_\mu(x), J_\nu(0)]|N\rangle . \qquad (2.29)$$

Note that in the derivation we have added an extra term that is proportional to $J_\nu(0)J_\mu(x)$. This is allowed because its contribution must vanish, as it would violate the kinematic of the physical region, i.e $M_X \geq m_N$ and $-q^2 < 0$.

From Eq. (2.29) it is evident that $W_{\mu\nu}$ can only receive non-zero contribution only for $x^2 \geq 0$, otherwise causality would be violated. Moreover, if we do not impose any constrain, for $Q \to \infty$ the exponential $e^{iq\cdot x}$ oscillates rapidly averaging out all contributions of the integrand. Thus, we can deduce that the hadronic tensor must have support only in the region where $|q \cdot x|$ is finite in the DIS limit. One can show that this condition is satisfied when $x^2 \leq const./Q^2$ [69], see Appendix A.1. Consequently, from the conditions $x^2 \geq 0$ and $x^2 \leq const./Q^2$, it follows that the hadronic tensor for DIS is governed by product of currents near the light-cone, $x^2 \sim 0$. In practice, this means that the cross section for $e-N$ inelastic scattering is dominated by short distance interactions, given that the interaction time is very small.

The light-cone dominance of the hadronic tensor is a crucial property in QCD, because is the basis for factorization theorems, whose essence is contained in Eq. (2.22). The derivation of factorization theorems, leading to parton distribution functions, makes use of the *operator product expansion* (OPE). The OPE has been proposed by Wilson as a way to deal with T-ordered product of fields that become singular when they are defined in the same points (for general reviews see e.g. textbooks [60, 61, 70]). According to the OPE, the product of any

two operators $O_1(x) O_2(0)$ can be written as expansion of local operators in the limit $x \to 0$

$$\lim_{x \to 0} O_1(x)O_2(0) = \sum_n C_n(x)O_n(0) \, , \tag{2.30}$$

where $O_n(0)$ are well-defined local operators and C_n (called Wilson coefficients) contain the singularities. In QCD and in the DIS limit, it can be shown that C_n are independent on the external states where the operator product is computed and can be obtained in perturbation theory, given the asymptotic freedom of QCD at small separations x. Transforming to momentum space, that is what we need to calculate the hadronic tensor, one then obtain

$$\int d^4x \, e^{iqx} O_1(x)O_2(0) = \sum_n C_n(q)O_n(0) \qquad \text{for } |q| \to \infty \, , \tag{2.31}$$

where the dependence on q is only contained in the Wilson coefficients. By applying the optical theorem to the hadronic tensor (see e.g. [60]), one can demonstrate that the local operators $O_n(0)$ in Eq. (2.31) depend on both quark and gluonic fields; for vector currents with quarks of flavor f, O_n takes the form

$$O_f^{(n)\mu_1...\mu_n} = \bar{\psi}_f \gamma^{\{\mu_1}(iD^{\mu_2})...(iD^{\mu_n\}})\psi_f - \text{traces} \, . \tag{2.32}$$

In the equation above, the spin indices $\mu_1...\mu_n$ are intended to be symmetrized and the traces of the operator have been subtracted. When the local operators O_f are evaluated between two proton states with momentum P, we get

$$\langle N| O_f^{(n)\mu_1...\mu_n} |N\rangle = 2A_f^{(n)} P^{\mu_1} P^{\mu_2}...P^{\mu_n} - \text{traces} \, , \tag{2.33}$$

where $A_f^{(n)}$ are dimensionless quantities, depending on the operator. Their physical interpretation becomes immediately clear considering the case of 1-spin operator ($n = 1$), which is just the vector current. Indeed, from Eqs. (2.32, 2.33), we have that the matrix element

$$\langle N|\bar{\psi}_f\gamma^\mu \psi|N\rangle = 2A_f^{(1)} P^\mu \tag{2.34}$$

has to be equal to $\langle N|\bar{\psi}_f\gamma^\mu \psi|N\rangle = \bar{u}(P)\gamma^\mu u(P) F_f$ after spin-average (namely $2P^\mu F_f$). F_f is a form factor analogous to the one introduced in Section 2.1.2, corresponding here to the number of quarks minus antiquarks of flavor f in a proton state. By consequence, $A_f^{(1)} = F_f$ and knowing that the valence quark content of the proton is *uud*, we obtain

$$A_f^{(1)} = 2 \quad \text{for } f = u \, , \qquad A_f^{(1)} = 1 \quad \text{for } f = d \, . \tag{2.35}$$

From this argument, it comes natural to introduce distribution functions $f_f(x)$ as quantities that count the number of quarks and antiquarks inside a hadron and whose *moments* match the coefficients $A_f^{(n)}$ of the OPE applied to the hadronic tensor.

2.3.2 Definition of parton distributions

Parton distribution functions are usually defined in the light-cone frame, where the hadron is moving along one direction with momentum $P = (P^+, P^-, \mathbf{0}_\perp)$, with *plus/minus* components $P^\pm = (P^0 \pm P^3)/\sqrt{2}$. For a non-polarized hadron, the unpolarized PDFs are defined as [70]

$$q_f(x) = \frac{1}{4\pi} \int_{-\infty}^{+\infty} d\xi^- e^{-ixP^+\xi^-} \langle N|\bar{\psi}_f(\xi^-)\gamma^+ W(\xi^-,0)\psi_f(0)|N\rangle \,, \qquad (2.36)$$

where $|N\rangle$ denotes the hadron state (in this work we consider only the proton) and γ^+ is the combination of the Dirac matrices given by $\gamma^+ = (\gamma^0 + \gamma^3)/\sqrt{2}$. The light-cone directions are taken as $\xi^\pm = (\xi^0 \pm \xi^3)/\sqrt{2}$ and $W(\xi^-,0) = e^{-ig\int_0^{\xi^-} d\eta^- A^+(\eta^-)}$ is a product of gluon fields that guarantee the gauge invariance of the distribution.

We note that, by the definition of PDFs, the transverse components of the parton momentum fraction with respect to the direction of the hadron momentum are integrated over and x represents the colliner momentum fraction. The matrix element in Eq. (2.36) can be interpreted as the probability amplitude that a quark f is extracted from the proton at coordinate 0 and is inserted back at ξ^-, propagating on the light-cone.

For a polarized hadron, one can study how partons are sensitive to its polarization and define two polarized distributions, known as *helicity* $\Delta q_f(x)$ and *transversity* $\delta q_f(x)$ PDFs. They quantify the parton densities with spin parallel and antiparallel to the one of a longitudinally and transversely polarized hadron and are defined in an analogous way to the unpolarized PDF [70]

$$\Delta q_f(x) = \frac{1}{4\pi} \int_{-\infty}^{+\infty} d\xi^- e^{-ixP^+\xi^-} \langle N|\bar{\psi}_f(\xi^-)\gamma^+\gamma_5 W(\xi^-,0)\psi_f(0)|N\rangle \,, \qquad (2.37)$$

$$\delta q_f(x) = \frac{1}{4\pi} \int_{-\infty}^{+\infty} d\xi^- e^{-ixP^+\xi^-} \langle N|\bar{\psi}_f(\xi^-)\gamma^+\gamma_5\gamma_j W(\xi^-,0)\psi_f(0)|N\rangle \,. \qquad (2.38)$$

In $\delta q_f(x)$, j-index is purely spatial and is orthogonal to the direction of the hadron momentum.

A simplified illustration of the physical interpretation of these three distributions is reported in Fig. 2.5, where the blue and black arrows denote the spin direction of the proton and quark respectively.

The definitions in Eqs. (2.36-2.38) hold only for quarks, and the following crossing relations

$$\bar{q}_f(x) = -q_f(-x)\,, \quad \Delta\bar{q}_f(x) = \Delta q_f(-x)\,, \quad \delta\bar{q}_f(x) = -\delta q_f(-x)\,, \qquad (2.39)$$

relate quark distributions to their antiquark counterparts [70]. Thus, from the negative x-region we can read the antiquark densities. As concerns the gluon PDFs, explicit formulae can be found for instance in Refs. [19, 71–73].

$$q(x) = q^{\rightarrow} + q^{\leftarrow} \qquad\qquad \Delta q(x) = q^{\rightarrow} - q^{\leftarrow}$$

$$\delta q(x) = q_{\perp} + q_{\top}$$

direction of motion
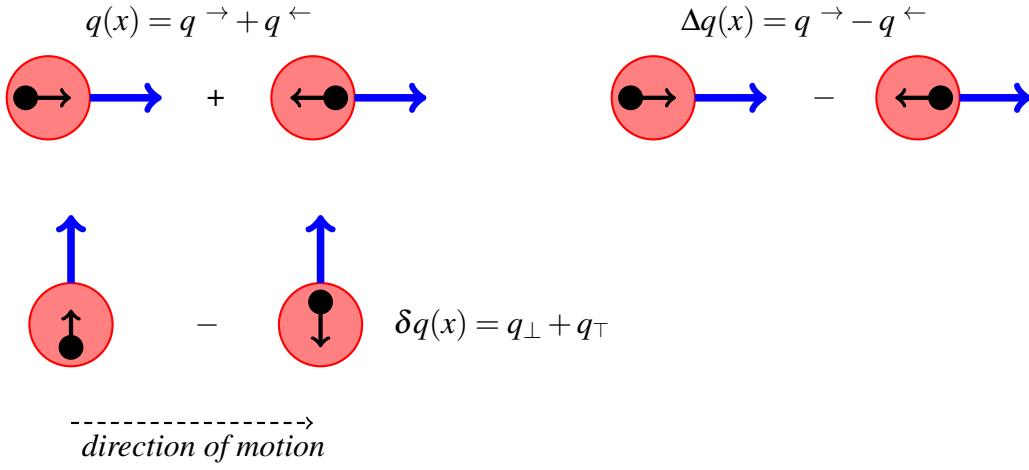
Figure 2.5 Schematic visualization of the three PDFs: unpolarized, helicity (left and right in the top panel) and transversity (low panel). The blue and black arrows denote the direction of the spin of the proton and quark respectively. In all three figures, it is assumed that the proton is moving along the direction depicted by the dashed line.

2.3.3 Moments of PDFs and sum rules

To reproduce the characteristics of a hadron (e.g. the valence quark content), PDFs have to satisfy certain constraints, which can be derived in a very intuitive way or directly from the operator definition of PDFs by applying a *Mellin transform*. The theoretical constraints are usually formulated in terms of *moments* which for a specific quark flavor are given by

$$\langle x^n \rangle_f \equiv \int_0^1 dx \, x^{n-1} q_f(x) \,. \tag{2.40}$$

Here q_f is the unpolarized PDF, but the same definition in Eq. (2.40) also applies for the helicity and transversity distributions. The integration range for computing the Mellin moments can be in principle extended to $x \to \infty$, since PDFs vanish for $x > 1$. This property can be used to derive the so-called *number sum rules*, which involve the zeroth moment of the difference between quark-antiquark unpolarized distributions. Indeed, for $n = 1$, we have

$$
\begin{aligned}
\int_0^1 dx \, [q_f(x) - q_{\bar{f}}(x)] &= \int_0^1 dx \, q_f(x) + \int_{-1}^0 dx \, q_f(x) = \int_{-\infty}^{\infty} dx \, q_f(x) \\
&= \frac{1}{4\pi} \int_{-\infty}^{\infty} dx \int_{-\infty}^{+\infty} d\xi^- e^{-ixP^+\xi^-} \langle N|\bar{\psi}_f(\xi^-)\gamma^+ W(\xi^-,0)\psi_f(0)|N\rangle \\
&= \frac{1}{4\pi} \int_{-\infty}^{+\infty} d\xi^- \delta(\xi^- P^+) \dots = \frac{1}{2P^+}\langle N|\bar{\psi}_f(0)\gamma^+ \psi_f(0)|N\rangle = N_f \,,
\end{aligned} \tag{2.41}
$$

where N_f is the net number of quarks with flavor f in the proton state and is exactly the moment we obtain from the OPE analysis, that we called $A_f^{(1)}$ in Eq. (2.35). Thus, to match the valence quark content of the proton (*uud*), the following sum rules have to be satisfied at

any energy scale

$$\int_0^1 dx\,[q_u(x) - \bar{q}_u(x)] = 2 \,, \qquad \int_0^1 dx\,[q_d(x) - \bar{q}_d(x)] = 1 \,,$$

$$\text{and} \quad \int_0^1 dx\,[q_f(x) - \bar{q}_f(x)] = 0 \quad \text{for } f = s,c,b,t \,. \tag{2.42}$$

For the separate flavors there is no constrain, since quarks can be continuously created via exchange of gluons.

Another theoretical constrain is the so-called *momentum sum rule*

$$\int_0^1 \sum_f x q_f(x)\,dx = 1 \quad \text{or} \quad \langle x \rangle_u + \langle x \rangle_{\bar{u}} + \ldots + \langle x \rangle_g = 1 \,, \tag{2.43}$$

which imposes that the total momentum fraction carried by all partons (including gluons) must be unity. Experimental results on the structure function F_2 have revealed that each parton contributes to the total momentum with a different amount and the gluon predominates at low-x, as illustrated in Section 2.4.1 in Fig. 2.7. In Appendix A.2 we generalize Eq. (2.41) and show that the moments of PDFs are always related to local matrix elements between two nucleon states. The derivation is carried out for the unpolarized case, but it also applies to the polarized distributions.

In analogy to the unpolarized case, also for the polarized PDFs it is possible to define moments of the distributions and relate them to specific matrix elements. Following the same logical steps as in Eq. (2.41), we get the zeroth moment of the helicity distribution

$$\int_0^1 dx\,[\Delta q_f(x) + \Delta q_{\bar{f}}(x)] = \frac{1}{2P^+} \langle N | \bar{\psi}_f(0) \gamma^+ \gamma_5 \psi_f(0) | N \rangle \,, \tag{2.44}$$

where the gamma structure γ^+ is now replaced with $\gamma^+ \gamma_5$. Unlike the unpolarized case, the antiquark helicity distribution has a plus sign in the integral of the left hand side, which is a consequence of the crossing relation $\Delta q_{\bar{f}}(x) = \Delta q_f(-x)$, see Eq. (2.39).

An important quantity is the zeroth moment of the flavor non-singlet combination $(\Delta q_u + \Delta q_{\bar{u}}) - (\Delta q_d + \Delta q_{\bar{d}})$. It is related to the neutron axial decay constant, the well-known nucleon *axial charge* g_A, via

$$\int_0^1 dx\,[(\Delta q_u + \Delta q_{\bar{u}}) - (\Delta q_d + \Delta q_{\bar{d}})] = \frac{1}{2P^+} \langle N | \bar{u}\gamma^+\gamma_5 u - \bar{d}\gamma^+\gamma_5 d | N \rangle = g_A^{u-d} \,. \tag{2.45}$$

g_A^{u-d} is extracted in beta decay experiments ($n \to p\,e\,\bar{\nu}_e$), aiming at the investigation of electroweak interactions in the Standard Model. The latest PDG value is $g_A = 1.2724(23)$ [11].

Another fundamental quantity describing the inner structure of the proton is the zeroth moment of the transversity distribution, the *tensor charge* g_T. The following integral

$$g_{T,f} = \int_0^1 dx\,(\delta q_f(x) - \delta \bar{q}_f(x)) \,, \tag{2.46}$$

19

quantifies the net number of quarks with helicity parallel and antiparallel to that of a transversely polarized proton, as indicated in Fig. 2.5. Thus, the tensor charge gives information about the transverse spin structure of the proton and it has been receiving a lot of attention from experiments because may provide a potential probe of new tensor interactions, as well as input for dark matter searches [74].

It is important to stress that, unlike the unpolarized case, the currents associated to the polarized PDFs are not conserved, so there is no direct determination of the corresponding charges. However, they can be extracted experimentally, as well as with non-perturbative methods.

2.4 Obtaining parton distributions

As mentioned in Section 2.3.1, factorization theorems applicable to a large class of deep inelastic scattering processes offer a well-consolidated framework to gain knowledge on parton distributions. The traditional method relies on a procedure called *global QCD analysis* [23, 24, 75–79]. PDFs are extracted through simultaneous fits to a wide set of experimental data, coming for instance from fixed target experiments and high energy collisions, where particle beams are directed against each other (such as $e^{\pm}p$, $p\bar{p}$ and pp) leading to heavy quarks and jet-production [23]. Each process, occurring at a certain value of the momentum transfer Q^2, gives information on a specific x-range of the distribution, as illustrated in Fig. 2.6 for the case of unpolarized scattering. As we can see, experimental data do not cover uniformly the
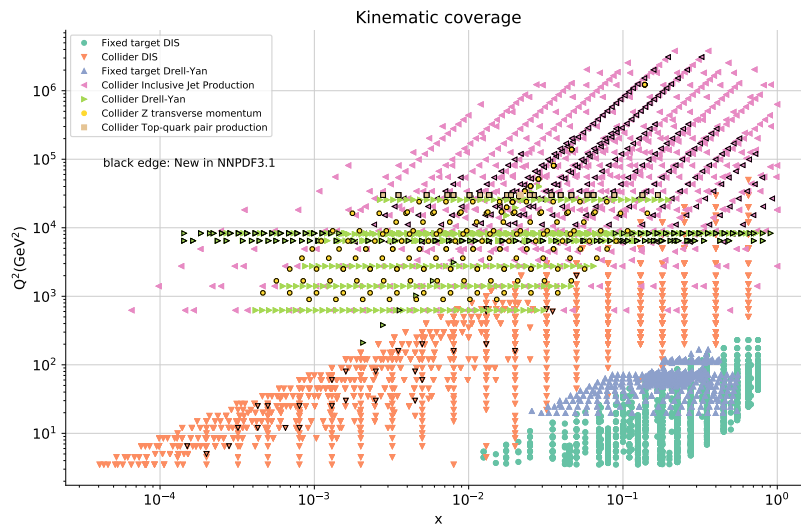
Figure 2.6 Typical kinematic coverage in the (x, Q^2) plane of the DIS and proton-(anti) proton scattering data, that are used as input to determine unpolarized PDFs. Every measurement can be mapped in the (x, Q^2) plane. Figure from Ref. [23].

entire domain and abound for intermediate x-values. The small x-region $(x \ll 1)$ is one of the less constrained, because it can only be accessed at energies much larger than the nucleon mass. This can be understood through the connection between the Bjorken x-variable and the

invariant mass squared M_X^2 of the scattering, given by

$$M_X^2 = (p+q)^2 = p^2 + 2p \cdot q - Q^2 = m_N^2 + \frac{Q^2}{x} - Q^2 \implies x = \frac{Q^2}{M_X^2 - m_N^2 + Q^2}. \qquad (2.47)$$

Thus, we can see that for $x \ll 1$ we must have $M_X^2 \gg m_N^2$.

From Fig. 2.6, it is also clear that the most complete information on the momentum structure of hadrons can be obtained by combining several data sets. This procedure is nowadays carried out by many collaborations performing global fits, such as the CT group [80], MMHT with the recent release [26], NNPDF, whose methodology for global fits was explained for the first time in [81], ABM [28], CJ collaboration from Jefferson Lab [82] and HERAPDF [83]. The fitting methodology relies first of all on the choice of a parametrization at a certain input scale Q_{ref}^2 ($\sim 1 - 2$ GeV^2), that can be written as [22]

$$f(x, Q_{ref}^2, \{a_i\}) = x^{a_1} (1-x)^{a_2} C(x, \{a_j\}). \qquad (2.48)$$

The terms x^{a_1} and $(1-x)^{a_2}$ govern the PDF behavior for small-x and in the elastic limit $x \to 1$ respectively, while $C(x, \{a_j\})$ is an interpolating function which determines the PDF shape away from the limits $x \to 0$ and $x \to 1$. The overall behavior of the distribution is characterized by the parameters $\{a_i\}$, which depend on the specific flavor combination and are determined through fits to structure functions. Moreover, the form of $C(x, \{a_j\})$ is not known a priori and many different approaches and parameterizations are usually employed in global analyses. This non-uniqueness choice is among the sources of uncertainties of PDFs determinations. Other delicate points involve the perturbative computation of the partonic cross section $\hat{\sigma}$, which is carried out with truncation up to a certain order in the perturbative expansion; this leads to different kinds of fits (leading-order (LO), next-to-leading order (NLO) etc...). Additional uncertainties are due to ambiguities in the fitting procedure and lack of experimental data in certain x-regions, as illustrated in the representative kinematic coverage of Fig. 2.6. For a detailed review about PDFs uncertainties and determinations from fitting procedure see for instance [22, 23].

The difficulties mentioned above motivate searches for alternative approaches that could provide important insight into the inner structure of hadrons not relying on any ansatz.

In the next Sections we report examples for start-of-the-art global analyses for the unpolarized, helicity and transversity distributions, with special focus on the light-content of the proton and in particular on the $u - d$ flavor structure, of interest in this work.

2.4.1 State-of-the-art unpolarized PDFs

In Fig. 2.7 we show the momentum decomposition of the proton among different partons, as obtained from PDF4LHC15 NLO analysis [84]. The distributions are shown at two different scales, $\mu^2 = Q^2 = 4$ GeV^2 and $\mu^2 = Q^2 = 10$ GeV^2. The evolution from the reference scale Q_{ref}^2 is determined by solving DGLAP evolution equations [85–87]. The energy scale μ denotes here both *factorization* (μ_F) and *renormalization* (μ_R) scales, which are usually

taken equal to the scale of the process ($\mu = \mu_F = \mu_R = Q$). Fig. 2.7 shows the unpolarized distributions for u, d quarks, for the valence combinations $u_v = u - \bar{u}$ and $d_v = d - \bar{d}$ and for the sea quarks and the gluon. The latter is scaled by a factor 10. We observe that the
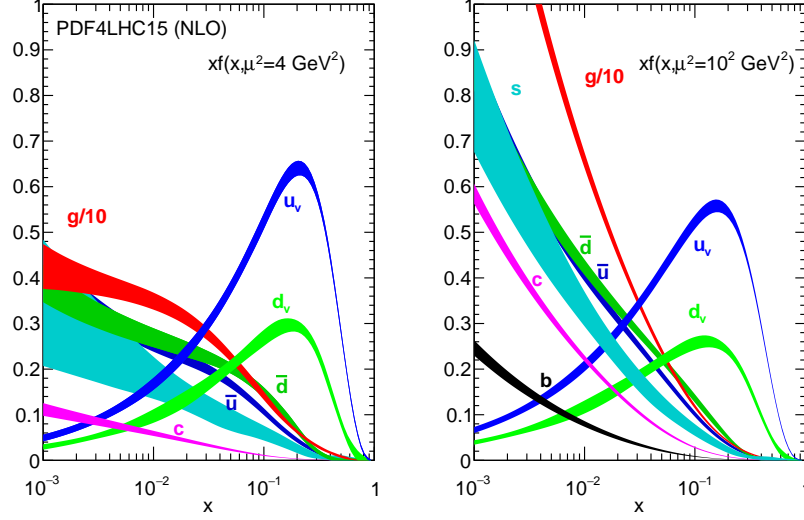
Figure 2.7 Unpolarized PDF4LHC15 NLO [84] PDFs at the scale $\mu^2 = Q^2 = 4 \text{ GeV}^2$ (left) and $\mu^2 = Q^2 = 10 \text{ GeV}^2$ (right). PDFs for different quark flavors are shown: u, d, the valence combinations $u_v = u - \bar{u}$ and $d_v = d - \bar{d}$ and sea quarks. The gluon PDF is scaled by a factor 10. Figure from Ref. [22].

valence distributions u_v and d_v reflect the constrain from the number sum rules of Eq. (2.42). The gluon and sea quarks PDFs grow rapidly in the small x-region and this suggests that high energy collisions can trigger processes initiated by gluons and sea quarks with higher probability. Moreover, the rapid grow at small-x is also more pronounced at a larger Q^2, as can be seen from the comparison of the two panels in Fig. 2.7. This feature reflects the fact that structure functions at low-x have a logarithmic increase with Q^2 and it is also a demonstration of Bjorken scaling violations, as seen in Section 2.3.

Information about possible asymmetries in the light sector can be extracted from the differences $u(x) - d(x)$ and $\bar{d}(x) - \bar{u}(x)$. The comparison between three different sets in Fig. 2.8 shows some tension, which is remarkable for the antiquarks at small-x values, although the PDFs shape is overall similar.

2.4.2 State-of-the-art helicity PDFs

Helicity distributions are determined with less accuracy than the unpolarized ones, because there is less abundance of data, limited in a restricted range in the (x, Q^2) plane [22].

An example of helicity distribution for separate flavors and the gluon is illustrated in Fig. 2.9 at two energy scales, namely $\mu^2 = Q^2 = 4 \text{ GeV}^2$ and 10 GeV^2. From the comparison with their unpolarized counterparts at the same scale (right plot in Fig. 2.7), one can observe that the helicity PDFs are suppressed in the entire x-range and especially at small x, validating the theoretical constrain $|\Delta f(x, Q^2)| \leq f(x, Q^2)$ [89]. In Fig. 2.10 we show the helicity PDFs
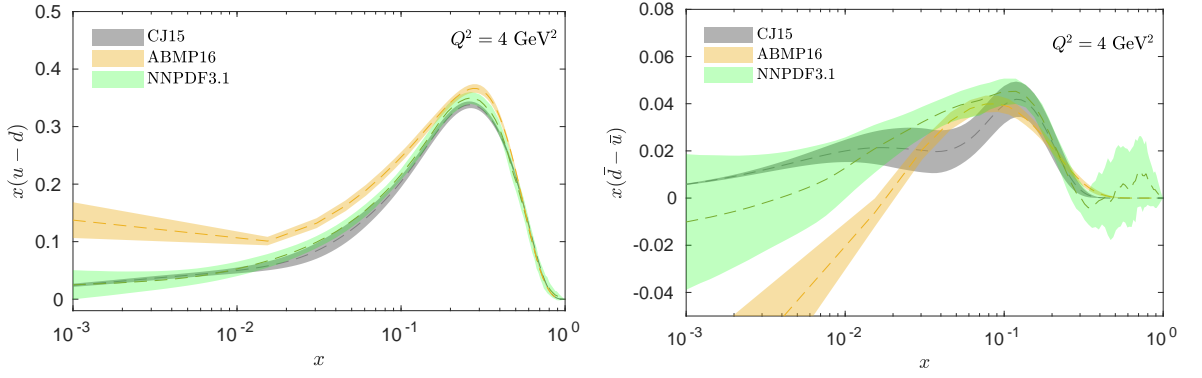
Figure 2.8 Unpolarized PDFs for the flavor structure $u - d$ (left) and $\bar{d} - \bar{u}$ (right), extracted from three global analyses: CJ15 [82], ABMP16 [28], NNPDF3.1 [25]. The scale is $Q^2 = 4\ \mathrm{GeV}^2$.
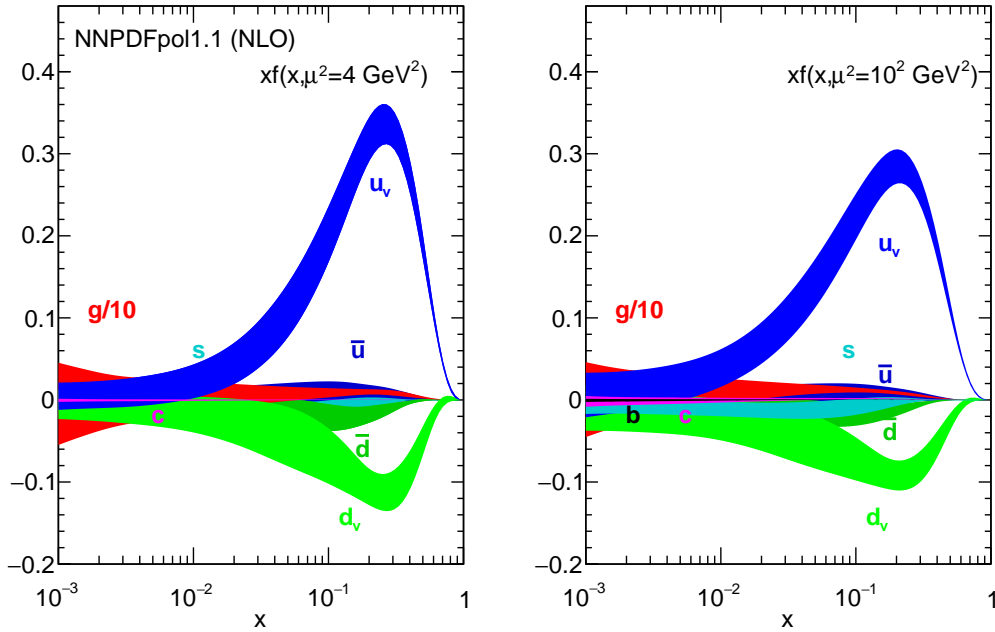
Figure 2.9 Momentum distribution for separate quark flavors and the gluon in a longitudinally polarized proton. The scale is $\mu^2 = 4\ \mathrm{GeV}^2$ (left) and $\mu^2 = 10\ \mathrm{GeV}^2$ (right). The distributions are extracted from NNPDFpol1.1 NLO analysis [88]. Figure from Ref. [22].

$\Delta u - \Delta d$ and $\Delta \bar{u} - \Delta \bar{d}$, which are among the distributions of interest in this work. From these PDFs one can quantify the flavor symmetry breaking for polarized quarks and antiquarks.

2.4.3 State-of-the-art transversity PDFs

The transversity distribution, $\delta q(x)$, is the collinear PDF that is determined with less accuracy up to date. In fact, in order to be measured, a change of the helicity state (from left- to right-handed or vice-versa) has to occur at the vertex interaction, but that is however forbidden in QED and QCD because of helicity conservation. This can be understood with the following argument. Let us denote with ϕ the angle between the spin and the direction of motion of a hadron. A transversely polarized state can be thus written as a linear combination of two
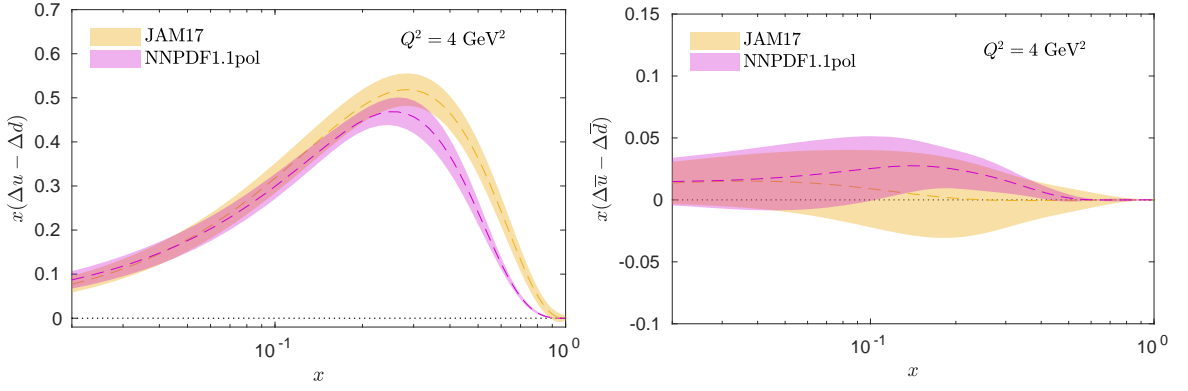
Figure 2.10 Comparison of helicity distributions $x(\Delta u - \Delta d)$ (left) and $x(\Delta \bar{u} - \Delta \bar{d})$ (right) between NNPDF1.1 [88] and JAM17 [90] global QCD analyses.

helicity states, $|L\rangle$ and $|R\rangle$

$$|\psi\rangle = \frac{1}{\sqrt{2}} \left(e^{-i\phi/2} |L\rangle + e^{i\phi/2} |R\rangle \right) . \tag{2.49}$$

From the equation above one can see that a cross section will depend on the angle ϕ if, and only if, a transition between two states with different chirality is allowed. For this reason, transversity PDF is a chiral-odd distribution and can be extracted only if coupled to other chiral-odd functions [91].

The first results for the transversity PDF for *up* and *down* quarks go back to 2007 only [92, 93] and use SIDIS data available from HERMES [94], COMPASS [95] and Belle [96] collaborations. Although estimates have noticeably improved over the years, phenomenological analyses based on only experimental data cannot impose tight constraints, as shown in Fig. 2.11 for the flavor combination $u - d$. These are the most recent determinations for the light quarks, obtained from the analysis in Ref. [97]. The tensor charge
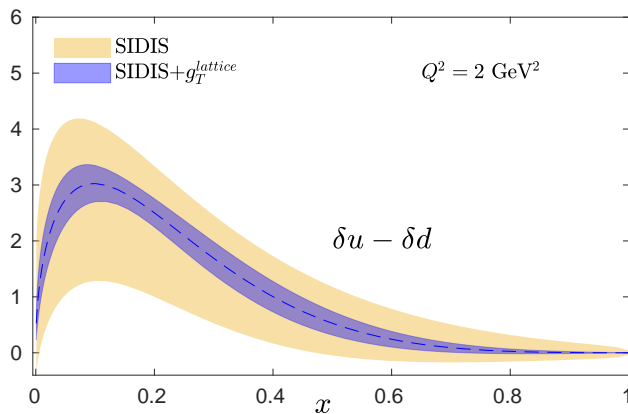
Figure 2.11 Transversity PDF, $\delta u - \delta d$, at $Q^2 = 2$ GeV^2 obtained from SIDIS data only (yellow) and SIDIS data analysis that uses as input the value of the tensor charge g_T^{u-d} extracted from lattice QCD (blue) [97].

$g_T^{u-d} = \int_0^1 dx \left(\delta u(x) - \delta d(x) \right)$ is found to be 0.9(8) when only SIDIS data are used. A more accurate determination of the distribution is obtained when the global fit is constrained via the non-perturbative estimate of g_T^{u-d} from lattice QCD. As can be seen, the inclusion of lattice

data for g_T^{u-d} strongly reduces the uncertainty in the x-dependence of the distribution by a factor of at least 3. This shows the enormous impact that information from first principles has on the determination of the transversity PDFs. The alternative tool to global analyses is called lattice QCD, which allows to study the dynamics of strong interactions in the non-perturbative regime. This approach and the method used in this work to extract PDFs are discussed in the next Chapter.

Chapter 3

Lattice QCD and parton physics in Euclidean space

As explained in the Introduction, perturbative methods cannot be applied to study quantities involving long distance physics, such as parton distribution functions. Lattice QCD is the only *ab initio* method to study the strong interactions in a non-perturbative regime. In this Chapter we describe the main ideas of lattice QCD and refer to Refs. [98, 99] for a more detailed introduction. In particular, we discuss the standard discretization of the fermion and gluon actions introduced by Wilson [13], and the improved discretization schemes that are relevant for our work. In the last Section we describe the method employed for the *ab initio* computation of parton distribution functions, namely the *quasi-PDF approach* [33]. Before introducing lattice QCD we give an overview of QCD in the continuum.

3.1   Introduction to QCD

The structure and interactions of hadrons are described by Quantum Chromodynamics (QCD), the gauge theory based on the SU(3) [100] *color* symmetry group, whose degrees of freedom are quarks and gluons. Quarks belong to the fundamental representation of the group and gluons are the generators, and therefore they carry three and eight values for the color charge respectively. More formally, the theory is formulated in terms of the following fields, defined at a specific point x of the space-time

$$\text{quarks}: \quad \psi(x)^f_{\alpha,c} \qquad\qquad \text{gluons}: \quad A^a_\mu(x) \quad . \tag{3.1}$$

Quarks exist in six different flavors, f, (*up, down, strange, charm, top, bottom*) and carry also Dirac and color indices, denoted by α, c respectively ($\alpha = 1, 2, 3, 4; c = 1, 2, 3$). Interactions among quarks are mediated by gluon fields, which are defined for every direction μ of the space-time and carry a color index a, running from one to eight. The gluon field can be written in a compact way as $A_\mu(x) = \sum_a A^a_\mu(x) T^a$, with T^a generators of the SU(3) group. The explicit form of T^a matrices strictly depends on the representation chosen for SU(3) group; for their expressions we refer to standard quantum field theory textbooks [60, 69].

The dynamics of the strong interactions is determined by the QCD Lagrangian density

$$\mathcal{L}_{QCD} = \mathcal{L}_G + \mathcal{L}_F \, , \tag{3.2}$$

with the action of the theory given by

$$S_{QCD} = \int d^4 x \, (\mathcal{L}_G + \mathcal{L}_F) \, . \tag{3.3}$$

$\mathcal{L}_G$ and $\mathcal{L}_F$ denote the gluon and fermion contributions to the QCD Lagrangian and read

$$\mathcal{L}_G = -\frac{1}{2}\mathrm{Tr}\left[F_{\mu\nu}F^{\mu\nu}\right] \, , \quad F_{\mu\nu} = \partial_\mu A_\nu - \partial_\nu A_\mu + i g_0 [A_\mu, A_\nu] \, , \tag{3.4}$$

$$\mathcal{L}_F = \sum_f \bar{\psi}_f(x)(i\gamma_\mu \overbrace{(\partial_\mu + ig_0 A_\mu)}^{D_\mu} - m_0^f) \, \psi_f(x) \, . \tag{3.5}$$

In the formulae above, g_0 is the *bare coupling constant*, $F_{\mu\nu}$ is the gluon field strength tensor, m_0^f the bare mass of a quark of flavor f and the operator D_μ is the so-called *covariant derivative*.

The QCD Lagrangian is constructed in such a way that the action is gauge invariant, i.e. it takes the same form when local rotations $\Omega(x)$ are applied to the quark fields

$$\psi(x) \to \psi'(x) = \Omega(x)\psi(x), \quad \bar{\psi}(x) \to \bar{\psi}'(x) = \bar{\psi}(x)\Omega(x) \, . \tag{3.6}$$

$\Omega(x) = e^{i\theta^a(x)T^a}$ are 3x3 unitary matrices ($\Omega^\dagger = \Omega^{-1}$ and $\det[\Omega] = 1$), acting in color space and depending on local parameters $\theta^a(x)$. For the QCD action to be gauge invariant, the gluon field, the covariant derivative and the strength tensor have to transform in the following way

$$A_\mu(x) \to A'_\mu(x) = \Omega(x)A_\mu(x)\Omega(x)^\dagger + \frac{i}{g_0}\left(\partial_\mu \Omega(x)\right)\Omega(x)^\dagger \, . \tag{3.7}$$

$$D_\mu(x) \to \Omega(x)D_\mu(x)\Omega(x)^\dagger, \qquad F(x) \to F'(x) = \Omega(x)F(x)\Omega(x)^\dagger \, . \tag{3.8}$$

From the relations above it follows that the object $D_\mu \psi(x)$ transforms exactly in the same way as the quark field $\psi(x)$, justifying the denomination of "covariant derivative".

It is important to remark that, unlike quantum electrodynamics (QED) that is based on the U(1) symmetry group, in QCD the commutator $[A_\mu, A_\nu]$ is non-zero. This allows for vertex interactions between a quark and gluon fields, and also vertices with three and four gluons that have no analogy with QED (see Fig.3.1). The presence of three- and four-gluon vertices makes QCD a highly non-trivial theory and increases the complexity of theoretical calculations. It is also believed that the structure of these interactions is responsible for the peculiar behavior of the strong coupling constant, which increases at large separations, confining quarks inside hadrons. This is a phenomenon for which there exists only a qualitative explanation and for this reason is known as *color confinement* problem.
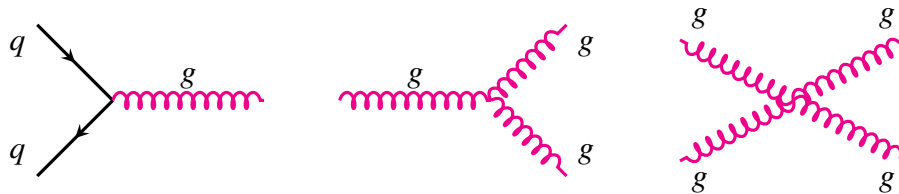
Figure 3.1 The interaction vertices of quarks and gluons. Solid (wavy) lines represent fermions (gluons).

An analytic determination of the strong coupling constant is impossible to achieve since that would require the evaluation of infinite diagrams, which take into account all possible vertex interactions between quarks and gluons. Calculations including 1-loop diagrams have indeed demonstrated that the value of the strong coupling increases as compared to the case of zero loop, implying that the higher contributions cannot be neglected in the series expansion. Moreover, complications arise when computing loop-graphs. Indeed, while the tree level diagrams are associated to well-defined amplitudes, in the loop diagrams one has to integrate over the internal momenta of the virtual particle. This leads to divergent integrals. This discussion is important because it allows us to introduce two fundamental concepts:

1. to study long distance physics we need to use alternative methodologies that do not rely on any assumption for the strong coupling value. These are usually refer to as *non-perturbative methods*. However, high energy processes can still be described in perturbative QCD and an example of those is the partonic cross section ($\hat{\sigma}$) of deep inelastic scattering, introduced in Eq. (2.22);

2. the parameters and fields contained in the QCD Lagrangian of Eqs. (3.4, 3.5) are not the physical ones and are called *bare*. The reason is that the divergences, arising from loop diagrams, make the amplitudes ill-defined. This issue is overcome via *regularization*, for instance by truncating the integrals up to some momentum Λ. Since eventually this cutoff must be removed ($\Lambda \rightarrow \infty$), all quantities have to be *renormalized*, in such a way that they remain finite order by order in perturbation theory. Thus, the physical values of the coupling constant and the mass of a quark of flavor f are given by

$$g_R^2 = Z_g g_0^2 \, , \quad m_R^2 = Z_m m_0^2 \, . \tag{3.9}$$

Z_g and Z_m are called *renormalization functions* (Z-factors) and are extracted by imposing a set of renormalization conditions.

3.2 Lattice QCD approach

The idea of a lattice as a way to regularize Yang-Mills theories was introduced by Wilson in his seminal work in 1974 [13] and the first numerical simulation on the lattice was performed by Creutz [101] in 1980 for the gauge group SU(2). The numerical approach applied to the theory of strong interactions is called lattice QCD. In this framework, physical observables

are computed by using the same tools as in statistical physics, or in other words through path integral formulation.

First of all, let us recall that within Feynman's path integral formalism the expectation value of a gauge invariant observable $\mathcal{O}$ in QCD is given by

$$\langle \mathcal{O} \rangle \equiv \langle \Omega | \mathcal{O} | \Omega \rangle = \frac{\int \mathcal{D}\psi \, \mathcal{D}\bar{\psi} \, \mathcal{D}A \, \mathcal{O}(\psi, \bar{\psi}, A) \, e^{iS}}{\int \mathcal{D}\psi \, \mathcal{D}\bar{\psi} \, \mathcal{D}A \, e^{iS}} \,, \tag{3.10}$$

where S is the continuum action given in Eq. (3.3).

To evaluate $\langle \mathcal{O} \rangle$ through statistical methods, it is necessary to switch from the Minkowskian to Euclidean space-time, by performing the following Wick rotation

$$(x_0, \vec{x}) \to (ix_0, \vec{x}) \,, \qquad d^4x \to id^4x \,. \tag{3.11}$$

In Euclidean space the action takes the form

$$S^E = \int d^4x \, (\mathcal{L}_F^E + \mathcal{L}_G^E) \,, \tag{3.12}$$

where $\mathcal{L}_F^E$ and $\mathcal{L}_G^E$ are

$$\mathcal{L}_F^E = \sum_f \bar{\psi}^f(x) \left(\gamma_\mu^E D_\mu(x) + m_0^f \right) \psi^f(x) \,, \tag{3.13}$$

$$\mathcal{L}_G^E = \frac{1}{2} \text{Tr}[F_{\mu\nu}(x) F_{\mu\nu}(x)] \,. \tag{3.14}$$

The Dirac matrices are related to the Minkownskian counterparts by

$$\gamma_0^E = \gamma_0 \,, \quad \gamma_{i=1,2,3}^E = -i\gamma_{i=1,2,3} \,, \quad \{\gamma_\mu^E, \gamma_\nu^E\} = 2\delta_{\mu\nu}\mathbb{1} \,. \tag{3.15}$$

The convention for the Dirac matrices used throughout this Thesis can be found in Appendix A.3. In Euclidean space, the expectation value in Eq. (3.10) becomes

$$\langle \mathcal{O} \rangle = \frac{1}{Z} \int D\bar{\psi} \, D\psi \, DA \, \mathcal{O}(\bar{\psi}, \psi, A) \, e^{-S^E} \,, \tag{3.16}$$

where Z is the QCD partition function

$$Z = \int D\bar{\psi} \, D\psi \, DA \, e^{-S^E} \,. \tag{3.17}$$

From Eqs. (3.16, 3.17) we can see that $\langle \mathcal{O} \rangle$ can be computed as an average with respect to the Boltzmann factor e^{-S^E} using Monte Carlo methods. From now on, we omit the index E and we will intend coordinates and fields as defined in Euclidean space, unless otherwise stated in the text.

However, the theory is not ready yet to be solved numerically, because the infinite degrees of freedom make impossible the treatment of the path integral. This difficulty is overcome replacing continuum space by a hypercubic grid of spatial and time extents L_x, L_y, L_z, L_t. The

neighboring points in each direction are separated by a distance a, called lattice spacing. In most practical applications, the spatial extent of the lattice is taken to be the same in all three directions, i.e. $L \equiv L_x, L_y, L_z$ and the hypercubic grid $L^3 \times L_t$ is said to be isotropic. A graphic representation of a 2-dimensional lattice is depicted in Fig. 3.2.
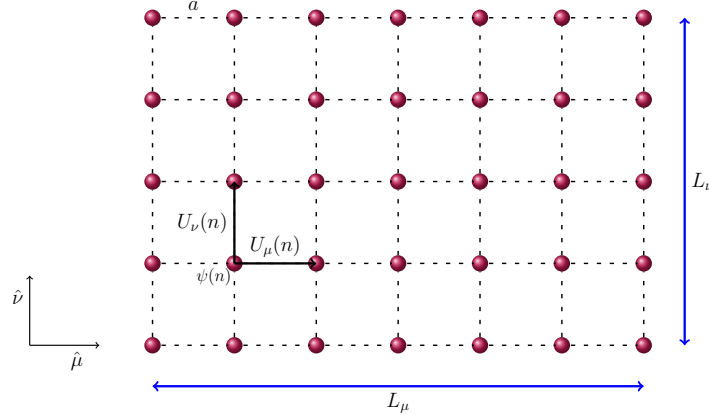
Figure 3.2 Schematic representation of a 2-dimensional lattice.

In the lattice, the Euclidean continuum coordinates x_μ assume discrete values

$$x_\mu \to n_\mu a, \quad a : \text{lattice spacing}, \quad n_\mu = 0, \ldots, L_\mu - 1, \tag{3.18}$$

and the 4-dimensional integral is transformed into a sum over all lattice sites as

$$\int d^4 x \to a^4 \sum_n . \tag{3.19}$$

The discretization of the space-time provides a natural way to regularize the theory, since the inverse of the lattice spacing serves as an ultra-violet momentum cutoff and makes all loop integrals finite. The reason is that on the lattice all functions are periodic in momentum space with a periodicity of $2\pi/a$, and the momenta p_μ are quantized as

$$p_\mu = \frac{2\pi}{L_\mu} n_\mu, \quad n_\mu = 0, 1, \ldots, L_\mu - 1. \tag{3.20}$$

The integrations are thus restricted to the interval $p_\mu \in [0, 2\pi/L)$ or alternatively to $(-\pi/a, \pi/a]$, making finite all quantities computed on the lattice.

Fermion fields (quarks and antiquarks) are placed at each point of the lattice, i.e. $\psi(x) \to \psi(n)$, $\bar{\psi}(x) \to \bar{\psi}(n)$ and they carry Dirac and color indices as in the continuum formulation. The gauge transformations of the fermion fields take the form

$$\psi(n) \to \psi'(n) = \Omega(n)\psi(n), \quad \bar{\psi}(n) \to \bar{\psi}'(n) = \bar{\psi}(n)\Omega(n), \tag{3.21}$$

where $\Omega(n)$ is an element of the SU(3) group defined at each lattice site n. To define a gauge invariant discretized version of the QCD continuum action, it is necessary to introduce *link*

variables $U_\mu(n)$ as a discrete version of the path ordered product

$$U_\mu(n) \equiv U(n, n+\hat{\mu}) = e^{iag_0 A_\mu(n)} \ . \tag{3.22}$$

$U_\mu(n)$ are SU(3) matrices that belong to the fundamental representation of SU(3) group, like the fermion fields, whilst $A_\mu(n)$ are algebra-valued lattice gauge fields. From Eq. (3.22), we can see that link variables connect neighboring sites on the lattice and are oriented, since they can also point to negative directions according to

$$U_{-\mu}(n) \equiv U(n, n-\hat{\mu}) = e^{-iagA_\mu(n-\hat{\mu})} = U_\mu(n-\hat{\mu}, n)^\dagger = U_\mu(n-\hat{\mu})^\dagger \ . \tag{3.23}$$

Finally, for the gauge action to be invariant under transformations $\Omega(n)$, the link variables have to transform in the following way

$$U_\mu(n) \rightarrow U'_\mu(n) = \Omega(n)\,U_\mu(n)\,\Omega(n+\hat{\mu})^\dagger \ . \tag{3.24}$$

Having discretized space-time, the theory can be solved numerically on a supercomputer. The number of degrees of freedom remains still large and simulations are computationally very demanding. In fact, the hypercubic grid must have sufficiently large volume and small enough lattice spacing so that finite volume and discretization effects are small or negligible. In practice, lattice spacings used in numerical simulations are typically restricted in the range 0.05 fm $\lesssim a \lesssim 0.1$ fm. Ideally, even smaller lattice spacing would be desirable, but the lower bound is limited by the increasing of computational cost. The reason is the critical slowing down [102], which affects lattice QCD simulations. Thus, to measure observables on the lattice, one has to perform computations at different values of lattice spacings (at least three) and eventually extrapolate the results to $a \rightarrow 0$. The limit $a \rightarrow 0$ is called *continuum limit*. The functional form of the extrapolation strictly depends on the observable under study and on the discretized version of the QCD action. Therefore, even if observables are not affected by any discretization effects after the continuum limit is performed, it is beneficial to construct lattice actions that have reduced cutoff effects. This also allows to employ relatively larger values of the lattice spacing (but still $a \leq 0.1$ fm) and obtain results of the same quality. Different discretization schemes, *naive* and *improved*, will be discussed in the next Sections.

3.3 Standard discretization schemes

The first formulation of non-Abelian gauge theories on a discretized space-time was proposed in 1974 by Wilson in the seminal work [13]. We first start with the description of the standard Wilson pure gauge action to move then to fermion action. The formulation of the fermionic part is much less trivial, because the Lagrangian contains derivative terms with respect to the fermion fields that need be properly discretized.

3.3.1 Wilson gauge action

The Wilson gauge action is constructed in such a way that gauge invariance is preserved if link variables transform as in Eq. (3.24). The QCD continuum gauge action is recovered for $a \to 0$. The choice is non-unique, since a gauge action on the lattice can be function of any extended products of link variables connecting two different lattice sites.

The simplest object from which a gluon action can be build on is given by a closed path of link variables, called *plaquette*

$$P_{\mu\nu}(n) \equiv U_{\mu}(n) U_{\nu}(n+\hat{\mu}) U_{-\mu}(n+\hat{\mu}+\hat{\nu}) U_{-\nu}(n+\hat{\nu}) , \qquad (3.25)$$

shown schematically in Fig. 3.3. As can be seen, it is the shortest path involving only four link variables. Under gauge transformations of Eq. (3.24), $P_{\mu\nu}(n)$ transforms as $\Omega(n) P_{\mu\nu}(n) \Omega(n)^{\dagger}$.
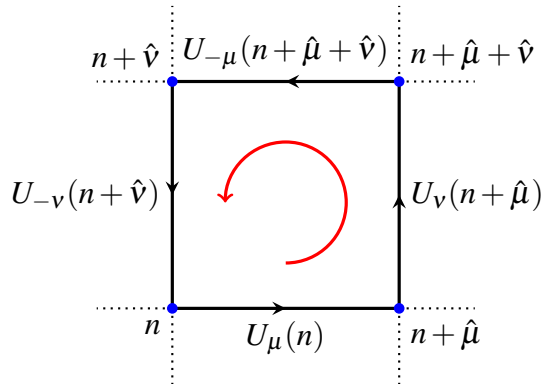
Figure 3.3 A plaquette on the $\mu\nu$-plane in a 4-dimensional grid.

Therefore, the two SU(3) matrices at the endpoints cancel out if we take the trace of $P_{\mu\nu}(n)$ over the color indices. This leads to the definition of the Wilson gauge action

$$S_G^W = \beta \sum_n \sum_{\mu \neq \nu} \left[1 - \frac{1}{N_c} \mathrm{Re\,Tr}[P_{\mu\nu}(n)] \right] = \beta \sum_n \sum_{\mu \neq \nu} \left[1 - \frac{1}{2N_c} \mathrm{Tr}[P_{\mu\nu}(n) + P_{\mu\nu}^{\dagger}(n)] \right] ,$$
$$(3.26)$$

where N_c is the number of colors ($N_c = 3$ in QCD) and the value of β has to be chosen in such a way that the lattice action recovers the Yang-Mills gauge action for vanishing lattice spacings. Rewriting the plaquette $P_{\mu\nu}(n)$ in terms of the lattice gluon fields $A_{\mu}(n)$, it is possible to see that S_G^W reduces to the Yang-Mills action in the continuum limit

$$S_W^G = \sum_n a^4 \frac{1}{2} \mathrm{Tr}[F_{\mu\nu} F^{\mu\nu}] + O(a^2) \xrightarrow{a \to 0} \frac{1}{2} \int d^4x\, F_{\mu\nu} F^{\mu\nu} , \qquad (3.27)$$

if g_0 satisfies the relation $\beta = 2N_c/g_0$.

3.3.2 Wilson fermions

The discretization procedure of the fermion action involves the issue called *fermion doubling*. As will be described in this Section, a *naive* discretization procedure leads to unwanted lattice

artifacts and unphysical particle states, that have to be removed in order to have the correct continuum limit. This problem was first solved by Wilson [13] and his formulation is still one of the most used in lattice QCD.

To define a lattice counterpart of the QCD Lagrangian given in Eq. (3.5), the continuum covariant derivative $D_\mu \psi(x)$ has to be replaced by some discretized form that ensures the gauge invariance of the action. This requirement is guaranteed with the following replacement

$$D_\mu \psi(x) \to \frac{U_\mu(n)\psi(n+\hat{\mu}) - U_{-\mu}(n)\psi(n-\hat{\mu})}{2a} \, . \tag{3.28}$$

Therefore, the discretized fermion action reads

$$S_F[\psi,\bar{\psi},U] = a^4 \sum_{f,n} \bar{\psi}^f(n)\left[\sum_{\mu=1}^{4} \gamma_\mu \frac{U_\mu(n)\psi^f(n+\hat{\mu}) - U_{-\mu}(n)\psi^f(n-\hat{\mu})}{2a} + m_0^f \psi^f(n)\right] \, . \tag{3.29}$$

The expression above cannot be considered as a good lattice representation of the fermion action and must be improved. To understand why, let us write the action in Eq. (3.29) as

$$S_F[\psi,\bar{\psi},U] = a^4 \sum_f \sum_{n,m} \bar{\psi}^f(n) D^f(n,m) \psi^f(m) \, , \tag{3.30}$$

where $D^f(n,m)$ is the *Dirac operator*

$$D^f(n,m) = \sum_{\mu=1}^{4} \gamma_\mu \frac{U_\mu(n)\delta_{n+\hat{\mu},m} - U_\mu^\dagger(n-\hat{\mu})\delta_{n-\hat{\mu},m}}{2a} + m_0^f \delta_{n,m} \, . \tag{3.31}$$

We now want to study the properties of $D^{-1}(n,m)$, the so-called fermion propagator, which represents the probability amplitude that fermions of flavor f propagate from the space-time points m to n on the lattice. An important property is that the singularities (poles) of the propagator in momentum space give the spectrum of the theory. Thus, to describe the same physics, continuum and lattice formulation have to share the same poles. To extract these singularities, we switch from the coordinate to the momentum space by taking the Fourier transform of the Dirac operator $D^f(n,m)$. To simplify the discussion, we consider the free case, i.e. $U_\mu(n) = 1$. Denoting with $V = L^3 \times L_t$ the lattice volume, for a specific fermion f we obtain

$$D(p',p) = \frac{1}{V}\sum_{n,m} e^{-ip'\cdot na} D(n,m) e^{ip\cdot ma} = \frac{1}{V}\sum_n e^{-i(p'-p)\cdot na}\left[\sum_\mu \gamma_\mu \frac{e^{ip_\mu a} - e^{-ip_\mu a}}{2a} + m_0\right]$$

$$= \delta(p'-p)\left[\sum_\mu \frac{i}{a}\gamma_\mu \sin(p_\mu a) + m_0\right] \, , \tag{3.32}$$

where we have used the following properties for the discrete Fourier transform

$$f(p) = \frac{1}{\sqrt{V}} \sum_n e^{-ip \cdot na} f(n), \quad \delta(p' - p) = \frac{1}{V} \sum_n e^{-i(p'-p) \cdot na} . \tag{3.33}$$

Thus, the free fermion propagator in momentum space reads

$$D^{-1}(p) = \left[\frac{i}{a} \sum_\mu \gamma_\mu \sin(p_\mu a) + m_0 \right]^{-1} = \frac{m_0^2 - ia^{-1}\gamma_\mu \sin(p_\mu a)}{m_0 + a^{-2} \sum_\mu \sin(p_\mu a)^2} , \tag{3.34}$$

and in the simplest case of zero quark masses it becomes

$$D^{-1}(p)|_{m_0=0} = -ia \frac{\gamma_\mu \sin(p_\mu a)}{\sum_\mu \sin(ap_\mu)^2} \xrightarrow{ap \to 0} \frac{-i\sum_\mu \gamma_\mu p_\mu}{p^2} . \tag{3.35}$$

At a fixed momentum (with the condition $ap \to 0$), $D^{-1}(p)$ has the correct continuum limit with the pole at $p_\mu = (0,0,0,0)$, as for the massless Dirac operator. On the lattice, $D^{-1}(p)$ has additional poles every time $\sin(ap_\mu) = 0$, i.e. when p_μ is either 0 or π/a. This implies that on the lattice there are additional fermion states which are unphysical, because they do not have analogy in the continuum theory. This effect can be interpreted as an artifact of the action of Eq. (3.29) and is known as *doubling problem*. Even though the above argument holds for the free case, one can still assume that the doublers appear in full QCD as the theory is considered asymptotically free at high energies.

Wilson added a higher order derivative term in order to eliminate the doubling problem. The additional contribution to the action was spotted to be a discretized form of the second derivative $(-ar/2)\partial_\mu \partial_\mu$, namely

$$-ar\,\bar\psi(n) \sum_\mu \left[\frac{U_\mu(n)\delta_{n+\hat\mu+m} - 2\delta_{n,m} + U_{-\mu}(n)\delta_{n-\hat\mu,m}}{2a^2} \right] \psi(m) , \tag{3.36}$$

where r is called Wilson coefficient (the standard choice is $r = 1$). The Wilson term vanishes in the continuum limit but leads to lattice artifacts of order a. Using the same logical steps leading to Eq. (3.32), one can see that the operator (3.36) in momentum space is

$$\frac{r}{a} \sum_\mu (1 - \cos(p_\mu a)) \tag{3.37}$$

for the free theory, $U_\mu(n) = 1$. With this addition, the modified fermion propagator reads

$$D^{-1}(p) = \left[\frac{i}{a} \sum_\mu \gamma_\mu \sin(p_\mu a) + m_0 + \frac{r}{a} \sum_\mu (1 - \cos(p_\mu a)) \right]^{-1} . \tag{3.38}$$

The physical pole at $p_\mu = (0,0,0,0)$ remains untouched, because the added term vanishes in the continuum limit. On the other hand, at $p_\mu = \pi/a$, $(1 - \cos(p_\mu a))$ gives an additional $2r/a$, which is of the order $\mathcal{O}(a^{-1})$. By consequence, for $a \to 0$, the Wilson term creates

particle states with infinite energy, which decouple from the theory. In this way, the Wilson term can remove the doubling problem.

To conclude, the Wilson fermion action S_F^W is given by

$$S_F^W[\psi, \bar{\psi}, U] = a^4 \sum_f \sum_{n,m} \bar{\psi}^f(n) \left[D_{F,W}^f(n,m) \right] \psi^f(m) , \tag{3.39}$$

where $D_{F,W}^f$ denotes the whole Wilson Dirac operator

$$D_{F,W}^f(n,m) = D_W(n,m) + m_0^f , \tag{3.40}$$

and $D_W(n,m)$ is the operator without the mass term

$$D_W(n,m)_{ab}^{\alpha\beta} = \frac{4r}{a} \delta_{\alpha\beta} \delta_{a,b} \delta_{n,m}$$
$$- \frac{1}{2a} \sum_\mu \left[(r - \gamma_\mu)_{\alpha\beta} U_\mu(n)_{ab} \delta_{n+\hat{\mu},m} + (r + \gamma_\mu)_{\alpha\beta} U_\mu(n - \hat{\mu})_{ab}^\dagger \delta_{n-\hat{\mu},m} \right] . \tag{3.41}$$

In the equation above, we have made explicit the dependence on the color and spin indices. Wilson's formulation has been the basis for lattice discretizations employed for studying QCD in the non-perturbative regime. Formulations introduced later differ in the treatment of the fermion and gluon sectors of the action and were proposed in order to overcome some disadvantages of the Wilson action, which are discussed in the next Section.

3.3.3 Properties of Wilson action

The Wilson action satisfies a number of crucial properties, besides being free of fermion doublers and preserving gauge symmetry. Firstly, as the continuum action, it is invariant under parity ($\mathcal{P}$), charge ($\mathcal{C}$) and time reversal ($\mathcal{T}$) transformations, that act on fermion and gluon fields as described in Table 3.1. Secondly, the Wilson-Dirac operator (3.40) has an

	$\mathcal{P}$	$\mathcal{C}$	$\mathcal{T}$
$U_4(\vec{x},t)$	$U_4(-\vec{x},t)$	$U_4^*(\vec{x},t)$	$U_{-4}(\vec{x},-t)$
$U_i(\vec{x},\tau)$	$U_{-i}(-\vec{x},t)$	$U_i^*(\vec{x},t)$	$U_i(\vec{x},-t)$
$\psi(\vec{x},t)$	$\gamma_4\psi(-\vec{x},t)$	$\mathcal{C}\bar{\psi}^T(\vec{x},t)$	$\gamma_4\gamma_5\psi(\vec{x},-t)$
$\bar{\psi}(\vec{x},t)$	$\bar{\psi}(-\vec{x},t)\gamma_4$	$-\psi^T(\vec{x},t)\mathcal{C}^{-1}$	$\bar{\psi}(\vec{x},-t)\gamma_5\gamma_4$

Table 3.1 Discrete transformations $\mathcal{C}, \mathcal{P}, \mathcal{T}$ on fermion and gluon fields [103].

additional symmetry called γ_5-Hermiticity, i.e it obeys to the following relation

$$D_{F,W}^f(n,m)^\dagger = \gamma_5 D_{F,W}^f(n,m) \gamma_5 . \tag{3.42}$$

Since $(D_{F,W}^f{}^\dagger)^{-1} = (D_{F,W}^f{}^{-1})^\dagger$, also the Wilson fermion propagator is γ_5-Hermitian. This implies that a quark propagator from the lattice points m to n can be reconstructed from the one having the opposite direction (from n to m) by applying only the γ_5-matrix, with no need of new inversions. The validity of Eq. (3.42) reduces therefore the computational effort in those lattice calculations in which the knowledge of hadron correlation functions is required.

On the other hand, the Wilson action has also some disadvantages:

1. The leading lattice artifacts of the fermion action are of order $\mathcal{O}(a)$, whilst for the gluon sector they contribute to $O(a^2)$.

2. The Wilson-Dirac operator $D_{F,W}^f$ (3.40) is non-protected by zero modes, and thus its inverse can be ill-defined. This can happen when for some gauge configurations, called *exceptional configurations*, the eigenvalues of the whole operator have quite small values which break down numerical inversions. To avoid exceptional configurations, the solution is to simulate at large enough values for the bare quark masses, that could balance the eigenvalues of the Wilson Dirac operator D_W (3.41). The drawback of this approach is that hadron masses may not correspond to their physical value. This represents therefore a strong limitation of Wilson formulation.

3. At finite lattice spacing all chiral symmetries are explicitly broken even in the massless case. We remind that, in the continuum theory, chiral rotations leave the Lagrangian invariant for vanishing quark masses. The origin of the chiral symmetry breaking can be traced back to the Wilson term, introduced to remove the doublers. Indeed, under the following chiral rotations

$$
\begin{aligned}
\psi'(x) &= e^{i\alpha\gamma_5}\psi, \quad \bar\psi'(x) = \bar\psi(x)e^{i\alpha\gamma_5}, \\
\psi'(x) &= e^{i\alpha\gamma_5 T_a}\psi, \quad \bar\psi'(x) = \bar\psi(x)e^{i\alpha\gamma_5 T_a},
\end{aligned}
\tag{3.43}
$$

where T_a are the generators of SU(3) color group and $\alpha \in \mathbb{R}$, the Wilson term transforms as

$$
r\,\bar\psi\psi \to r\,e^{2i\alpha\gamma_5}\bar\psi\psi, \quad r\,\bar\psi\psi \to r\,e^{2i\alpha\gamma_5 T_a}\bar\psi\psi \quad,
\tag{3.44}
$$

behaving like a mass term. By consequence, Wilson fermions are not suitable to study phenomena connected to chiral symmetries, such as the spontaneous chiral symmetry breaking which has important phenomenological implications [104].

In light of the above, one might wonder whether there exists another way to remove the doublers, while keeping the chiral symmetry on the lattice. The connection between chiral symmetries and fermion doubling was established by Nielsen and Ninomiya in the famous No-Go theorem [105] published in 1981. It states that it is impossible to formulate a lattice theory that reproduces the correct fermion spectrum and whose Lagrangian is at the same time Hermitian, local and invariant under translational and chiral transformations of the form (3.43). However, years later, Ginsparg and Wilson demonstrated that these limitations can be overcome into two main steps: **i)** employing a different Dirac operator [106];

ii) defining on the lattice new chiral transformations, that act on both gluon and fermion fields [107] and that reduce to the ones of the continuum theory for $a \to 0$. This has led to the introduction of two kinds of QCD lattice discretizations: the overlap fermions [108] and the so-called *domain wall fermions* [109]. We omit details about these discretizations since they are not used in this work.

3.4 Improved discretization schemes

3.4.1 Fermion action with clover term

Even if the discretization errors vanish for $a \to 0$, it is very advantageous to deal with *improved* actions that ensure a faster convergence towards the continuum limit. A way to achieve this improvement in lattice QCD was proposed by Sheikholeslami and Wohlert [110] and makes use of the Symanzik improvement program [111, 112]. The idea is that $\mathcal{O}(a)$ contributions, and in principle higher order discretization effects, can be removed by adding extra terms to the lattice action. This role, in Wilson's formulation, is played by the so-called *clover* term.

To understand the origin of the clover term we first recall the Symanzik program, according to which the lattice theory for $a \to 0$ can be described by an effective action expandable in powers of the lattice spacing

$$\mathcal{L}_{eff} = \mathcal{L}_0 + a\mathcal{L}_1 + a^2\mathcal{L}_2 + \dots , \quad S_{eff} = \int d^4x \, (\mathcal{L}_0 + a\mathcal{L}_1 + a^2\mathcal{L}_2 + \dots) . \quad (3.45)$$

$\mathcal{L}_0$ is the QCD Lagrangian in the continuum and $\mathcal{L}_1$, $\mathcal{L}_2$ etc. are terms made of composite operators, depending on gluon and fermion fields. They have to share the same symmetries of the continuum theory (invariance under gauge, parity, Lorentz, charge-conjugation transformations). To remove $\mathcal{O}(a)$ effects, the proposal is to add counterterms that cancel all possible operators $O_i^{(1)}$ contained in $\mathcal{L}_1$. Since the action is dimensionless, $\mathcal{L}_1$ must be a linear combination of operators with dimension (energy)[5] [113, 114], given by

$$\begin{aligned}
O_1^{(1)} &= \bar{\psi} i \sigma_{\mu\nu} F_{\mu\nu} \psi , \\
O_2^{(1)} &= \bar{\psi} D_\mu D_\mu \psi + \bar{\psi}(x) \overleftarrow{D}_\mu \overleftarrow{D}_\mu \psi , \\
O_3^{(1)} &= m_0 \, \text{Tr}[F_{\mu\nu} F_{\mu\nu}] , \\
O_4^{(1)} &= m_0 [\bar{\psi}\gamma_\mu D_\mu \psi - \bar{\psi}\overleftarrow{D}_\mu \gamma_\mu \psi] , \\
O_5^{(1)} &= m_0^2 \bar{\psi}\psi ,
\end{aligned} \quad (3.46)$$

where $\sigma_{\mu\nu} = i/2[\gamma_\mu, \gamma_\nu]$ and $F_{\mu\nu}$ is the gluon operator in the continuum. The discretized version of the backward covariant derivative $\overleftarrow{D}_\mu \psi(x)$ is defined as

$$\overleftarrow{D}_\mu \psi(n) = \frac{1}{a}\left[\psi(n) - U_\mu^{-1}(n - \hat{\mu})\psi(n - \hat{\mu})\right] . \quad (3.47)$$

The dependence of $\mathcal{L}_1$ on the operators in Eq. (3.46) can be simplified by employing the equation of motion $(\gamma_\mu D_\mu + m)\psi(x) = 0$, which leads to the following conditions

$$O_1^{(1)} + O_2^{(1)} + 2O_5^{(1)} = 0 \,, \quad O_4^{(1)} + 2O_5^{(1)} = 0 \,. \tag{3.48}$$

The relations above can be used to write $O_2^{(1)}$ and $O_4^{(1)}$ in terms of the simpler operators $O_1^{(1)}$, $O_3^{(1)}$ and $O_5^{(1)}$. This is a strategic choice, since $O_3^{(1)}$ and $O_5^{(1)}$ are already part of the continuum QCD Lagrangian (up to some multiplicative factors). Therefore, they can be absorbed into Wilson gluon action and in the local product $\bar{\psi}(n)\psi(n)$, by a simple redefinition of the bare coupling g_0 and bare quark mass m_0.

Thus, the only term left is $O_1^{(1)}$ and the improved Wilson action reads

$$S_{W,I} = S_W^G + S_W^F + i a^5 \frac{c_{sw}}{4} \sum_{n,\mu,\nu} \bar{\psi}(n)\sigma_{\mu\nu}\hat{F}_{\mu\nu}(n)\psi(n) \,, \tag{3.49}$$

where c_{sw} is called *clover* parameter. $\hat{F}_{\mu\nu}$ is an antisymmetric tensor under exchange $\mu \leftrightarrow \nu$ and represents the lattice counterpart of the gluon operator $F_{\mu\nu}$, chosen by Sheikholeslami and Wohlert to be

$$\hat{F}_{\mu\nu}(n) = \frac{1}{8a^2} \left[Q_{\mu\nu}(n) - Q_{\nu\mu}(n) \right] \,. \tag{3.50}$$

$Q_{\mu\nu}(n)$ is a sum over the plaquettes in the plane $\mu - \nu$

$$
\begin{aligned}
Q_{\mu\nu}(n) = \; & U_\mu(n)U_\nu(n+\hat{\mu})U_{-\mu}(n+\hat{\mu}+\hat{\nu})U_{-\nu}(n+\hat{\nu}) \\
& + U_{-\nu}(n)U_\mu(n-\hat{\nu})U_\nu(n-\hat{\nu}-\hat{\mu})U_{-\mu}(n+\hat{\mu}) \\
& + U_{-\mu}(n)U_{-\nu}(n-\hat{\mu})U_\mu(n-\hat{\mu}-\hat{\nu})U_\nu(n-\hat{\nu}) \\
& + U_\nu(n) + U_{-\mu}(n+\hat{\nu})U_{-\nu}(n+\hat{\nu}-\hat{\mu})U_\mu(n-n-\mu) \,,
\end{aligned} \tag{3.51}
$$

as shown in Fig. 3.4. The value of c_{sw} has to be tuned in order to remove $\mathcal{O}(a)$ effects. A
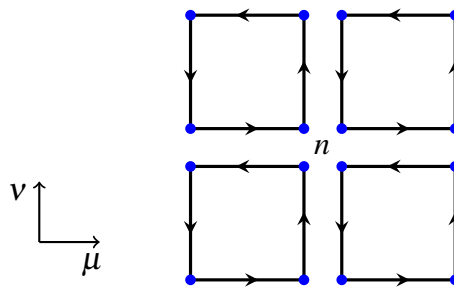
Figure 3.4 Graphical representation of $Q_{\mu\nu}$ (Eq.(3.51)) entering the clover action.

correct choice for c_{sw} leads to $\mathcal{O}(a)$ improvement for on-shell quantities, such as hadron masses. This task can be achieved non-perturbatively through lattice calculations, see e.g Refs. [115–118] for determinations of c_{sw} using the Wilson plaquette action and different dynamical flavors.

It is important to mention that the introduction of the clover term in Wilson formulation removes effects of order a only for on-shell observables. Other quantities, such as the fermion propagator or quark currents of the form $\psi(x)\Gamma\psi(x)$, where Γ is a Dirac matrix, are not

improved and $\mathcal{O}(a)$ improvement can be achieved by adding appropriate terms to the operator under study.

3.4.2 Twisted mass fermions

In this Section we present the twisted mass fermion formulation for QCD (tmQCD) [119], which is the one used in this work. In particular, we focus on its simplest form, which involves two light degenerate quarks ($N_f = 2$ QCD). Generalizations of the twisted mass action with a further doublet of non-degenerate quarks can be found in Refs. [120, 121].

Twisted mass action has two fundamental properties: **1)** it is protected against zero modes, unlike Wilson formulation; **2)** a large class of operators are *authomatically $O(a)$* improved, provided that some parameters of the action are properly tuned. These two nice aspects make tmQCD a very attractive framework for studying strong interactions in a non-perturbative regime. tmQCD has also became a very popular variant of Wilson formulation. Using twisted mass fermions, a wide variety of aspects in QCD have been investigated over the years, that are related to topological properties and hadron structure, such as baryon and meson spectrum, form factors, nucleon spin and recently also nucleon parton distribution functions.

Action for $N_f = 2$ degenerate quarks

We consider two quark fields with the same bare mass m_0 that form doublets $\{\chi, \bar{\chi}\}$ in flavor space. For light quarks $\chi = (u, d)^T$. The tmQCD action is given by

$$S_{tm}^{\{\chi\}} = a^4 \sum_{n,m} \bar{\chi}(n) \left[D_W(n,m) + m_0 \mathbb{1}_f + i\mu_q \gamma_5 \tau_3 \right] \chi(m) , \qquad (3.52)$$

where $\mathbb{1}_f$ and $\tau_3 = \text{diag}(1, -1)$ are the identity matrix and the third Pauli matrix acting in flavor space, and m_0^f is the bare mass. D_W is the Wilson Dirac operator defined in Eq. (3.41) with $r = 1$ and μ_q is the so-called bare *twisted mass parameter*. The last term in the action, known as *twisted mass term*, is crucial to protect the Dirac operator against zero modes. To see this, we analyze the determinant employing the γ_5-Hermiticity property of Wilson operator and we obtain

$$
\begin{aligned}
\det \left[D_W + m_0 \mathbb{1}_f + i\mu_q \gamma_5 \tau_3 \right] &= \det \left[D_W + m_0 \mathbb{1}_f + i\mu_q \gamma_5 \right] \det \left[D_W + m_0 \mathbb{1}_f - i\mu_q \gamma_5 \right] \\
&= \det \left[D_W + m_0 \mathbb{1}_f + i\mu_q \gamma_5 \right] \det \left[\gamma_5 (D_W + m_0 \mathbb{1}_f - i\mu_q \gamma_5) \gamma_5 \right] \\
&= \det \left[(D_W + m_0 \mathbb{1}_f + i\mu_q \gamma_5)(D_W^\dagger + m_0 \mathbb{1}_f - i\mu_q \gamma_5) \right] \\
&= \det \left[(D_W + m_0 \mathbb{1}_f)(D_W + m_0 \mathbb{1}_f)^\dagger + \mu_q^2 \right] .
\end{aligned}
$$

$$(3.53)$$

For any finite value of μ_q the determinant is always positive and thus the twisted Dirac operator does not have zero modes. Consequently, the additional term in μ_q acts like a mass term and can be incorporated with m_0 to form a unique mass term in the action. This is

achieved by applying the flavor-dependent axial transformations

$$\psi(n) = e^{i\alpha\gamma_5\tau_3/2}\chi(n) \longrightarrow \chi(n) = e^{-i\alpha\gamma_5\tau_3/2}\psi(n) ,$$
$$\bar{\psi}(n) = \bar{\chi}(n)e^{i\alpha\gamma_5\tau_3/2} \longrightarrow \bar{\chi}(n) = \bar{\psi}(n)e^{-i\alpha\gamma_5\tau_3/2} ,$$

(3.54)

where α is the *twist angle* and $\{\psi, \bar{\psi}\}$ are doublets in flavor space in the so-called *physical basis*. The "mass term" transforms as

$$\bar{\chi}(m_0 + i\mu_q\gamma_5\tau_3)\chi \to \bar{\psi}e^{-i\alpha\gamma_5\tau_3}(m_0 + i\mu_q\gamma_5\tau_3)\psi ,$$

(3.55)

and can be written in a compact form defining the *polar mass M* via

$$m_0 + i\mu_q\gamma_5\tau_3 \equiv Me^{i\alpha\gamma_5\tau_3} \quad \text{with} \quad m_0 = M\cos(\alpha), \; \mu_q = M\sin(\alpha) .$$

(3.56)

Moreover, under transformations (3.54) the Dirac operator D_W gets modified into D_W^{tm}, in which only the Wilson term is rotated by $e^{-i\alpha\gamma_5\tau_3}$. Thus, the twisted mass action in the physical basis

$$S_{tm}^{\{\psi\}} = a^4 \sum_{n,m} \bar{\psi}(n) \left[D_W^{tm}(n,m) + M\mathbb{1}_f \right] \psi(m)$$

(3.57)

assumes the standard form of the QCD action, with a kinetic part and only one mass term, given by $M = \sqrt{m_0^2 + \mu_q^2}$. In the continuum limit, where the Wilson term vanishes, tmQCD is equivalent to the standard QCD, provided that in the axial rotations of Eq. (3.54) $\tan(\alpha) = \mu_q/m_0$.

Chiral symmetry and maximal twist

We have pointed out above that in the continuum limit the axial rotations (3.54) relate tmQCD to the standard QCD. However, the relation between the two formulations needs to involve renormalized quantities when working at finite lattice spacing. In this respect, we observe that the transformations from twisted to physical basis do not leave tmQCD action invariant even at zero bare quark masses, because of the Wilson term. In other words, at finite a, chiral symmetry is explicitly broken. This has an important implication because it determines the renormalization properties of the bare mass. In the continuum theory, masses renormalize multiplicatively ($m_R = Z_m m_0$) because the chiral symmetry is fully restored in the limit of zero mass. In presence of an explicit symmetry breaking, the mass takes an additive renormalization

$$m_R = Z_m(m_0 - m_{cr}) .$$

(3.58)

This is due to the fact that breaking of chiral symmetry shifts the chiral point by a certain value m_{cr} and to achieve vanishing renormalized masses (recovery of the chiral limit) m_0 needs to be subtracted by m_{cr}. After this subtraction, the difference $m_0 - m_{cr}$ renormalizes multiplicatively. Thus, the relation tmQCD and standard QCD rather involves renormalized quantities such that $\tan(\alpha) = \mu_R/m_R$, where $\mu_R = Z_\mu\mu_q$ [122, 123]. It is particularly interesting the case usually called *full* or *maximal twist*, in which $m_R = 0$ and consequently $\alpha = \pi/2$. In fact, it

has been demonstrated [124] that a large class of observables is *automatically* free of order a effects when the physical quark mass is solely given by μ_R. In numerical simulations, the standard procedure to achieve maximal twist is to tune the bare mass m_0 to the critical value m_{cr}, such that the so-called PCAC mass [125, 126]

$$m_{\text{PCAC}} = \frac{\sum_{\mathbf{x}} \langle \partial_0 A_0^a(x) P^a(0) \rangle}{2\mathbf{x} \langle P^a(x) P^a(0) \rangle} \quad a = 1, 2 \tag{3.59}$$

vanishes for large Euclidean times. The relation above, which written in this form is valid for degenerate quarks, follows from the well-known nonsinglet axial Ward identity (AWI) [127, 128]. The AWI states that, under global transformations $\psi \to e^{i\theta^a \gamma_5 \tau^a/2} \psi$, the divergence of the axial vector current ($\mathcal{A}_\mu^a$) is related to the pseudoscalar current ($\mathcal{P}^a$) via

$$\partial_\mu \mathcal{A}_\mu^a = \frac{1}{2} \bar{\psi} \{M, \tau^a\} \gamma_5 \psi, \quad \text{where} \quad \mathcal{A}_\mu^a = \frac{1}{2} \bar{\psi} \gamma_\mu \gamma_5 \tau^a \psi, \quad \mathcal{P}^a = \frac{1}{2} \bar{\psi} \gamma_5 \tau^a \psi. \tag{3.60}$$

The relations above hold in physical basis and for a generic mass matrix M.
Performing the rotations (3.54), it can be easily proved that in twisted basis and for degenerate quarks the AWI is given by

$$\partial_\mu A_\mu^a = 2m_0 P^a + i\mu_q \delta^{3a} S^0, \quad \text{where} \quad A_\mu^a = \frac{1}{2} \bar{\chi} \gamma_\mu \gamma_5 \tau^a \chi, \quad S^0 = \bar{\chi} \chi. \tag{3.61}$$

In the following we review a simple proof of the *automatic $\mathcal{O}(a)$ improvement* at maximal twist, which is one of the biggest advantages of tmQCD.

Automatic O(a) improvement

Automatic $\mathcal{O}(a)$, that holds at maximal twist, means that composite operators are automatically improved having discretization errors only at order a^2. The proof applies to a large class of correlation functions involving multi-local fields, such as two currents applied in two different lattice points, and it is based on the Symanzik improvement program already used in Section 3.4.1. For the proof we follow the arguments of Refs. [122, 123]. According to the effective Symanzik theory, in the limit $a \to 0$ the action and a generic operator can be expanded as

$$S_{eff} = S_0 + aS_1 + O(a^2), \quad O_{eff} = O_0 + aO_1 + O(a^2). \tag{3.62}$$

S_0 is the twisted mass continuum action at maximal twist ($m_R = 0$)

$$S_0 = \int d^4x \, \bar{\chi}(x) \left[\gamma_\mu D_\mu(x) + i\mu \gamma_5 \tau^3 \right] \chi(x), \quad \text{with} \quad D_\mu(x) = \partial_\mu + iA_\mu(x), \tag{3.63}$$

while S_1 is the continuum counterpart of the clover fermion action (3.49) and reads

$$S_1 = c_{\text{sw}} \int d^4x \, \bar{\chi}(x) i\sigma_{\mu\nu} F_{\mu\nu} \chi(x). \tag{3.64}$$

In Eq. (3.62), O_0 denotes the continuum expression of the lattice operator under study and O_1 is a suitable operator with the correct dimension and symmetry properties of O_0. After

renormalization, the expectation value $\langle O \rangle_{eff}$ on the lattice can be expanded as well in powers of a and in terms of quantities evaluated in the continuum. Indeed, using path integral formulation we have

$$
\begin{aligned}
\langle O \rangle_{eff} &= \frac{1}{Z} \int [DU][D\psi][D\bar{\psi}] \, e^{-S_0} \, e^{-(aS_1 + \mathcal{O}(a^2))} \left[O_0 + aO_1 + \mathcal{O}(a^2) \right] \\
&= \frac{1}{Z} \int [DU][D\psi][D\bar{\psi}] \, e^{-S_0} \left[1 - aS_1 - \mathcal{O}(a^2) \right] \left[O_0 + aO_1 + \mathcal{O}(a^2) \right] \\
&= \langle O \rangle_0 - a \langle S_1 O_0 \rangle_0 + a \langle O_1 \rangle_0 + \mathcal{O}(a^2) ,
\end{aligned}
\tag{3.65}
$$

where $\langle \ldots \rangle_0$ stands for continuum expectation value evaluated with the action S_0. We now examine the symmetry property of all terms in Eq. (3.65) with respect to the transformations

$$
R^{1,2} : \qquad \chi \to i\gamma_5 \tau^{1,2} \chi , \quad \bar{\chi} \to \bar{\chi} i\gamma_5 \tau^{1,2}
\tag{3.66}
$$

for which the continuum action S_0 is invariant. We note that S_0 is invariant only at maximal twist, because otherwise we would have in the action a non-invariant term, i.e. $\bar{\chi} m_0 \chi$. This is a key ingredient for this proof, that allows us to establish the following symmetries under $R^{1,2}$ rotations

$$
S_0 \xrightarrow{R^{1,2}} S_0 , \quad S_1 \xrightarrow{R^{1,2}} -S_1 .
\tag{3.67}
$$

As concerns the operators, they can be odd or even under $R^{1,2}$, but the transformation properties of O_0 automatically fix the ones of the correction term O_1 [123]. In particular, the following relations hold [123]

$$
O_0 \xrightarrow{R^{1,2}} \pm O_0 \ \Rightarrow \ O_1 \xrightarrow{R^{1,2}} \mp O_1 .
\tag{3.68}
$$

Consequently, by combining the relations (3.67) and (3.68), we can now finalize our proof and distinguish between the two possible cases:

1. If O_0 is even under $R^{1,2}$, then $\langle S_1 O_0 \rangle_0 = \langle O_1 \rangle = 0$ and we obtain

$$
\langle O \rangle_{eff} = \langle O \rangle_0 + \mathcal{O}(a^2) .
\tag{3.69}
$$

2. If O_0 is odd under $R^{1,2}$, then $\langle O \rangle_0 = 0$ and therefore

$$
\langle O \rangle_{eff} = -a \langle S_1 O_0 \rangle_0 + a \langle O_1 \rangle_0 + \mathcal{O}(a^2) .
\tag{3.70}
$$

Thus, at maximal twist, physical observables that are $R^{1,2}$-even have lattice artifacts of order a^2, whilst odd operators have a vanishing expectation value in the continuum limit.

Some remarks

So far we have seen that, unlike Wilson fermions, in tmQCD the clover term of Eq. (3.51) is not needed for $\mathcal{O}(a)$ improvement if maximal twist is achieved. However, including a clover

term in the action has been found very advantageous because it can further reduce lattice artifacts. Also, it has made feasible the production of gauge ensembles at quark masses close to their physical value. The ensemble at the physical point used in this work has been indeed produced incorporating the clover term in the twisted mass formulation.

The crucial point is that tmQCD action is not invariant under isospin transformations at finite lattice spacing. This is due the twisted mass term, which in flavor space takes values $+i\mu_q$ and $-i\mu_q$ for *up* and *down* quarks. In the continuum limit, however, this symmetry is fully restored. The biggest effect of isospin symmetry breaking has been observed in past simulations via a mass splitting in the pion sector, with the neutral pion being lighter than the charged one. The difference in mass is responsible for the lower bound of the bare light quark mass, under which the mass of the neutral pion approaches zero triggering a phase transition that is not observed in the QCD vacuum in the real world. This problem has been recently overcome by including the clover term in tmQCD action. There is indeed evidence that the mass splitting gets significantly reduced than the one measured on ensembles without clover term [129], enabling the production of gauge ensembles with quark masses tuned to their physical value [130, 131].

3.5 Computing observables in lattice QCD

Once a lattice representation of the gluon and fermion action has been chosen, physical observables are computed using Feynman's path integral formulation. The goal is to estimate expectation values of observables $\mathcal{O}(\psi, \bar{\psi}, U)$, which in general depend on gluon and fermion fields. After Wick rotation, we have seen that the expectation value takes the form

$$\langle \Omega | \mathcal{O}(\psi, \bar{\psi}, U) | \Omega \rangle = \frac{1}{Z} \int \mathcal{D}\psi \mathcal{D}\bar{\psi} \mathcal{D}\mathcal{U} \; \mathcal{O}(\psi, \bar{\psi}, U) \, e^{-S_G[U] - S_F[\psi, \bar{\psi}, U]} \, , \qquad (3.71)$$

where Z is the partition function

$$Z = \int \mathcal{D}\psi \mathcal{D}\bar{\psi} \mathcal{D}\mathcal{U} \; e^{-S_G[U] - S_F[\psi, \bar{\psi}, U]} \, . \qquad (3.72)$$

The path integral must be solved numerically, but there is an intrinsic problem: ψ, $\bar{\psi}$ are defined through anti-commutation relations and is very difficult to represent such numbers at low-level on a computer. The way around this problem is to integrate over the fermion fields analytically and use the fact that ψ and $\bar{\psi}$ are Grassmann numbers.

If $\{\eta_1, \ldots, \eta_N\}$ are Grassmann variables, namely

$$\{\eta_i, \eta_j\} = \eta_i \eta_j + \eta_j \eta_i = 0, \quad i, j = 1, \ldots, N \, , \qquad (3.73)$$

they have to satisfy the following properties

$$\int d\eta_i = 0, \quad \int d\eta_i \eta_i = 1, \quad \int \prod_{l=1}^{N} d\bar{\eta}_l d\eta_l \, e^{-\sum_{i,j} \bar{\eta}_i A_{ij} \eta_j} = \det[A] \, , \qquad (3.74)$$

where det $[A]$ is the determinant of a generic matrix.

The relations above can be directly used to carry out the integration over $\psi, \bar{\psi}$ in the partition function. The fermion action is indeed bilinear in the fermion fields and can be written as

$$S_F[\psi, \bar{\psi}, U] = \sum_{n,m,\alpha,\beta,a,b} \bar{\psi}_{n,\alpha,a}(D[U])_{\alpha\beta,a,b}\,\psi_{m,\beta,b}\,, \qquad (3.75)$$

where D is the Dirac operator. Thus, the integration over the fermion variables gives rise to the determinant of the Dirac operator, and the partition function becomes

$$Z = \int \mathcal{D}\psi \mathcal{D}\bar{\psi} \mathcal{D}\mathcal{U}\ e^{-S_G[U]-S_F[\psi,\bar{\psi},U]} = \int \mathcal{D}\mathcal{U}\ e^{-S_G[U]}\ \det[\mathrm{D}]\,. \qquad (3.76)$$

Now we have to carry out the integration left in Eq. (3.71). To simplify the derivation, let us suppose that the observable $\mathcal{O}$ involves only two fermion fields $\psi(x_1), \bar{\psi}(x_2)$, and the expectation value of interest is

$$\begin{aligned}\langle\mathcal{O}(\psi,\bar{\psi})\rangle &= \langle\Omega|\psi(x_1)\bar{\psi}(x_2)|\Omega\rangle \\ &= \frac{1}{Z}\int\mathcal{D}\psi\mathcal{D}\bar{\psi}\mathcal{D}\mathcal{U}\ \psi(x_1)\bar{\psi}(x_2)\ e^{-S_F[\psi,\bar{\psi},U]}e^{-S_G[U]}\,.\end{aligned} \qquad (3.77)$$

The discussion can be, however, easily generalized for any quantity, including gluon-dependent ones. The integration in (3.77) is now less straightforward than the one in (3.76) and can be performed by introducing a functional integral dependent on two auxiliary Grassmann variables $\eta, \bar{\eta}$

$$Z_{\eta,\bar{\eta}} = \int \mathcal{D}\psi\mathcal{D}\bar{\psi}\mathcal{D}\mathcal{U}\ e^{-\sum\bar{\psi}D[U]\psi+\sum(\bar{\psi}\eta+\bar{\eta}\psi)}e^{-S_G[U]}\,. \qquad (3.78)$$

In the expression above we have replaced S_F by its the compact form $\bar{\psi}D[U]\psi$, according to Eq. (3.75). The expectation value (3.77) can now be obtained through derivation procedure

$$\begin{aligned}\langle\mathcal{O}(\psi,\bar{\psi})\rangle &= \frac{1}{Z_{\eta,\bar{\eta}}}\left(\partial_{\bar{\eta}(x_1)}\partial_{\eta(x_2)}Z_{\eta,\bar{\eta}}\right)\Big|_{\eta,\bar{\eta}=0} \\ &= \frac{1}{Z_{\eta,\bar{\eta}}}\partial_{\bar{\eta}(x_1)}\partial_{\eta(x_2)}\int\mathcal{D}\psi\mathcal{D}\bar{\psi}\mathcal{D}\mathcal{U}\ e^{-\sum\bar{\psi}D[U]\psi+\sum(\bar{\psi}\eta+\bar{\eta}\psi)}e^{-S_G[U]}\Big|_{\eta,\bar{\eta}=0}\,.\end{aligned} \qquad (3.79)$$

If we perform the change of variables $\psi \to \psi + D^{-1}[U]\eta$ and $\bar{\psi} \to \bar{\psi} + \bar{\eta}D^{-1}[U]$, the exponential in the integral above can be decomposed into two quadratic expressions in terms of the Grassmann variables, and the integration over $\psi, \bar{\psi}$ gives rise to another fermion determinant

$$Z_{\eta,\bar{\eta}} = \int\mathcal{D}\psi\mathcal{D}\bar{\psi}\mathcal{D}\mathcal{U}\,e^{-\bar{\psi}D[U]\psi+\bar{\eta}D^{-1}[U]\eta}\,e^{-S_G[U]} = \int\mathcal{D}\mathcal{U}\,\det D[U]\,e^{+\bar{\eta}D^{-1}[U]\eta}\,e^{-S_G[U]}\,. \qquad (3.80)$$

Thus, from the repeated differentiation of the exponent $\bar{\eta} D^{-1}[U] \eta$, the expectation value (3.77) can be finally written as

$$\langle \Omega | \psi(x_1) \bar{\psi}(x_2) | \Omega \rangle = \frac{\int \mathcal{DU} \ D^{-1}[U](x_1, x_2) \det D[U] \, e^{-S_G[U]}}{\int \mathcal{DU} \ \det D[U] e^{-S_G[U]}} \ . \tag{3.81}$$

This result can be generalized for any observable of interest and the expectation value reads

$$\langle \mathcal{O} \rangle = \frac{\int \mathcal{DU} \ \tilde{\mathcal{O}}[U] \det D[U]] e^{-S_G[U]}}{\int \mathcal{DU} \ \det D[U] \, e^{-S_G[U]}} \ , \tag{3.82}$$

where $\tilde{\mathcal{O}}[U]$ may depend on the gluon fields either explicitly or implicitly through the inverse of the Dirac operator, as seen in our example.

In Eqs. (3.81, 3.82) we are left with the integration over the gluon fields, which still cannot be performed analytically. In practice, in numerical simulations, a representative set of gluon configurations, $\{U_1, U_2, \ldots, U_N\}$, is generated using Monte Carlo methods with probability density $(\det D[U] e^{-S_G[U]})/Z$. To simulate QCD with N_f quark flavors, $\det D[U]$ in Eq. (3.82) gets replaced by

$$\det D[U] \rightarrow \prod_{f=1}^{N_f} \det D_f[U] \ . \tag{3.83}$$

The so-called (partial) *quenched approximation* consists in neglecting (some) the contribution of $\det D_f[U]$ in Monte Carlo simulations.

Once gauge configurations have been produced, the expectation value $\langle \mathcal{O} \rangle$ is estimated via its sample average

$$\langle \mathcal{O} \rangle = \bar{\mathcal{O}} \pm \Delta \bar{\mathcal{O}}, \quad \bar{\mathcal{O}} = \frac{1}{N} \sum_{k=1}^{N} \mathcal{O}[U_k], \quad \Delta \bar{\mathcal{O}} \propto \frac{1}{\sqrt{N}} \ . \tag{3.84}$$

The statistical error $\Delta \bar{\mathcal{O}}$ is due to the fact that the number of measurements is always finite and it is usually called *gauge noise*. Moreover, $\Delta \bar{\mathcal{O}}$ does not scale exactly as $1/\sqrt{N}$, because the gauge configurations generated with Monte Carlo methods are correlated with each other. It is possible to show that $\Delta \bar{\mathcal{O}}$ is rather increased by a factor $\sqrt{2\tau_{int}(\mathcal{O})}$ than what expected for uncorrelated measurements. Here we indicate with $\tau_{int}(\mathcal{O})$ the so-called *integrated autocorrelation time*, defined as

$$\tau_{int}(\mathcal{O}) = \frac{1}{2} \sum_{t=-\infty}^{t=+\infty} \frac{\Gamma_{\mathcal{O}}(t)}{\Gamma_{\mathcal{O}}(0)} \ , \tag{3.85}$$

where $t = i - j$ is the distance between the measurements i and j in the Monte Carlo history, while $\Gamma_{\mathcal{O}}(0)$ is the variance of the observable $\mathcal{O}$ and $\Gamma_{\mathcal{O}}(t)$ the autocorrelation function given by

$$\Gamma_{\mathcal{O}}(0) = \langle (\mathcal{O} - \langle \mathcal{O} \rangle)^2 \rangle \ , \tag{3.86}$$

$$\Gamma_{\mathcal{O}}(i - j) = \langle (\mathcal{O}_i - \langle \mathcal{O} \rangle)(\mathcal{O}_j - \langle \mathcal{O} \rangle) \rangle \ . \tag{3.87}$$

Different techniques can be in general used to estimate the statistical errors of correlated data. In this work we use the so-called Jackknife binning, that is among the simplest analysis methods and easily applicable to any complicated function of the primary data, which are directly extracted from lattice calculations. Details about the method can be found in Refs. [132, 133].

3.6 Quasi-distributions on a Euclidean space-time

Having described how observables are computed in lattice QCD, we now explain the method used in this work to study parton physics on a Euclidean lattice. The focus is on the *quasi-PDF* approach, a novel method proposed by X.Ji in 2013 [33]. This approach has opened the path to many *ab initio* calculations of quark distribution functions, with the idea that these observables can be accessed on the lattice through appropriate matrix elements.

To explain the theoretical principles of the quasi-PDF approach, let us first recall the definitions of parton distribution function (PDF), already stated in Eqs. (2.36-2.38) in Minkowski space. In this Section we consider the unpolarized PDF, but the arguments described below also extend to other kinds of quark distributions. The unpolarized PDF for a given quark is defined on the light-cone and reads

$$q(x) = \frac{1}{4\pi} \int_{-\infty}^{+\infty} d\xi^- \, e^{-ixP^+\xi^-} \, \langle N|\bar{\psi}(\xi^-)\gamma^+ W(\xi^-,0)\psi(0)|N \rangle \, , \qquad (3.88)$$

where $P^+ = (P^0 + P^3)/\sqrt{2}$ is the *plus* component of the hadron momentum, $\xi^- = (\xi^0 - \xi^3)/\sqrt{2}$, $\gamma^+ = (\gamma^0 + \gamma^3)/\sqrt{2}$ and $W(\xi^-,0) = e^{-ig\int_0^{\xi^-} d\eta^- A^+(\eta^-)}$ is the Wilson line connecting the light-cone points ξ^- and 0. The difficulty in computing PDFs in lattice QCD is due to the fact that the definition in Eq. (3.88) cannot be used in Euclidean space. As seen in Section 2.3.1, the integral (3.88) receives non-zero contributions in an area which is close to the light-cone, i.e. $\xi^2 = t^2 - \vec{r}^2 \approx 0$. Applying the rotation to imaginary time, we see that in Euclidean space the light-cone condition becomes $-t^2 - \vec{r}^2 \approx 0$, that on the lattice is satisfied only at the origin. On the other hand, the moments of PDFs are related to matrix elements of local operators (see Section 2.3.3 and Appendix A.2) and can be accessed on the lattice. However, only the first few moments can be realistically computed, making impossible a full reconstruction of PDFs from first principles. It is at this point that the quasi-PDF approach comes into play.

The approach by X.Ji relies on the fact that parton distributions can be equivalently defined in two different frames: on the light-cone, where a hadron is moving with momentum P, or in the infinite momentum frame (IMF) according to Feynman's original parton model [6]. As explained in Section 2.3, partons do not have time to interact if a hadron is moving with infinite momentum and the definition of parton distribution functions emerges naturally in this framework. Therefore, if we find a way to boost the nucleon with very large momentum, we should be able to reconstruct PDFs and get closer to the physics of the light-cone as well.

More formally, we compute on the lattice the following distribution, called quasi-distribution

$$\tilde{q}(x,\Lambda,P_3) = \int_{-\infty}^{+\infty} \frac{1}{4\pi} e^{-izxP_3} \langle N|\bar{\psi}(z)\gamma^3 W(z,0)\psi(0)|N\rangle \,, \qquad (3.89)$$

where $\Lambda \sim 1/a$ is a ultra-violet cutoff (being a the lattice spacing), $P = (P_0,0,0,P_3)$, x is the "quark momentum fraction" and $W(z,0) = e^{-ig\int_0^z dz' A_3(z')}$ is the Wilson line in the boost direction. The quark field $\bar{\psi}$ is defined in the space-time point $z^\mu \equiv (0,0,0,z)$, from which we can see that the quasi-distributions are purely spatial correlation functions. The light-cone definition of PDF corresponds to the Eq. (3.89) evaluated at $P_3 \to \infty$, in line with Feynman's original parton model. Since the momentum employed on the lattice is finite, the variable x in Eq. (3.89) does not represent the quark momentum fraction. Indeed, as we will see with our results in Chapter 7, the quasi-distribution does not vanish for $x > 1$, meaning that the partonic interpretation is lost at this stage.

The connection between quasi-PDF, Eq. (3.89), and physical PDF, Eq. (3.88), is established in the framework of Large Momentum Effective Theory (LaMET) [34]. In this context, one has to apply a matching procedure, that was discussed for the first time in Ref. [134]. The matching condition takes the form

$$\tilde{q}(x,\mu,P_3) = \int_{-1}^{-1} \frac{dy}{|y|} \mathcal{C}\left(\frac{x}{y},\frac{\mu}{P_3}\right) q(x,\mu) + \mathcal{O}\left(\frac{\Lambda_{QCD}^2}{P_3^2}, \frac{m_N^2}{P_3^2}\right) \,, \qquad (3.90)$$

where $\tilde{q}(x,\mu,P_3)$ is the renormalized quasi-PDF at a scale μ and $q(x,\mu)$ is the light-cone PDF. In the expression above, $\mathcal{C}$ is the matching coefficient (or matching kernel), computable in perturbation theory as an expansion in the strong coupling constant. The quasi-PDFs differ from the light-cone distributions by corrections which are suppressed with Λ_{QCD}^2/P_3^2 and m_N^2/P_3^2, where m_N is the nucleon mass. The mass-dependent corrections are known as *nucleon mass corrections* (NMCs) and can be computed analytically to all orders and subtracted out, as proved in Ref. [38]. In Eq. (3.90), the corrections in Λ_{QCD}^2/P_3^2 are generic *higher twist* effects [33], in principle computable in perturbative QCD. So far their contribution has not been estimated and thus they can be made smaller by boosting the nucleon with very large momentum, and using the matching procedure.

The approaching of the quasi-PDF to the light-cone physics is schematically represented in Fig. 3.5. The dashed lines in the diagram denote the light-like separations, where PDFs are defined, whilst the thick blue line represents non-local matrix elements with an extended Wilson line in the z-direction in the rest frame of the hadron. Introducing a momentum boost (red arrow), the space-like matrix elements are tilted to the light-cone directions. The difference between the final correlation functions after matching (diagonal solid line) and PDFs is given at the leading order by $\mathcal{O}(\Lambda_{QCD}^2/P_3^2, m_N^2/P_3^2)$ terms.

Summarizing, the *ab initio* extraction of parton distribution functions, within the quasi-PDF approach, requires the following steps:
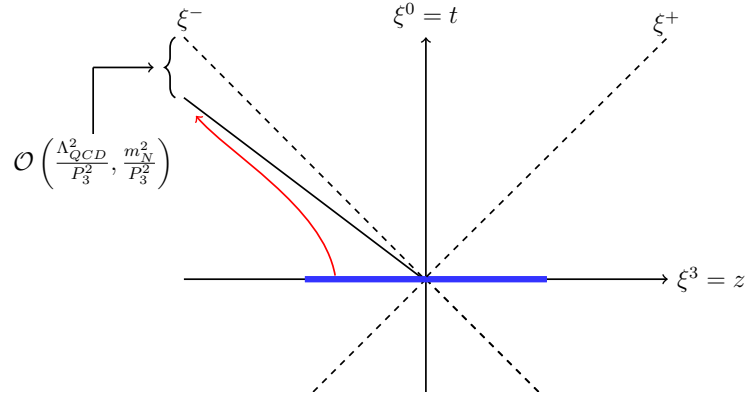
Figure 3.5 Approaching of the space-like correlation functions with Wilson line in the z-direction (blue) to the light-cone PDFs. The dashed lines indicate the light-cone directions and the red arrow denotes the nucleon boost. The diagonal black solid line represents the estimate of the light-cone PDF from the lattice.

1. computation and renormalization of the non-local matrix elements

$$h_\Gamma(P_3, z) = \langle N | \bar{\psi}(z) \Gamma W(z) \psi(0) | N \rangle, \tag{3.91}$$

where P_3 is the momentum in the z-direction and Γ is some combination of Dirac matrices, whose structure gives access to a specific quark distribution;

2. computation of the Fourier transform of the renormalized matrix elements, yielding the quasi-distribution $\tilde{q}(x, \mu, P_3)$;

3. application of the matching procedure, Eq. (3.90), to relate quasi- to physical PDFs.

Chapter 4

Nucleon correlation functions on the lattice

In this Chapter we describe how to extract the matrix elements of interest in this work. They are of the type $\langle N(\vec{p})|\mathcal{O}|N(\vec{p})\rangle$, where $N(\vec{p})$ is a nucleon state with momentum $\vec{p}$ and $\mathcal{O}$ is an operator having the form $\bar{q}\Gamma q$, where q is a quark field and Γ some combination of Dirac γ-matrices. We find that matrix elements can be obtained by taking suitable ratios of *three*- and *two*-point correlation functions, and the ground state dominates in the limit of large Euclidean time. First of all, it is important to establish the notation and introduce the concept of *interpolating fields*, which share the same quantum numbers of the desired particle. Then, we discuss the basic structure of the correlation functions that are computed in this work, together with their building blocks (the *quark propagators*). Finally, we describe the main lattice techniques that we employ to improve the signal-to-noise ratio on the correlators.

4.1   Nucleon field

In hadron structure calculations it is necessary to introduce *interpolating fields*, that applied to the *vacuum* of the theory create and annihilate particle states at two specific space-time points. The choice of the interpolating field is in general not unique, because the same fermion fields may be combined in different ways reproducing the same quantum numbers of the particle state. Here we discuss only the interpolating field of the nucleon, since this is what we used in this work. For a detail review about other baryons and mesons see for instance Ref. [98].

Nucleon is the lightest positive parity state of the baryon spectrum and it is either a proton (p) or a neutron (n). Proton and neutron form a doublet of $1/2$-spin, with isospin components $I_z = +1/2$ (p) and $I_z = -1/2$ (n); their valence quark content is *uud* and *duu* respectively. They are almost degenerate in mass ($m_p \simeq 938$ MeV against $m_n \simeq 940$ MeV), indicating that isospin is a good symmetry. The interpolating fields on the lattice must be constructed in such a way that the quantum numbers of the particles are preserved: baryon number, parity, spin, isospin and valence quark content. For the proton interpolating field, we make the following

choice

$$N_\alpha^p(x) = \varepsilon^{abc} u_\alpha^a(x) \left(d^{b^T}(x) \mathcal{C} \gamma_5 u^c(x) \right) , \tag{4.1}$$

where $\mathcal{C} = i\gamma_2\gamma_4$ is the charge conjugation matrix and the transposition T acts only on the Dirac indices. As can we see, the antisymmetric tensor ε^{abc} ensures that the proton is color-singlet. Moreover, with the choice (4.1), the proton quantum numbers relative to the electric charge, spin and isospin are fully reproduced.

In a similar way, one can define the interpolating field for the neutron as

$$N_\alpha^n(x) = \varepsilon^{abc} d_\alpha^a(x) \left(u^{b^T}(x) \mathcal{C} \gamma_5 d^c(x) \right) . \tag{4.2}$$

However, under parity transformation $\psi(\vec{x},t) \xrightarrow{\mathcal{P}} \gamma_4 \psi(-\vec{x},t)$, the interpolating fields transform in a non-trivial way

$$N_\alpha^p(\vec{x},t) \xrightarrow{\mathcal{P}} \gamma_4 N_\alpha^p(-\vec{x},t), \quad N_\alpha^n(\vec{x},t) \xrightarrow{\mathcal{P}} \gamma_4 N_\alpha^n(-\vec{x},t) . \tag{4.3}$$

Therefore, to ensure that the nucleon has positive parity we need to apply a projection matrix and we define

$$\mathcal{N}^p(x) \equiv P_+ N^p(x), \quad \mathcal{N}^n(x) \equiv P_+ N^n(x) \qquad \text{with} \quad P_+ = \frac{1 + \gamma_4}{2} . \tag{4.4}$$

The projection by $P_- = (1 - \gamma_4)/2$ is also possible, but that would give a state with negative parity, which physically corresponds to the negative parity partner of the nucleon with mass $M \simeq 1535$ MeV.

To conclude, we also specify the interpolating fields (with positive parity) for the creation operators for both proton and neutron

$$\overline{\mathcal{N}}^p(x) = \varepsilon^{abc} \left(\bar{d}^a(x) \mathcal{C} \gamma_5 \bar{u}^{b^T}(x) \right) \bar{u}^c(x) P_+ , \tag{4.5}$$

$$\overline{\mathcal{N}}^n(x) = \varepsilon^{abc} \left(\bar{d}^a(x) \mathcal{C} \gamma_5 \bar{u}^{b^T}(x) \right) \bar{d}^c(x) P_+ , \tag{4.6}$$

where only the color indices have been made explicit.

4.2 Nucleon two-point functions

The basic nucleon two-point function in position space is defined as

$$C_{\alpha\beta}^{2pt}(x',x) = \langle \Omega | N_\alpha(x') \, \overline{N}_\beta(x) | \Omega \rangle , \tag{4.7}$$

where $\overline{N}_\beta(x)$ is the nucleon operator that applied to the vacuum creates a nucleon state at position x, which is in turn annihilated by $N_\alpha(x')$. The open Dirac indices are saturated in such a way that the nucleon state has positive parity. In the previous Section we have seen that the projection matrix is given by the combination $\Gamma = (1 + \gamma_4)/2$ and thus the *spin projected*

two-point function is

$$C_\Gamma^{2pt}(x',x) = \Gamma_{\beta\alpha} \langle\Omega|N_\alpha(x')\,\overline{N}_\beta(x)|\Omega\rangle \,. \tag{4.8}$$

Written in this form, the two-point function can be interpreted as the probability amplitude that a nucleon propagates from x to x' on a given background gauge configuration, see Eq. (3.81). However, in lattice QCD we are actually interested in its average value over a sample of gluon configurations, indicated via

$$\langle C^{2pt}(x',x)\rangle = \langle N(x')\,\overline{N}(x)\rangle \,. \tag{4.9}$$

We refer to $x = (\vec{x},t)$ as the *source position*, where a nucleon state is created, and $x' = (\vec{x}',t')$ as *sink position*. Note that we have assumed $t' > t$, since a T-ordered product is implicit in Eq. (4.7).

Moreover, we can use the translational invariance property on the lattice to simplify the notation and the derivations of the formulae from now on. Indeed, correlation functions evaluated as path integral depend only on the difference $x' - x$. Consequently, without loss of generality, we can shift x' by the position of the source and consider the following expressions

$$C^{2pt}(x',0) \equiv C^{2pt}(\vec{x}',t';0)\,, \quad \langle C^{2pt}(x',0)\rangle = \langle N(x')\,\overline{N}(0)\rangle \,. \tag{4.10}$$

In the following, we study in detail the structure of the two-point functions in terms of quark propagators (quark level) and energy states of the nucleon (hadron level).

4.2.1 Quark level

The aim here is to write down the nucleon two-point function in terms of Wick contractions of the quark fields. Since the logic is very similar, we consider only the proton for which we have

$$C_{\alpha,\alpha}^{2pt}(x',0) = \langle\Omega|\mathcal{N}_\alpha(x')\,\overline{\mathcal{N}}_\alpha(0)|\Omega\rangle = -\langle\Omega|\overline{\mathcal{N}}_\alpha(0)\,\mathcal{N}_\alpha(x')|\Omega\rangle$$
$$= -\langle\Omega|(\overline{N}P_+)_\alpha(0)\,(P_+N)_\alpha(x')|\Omega\rangle \,. \tag{4.11}$$

Using the property $P_+^2 = 1$ and applying the Wick theorem, we get

$$C_{\alpha,\alpha}^{2pt}(x',0) = -\varepsilon^{abc}\varepsilon^{a'b'c'}\langle\Omega|\,\bar{d}_\alpha^a(0)\,(C\gamma_5)_{\alpha\beta}\,\bar{u}_\beta^{bT}(0)\,\bar{u}_\gamma^c(0)\,P_{\gamma\gamma'} \tag{4.12}$$
$$\qquad u_{\gamma'}^{a'}(x')\,d_{\alpha'}^{b'T}(x')\,(C\gamma_5)_{\alpha'\beta'}\,u_{\beta'}^{c'}(x')\,|\Omega\rangle$$
$$= -\varepsilon^{abc}\varepsilon^{a'b'c'}(C\gamma_5)_{\alpha\beta}(C\gamma_5)_{\alpha'\beta'}P_{\gamma\gamma'}$$
$$\qquad \langle\Omega|\,\bar{d}_\alpha^a(0)\,\bar{u}_\beta^{bT}(0)\,\bar{u}_\gamma^c(0)\,u_{\gamma'}^{a'}(x')\,d_{\alpha'}^{b'T}(x')\,u_{\beta'}^{c'}(x')\,|\Omega\rangle$$
$$= \varepsilon^{abc}\varepsilon^{a'b'c'}(C\gamma_5)_{\alpha\beta}\,(C\gamma_5)_{\alpha'\beta'}\,P_{\gamma\gamma'}\,D_d^{-1}(x',0)_{\alpha'\alpha}^{b'a}$$
$$\qquad \left[D_u^{-1}(x',0)_{\gamma'\beta}^{a'b}\,D_u^{-1}(x',0)_{\beta'\gamma}^{c'c} - D_u^{-1}(x',0)_{\beta'\beta}^{c'b}\,D_u^{-1}(x',0)_{\gamma'\beta}^{a'c}\right]\,, \tag{4.13}$$

where we have contracted all quark fields using the Grassmann properties for anti-commuting numbers. $D_u^{-1}(x',0)$ and $D_d^{-1}(x',0)$ denote the *up* and *down* quark propagators from 0 to x',

on a given gauge field configuration. From Eq. (4.13) it is thus clear that *up* quark fields can be contracted in two possible ways, that give rise to *connected* diagrams. This contraction pattern is depicted schematically in Fig. 4.1, where the solid lines denote the quark propagators connecting the lattice points 0 and x'.

Figure 4.1 Schematic representation of the proton two-point function. The solid lines indicate the quark propagators connecting the points 0 and x', in which the particle is created and annihilated respectively.

The fact that solely connected pieces contribute to the two-point function is a result that can be extended also to the other baryons. On the other hand, this is not valid in general for all mesons, and examples are the pseudoscalar π^0 and η^0 mesons. For these particles it is possible to have a quark propagating from one point to the same point of the lattice, which produces *disconnected diagrams*. These diagrams are notoriously much more difficult to compute and require the use of appropriate gauge-noise reduction techniques. Disconnected contributions appear also in *three-point function* calculations, as we will see in Section 4.3.1. However, in this work they are not computed as we focus on the non-singlet flavor structure $u - d$, in which disconnected diagrams cancel out under isospin symmetry.

4.2.2 Hadron level

Having discussed how the two-point functions are built from quark propagators, we want to study these correlation functions also from another point of view, i.e. in terms of energy states.

In our practical applications we are interested in the momentum dependence of the matrix elements extracted from the lattice. To this aim, we need to do a *momentum-projection* onto states with well-defined momentum $\vec{p}$. This is realized via a sum over the sink positions, as

$$C_{\alpha\beta}^{2pt}(\vec{p},t') = \frac{1}{V}\sum_{\vec{x}'} e^{-i\vec{p}\cdot\vec{x}'} C_{\alpha\beta}^{2pt}(\vec{x}',t') = \frac{1}{V}\sum_{\vec{x}'} e^{-i\vec{p}\cdot\vec{x}'} \langle\Omega| N_\alpha(\vec{x}',t')\overline{N}_\beta(0)|\Omega\rangle \,, \qquad (4.14)$$

where $V = L^3$ is the spatial volume of the lattice. From the two-point function in momentum space one can extract physical quantities, like energies and masses of particles if $\vec{p} = 0$. To do this, we first have to shift the interpolating field to the origin via unitary operators

$$C_{\alpha\beta}^{2pt}(\vec{p},t') = \frac{1}{V}\sum_{\vec{x}'} e^{-i\vec{p}\cdot\vec{x}'} \, \langle\Omega|e^{-i\hat{p}\vec{x}'}e^{\hat{H}t'}N_\alpha(0)e^{-\hat{H}t'}e^{i\hat{p}\vec{x}'}\overline{N}_\beta(0)|\Omega\rangle \,, \qquad (4.15)$$

where $\hat{p}$ and $\hat{H}$ are the momentum operator and the QCD Hamiltonian, and then insert a complete set of eigenstates. We assume that the states are normalized as

$$\langle \vec{p}, n | \vec{k}, m \rangle = \delta_{n,m} \delta_{\vec{p},\vec{k}}, \quad \text{with} \quad \mathbb{1} = \sum_{\vec{p},n} |\vec{p}, n \rangle \langle \vec{p}, n| \,. \tag{4.16}$$

Thus, using Eqs. (4.15) and (4.16), we obtain the spectral decomposition

$$C^{2pt}_{\alpha\beta}(\vec{p}, t') = \sum_n e^{-E_{\vec{p}}^{(n)} t'} \langle \Omega | N_\alpha(0) | n, \vec{p} \rangle \langle n, \vec{p} | \overline{N}_\beta(0) | \Omega \rangle \,, \tag{4.17}$$

according to which the two-point function receives contributions by all states that share the same quantum numbers of the nucleon. The n-th eigenstate of the spectrum is an excitation of the nucleon with energy $E_{\vec{p}}^{(n)}$. However, all this "tower" of states does not contribute to the sum with the same amount for two main reasons. First of all, the correlator decays exponentially with the energy of the particle, implying that excited states are suppressed for sufficiently large time separation, t'. Secondly, the nucleon interpolating field has a different overlap with the eigenstates $|n, \vec{p}\rangle$, which are then created with different probabilities. To quantify this overlap we can introduce some factors Z_n for each state, through the following Euclidean relations

$$\langle \Omega | N_\alpha | n, \vec{p} \rangle = Z_n u_\alpha(p^{(n)}, s), \qquad \sum_s u_\alpha(p,s) \bar{u}_\beta(p,s) = (-i\slashed{p} + m)_{\alpha\beta} \,. \tag{4.18}$$

Therefore, the spectral decomposition of the two-point function becomes

$$C^{2pt}_{\alpha\beta}(\vec{p}, t') = \sum_n |Z_n|^2 e^{-E_{\vec{p}}^{(n)} t'} \left(-i\slashed{p} + m_n \right)_{\alpha\beta} \,. \tag{4.19}$$

In the asymptotic limit, $t' \to \infty$, only the ground state will dominate the sum

$$C^{2pt}_{\alpha\beta}(\vec{p}, t') \xrightarrow{t \gg 0} |Z_0|^2 e^{-E_{\vec{p}}^{(0)} t'} \left(-i\slashed{p} + m_N \right)_{\alpha\beta} \,, \tag{4.20}$$

where m_N is the nucleon mass. As a result, the energy of the ground state can be extracted by using the exponential decay of the two-point function over the time. The standard procedure is to define the *effective energy* as a ratio of correlators at two consecutive time-slices

$$E^N_{eff}\left(\vec{p}, t + \frac{1}{2}\right) = \frac{C^{2pt}(\vec{p}, t)}{C^{2pt}(\vec{p}, t + 1)} \xrightarrow{t \gg 0} E_N(\vec{p}) \tag{4.21}$$

and seek the range in which its value becomes constant. We note that in Eq. (4.21) we have assumed that the two-point function is already spin-projected and the average over a sample of gauge configurations has been already carried out.

In Fig. 4.2 we show the nucleon effective energies and their plateau averages obtained on the twisted mass cA2.09.48 ensemble [130], used in this work to extract parton distribution functions. The cA2.09.48 ensemble is simulated on a lattice volume $V = 48^3 \times 96$ with lattice spacing $a \simeq 0.0938$ fm, using two light degenerate quarks ($N_f = 2$) with mass tuned to their

physical value. The complete list of parameters is given in Table 5.1. The nucleon energies are extracted at momenta $|\vec{p}| = \{0, 6, 8, 10\}\pi/L \simeq \{0, 0.83, 1.11, 1.38\}$ GeV (blue, red, magenta, green) using $\{20, 99, 425, 811\}$ configurations with multiple random source positions. The total statistics consists of $\{320, 9504, 38250, 72990\}$ measurements respectively (see Section 5.2). We also note that these results are obtained by using *smearing* techniques to improve the overlap of the interpolating fields with the particle states; in particular, Wuppertal-, APE- and momentum smearing techniques have been employed. The smearing methods used in this work are discussed in Section 4.6.
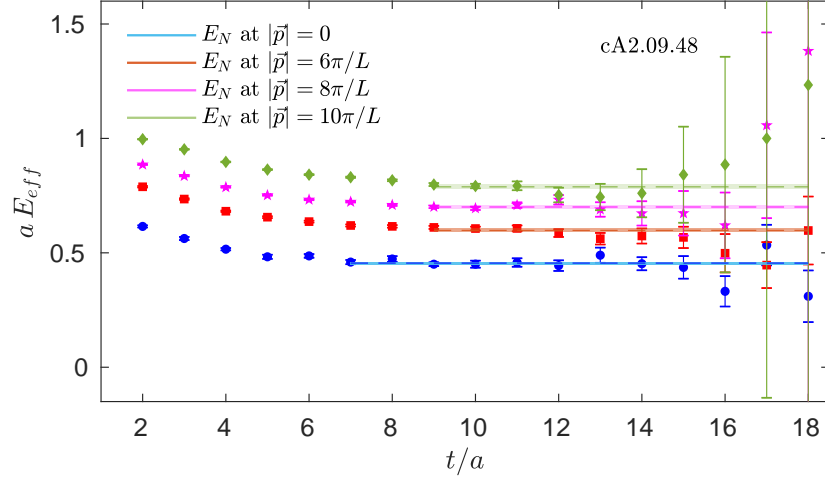
Figure 4.2 Nucleon effective energies as a function of time and plateau averages, extracted at $|\vec{p}| = \{0, 6, 8, 10\}\pi/L \simeq \{0, 0.83, 1.11, 1.38\}$ GeV (blue, red, magenta, green respectively). The measurements are performed on the physical point cA2.09.48 ensemble [130] of lattice volume $V = 48^3 \times 96$. Due to a rapid increase of the noise-to-signal ratio with time and nucleon momentum, we perform $\{320, 9504, 38250, 72990\}$ measurements to reach sufficiently high accuracy. The results are obtained using Wuppertal-, APE- and momentum smearing techniques discussed in Section 4.6.

4.3 Nucleon three-point functions

To study the inner structure of hadrons one also needs to compute more complicated objects than two-point functions. Indeed, as seen in Chapter 2, the operator product expansion of deep inelastic scattering relates form factors and parton distributions to matrix elements of composite operators. In our work, essential ingredients of the calculation are nucleon three-point functions. The most general form is

$$C^{3pt}_{\alpha\beta}(x'; x_1; x) = \langle\Omega|N_\alpha(x')\mathcal{O}(x_1)\overline{N}_\beta(x)|\Omega\rangle \,, \tag{4.22}$$

where $\overline{N}_\beta(x)$, $N_\alpha(x')$ are the nucleon interpolating fields at the source and sink respectively and $\mathcal{O}$ is a composite operator applied at some insertion point x_1 of the lattice. In general $\mathcal{O}$ carries Dirac and color indices, that have to be properly contracted. $\mathcal{O}$ can be distinguished in: **i)** *ultra-local* operator, if it is of the form $\bar{q}\Gamma q$, where the quark fields $q, \bar{q}$ are applied at the same lattice points; **ii)** *local* operator, if a finite number of derivatives in the quark fields are

involved; **iii**) *non-local* operator, as in our case, if q and $\bar{q}$ are applied at two different points of the lattice and are connected by gauge links that make the whole object gauge invariant.

In analogy to two-point functions, translational invariance implies here that C^{3pt} is only a function of the distances $x' - x$ and $x_1 - x$. Consequently, we can use this property to simplify the notation and set the source to the origin. Having this in mind, we consider from now on the following object

$$C^{3pt}_{\alpha\beta}(x';x_1;0) \equiv C^{3pt}_{\alpha\beta}(\vec{x}',t';\vec{x}_1,\tau;0) \quad \text{with } x' = (\vec{x}',t'), \; x_1 = (\vec{x}_1,\tau), \tag{4.23}$$

where t' and τ denote the time-slices of the sink and insertion point respectively. They must satisfy the condition $t' < \tau < 0$, as we have implicitly assumed a T-ordered product in Eq. (4.22).

As for the two-point case, the three-point functions can be studied at the quark level, i.e. in terms of Wick contractions, or at the hadron level via a spectral decomposition. This is discussed in the following two Sections.

4.3.1 Quark level

Compared to the two-point case, in the three-point functions there are two additional quark fields that have to be contracted. Moreover, the contraction pattern depends on the flavor structure of the composite operator. Indeed, it is easy to see that for the proton with interpolating field as in Eq. (4.1), we have more terms to sum if the operator is of the type $\mathcal{O} = \bar{u}Xu$ than $\mathcal{O} = \bar{d}Xd$. Here X indicates anything the operator is made of: Dirac gamma structure (γ_μ, γ_5, etc.) and/or link variables.

Since in our work we are interested in the non-singlet flavor combination $u - d$, we consider the following operator

$$\mathcal{O}(x_1) = \bar{u}(x_1)Xu(x_1) - \bar{d}(x_1)Xd(x_1) . \tag{4.24}$$

For the time being we keep X generic, because contractions among quark fields are not affected by its specific structure.

Expanding the three-point function $\langle\Omega|N_\alpha(x')\mathcal{O}(x_1)\overline{N}_\beta(x)|\Omega\rangle$, we have

$$\begin{aligned}
C^{3pt}_{\alpha\beta}(x';x_1;0) =& \langle\Omega|\varepsilon^{abc}u^a_\alpha(x)\left(d^{b^T}(x)C\gamma_5 u^c(x)\right) \times \\
& [\bar{u}^f_\mu(x_1)X_{\mu\nu}u^f_\nu(x_1) - \bar{d}^f_\mu(x_1)X_{\mu\nu}d^f_\nu(x_1)] \times \\
& \varepsilon^{a'b'c'}\left(\bar{d}^{a'}(0)(C\gamma_5)\bar{u}^{b'^T}(0)\right)u^{c'}_\beta(0)|\Omega\rangle .
\end{aligned} \tag{4.25}$$

For clarity reasons we have written explicitly only the open Dirac indices for the interpolating fields. From Eq. (4.25) we can see that the three-point function can be splitted into two main

components, the *up-part* ($U_{\alpha\beta}$) and the *down-part* ($D_{\alpha\beta}$), and therefore

$$C^{3pt}_{\alpha\beta}(x';x_1;0) = U_{\alpha\beta}(x';x_1;0) - D_{\alpha\beta}(x';x_1;0) \,. \tag{4.26}$$

Both terms contain two disconnected diagrams each, that arise from contractions of quark fields placed at the same insertion points. An example of this kind of contraction is shown in the right panel of Fig. 4.27, for the insertion with the *down* quark. In the diagram we indicate the generic operator with the black circle and the arrow circulating inside loop stands for the propagator $G_d^{-1}(x_1,x_1)$. If one is interested in the single up and down components of the three-point function, the computation of disconnected diagrams cannot be avoided. However, if we focus on the flavor structure $u - d$, disconnected terms can be neglected, since they appear in $U_{\alpha\beta}$ and $D_{\alpha\beta}$ with opposite signs and cancel out invoking isospin symmetry. This is the reason why in our lattice calculations only connected diagrams are considered.

After Wick contractions with the down quarks in the current, the connected part reads

$$\begin{aligned}
\mathcal{D}_{\alpha\beta}(x';x_1;0)\big|_{\text{CONN}} = & \, \varepsilon^{abc}\varepsilon^{a'b'c'}[(C\gamma_5)^T D_d^{-1}(x',x_1)\,X\,D_d^{-1}(x_1,0)(C\gamma_5)]^{ba'}_{\delta\delta'} \\
& \times \left\{ D_u^{-1}(x',0)^{ac'}_{\alpha\beta}D^{-1}(x',0)^{cb'}_{\delta\delta'} - D_u^{-1}(x',0)^{ab'}_{\alpha\delta'}D_u^{-1}(x',0)^{cc'}_{\delta\beta} \right\},
\end{aligned} \tag{4.27}$$

where the transposition acts on the Dirac indices. This contraction pattern for the connected part of $D_{\alpha\beta}$ is illustrated in the left panel of Fig. 4.3.
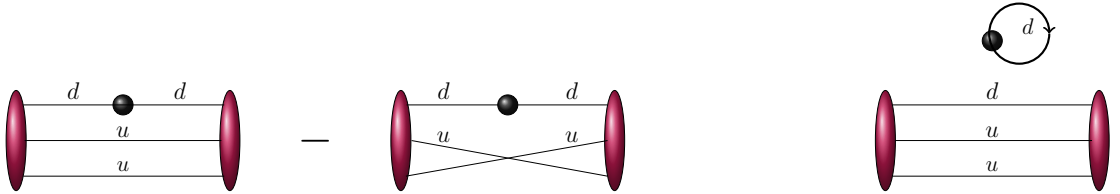
Figure 4.3 Wick contractions for the proton three-point function using an inserted operator of the type $\bar{d}\,X\,d$. The hadron states are on each side of the diagrams and the insertion operator is indicated via the black circle. Left: Difference between the two connected diagrams in Eq. (4.27). Right: Illustration of one possible disconnected diagram.

The expression of $U_{\alpha\beta}(x';x_1;0)$ is slightly more involved than the one of $D_{\alpha\beta}(x';x_1;0)$, because there are more possibilities to contract the *up* quarks to each other; the contractions result in four terms in total. We omit writing the final result, since Wick contractions proceed in a similar way as the ones just showed above.

We have thus seen that computing correlation functions of the nucleon requires the inversion of the Dirac operator for both *up* and *down* quarks, followed by the contraction of propagators according to the specific pattern. Moreover, the momentum projection for the three-point functions requires the knowledge of *all-to-all* propagators, i.e propagators from all to all lattice sites of the lattice, as Eq. (4.27) suggests. To be computed explicitly, the all-to-all propagators would require sets of inversions proportional to the lattice volume. This procedure is far too computationally demanding. Fortunately, different methods have been developed

for making this feasible, leaving on the other hand some flexibility in the treatment of such propagators. The approach used in this work is described in Section 4.5.2.

4.3.2 Hadron level

Here we want to extract the spectral decomposition of nucleon three-point functions, which is an important step for introducing the matrix elements computed in this work.

The spectral decomposition is performed by summing over the spatial positions of the sink and the insertion. The difference with the two-point case is that now the momentum projection introduces dependency on two momenta, $\vec{p}'$ and $\vec{q}$. The three-point function in momentum space reads

$$C^{3pt}_{\alpha\beta}(\vec{p}',t;\vec{q},\tau;0) = \frac{1}{V^2}\sum_{\vec{x}',\vec{x}_1} e^{-i\vec{p}'\cdot\vec{x}'} \langle\Omega|N_\alpha(x')\mathcal{O}(x_1)\overline{N}_\beta(0)|\Omega\rangle \, e^{+i\vec{q}\cdot\vec{x}_1} \ . \tag{4.28}$$

Writing the interpolating fields and the insertion operator in the Heisenberg picture

$$\begin{aligned} C^{3pt}_{\alpha\beta}(\vec{p}',t;\vec{q},\tau;0) &= \frac{1}{V^2}\sum_{\vec{x}',\vec{x}_1} e^{-i\vec{p}'\cdot\vec{x}'} \, e^{+i\vec{q}\cdot\vec{x}_1} \\ &\times \langle\Omega|N_\alpha(0)e^{-\hat{H}t'}e^{i\hat{p}\cdot\vec{x}'}e^{-i\hat{p}\cdot\vec{x}_1}e^{\hat{H}\tau}\mathcal{O}(0)e^{-\hat{H}\tau}e^{i\hat{p}\cdot\vec{x}_1}\overline{N}(0)|\Omega\rangle \ , \end{aligned} \tag{4.29}$$

and inserting two sets of complete eigenstates, the three-point function becomes

$$\begin{aligned} C^{3pt}_{\alpha\beta}(\vec{p}',t;\vec{q},\tau;0) &= \frac{1}{V^2}\sum_{\substack{\vec{x}',\vec{x}_1 \\ \vec{k},\vec{k}',n,n'}} \langle\Omega|N_\alpha|n',\vec{k}'\rangle \, \langle n',\vec{k}'|\mathcal{O}|n,\vec{k}\rangle \, \langle n,\vec{k}|\overline{N}_\beta|\Omega\rangle \\ &\times e^{-i\vec{x}'(\vec{p}'-\vec{k}')} \, e^{-i\vec{x}_1(\vec{k}'-\vec{k}-\vec{q})} e^{-E^{(n')}_{\vec{k}'}(t'-\tau)} e^{-E^{(n)}_{\vec{k}}\tau} \ . \end{aligned} \tag{4.30}$$

Here we have assumed the states normalized as in Eq. (4.16). As we can see, the sum over the sink and insertion points fixes the momentum of the final state to $\vec{k}' = \vec{p}'$ and the one of the initial state to $\vec{p} \equiv \vec{p}' - \vec{q}$. Thus, the difference $\vec{q} = \vec{p}' - \vec{p}$ can be interpreted as the momentum transferred to an outgoing proton. Eliminating the volume sums over $\vec{x}'$ and $\vec{x}_1$, we finally get the spectral decomposition

$$C^{3pt}_{\alpha\beta}(\vec{p}',t;\vec{q},\tau;0) = \sum_{n,n'} e^{-E^{(n')}_{\vec{p}'}(t'-\tau)} e^{-E^{(n)}_{\vec{p}}\tau} \langle\Omega|N_\alpha|n',\vec{p}'\rangle \, \langle n',\vec{p}'|\mathcal{O}|n,\vec{p}\rangle \, \langle n,\vec{p}|\overline{N}_\beta|\Omega\rangle \ . \tag{4.31}$$

As for the two-point functions, hadron states with the same quantum numbers of the proton give non-zero contributions, but the proton ground state will dominate the sums in the asymptotic limit $t' - \tau \to \infty$ and $\tau \to \infty$. Denoting the proton ground state by $\mathcal{H}$ [1], the

---

[1]We use this notation to avoid confusion with the proton interpolating field.

asymptotic limit of the three-point function reads

$$C_{\alpha\beta}^{3pt}(\vec{p}',t;\vec{q},\tau;0) \overset{t'\ll\tau\ll0}{=} e^{-E_{\vec{p}'}^{(0)}(t'-\tau)} e^{-E_{\vec{p}}^{(0)}\tau}$$

$$\times \langle\Omega|N_\alpha|\mathcal{H}(\vec{p}')\rangle \langle\mathcal{H}(\vec{p}')|\mathcal{O}|\mathcal{H}(\vec{p})\rangle \langle\mathcal{H}(\vec{p})|\overline{N}_\beta|\Omega\rangle. \qquad (4.32)$$

An important conclusion follows from the above result: excited states are suppressed for large time separations of the sink and the insertion relative to the source. Consequently, in order to isolate the ground state, one should let the nucleon propagate long enough on the lattice. However, this is not an easy task because the correlation functions decay exponentially with time and one would need to accumulate a large amount of statistics to have a clear signal. This point is discussed in detail in Chapter 5, but can already be evinced from Fig. 4.2.

In our work, it is also important to derive the form factor decomposition of the three-point functions, because it determines the structure of the projection matrix and kinematic factors associated to a specific insertion. To this aim, first of all we write the amplitudes in Eq. (4.32) in terms of overlap factors (Z_0) between the proton state and the interpolating field

$$\langle\Omega|N_\alpha|\mathcal{H}(p') = Z_0\, u_\alpha(p'), \quad \langle\mathcal{H}(p')|\mathcal{O}|\mathcal{H}(p)\rangle = \bar{u}(p')\mathcal{O}_{00}\,u(p), \qquad (4.33)$$

where u, $\bar{u}$ are the usual Dirac spinors and O_{00} is the matrix element evaluated between the two proton ground states. Finally, applying the spinor completeness relation as in Eq. (4.18), the three-point function can be decomposed as

$$C_{\alpha\beta}^{3pt}(\vec{p}',t;\vec{q},\tau;0) \overset{t'\ll\tau\ll0}{=} |Z_0|^2\, e^{-E_{\vec{p}'}^{(0)}(t'-\tau)} e^{-E_{\vec{p}}^{(0)}\tau} \left[(-i\slashed{p}'+m_N)\,O_{00}\,(-i\slashed{p}+m_N)\right]_{\alpha\beta},$$
$$(4.34)$$

where m_N is the nucleon mass. The open Dirac indices in the above equation are then saturated by using a projection matrix $\tilde{\Gamma}$, which defines a spin-projected three-point function

$$C_{\tilde{\Gamma}}^{3pt}(\vec{p}',t;\vec{q},\tau;0) = \tilde{\Gamma}_{\alpha\beta}\, C_{\alpha\beta}^{3pt}(\vec{p}',t;\vec{q},\tau;0). \qquad (4.35)$$

The structure of $\tilde{\Gamma}$ in terms of γ-matrices strictly depends on the operator $\mathcal{O}$ and on the physics we want to study. In our computation we use different projectors for the three-point functions, as described in Section 5.1.2.

So far we have kept the discussion very general, assuming that the momentum of the initial and final proton states is different. However, in our calculations the momentum transfer is set to zero, because parton distribution functions are defined as matrix elements between particle states sharing the same momentum. Consequently, from now on, we take $\vec{q} = 0$ and $\vec{p}' = \vec{p}$, unless otherwise specified in the text.

4.4 Nucleon matrix elements

From the spectral decomposition of the three-point function, see Eq. (4.32), we can extract the matrix element $\langle \mathcal{H}(p)| \mathcal{O} |\mathcal{H}(p)\rangle$ of an operator $\mathcal{O}$ between the nucleon ground states. This object encodes information about the nucleon inner structure. For instance, from $\mathcal{O} = \bar{\psi}\gamma_5\gamma_\mu\tau_3\psi$ one can compute the nucleon axial charge g_A^{u-d} as seen in Section 2.3.3, or from a twist-two non-local operator we obtain parton distribution functions and their generalizations.

To isolate the matrix element $h_O = \langle \mathcal{H}(p)| \mathcal{O} |\mathcal{H}(p)\rangle$, it is necessary to remove from the three-point functions the exponential factors energy-dependent, as well as the overlap terms Z_n that appear in the spectral decomposition. Since these unwanted terms also enter the two-point functions, see Eq.(4.20), we can simply take their ratio in the time window in which the ground state dominates. Using the Lorentz invariant normalization of the states

$$\langle \vec{p}|\vec{k}\rangle = 2E\left(\vec{p}\right)V\,\delta_{\vec{p},\vec{k}}\,, \tag{4.36}$$

where $V = L^3$ is the lattice volume, we obtain

$$\frac{C_{\tilde{\Gamma}}^{3pt}(\vec{p},t;\vec{q},\tau;0)}{C_{\Gamma}^{2pt}(\vec{p},t)} \underset{t'\ll\tau\ll0}{=\!=} \frac{\mathrm{Tr}\left[\tilde{\Gamma}(-i\slashed{p}+m_N)\,O_{00}\,(-i\slashed{p}+m_N)\right]}{2E_{\vec{p}}\mathrm{Tr}\left[\Gamma(-i\slashed{p}+m_N)\right]} = K(\vec{p})\,h_O(\Gamma,\tilde{\Gamma})\,. \tag{4.37}$$

$h_O(\Gamma,\tilde{\Gamma}) = \langle \mathcal{H}(p)| \mathcal{O} |\mathcal{H}(p)\rangle$ is the desired matrix element, obtained by projecting the two- and three-point functions with γ-matrices, indicated with Γ and $\tilde{\Gamma}$ respectively. A kinematic factor $K(\vec{p})$ is associated at every matrix element and depends on the nucleon momentum and inserted operator.

For non-zero momentum transfer ($\vec{p}' \neq \vec{p}$), the matrix elements can be obtained in a similar way, building suitable ratios of three- and two-point functions that cancel the unwanted terms.

4.5 Quark propagator

Having established how matrix elements can be extracted in Euclidean field theory, it is important to see in detail the building blocks of every hadron correlation function, namely the *quark propagators*. In our calculation we need to evaluate two kinds of propagators, *point-to-all* and *all-to-all propagators*, that are discussed in the next two Sections.

4.5.1 Point-to-all propagator

The quark propagator on a given gauge field configuration is defined as the inverse of the Dirac operator

$$\langle\Omega| \psi_\alpha^a(x')\bar{\psi}_\beta^b(x)|\Omega\rangle = D_{\alpha\beta}^{-1\,ab}(x',x)[U]\,. \tag{4.38}$$

Computing quark propagators is in general the most demanding component of a typical hadron structure calculation. Indeed, if n is the dimension of a Dirac spinor

$$n = dim(\psi) = V \times 4\,[\text{spin}] \times 3\,[\text{color}] \times 2\,[\text{complex}]\,, \qquad (4.39)$$

the dimension of the Dirac operator will be $n \times n$ and an inversion of such a matrix has a computational cost $\propto n^2$. To make some examples, typical lattice settings require the solution of linear systems with not less than 10^7 unknowns. For instance, the gauge ensemble on which our computations have been performed has $V = 48^3 \times 96$ lattice points, for a total of 254.803.968 systems to be inverted. This lattice might also tend to be small compared to state-of-the-art lattices currently under production. Moreover, this is also made worse by the very large number of quark propagators needed to collect enough statistics for the observable under study. For instance, in our numerical setup we need to invert 576 vectors for each source position (see Section 5.1.4). The number of inversions (and also measurements) depend on several factors, such as the kind of observable, the gauge ensemble and value of the quark masses, the reference frame needed for the specific calculation (e.g. rest frame $\vec{p}' = 0$, or boosted frame $\vec{p}' \neq 0$) and also the value of the source-sink time separation chosen in case of three-point function computations.

In actual lattice calculations, instead of inverting the whole Dirac operator that is not feasible, one makes use of the translational invariance property to invert the matrix from one fixed space-time point x_0 to any lattice site. This means solving a set of linear equations

$$\begin{aligned} D[U]\,\phi &= S, \quad \text{where} \quad S^{x_0,\alpha_0,a_0}(x)_{\alpha a} = \delta(x-x_0)\delta_{\alpha\alpha_0}\delta_{aa_0}\,, \\ \phi &= D^{-1}(x',x)[U]\,S^{x_0,\alpha_0,a_0}(x)_{\alpha a}\,, \end{aligned} \qquad (4.40)$$

where S is called *point source*, carrying Dirac and color indices. The inversion at fixed α and a indices of the source gives only one column of the quark propagator, indicated here by ϕ. Therefore, a complete point-to-all propagator is obtained by solving Eq. (4.40) for 12 (4×3) different rhs.

Since inversions of Dirac operators are fundamental components of numerical computations, the optimization of strategies for solving very large linear systems has been receiving particular attention in the lattice community. This effort results nowadays in a wide variety of approaches based on iterative methods, among which are Krylov space solvers using a preconditioner in order to speed up the inversions (see for instance [135–139]). The solution is not exact, but up to a precision fixed by the norm of the residual $r = D\phi - S$. Moreover, the solving time mainly depends on two aspects: the volume V, as the application of D scales with the dimension of the lattice, and quark masses. It is indeed well known that the smaller quark masses, the more ill-conditioned the operator, yielding an increased time to solution. This is one of the reasons why observables were being computed at quark masses heavier than the physical ones. However, nowadays, thanks to advances in algorithms and the use of large-scale supercomputers, computations at physical quark masses have become feasible, although they still remain difficult and represent a computational challenge in lattice QCD.

4.5.2 All-to-all propagator

Computing quark propagators from a fixed source, as seen in the previous Section, is not enough to extract the three-point functions and therefore the desired nucleon matrix elements. The reason is that the momentum-projection leads to a sum over all spatial sink ($\vec{x}'$) and insertion positions ($\vec{x}_1$), and involves propagators like $D_u^{-1}(x_1, x')$ or $D_d^{-1}(x_1, x')$, see Eq. (4.27). It is thus clear that point-source methods cannot be used in these cases, as we need to compute all-to-all propagators.

The lattice methods for computing all-to-all-propagators can be divided in two main categories:

1. *Stochastic methods* [140, 141], where a set N_r of orthogonal random sources are used to invert the Dirac operator. The all-to-all propagator is then reconstructed by combining solution vectors with the random sources. This approach is currently applied in a wide variety of hadron structure calculations and was also used for nucleon parton distribution functions in Refs. [37, 39]. In this method, one can freely choose different nucleon momenta at the sink, with no additional inversion. However, the presence of a stochastic noise is unavoidable, unless the stochastic ensemble (N_r) has a reasonable size. The ideal number of stochastic sources to use is not known *a priori* and needs to be investigated for every specific setup. Also, the flexibility of stochastic methods is lost if *momentum smeared* interpolating fields [142] are applied in the calculations, as pointed out in Ref. [39]. Therefore, for the reasons mentioned above, stochastic techniques are not employed in our setup.

2. *Sequential methods* [143], where one of the volume sums (at the sink-$\vec{x}'$ or insertion-$\vec{x}_1$) is carried out through an inversion of the Dirac operator. This method is exact and exists in two variants, *fixed sink* and *fixed current* approach, if the inversions perform the sum over $\vec{x}'$ or $\vec{x}_1$ respectively. In this work, we employ the fixed sink approach for the reasons that will be explained in this Section.

Below we describe the fixed sink method to compute the nucleon all-to-all propagator and we consider only the connected part of the three-point function.

The idea is to construct an appropriate *sequential source* (*S*) by contracting point-to-all propagators. To illustrate the procedure, let us suppose that the insertion operator is $\bar{d}Xd$, where X is a generic Dirac matrix[2] and the momentum transfer is set to zero. The goal is to compute the following three-point function with *down* quark insertion

$$C_{\tilde{\Gamma},d}^{3pt}(\vec{p}', t'; \vec{0}, \tau) = \sum_{\vec{x}', \vec{x}_1} \tilde{\Gamma}_{\alpha\beta} \, \mathcal{D}_{\alpha\beta}(\vec{x}', t'; \vec{x}_1, \tau; 0) \cdot e^{-i\vec{p}' \cdot \vec{x}'} \,, \tag{4.41}$$

where $\mathcal{D}_{\alpha\beta}(\vec{x}', t'; \vec{x}_1, \tau; 0)$ is given in Eq. (4.27). $\tilde{\Gamma}$ is the projector used for the three-point function and introduced in Section 4.3.2. The trick is to rewrite $\mathcal{D}_{\alpha\beta}$ and split it into a product

---

[2]The discussion here applies to any type of operator, provided that is of the form $\bar{d}Xd$.

of two terms. After some algebra we obtain

$$C^{3pt}_{\tilde{\Gamma},d}(\vec{p}',t';\vec{0},\tau) = \sum_{\vec{x}',\vec{x}_1} X D_d^{-1}(x_1;0)\Big|^{da'}_{\mu\nu} D_d^{-1}(x';x_1)^{bd}_{\kappa\mu} \cdot e^{-i\vec{p}'\cdot\vec{x}'} \times$$

$$\tilde{\Gamma}_{\alpha\beta}\, \varepsilon^{abc}\, \varepsilon^{a'b'c'} \left[C\gamma_5 D_u^{-1}(x';0)(C\gamma_5)^T \Big|^{cb'}_{\kappa\nu} D_u^{-1}(x',0)^{ac'}_{\alpha\beta} - (C\gamma_5) D_u^{-1}(x';0)\Big|^{cc'}_{\kappa\beta} D_u^{-1}(x',0)(C\gamma_5)^T \Big|^{ab'}_{\alpha\nu} \right] .$$
(4.42)

If we identify all the second row of the equation above to be $P(x';0)^{ba'}_{\kappa\nu}$ and we use γ_5-hermiticity property of the twisted mass operator, we get

$$C^{3pt}_{\tilde{\Gamma},d}(\vec{p}',t';\vec{0},\tau) = \sum_{\vec{x}',\vec{x}_1} X D_d^{-1}(x_1;0)\Big|^{da'}_{\mu\nu} \left[\gamma_5 (D_u^{-1})^*(x_1;x')\right]^{db}_{\mu\kappa} \left[\gamma_5 P(x';0)\right]^{ab'}_{\kappa\nu} \cdot e^{-i\vec{p}'\cdot\vec{x}'} .$$
(4.43)

From the result above, one can see that the sequential source can be identified via

$$S(x';0)^{ab'}_{\kappa\nu} = \left[\gamma_5 P(x';0)\right]^{*\,ab'}_{\kappa\nu} \cdot e^{+i\vec{p}'\cdot\vec{x}'} \quad .$$
(4.44)

Indeed, upon inversion for each of the indices b' and ν, we obtain[3]

$$S^{-1}(x_1;0) = \sum_{\vec{x}'} D_u^{-1}(x_1;x') S(x') = \sum_{\vec{x}'} D_u^{-1}(x_1;x') \left[\gamma_5 P(x';0)\right]^* \cdot e^{+i\vec{p}'\cdot\vec{x}'}$$

$$\Rightarrow \left[\gamma_5 S^{-1}(x_1;0)\right]^* = \sum_{\vec{x}'} \left[\gamma_5 D_u^{-1}(x_1;x')\right]^* \gamma_5 P(x';0) \cdot e^{-i\vec{p}'\cdot\vec{x}'} ,$$
(4.45)

which is exactly what we can read in Eq. (4.43).

Summarizing, the momentum-projected three-point function for an operator $\bar{d}Xd$ is computed by

$$C^{3pt}_{\tilde{\Gamma},d}(\vec{p}',t';\vec{0},\tau) = \sum_{\vec{x}_1} \text{Tr}\left\{ X D_d^{-1}(x_1;0) \left[\gamma_5 S^{-1}(x_1;0)\right]^* \right\} ,$$
(4.46)

where S^{-1}, given in Eq. (4.45), is called *sequential propagator*. Quite often it is also referred to as *backward propagator*, because one has to take its conjugate to reconstruct the correct direction of the fermion lines of the diagram. Following this logic, $D_d^{-1}(x_1;0)$ in Eq. (4.46) is instead a *forward propagator*.

In a similar way, one can derive the expression for the sequential source with an operator $\bar{u}Xu$ and get an analogous formula to the one in Eq. (4.46). Once computed the three-point functions with *up* and *down* quark insertions, the difference $C^{3pt}_{\tilde{\Gamma},u} - C^{3pt}_{\tilde{\Gamma},d}$ will give the non-singlet contribution corresponding to the flavor structure $u - d$.

We observe that two important aspects follow from the discussion above. By construction, the momentum, $\vec{p}'$, and time-slice of the sink , t', must be fixed when computing the sequential source; when varying one of these two parameters, new inversions of the Dirac operator are

---

[3]We generate an *up* propagator through inversion of the Dirac operator. We also omit color and Dirac indices for clarity.

needed. On the other hand, the insertion operator (X) can change arbitrarily as well as the momentum transfer, which has always to preserve the momentum conservation $\vec{q} = \vec{p}' - \vec{p}$ (see Section 4.3.2).

The logic in the fixed current approach is instead reversed: the momentum transfer and the operator X have to be fixed prior performing sequential inversions. The sequential source for *down* quark insertion now reads

$$S(x_1; 0) = X D_d^{-1}(x_1; 0) \cdot e^{+i\vec{q} \cdot \vec{x}_1} \ . \tag{4.47}$$

Upon inversion, the sequential propagator is given by

$$S^{-1}(x'; 0) = \sum_{\vec{x}_1} D_d^{-1}(x'; x_1) X D_d^{-1}(x_1; 0) \cdot e^{+i\vec{q} \cdot \vec{x}_1} \ . \tag{4.48}$$

The method of the fixed current is thus particularly convenient when one is interested in matrix elements at a specific value of the momentum transfer and in varying the state at the sink. Therefore, this approach is not advantageous for our computation, in which the initial and final states are kept to be the same. However, in the fixed sink method we need to repeat the inversions for each momentum employed at the sink ($\vec{p}'$) and for each projector ($\tilde{\Gamma}$), coupled to the operator X under study.

4.6 Smearing techniques

To get a signal as clear as possible for the correlation functions, we employ different *smearing* methods, that are described in the following Sections. They are used in order to optimize the overlap of the interpolating fields with the nucleon ground state, reducing contamination by excited states. In lattice QCD this is in general achieved by applying smearing functions to gluon fields and interpolating operators, with parameters that must be properly tuned. An exception has been for us the *stout smearing link*, employed not to improve the overlap factors with the ground state, but to smooth the power divergences typical of non-local operators with Wilson line. This point is discussed in detail in Sections 5.2.1 and 6.4.

4.6.1 Wuppertal smearing

Although the easiest way to create a particle state is to use point sources (see Section 4.5.1), this is not the optimal choice because hadrons are extended particles with a given radius. Moreover, using the point source method, we are also forcing quarks to a specific spin and color state. Although for large time separations results do not depend on the initial state, excited states might not be sufficiently suppressed at moderate time-slices far from the source if the overlap is not optimal. The risk is that the ground state dominates in a time range in which the signal-to-noise ratio is very poor. Indeed, as we have seen in Eq. (4.20), the two-point functions decay exponentially as $e^{-Et'}$, while the gauge noise affects all time-slices in the same way, leading to a quick deterioration of the signal.

The standard method used in lattice QCD to deal efficiently with hadron correlation functions is the so-called *Gaussian smearing*, also known as *Wuppertal smearing* [144, 145]. Within this approach, one constructs new hadron operators from point sources (S) via

$$S^{sm}(\vec{x},t) = \sum_{\vec{y}} F(\vec{x},\vec{y};U(t)) \, S(\vec{y},t) \,, \tag{4.49}$$

where

$$F(\vec{x},\vec{y};U(t)) = [\delta_{\vec{x},\vec{y}} + \alpha H(\vec{x},\vec{y};U(t))] \,, \tag{4.50}$$

and α is the coupling strength of the nearest neighbours in the *hopping matrix*

$$H(\vec{x},\vec{y};U(t)) = \sum_{\mu=1}^{3} \left[U_\mu(\vec{x},t)\,\delta_{\vec{y},\vec{x}+\hat{\mu}} + U^\dagger(\vec{x}-\hat{\mu},t)\,\delta_{\vec{y},\vec{x}-\hat{\mu}} \right] \,. \tag{4.51}$$

The algorithm can be applied recursively n times and thus the smeared source will be

$$S^{sm}(\vec{x},t) = \sum_{\vec{y}} [\delta_{\vec{x},\vec{y}} + \alpha H(\vec{x},\vec{y};U(t))]^n \, S(\vec{y},t) \,. \tag{4.52}$$

The parameters (α,n) must be tuned for every specific gauge ensemble, to optimize the overlap of the hadron operators with their respective ground states. Typically, they are tuned in such a way that the root mean square (r.m.s)

$$\langle r^2 \rangle = \frac{\sum_{\vec{r}} r^2 S^\dagger(\vec{r})\,S(\vec{r})}{\sum_{\vec{r}} S^\dagger(\vec{r})\,S(\vec{r})} \,, \tag{4.53}$$

reproduces approximately the electric charge radius of the particle under study. In Fig. 4.4 we show the effect of the smearing on a point source, keeping $\alpha = 4$ fixed and varying the number of iterations. The more iterations are, wider is the region where the norm squared of the source vector is non-zero. The profile of the distribution takes the form of a typical Gaussian.

To avoid a numerical overflow for a large number of smearing iterations, an arbitrary normalization α-dependent is usually employed. In our computations we adopt the following definition of Gaussian smearing function

$$(F\,q_{\vec{x}}) = \frac{1}{1+6\alpha} \left[q_{\vec{x}} + \alpha \sum_{j=\pm 1}^{\pm 3} U_{\vec{x},\hat{j}}\, q_{\vec{x}+\hat{j}} \right] \,, \tag{4.54}$$

which is just a rewriting of the Eqs. (4.49, 4.50) with an additional factor in front. In the equation above, $q_{\vec{x}}$ denotes the quark field at coordinate $\vec{x}$ and $U_{\vec{x},\hat{j}}$ the link variable along the direction pointed by the vector $\hat{j}$ of unit length. The time coordinate has been suppressed because the smearing operator acts only on the spatial positions and color indices of quark fields, leaving untouched also the spin state.
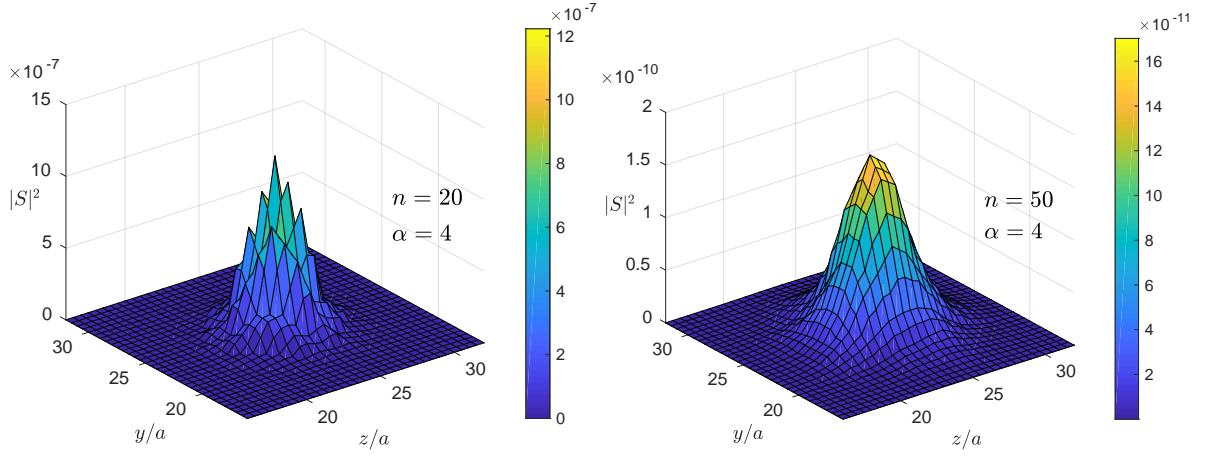
Figure 4.4 Qualitative effect of the Gaussian smearing applied on a point-like source. The norm squared of the source is plotted in the yz-plane, for 20 (left) and 50 (right) smearing iterations, at $\alpha = 4$. The results are obtained using a single gauge configuration from the ensemble cA2.09.48 [130] with lattice volume $V = 48^3 \times 96$.

To improve the efficiency of Gaussian smearing, *link-smearing* techniques are usually employed as well, such as APE-[146], Stout-[147] and HYP-[148] smearing. In the next Sections we describe the ones employed in this work.

4.6.2   APE smearing

APE-smearing [146] was one of the earliest introduced smearing methods, belonging to the class of link-smearing techniques. It is used not only to reduce excited states effects, but also to limit the presence of *exceptional configurations*, which lead to small eigenvalues of the Dirac operator as discussed in Section 3.3.3. This improvement is achieved by replacing each link variable $U_\mu(x)$ with a well-defined path of gluon fields, which connect the same endpoints on the lattice.

In the APE-smearing, each link variable $U_\mu(x)$ is replaced by taking the following combination

$$U_\mu^{APE}(x) = \mathrm{Proj}_{SU(3)} \left[(1 - \alpha_{APE}) U_\mu(x) + \frac{\alpha_{APE}}{6} \sum_{\mu \neq \nu} C_{\mu\nu}(x) \right] , \qquad (4.55)$$

where $C_{\mu\nu}(x)$ is the sum of the staples

$$C_{\mu\nu}(x) = U_\nu(x) U_\mu(x + \hat{\nu}) U_\nu^\dagger(x + \hat{\mu}) + U_\nu^\dagger(x - \hat{\nu}) U_\mu(x - \hat{\nu}) U_\nu(x - \nu \hat{+} \hat{\mu}) , \qquad (4.56)$$

sketched in Fig. 4.5 for a 3-dimensional lattice.

Like Gaussian smearing, APE-smearing is a recursive method. The number of iterations n_{APE} as well as α_{APE} parameter must be optimized according to the problem at hand.

We note that the sum of the staples is not an element of the SU(3) group and therefore the smeared links must be projected back to SU(3) at every iteration, to ensure that the algorithm remains effective. There are different ways of performing the SU(3) projection (see e.g. [149, 150]) and this non-uniqueness is sometimes regarded as a limit of this type of gauge smoothing. Moreover, due to the SU(3) projection, APE-smearing is a non-differentiable

$$\underset{\underset{\longrightarrow}{U_\mu^{APE}(x)}}{} = (1 - \alpha_{APE}) \times \underset{\underset{\longrightarrow}{U_\mu(x)}}{} + \frac{\alpha_{APE}}{4} \times$$
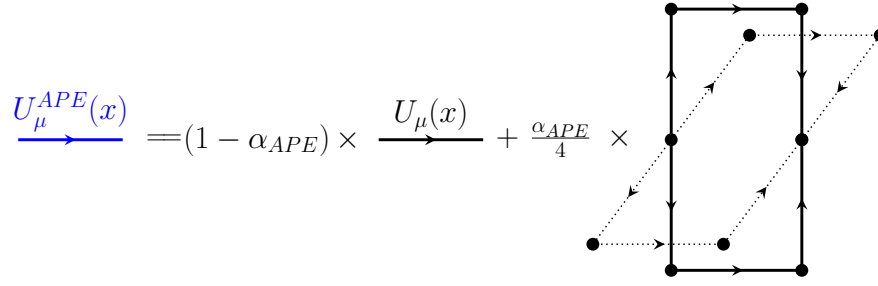
Figure 4.5 Schematic 3-D representation of the APE-smearing procedure. In a 4-D lattice, two additional staples in perpendicular directions contribute.

smearing and consequently non-applicable in Hybrid Monte Carlo [151] updating techniques, that require knowing the response of the action to a small change of the link variables. Another example of non-analytic gauge smoothing is the HYP-smearing [148], in which gauge links are replaced by using hypercubes attached to the original links. This method involves three levels of modified APE-smearing and three SU(3) projections for every complete iteration. For a detailed description of HYP-smearing procedure we refer to the original work of Ref. [148].

4.6.3 Stout smearing

An alternative link-variable smoothing to the before introduced APE-smearing is the *stout smearing*, proposed and tested in Ref. [147]. It has the big advantage of being analytic in the finite complex plane and therefore applicable in Monte Carlo methods that use gauge actions built from stout smeared links. According to [147], an analytic smearing can be constructed by taking a weighted sum of perpendicular staples to the original link, $U_\mu(x)$, as

$$C_\mu(x) = \sum_{\nu \neq \mu} \rho_{\mu\nu} \left(U_\nu(x) U_\mu(x + \hat{\nu}) U_\nu^\dagger(x + \hat{\mu}) + U_\nu^\dagger(x - \hat{\nu}) U_\mu(x - \hat{\nu}) U_\nu(x - \nu \hat{+} \hat{\mu}) \right) , \tag{4.57}$$

where $\rho_{\mu\nu}$ are real tunable parameters. One then defines the matrix $Q_\mu(x)$ through the following relations

$$Q_\mu(x) = \frac{i}{2} \left(\Omega_\mu^\dagger(x) - \Omega_\mu(x) \right) - \frac{i}{2N} \mathrm{Tr} \left(\Omega_\mu^\dagger(x) - \Omega_\mu(x) \right) ,$$
$$\Omega_\mu(x) = C_\mu(x) U_\mu^\dagger(x) \quad \text{(no summation over } \mu) . \tag{4.58}$$

Since $Q_\mu(x)$ is a traceless Hermitian matrix defined in SU(3), $e^{iQ_\mu(x)}$ is an element of SU(3) and therefore the algorithm is iteratively defined in such a way that the links $U_\mu^{(n)}(x)$ at step n are mapped into links $U_\mu^{(n+1)}(x)$ via

$$U_\mu^{(n+1)}(x) = e^{iQ_\mu^{(n)}} U_\mu^{(n)}(x) . \tag{4.59}$$

It is important to note that the exponential function ensures that $U_\mu^{(n+1)}(x)$ are elements of SU(3), eliminating the need of any projection back into the group. Moreover, under any local gauge transformations $G(x)$, the updated links, as well as $Q_\mu(x)$ and $\exp(iQ_\mu(x))$,

share the same transformation properties as the standard link variables, e.g. $U_\mu^{(n+1)}(x) \to G(x)U_\mu^{(n+1)}(x)G^\dagger(x+\hat{\mu})$.

The most common choices for the weighted factors $\rho_{\mu\nu}$ are:

$$\rho_{ij} = \rho \quad \text{with } \rho_{4\mu} = \rho_{\mu 4} = 0, \qquad \text{or} \quad \rho_{\mu\nu} = \rho, \qquad (4.60)$$

corresponding to an isotropic three-dimensional and four-dimensional smearing respectively. The choice of the scheme depends on the problem at hand. In our calculation, we smear only the spatial links of the inserted operator, as the ones in the time direction do not enter the matrix elements under study (see Section 5.1.2).

There are also two other important aspects worth mentioning and for further details we refer to Ref. [147]. Firstly, there is a certain freedom in the choice of $C_\mu(x)$ in Eq. (4.57); in principle, any path with the same endpoints can be employed, such as the one proposed for the HYP-smearing. Secondly, the stout smearing is particularly sensitive to the ρ parameter, as it appears inside the exponential function $\exp(iQ_\mu(x))$. A careful tuning is therefore necessary, as shown in Fig. 4.6. The mean value for the 3-D plaquette is plotted for five ρ-values, varying
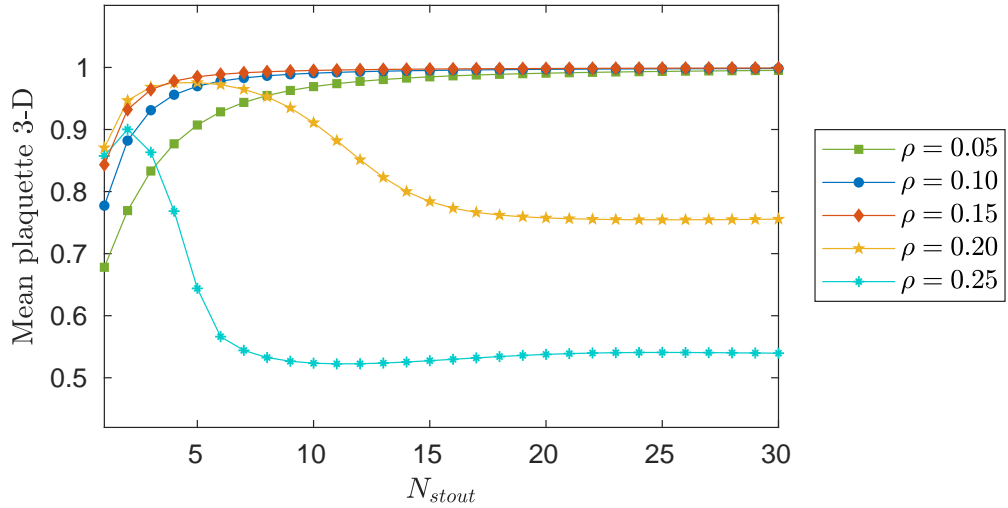
Figure 4.6 The mean smeared 3-D plaquette against stout smearing iterations, for different ρ values. In all cases an isotropic three-dimensional scheme has been applied. These results were obtained using an ensemble simulated with the Symanzik improved gauge action on a $64^3 \times 128$ lattice [131].

the number of smearing iterations (N_{stout}). As can be seen, for small values $\rho \in [0.05 - 0.15]$ the plaquette value increases towards unity and remains stable as the levels of smearing increase. On the other hand, at $\rho = 0.20$ and $\rho = 0.25$, the plaquette initially increases and then begins to fall, reaching a minimum value. A similar behavior has also been observed for the smeared 4-D plaquette and more sophisticated quantities, such as the effective energy of a static quark-antiquark pair extracted from Wilson loop calculations [147].

4.6.4 Momentum smearing

Many applications in lattice QCD require hadrons moving at high momenta. Among these are parton distribution functions (PDFs) and their generalizations (GPDs), and transverse-

momentum dependent parton distribution functions (TMDs). These are all examples of quantities that are defined on the light-cone and require very large boosts to be reliably determined. A novel technique to improve the signal-to-noise ratio for this kind of applications has been recently proposed and tested in Ref. [142] and is known as *momentum smearing*. The idea consists in constructing improved interpolators, having a better overlap with the state of a boosted particle. In Ref. [142] was indeed shown why the standard Gaussian smearing is not efficient for large boosts and the reason relies on the form of the smearing operator F, here rewritten in a more simplified way

$$F = \sum_{\vec{y}} f_{\vec{x}-\vec{y}} G_{\vec{x}\vec{y}} \quad \Rightarrow \quad (Fq)_{\vec{x}} = \sum_{\vec{y}} f_{\vec{x}-\vec{y}} G_{\vec{x}\vec{y}} q_{\vec{y}} \,. \tag{4.61}$$

The sum is over all spatial lattice sites and G stands for the link variables entering the smearing operator. In the free case $(G = \mathbb{1})$ and assuming a Gaussian distribution for the scalar function $f_{\vec{x}-\vec{y}}$

$$f_{\vec{x}-\vec{y}} = f_{\vec{0}} \, \exp\left(-\frac{|\vec{x}-\vec{y}|^2}{2\sigma^2} \right) \,, \tag{4.62}$$

the smearing kernel in momentum space $(\tilde{f})$ is also a Gaussian

$$\tilde{f}(\vec{p}) = \sum_{\vec{z}} e^{i\vec{p}\cdot\vec{z}} f_{\vec{z}} = \sum_{\vec{z}} f_{\vec{0}} \, e^{i\vec{p}\cdot\vec{z}} e^{-\frac{|\vec{z}|^2}{2\sigma^2}} = \tilde{f}(\vec{0}) \exp\left(-\frac{\vec{p}^2 \sigma^2}{2} \right) \,, \tag{4.63}$$

centered at $\vec{p} = 0$. This implies that the smearing operator has maximal overlap with quarks at rest and therefore is not effective for fast moving hadrons. Hence, it would be beneficial to distribute part of the nucleon momentum among quarks. The aim is thus to shift the quark momentum distributions in such a way that they are centered around a finite momentum $\vec{k}$. This is achieved by the following replacement in position space

$$f_{\vec{z}} \mapsto e^{-i\vec{k}\cdot\vec{z}} f_{\vec{z}} \,. \tag{4.64}$$

In this way, the modified smearing operator $(F_{(\vec{k})}q)_{\vec{x}}$ contains the additional phase factor $\exp(-i\vec{k}\cdot(\vec{x}-\vec{y}))$ and can be expressed as

$$(F_{(\vec{k})}q)_{\vec{x}} = \sum_{\vec{y}} e^{-i\vec{k}\cdot(\vec{x}-\vec{y})} f_{\vec{x}-\vec{y}} G_{\vec{x}\vec{y}} q_{\vec{y}} \,. \tag{4.65}$$

The basic idea of *momentum smearing* is illustrated in Fig. 4.7. Taking into account the phase $\exp(-i\vec{k}\cdot\vec{z})$ in position space (see Eq. (4.65)), the Wuppertal momentum smearing function reads

$$(F_{(\vec{k})}q)_{\vec{x}} = \frac{1}{1+6\alpha} \left[q_{\vec{x}} + \alpha \sum_{j=\pm 1}^{\pm 3} U_{\vec{x},\hat{j}} e^{-i\vec{k}\cdot\hat{j}} q_{\vec{x}+\hat{j}} \right] \,, \tag{4.66}$$

where α is the standard Gaussian smearing parameter. In the free case, it has been shown [142] that the optimal value of $\vec{k}$ is given by the hadron momentum divided by the number of valence quarks, for instance $\vec{p}/2$ for mesons or $\vec{p}/3$ for baryonic states, leading to the interpretation
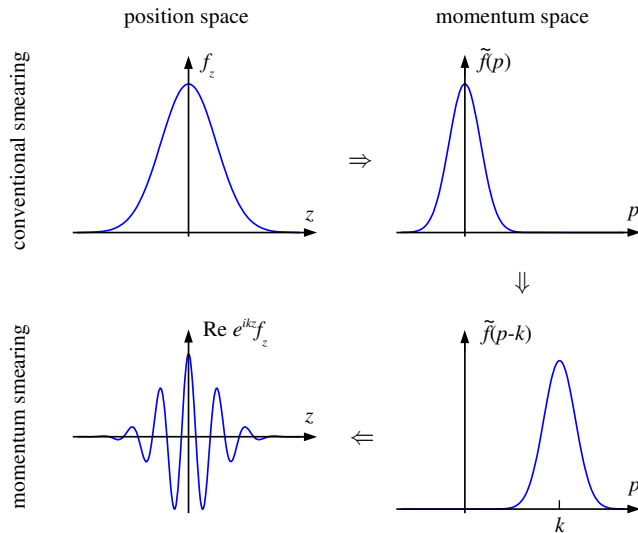
Figure 4.7 Wuppertal smearing (top) and momentum smearing (low) for the example of a Gaussian wave function in 1-D space. The phase *k*-dependent makes the distribution centered around *k* in momentum space. Figure taken from Ref. [142].

that $\vec{k}$ is the momentum carried by the smeared quark. However, this interpretation is not so straightforward in the interacting case, where the gluons can carry an important fraction of the total momentum. In general, $\vec{k}$ is some fraction ξ of the hadron boost and does not need to be quantized

$$\vec{k} = \xi\vec{p} = \xi\frac{2\pi}{L}\vec{n} \qquad (\vec{p}: \text{ hadron momentum}) . \qquad (4.67)$$

The real parameter ξ has to be tuned to maximize the signal-to-noise ratio for each value of the boost employed for correlation function calculations, as demonstrated for the first time in Ref. [142].

In our calculation we make use of this approach, since we need to simulate at as high momenta as possible. In Fig. 4.8 we show the effect of the momentum smearing on the effective energy of a nucleon boosted with $|\vec{p}| = 10\pi/L$, which for the ensemble used in this work corresponds to $|\vec{p}| = 1.38$ GeV. The improvement in the quality of the signal is valuable, as can be observed comparing different ξ values ($\xi = 0$ corresponds to the standard Gaussian smearing). The improvement also becomes more and more evident as the ratio $\gamma = E(\vec{p})/m_N$ increases. For a detailed description of our implementation of momentum smearing and results for other boosts see Section 5.1.3 in the next Chapter.

Since the introduction of momentum smearing, lattice studies in which large boosts are required have benefited from such approach. Indeed, as can be seen from Fig. 4.8 and described in Section 5.1.3, momentum smearing technique allows to achieve momenta that otherwise are not accessible without accumulating huge statistics and using a huge amount of computational resources.
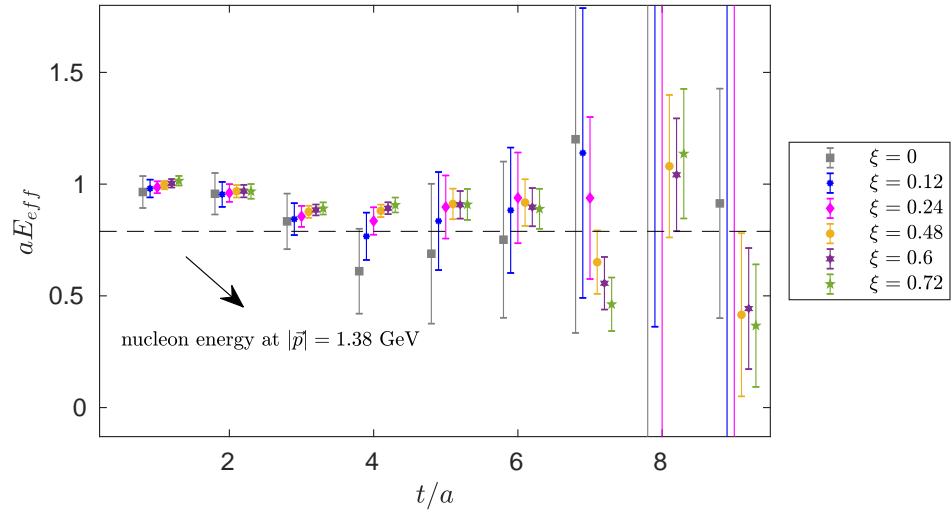
Figure 4.8 Nucleon effective energy at boost $|\vec{p}| = 10\pi/L \approx 1.38$ GeV, extracted from 100 measurements using the physical point ensemble cA2.09.48 [130]. In this setup $\gamma = E(\vec{p})/m_N \approx 1.78$. Different values of the ξ parameters have been tested to optimize the overlap with the boosted nucleon. The result for $\xi = 0$ (gray squares) corresponds to the conventional Gaussian smearing.

Chapter 5

Bare matrix elements for quark distribution functions

In this Chapter we present our results for the relevant matrix elements that allow to extract the spin-averaged (unpolarized), helicity and transversity parton distribution functions of the nucleon (PDFs), using the quasi-PDF approach [34]. The computation is performed on a twisted mass ensemble $N_f = 2$ and is focused on the nucleon flavor structure $u - d$, which receives contributions only from connected diagrams (up to cutoff effects).

In particular, here we focus on the non-local unrenormalized matrix elements of the form $\langle N|\bar{\psi}(z)\Gamma W(z,0)\psi(0)|N\rangle$ that, as explained in Chapter 2, give access to a specific PDF depending on the Dirac Γ structure in the inserted operator. The numerical setup of our simulations, the investigation of excited states contamination, as well as the computational cost to extract these observables in lattice QCD are discussed in detail along this Chapter.

A schematic picture of all the steps we need to go through in this work is shown in Fig. 5.1. The renormalization procedure for the operators is addressed in Chapter 6, whereas the computation of quasi-distributions and implementation of the matching procedure yielding the physical PDFs are described in Chapter 7.
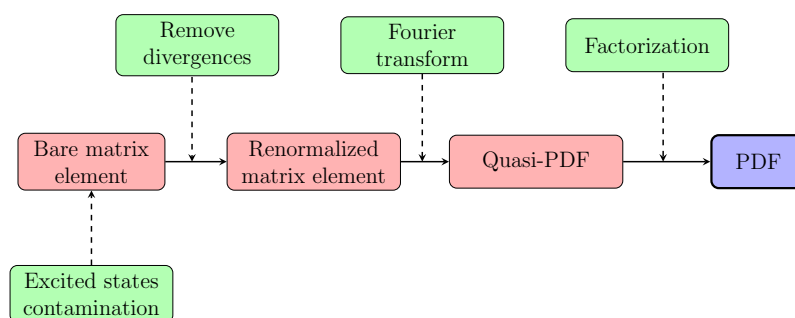
Figure 5.1 Schematic representation of the procedure leading to the physical PDFs from the quasi-PDFs. The main steps and challenges are outlined with red and green blocks respectively.

5.1   Lattice setup

In this Section we give details on the ensemble used in our computations and the operators employed to extract the unpolarized, helicity and transversity distributions. The optimization of the lattice computation is discussed in Sections 5.1.3 and 5.1.4.

5.1.1 $N_f = 2$ physical point ensemble

This work is conducted within the ETM (Extended Twisted Mass) Collaboration, that has provided the necessary gauge field configurations. In particular, here we focus only on one gauge ensemble of ETMC production, labeled cA2.09.48 in Ref. [130] and indicated with a blue filled circle in Fig. 5.2. The cA2.09.48 ensemble includes two dynamical degenerate light
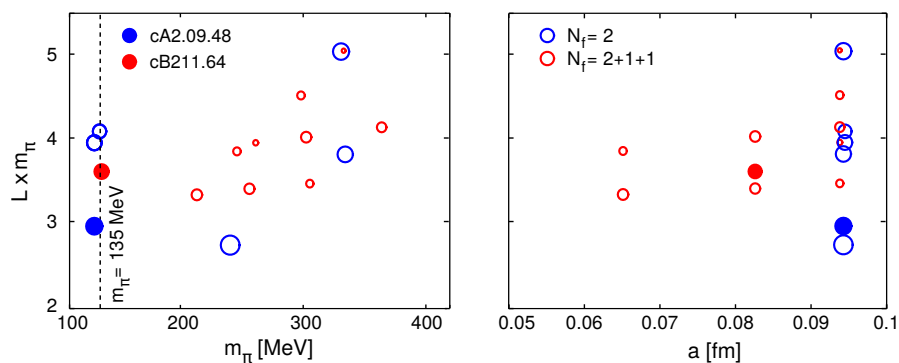
Figure 5.2 Twisted mass ensembles as a function of the pion mass m_π (left) and lattice spacing a (right). The dotted line shows $m_\pi = 135$ MeV. The radius of the circles is proportional to the number of independent gauge configurations. Open red (blue) circles denote $N_f = 2$ ($N_f = 2 + 1 + 1$) ensembles without a clover term [110]. The results that are presented in this Thesis use the cA2.09.48 ensemble [130]. The computation of parton distribution functions on the recent ensemble cB211.64 [131] is currently in progress.

quarks ($N_f = 2$) at maximal twist, whose masses have been tuned to reproduce the physical value of the pion mass, condition that is often referred to as *physical point*. It is simulated on a lattice volume $48^3 \times 96$, with lattice spacing a = 0.0938(2)(3) fm [152], corresponding to a spatial lattice extent $L \approx 4.5$ fm and $m_\pi L \simeq 2.98$. The complete list of parameters is reported in Table 5.1 . The gauge configurations were generated using the Iwasaki improved gauge

$\beta = 2.10$, $c_{\text{SW}} = 1.57751$, $a = 0.0938(3)(2)$ fm, $r_0/a = 5.32(5)$	
	$a\mu = 0.0009$
$48^3 \times 96$, $L = 4.5$ fm	$m_\pi = 0.1304(4)$ GeV
	$m_\pi L = 2.98(1)$
	$m_N = 0.932(4)$ GeV

Table 5.1 Parameters of the ensemble used in this work. The nucleon mass (m_N), the pion mass (m_π) and the lattice spacing (a) have been determined in Ref. [152].

action [153–155] for the gluonic sector, which includes besides the plaquette term $U_{x,\mu,\nu}^{1\times1}$ also rectangular (1 x 2) Wilson loops $U_{x,\mu\nu}^{1\times2}$ and is given by

$$S_G = \frac{\beta}{3} \sum_x \left(b_0 \sum_{\substack{\mu,\nu=1 \\ 1\leq\mu\leq\nu}} \left\{ 1 - \mathrm{Re}\,\mathrm{Tr}(U_{x,\mu,\nu}^{1\times1}) \right\} + b_1 \sum_{\substack{\mu,\nu=1 \\ \mu\neq\nu}} \left\{ 1 - \mathrm{Re}\,\mathrm{Tr}(U_{x,\mu,\nu}^{1\times2}) \right\} \right) . \quad (5.1)$$

In the above expression $\beta = 6/g_0^2$ is the bare inverse coupling, $b_1 = -0.331$ and the normalization condition is $b_0 = 1 - 8b_1$. For $b_1 = 0$ this action recovers the standard Wilson plaquette gauge action. For the fermionic sector, the twisted mass Wilson action [119, 124] described in Section 3.4.2 was employed, with in a addition a clover term [110] whose form is described in Section 3.4.1. The complete fermion action reads

$$S_F[\chi,\bar{\chi},U] = a^4 \sum_x \bar{\chi} \left(D_W[U] + m_0 + i\mu\gamma_5\tau_3 + \frac{ia}{4} c_{\mathrm{sw}}\sigma_{\mu\nu}\mathcal{F}_{\mu\nu}[U] \right) \chi(x) , \quad (5.2)$$

where D_W is the Wilson-Dirac operator (3.41) (with $r = 1$), m_0 is the bare Wilson mass parameter, μ is the bare twisted mass for the light quarks and $\tau_3 = \mathrm{diag}(1,-1)$ is the third Pauli matrix in flavor space. The last term includes the field strength tensor $\mathcal{F}_{\mu\nu}[U]$ weighted by the clover coefficient introduced in Section 3.4.1.

In the fermion action of Eq. (5.2), $\chi(x) = (u,d)^T$ denotes the light quark doublet in the "twisted basis" at maximal twist. It is related to the doublet of fermion fields in the "physical basis" $\psi(x)$ by the following chiral rotation

$$\begin{aligned}
\psi(x) &\equiv e^{i\frac{\alpha}{2}\gamma_5\tau_3} \chi(x) \quad\xrightarrow{\alpha=\pi/2}\quad \psi(x) \equiv \frac{1}{\sqrt{2}}(\mathbb{1}+i\gamma_5\tau_3)\chi(x) , \\
\bar{\psi}(x) &\equiv \bar{\chi}(x) e^{i\frac{\alpha}{2}\gamma_5\tau_3} \quad\xrightarrow{\alpha=\pi/2}\quad \bar{\psi}(x) = \bar{\chi}(x)\frac{1}{\sqrt{2}}(\mathbb{1}+i\gamma_5\tau_3) .
\end{aligned} \quad (5.3)$$

The above relations determine the transformation laws of the interpolating fields and currents. Since gauge ensembles are simulated with the twisted mass action in the form (5.2), the operators used for computing observables have to be expressed in twisted basis, $\{\chi,\bar{\chi}\}$. However, in the next Sections and following Chapters, the interpolating fields and the nucleon matrix elements have to be understood with quark fields in the physical basis unless otherwise specified, keeping in mind that the proper chiral rotations are used in the actual lattice computation.

5.1.2 Definition of operators

According to the quasi-PDF approach, the unpolarized, helicity and transversity quark distribution functions are extracted from matrix elements between nucleon states moving at very large momentum along one direction. The matrix elements of interest are given by

$$h_\Gamma(P_3,z) = \langle N|\mathcal{O}(\tau;z)|N\rangle = \langle N|\sum_{\vec{y}} \bar{\psi}(\tau,\vec{y})\,\Gamma\,W(\vec{y},\vec{y}+\hat{e}_\mu z)\,\tau^3\,\psi(\tau,\vec{y}+\hat{e}_\mu z)|N\rangle , \quad (5.4)$$

where $\psi = (u,d)^T$ is the light quark doublet, Γ is some Dirac combination of γ-matrices and $\tau^3 = \text{diag}(1,-1)$ the third Pauli matrix. The matrix τ^3 acts only in flavor space and allows us to extract distribution functions relative to the flavor structure $u - d$. With this choice, disconnected diagrams cancel due to isospin symmetry, and we need to evaluate only connected contributions as shown schematically in Fig. 5.3. Moreover, in Eq. (5.4) $|N\rangle$ represents a nucleon state boosted in the z-direction with momentum $P = (P_0, 0, 0, P_3)$. We take the Wilson line W to be a straight path of link variables of length z, connecting the points $\vec{y}$ and $\vec{y} + \hat{e}_\mu z$. Considering a straight Wilson line is the standard choice in the quasi-PDF approach, but in principle other paths with the same endpoints are possible, such as two pieces of links oriented in orthogonal directions, as suggested in Ref. [156]. However, this possibility has never been explored in lattice calculations so far, also because the implementation is much less practical than assuming gauge links displaced only along one direction. In Eq. (5.4) we have made explicit the dependence of the matrix elements on the nucleon momentum, P_3, as well as the dependence on the Wilson line length z. For each value of z we have a different operator, which becomes ultra-local for $z = 0$.

To compute the matrix elements in Eq. (5.4) we take a ratio of three- and two-point functions, averaged over a sample of gauge configurations. A schematic illustration of the diagrams is reported in Fig. 5.3.
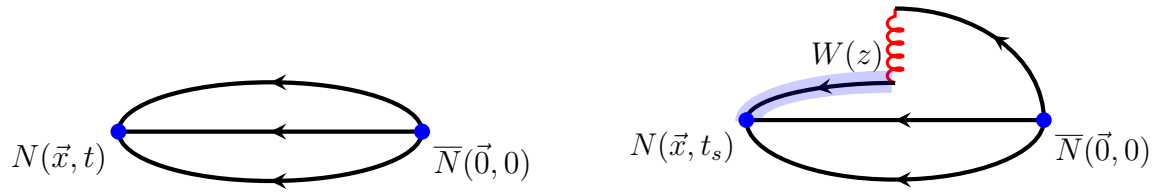
Figure 5.3 Schematic representation of the nucleon two- (left) and three-point (right) functions. The nucleon is created at the source at $(\vec{0}, 0)$, and annihilated at (x, t) and (x, t_s) for the two- and three-point functions, respectively. The solid lines represent the quark propagators, the curly line denotes the Wilson line of length z and the highlighted arc is an all-to-all propagator.

The two-point and three-point functions are given by

$$C^{2pt}(\vec{P}, t; 0) = \mathcal{P}_{\alpha\beta} \sum_{\vec{x}} e^{-i\vec{P}\cdot\vec{x}} \langle \Omega | N_\alpha(\vec{x}, t) \overline{N}_\beta(\vec{0}, 0) | \Omega \rangle , \qquad (5.5)$$

$$C^{3pt}(\vec{P}, t_s; \tau; 0) = \tilde{\mathcal{P}}_{\alpha\beta} \sum_{\vec{x}, \vec{y}} e^{-i\vec{P}\cdot\vec{x}} \langle \Omega | N_\alpha(\vec{x}, t_s) \mathcal{O}(\vec{y}, \tau; z) \overline{N}_\beta(\vec{0}, 0) | \Omega \rangle , \qquad (5.6)$$

where $\vec{P} = (0, 0, P_3)$, $N_\alpha(x) = \varepsilon^{abc} u_\alpha^a(x) \left(d^{bT}(x) \mathcal{C} \gamma_5 u^c(x) \right)$ is the proton interpolating field. $\mathcal{P}_{\alpha\beta}$ and $\tilde{\mathcal{P}}_{\alpha\beta}$ denote the parity projectors for the two- and three-point functions respectively, $\mathcal{O}$ is the insertion operator of Eq. (5.4) and t (t_s) is the time separation of the sink relative to the source in the two-point (three-point) function. We use different symbols to highlight that three-point functions are computed using sequential inversions through the sink, at fixed source-sink time separation (t_s). The sequential method for computing all-to-all propagators has been discussed in detail in Section 4.5.2 in Chapter 4.

To gain in statistics, the two-point functions are projected using the plus and minus parity projectors $\mathcal{P}^{\pm} = \frac{1 \pm \gamma_0}{2}$, and we take the average over the forward and backward correlators. According to the CPT symmetry, forward and backward correlators correspond to correlation functions of protons and anti-protons respectively. In addition, to gain further in statistics, the Wilson line in the operator is computed with plus and negative orientations along z-direction. This means considering the following two possibilities

$$
\begin{aligned}
\mathcal{O}(\vec{y}, \tau; +z) &= \bar{\psi}(\tau, \vec{y}) \, \Gamma \, W(\vec{y}, \vec{y} + \hat{e}_\mu \, z) \, \tau^3 \, \psi(\tau, \vec{y} + \hat{e}_\mu \, z) \,, \\
\mathcal{O}(\vec{y}, \tau; -z) &= \bar{\psi}(\tau, \vec{y}) \, \Gamma \, W(\vec{y}, \vec{y} - \hat{e}_\mu \, z) \, \tau^3 \, \psi(\tau, \vec{y} - \hat{e}_\mu \, z) \,.
\end{aligned}
\tag{5.7}
$$

Using the property $W_\mu(x) = W_{-\mu}(x + \hat{e}_\mu)^\dagger$, one can see that the matrix elements above are related by

$$
\mathcal{O}(\vec{y}, \tau; +z) = \mathcal{O}(\vec{y}, \tau; -z)^\dagger \,,
\tag{5.8}
$$

independently on the Dirac structure, Γ. Consequently, all operators considered in this work satisfy the property $h_\Gamma(P_3, +z) = h_\Gamma(P_3, -z)^\dagger$. This relation can be used as a cross-check of our results in the first place, but also to average the matrix elements obtained at fixed length $|z|$ of the Wilson line.

As mentioned above, to extract the unpolarized, helicity and transversity distributions we need to select a particular Dirac structure in the operator of Eq (5.4). In principle, different Γ matrices may be used to compute a given PDF. For example, if the nucleon momentum and the Wilson line are in the 3-direction (z), we can access to the unpolarized PDF via γ_3 or γ_0 (temporal direction). However, some choices are preferable (e.g. γ_0 in this example), as they simplify the renormalization properties of matrix elements in lattice regularization [55]. In this work, we make the following choices:

- $\Gamma = \gamma_3, \gamma_0$ for the unpolarized distribution, $\tilde{q}(x) = \overrightarrow{\tilde{q}}(x) + \overleftarrow{\tilde{q}}(x)$,

- $\Gamma = \gamma_5 \gamma_3$ for the helicity distribution, $\Delta \tilde{q}(x) = \overrightarrow{\tilde{q}}(x) - \overleftarrow{\tilde{q}}(x)$,

- $\Gamma = \sigma_{3j}$ for the transversity distribution, $\delta \tilde{q}(x) = \tilde{q}_\perp(x) + \tilde{q}_\top(x)$,

where $\overleftarrow{\tilde{q}}$ ($\overrightarrow{\tilde{q}}$) and $q_\perp$ ($q_\top$) indicate momentum distributions of quarks with helicity aligned (anti-aligned) with that of a longitudinally and transversely polarized proton respectively, see Fig. 2.5. For transversity distribution, j-index denotes the direction of the quark spin, which is orthogonal to the proton momentum and purely spatial. Each of these choices of the Dirac structure requires a specific parity projector $\tilde{\mathcal{P}}_{\alpha\beta}$ for the three-point functions, as anticipated in Chapter 4. For the choices of γ-matrices made in this work, the only non-zero contributions come from:

- $\tilde{\mathcal{P}}_{\alpha\beta} = \frac{1 + \gamma_0}{2}$ for the unpolarized $\tilde{q}(x)$,

- $\tilde{\mathcal{P}}_{\alpha\beta} = i \gamma_3 \gamma_5 \frac{1 + \gamma_0}{2}$ for the helicity $\Delta \tilde{q}(x)$,

- $\tilde{\mathcal{P}}_{\alpha\beta} = i \gamma_5 \gamma_k \frac{1 + \gamma_0}{2}$ for transversity $\delta \tilde{q}(x)$, where $k \neq j$.

The explicit form of the projector can be obtained by the trace algebra in Eq. (4.37).

Once having the two- and three-point functions spin-projected, we extract the matrix elements of Eq. (5.4) for each nucleon boost, by forming a ratio of three-point over two-point functions. As will be described in Section 5.3, there are different ways to isolate the ground state contribution and one possibility is to perform a plateau fit

$$h_\Gamma(P_3, z) \stackrel{t_s \ll \tau \ll 0}{=} \mathcal{K} \frac{\langle C^{3pt}(P_3, t_s; \tau; 0) \rangle_G}{\langle C^{2pt}(P_3, t_s; 0) \rangle_G} , \qquad (5.9)$$

where we have replaced $\vec{P}$ with P_3 in the argument of the correlation functions because the momentum is always taken along only one spatial direction. The kinematic factor $\mathcal{K}$ depends on the Dirac structure used in the insertion operator and, for the choices made in this work, it is equal to $\mathcal{K} = iE/P_3$ for the vector current γ_3, whereas $\mathcal{K} = 1$ for all other cases. Its value can be derived again from Eq. (4.37).

5.1.3 Improvement with momentum smearing

To make contact with the light-cone frame one needs to achieve very large nucleon boosts and this is one of main practical difficulties of PDFs calculations. Indeed, as shown explicitly in Chapter 4, two- and three-point functions decay exponentially with time and the energy of the state, leading to a rapid degradation of the signal at already few time-slices far from the source position.

To optimize our setup we employ the momentum smearing technique (see description in Section 4.6.4), following the implementation of Ref. [142]. Momentum smearing modifies the standard Gaussian smearing function by including a complex phase factor

$$\mathcal{S}_{mom} = \frac{1}{1 + 6\alpha_G} \left(\psi(x) + \alpha_G \sum_j U_j(x) e^{-i\xi \vec{P} \cdot \mathbf{j}} \psi(x + \hat{j}) \right) \qquad (5.10)$$

that in our case multiplies the gauge links only along one direction, being for instance $\vec{P} = (0, 0, P_3)$. Here U_j denotes a gauge link in the spatial j-direction, α_G is the parameter of the conventional Gaussian smearing and ξ the momentum smearing parameter, which must be optimized for each value of the boost employed.

Our practical implementation is as follows. Firstly, we apply APE-smearing [146] (see Section 4.6.2) on the gauge links using parameters $(\alpha_{APE}, N_{APE}) = (0.5, 50)$, optimized in previous works that used the same gauge ensemble [157]. Then we iterate Eq. (5.10) using $(\alpha_G, N_G) = (4, 50)$ [157], at a given value of the momentum smearing parameter. In order to improve the overlap of our interpolator with the boosted proton, we optimize the parameter ξ by minimizing the statistical errors of the nucleon two-point functions.

In Figs. 5.4 and 5.5 we demonstrate the effect of the momentum smearing, by plotting the scaling of the error of the nucleon effective energy and two-point correlator, obtained from 100 measurements for boosts $P_3 = 6\pi/L$ and $P_3 = 8\pi/L$, or 0.83 and 1.11 GeV in physical units.

For comparison we also include the results obtained with the standard Gaussian smearing
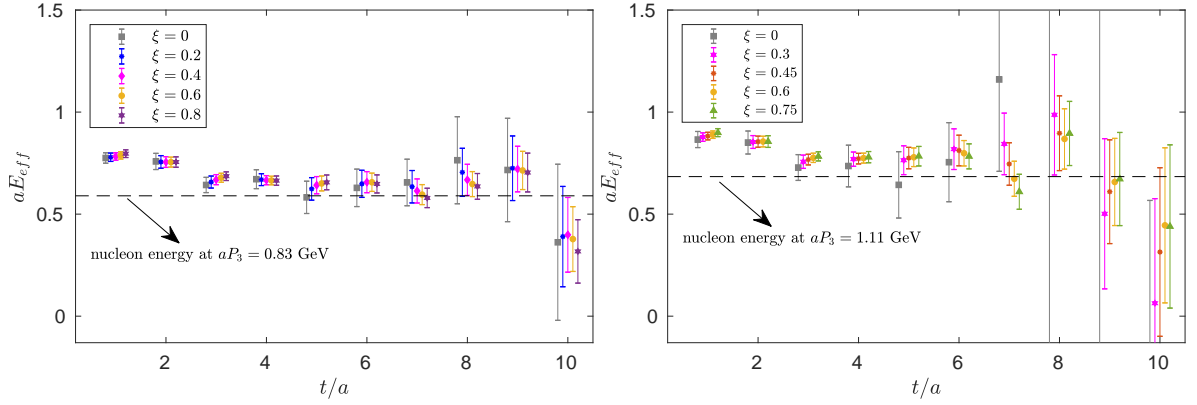
Figure 5.4 Effective nucleon energies with boost $P_3 = 6\pi/L$ (left) and $P_3 = 8\pi/L$ (right) for different values of ξ. The value $\xi = 0$ (gray points) corresponds to the standard Gaussian smearing. The dashed lines indicate the nucleon energy in lattice units, obtained at the nucleon mass $am_N = 0.4436(11)$ [152]. The statistics consists of 100 measurements. Symbols are shifted horizontally for a better legibility.
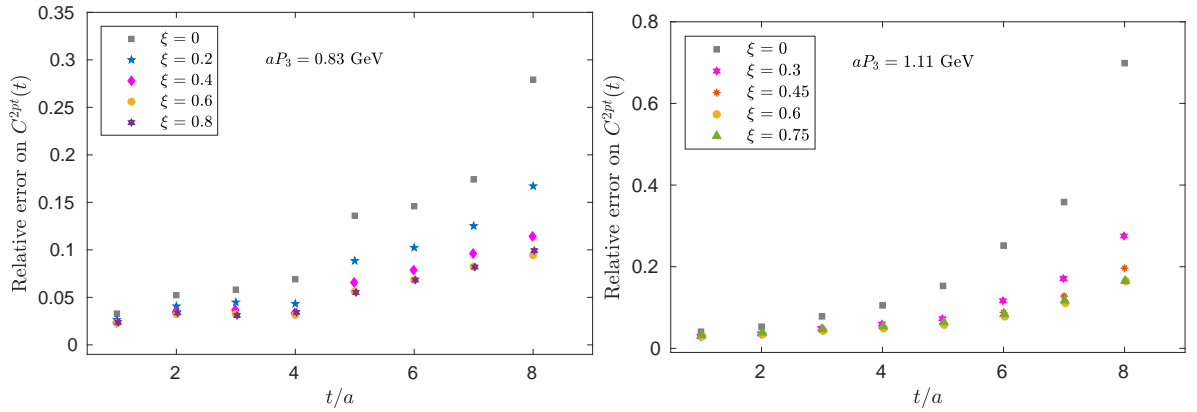
Figure 5.5 Relative error of the nucleon two-point correlator as a function of the Euclidean time t/a for different values of ξ. The results are obtained from 100 measurements. The nucleon boosts are: $P_3 = 6\pi/L$ (left) and $P_3 = 10\pi/L$ (right).

($\xi = 0$). As can be seen, the errors in the correlation functions reduce dramatically as the value of ξ increases and convergence is observed in the range $\xi \in [0.6 - 0.75]$. Thus, any value of ξ in this window of values leads to a similar signal-to-noise ratio. Similar conclusions also hold for a boost $P_3 = 10\pi/L \simeq 1.38$ GeV, shown in Fig. 4.8 in Section 4.6.4. Thus, we fix $\xi = 0.6$ throughout this work. Moreover, from the comparison between the two plots in Fig. 5.4, it is clear that the gain of using momentum smearing increases with the value of the boost, and the conventional smearing becomes less and less effective. From Fig. 5.5, one can also see that the noise-to-signal ratio of the two-point correlator increases exponentially with the time separation from the source, but with a reduced slope when momentum smearing is employed. The only drawback of momentum smearing is that each value of $\vec{\xi}$ employed at the source requires us to compute the respective quark propagator, but overall the effort pays off since also the three-point functions have reduced statistical errors. In fact, in the first exploratory study of momentum smearing for PDFs calculation [39], a factor of 200

fewer measurements was found to produce the same statistical errors as the ones obtained with standard Gaussian smearing, at nucleon boost $P_3 = 10\pi/L \simeq 2.4$ GeV and source-sink separation $t_s = 8a \simeq 0.7$ fm.

5.1.4 Choosing the optimal setup

The optimization of the lattice setup for computing the matrix elements at the physical point ensemble, and for different momenta, has been a crucial step in this work, that has required tuning of different parameters. Apart from the momentum smearing parameter discussed previously, another parameter to tune is the number of random point sources (N_{src}) to use for each configuration, making sure the correlation among measurements remains under control. This test is performed at the lowest momentum used in this work ($P_3 = 6\pi/L$), for which we vary the number of source positions extracted randomly in the lattice volume, from $N_{src} = 1$ to $N_{src} = 16$. The result of this test is shown in Fig. 5.6 for the matrix elements at $z/a = 0$ (no Wilson line) and for the three Γ structures. For comparison purpose, the absolute error is
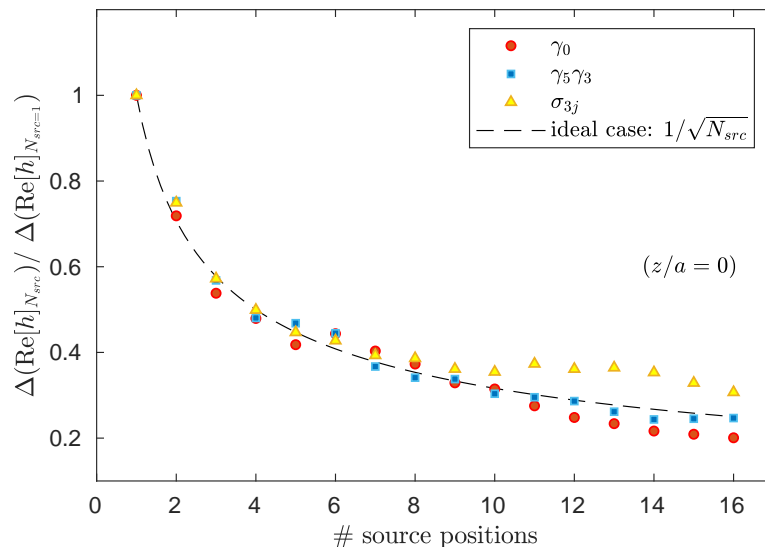
Figure 5.6 Scaling of the statistical errors varying the number of random source positions on each configuration. The absolute error of the matrix elements at $z/a = 0$ for the unpolarized, helicity and transversity distributions (red circles, blue squares, yellow triangles, respectively) is normalized to the corresponding one obtained from only one source position.

normalized to the one obtained using only one source position per configuration. As can be seen, the scaling of the statistical errors follows approximately the ideal behavior $1/\sqrt{N_{src}}$ expected for uncorrelated measurements (dashed line in the figure), implying that the data are weakly correlated. Thus, also for the higher momenta we use multiple source positions in order to increase our statistics. Same qualitative conclusions also hold for correlation functions obtained by boosting the nucleon along all possible directions, $\pm x$, $\pm y$, $\pm z$. The error scaling is shown in Fig. 5.7 for the matrix element with zero length of the Wilson line.

However, despite the use of momentum smearing, the noise-to-signal ratio grows exponentially as the nucleon momentum is increased. This is also shown in Fig. 5.8, in which we plot the relative error on the nucleon two-point correlator at a fixed time-slice $t = 9a \approx 0.85$ fm
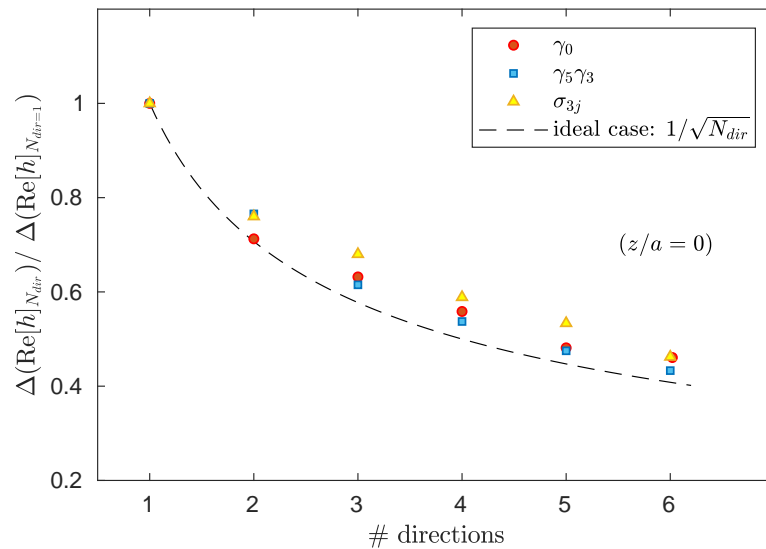
Figure 5.7 Scaling of the statistical errors averaging over the directions of the nucleon boost in $\pm x$, $\pm y$, $\pm z$. Same convention of colors as in Fig. 5.6. The absolute error is normalized to the one obtained from one boost direction and the result is compared with the ideal scaling (dashed line) expected from statistically independent measurements.

from the source, when the boost increases by one lattice unit at a time. Thus, it is important
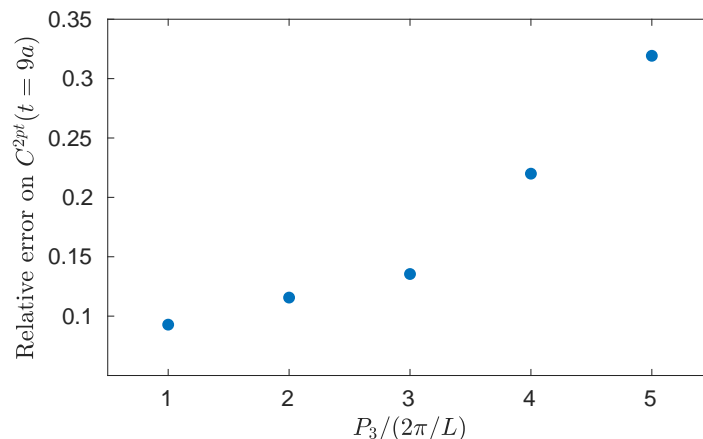
Figure 5.8 Relative error of the nucleon two-point correlator at fixed time separation from the source ($t = 9a \approx 0.85$ fm) as the momentum increases by one lattice unit. Momentum smearing is applied and the statistics consists of 100 measurements for all momenta.

to find another method that allows to accumulate sufficiently high statistics but at reduced computational cost. The most computationally demanding components are the inversions of the Dirac operator, which for one single source position amount to

$$\text{\# inversions for } C^{2pt} : 6\,(\text{dir}) \times 2\,(\text{up/down}) \times 12\,(\text{color and spin}) = 144 \,,$$
$$\text{\# inversions for } C^{3pt} : 6\,(\text{dir}) \times 2\,(\text{up/down}) \times 12\,(\text{color and spin}) \times 3\,(\Gamma \text{ structure}) = 432 \,.$$

$$(5.11)$$

To reduce the computational cost we apply the Covariant Approximation Averaging (CAA) [158], which belongs to the class of truncated solver methods with bias correction. CAA prescribes

the improved observable

$$O^{imp} = \frac{1}{N_{LP}} \sum_{i=1}^{N_{LP}} O_{i,LP} + \frac{1}{N_{HP}} \sum_{i=1}^{N_{HP}} (O_{i,HP} - O_{i,LP}) , \qquad (5.12)$$

where N_{HP} and N_{LP} represent the number of source positions in which an observable O is evaluated at high-precision ($O_{i,HP}$) and low-precision ($O_{i,LP}$) inversions of the Dirac operator. The first term in the equation above introduces a bias in the measurements, which is however corrected if $\langle \frac{1}{N_{LP}} \sum_{i=1}^{N_{LP}} O_{i,LP} \rangle = \langle \frac{1}{N_{HP}} \sum_{i=1}^{N_{HP}} O_{i,LP} \rangle$. The statistical error of O^{imp} [158] is expected to scale as

$$\tilde{\delta} = \delta \sqrt{2(1 - r_c) + \frac{1}{N_{LP}}} , \qquad (5.13)$$

where δ is the original error and r_c the correlation coefficient among correlators computed at high- and low-precision. For an overall error not be larger than the original one, r_c has to be very close to unity. For this to happen, a reasonable precision of the inverter must be employed and $O_{i,HP}$, $O_{i,LP}$ in the second sum of Eq. (5.12) must be computed on the same source positions.

In this work the inversions of the Dirac matrix are performed using the adaptive multigrid solver with twisted mass fermion support [136] and the relative residual for high-precision measurements is set to be $r_{HP} = |\text{residue}|_{HP}/|\text{source}| = 10^{-10}$. To decide about the value of the relative residual for low-precision inversions, we study how the correlation coefficient for two- and three-point functions varies at different precisions of the solver. We find that the stopping criterion $r_{LP} = 2 \cdot 10^{-3}$ guarantees a correlation coefficient $r_c \geq 0.999$, with a considerable speed-up in the inversion time. As a next step, at $r_{LP} = 2 \cdot 10^{-3}$, we tune the number of correlation functions $O_{i,LP}$, $O_{i,HP}$ to use within each configuration in order to avoid unbiased results. Taking 15 HP source positions as reference setup, we find that the bias introduced from low-precision inversions is negligible compared to the gauge noise for a CAA setup of $(N_{HP}, N_{LP}) = (1, 16)$. In Fig. 5.9 we show a comparison of HP and CAA estimates on the nucleon two-point correlator and effective energy at boost $P_3 = 8\pi/L$, performed on 20 configurations using the setup mentioned above. As can be seen, the mean values of the
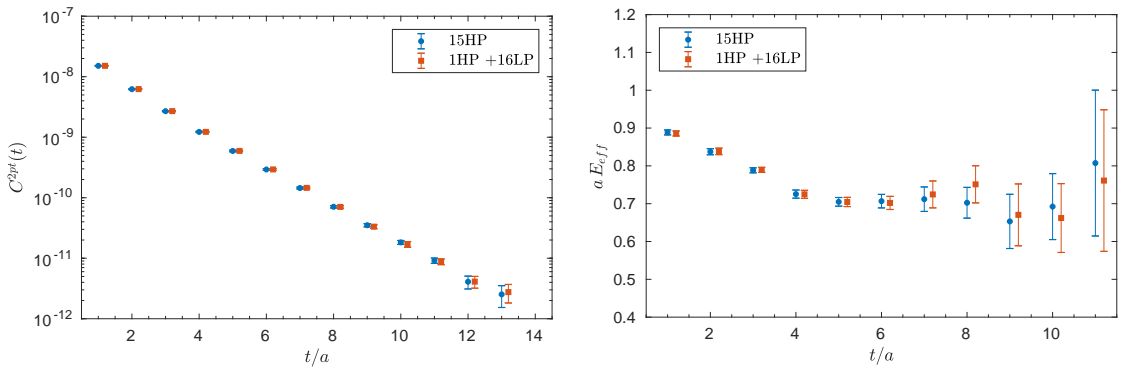

Figure 5.9 Comparison of nucleon two-point correlator (left) and effective energy (right) using 15 inversions with high-precision (15 HP) and 1 and 16 inversions with high- and low- precisions (1 HP+16 LP), on a sample of 20 configurations.

CAA results fluctuate very closely to the ones extracted from high-precision inversions and the slight shift is within statistical errors.

Therefore, at the higher momenta $P_3 = 8\pi/L$ and $P_3 = 10\pi/L$ for which we need a much increased statistics than for boost $P_3 = 6\pi/L$, we use the CAA method. Within each configuration we first construct the improved two- and three-point correlators using Eq. (5.12) and then apply Jackknife procedure over these configuration averages.

Before presenting any results we also mention that in this work we apply another lattice technique to reduce the noise-to-signal ratio, namely the 3-dimensional stout smearing. This is applied only to the Wilson line in the insertion operator, given in Eq. (5.4). In this Chapter we show how the smearing modifies the bare matrix elements, postponing to Chapter 6 the consistency check between renormalized smeared and non-smeared results.

5.2   Lattice results at the largest source-sink separation

In this Section we focus on the results extracted at the highest source-sink separation employed in this work, namely $t_s = 12a \simeq 1.13$ fm. The matrix elements at $t_s = 12a$ are the ones used by us to compute the final quark distributions, presented in Chapter 7, as excited state effects are found to be suppressed at a level of precision of 10%, see Sections 5.3.3-5.3.5. The statistics is listed in Table 5.2 for the three momenta, $P_3 = \{6\pi/L, 8\pi/L, 10\pi/L\}$ or $\{0.83, 1.11, 1.38\}$ GeV in physical units. The dashed lines in the Table separate the operators that are used for the unpolarized PDFs (γ_3, γ_0), helicity PDFs ($\gamma_5\gamma_3$) and transversity PDFs (σ_{3j}).

$P_3 = \frac{6\pi}{L}$			$P_3 = \frac{8\pi}{L}$			$P_3 = \frac{10\pi}{L}$		
Ins.	N_{conf}	N_{meas}	Ins.	N_{conf}	N_{meas}	Ins.	N_{conf}	N_{meas}
γ_3	100	9600	γ_3	425	38250	γ_3	811	72990
γ_0	50	4800	γ_0	425	38250	γ_0	811	72990
$\gamma_5\gamma_3$	65	6240	$\gamma_5\gamma_3$	425	38250	$\gamma_5\gamma_3$	811	72990
σ_{3j}	50	9600	σ_{3j}	425	38250	σ_{3j}	811	72990

Table 5.2 Statistics of our calculation at source-sink time separation $t_s = 12a$, for each Dirac structure in the insertion operator and each boost. N_{conf} is the number of analyzed gauge configurations and N_{meas} the total number of measurements.

The number of measurements, for each Γ insertion reported in Table 5.2, is computed as follows:

- $N_{\text{meas}} = N_{\text{conf}} \times 16_{\text{src}} \times 6_{\text{dir}}$,   at $P_3 = 6\pi/L$ and $\Gamma = \{\gamma_0, \gamma_3, \gamma_5\gamma_3\}$,

- $N_{\text{meas}} = N_{\text{conf}} \times 16_{\text{src}} \times 6_{\text{dir}} \times 2_{j=1,2}$,   at $P_3 = 6\pi/L$ and $\Gamma = \sigma_{3j}$,

- $N_{\text{meas}} = N_{\text{conf}} \times 15_{\text{src}} \times 6_{\text{dir}}$,   at $P_3 = \{8\pi/L, 10\pi/L\}$.

In the count above, the extra factor of 2 for $P_3 = 6\pi/L$ and $\Gamma = \sigma_{3j}$ comes from the average over the two possible tensor structures that we can have if a nucleon is moving along the 3-direction; for $P_3 = \{8\pi/L, 10\pi/L\}$ we have considered that 15 source positions contribute to the number of measurements when the CAA setup (1 HP, 16 LP) is employed, as described in the previous Section.

5.2.1 Matrix elements with stout smearing

In this Section we present our lattice results for the matrix elements obtained by forming the ratio in Eq. (5.9). This approach is usually known as *plateau method*.

An example of fitting procedure is shown in Fig. 5.10 for the real and imaginary part of the operator with γ_0 as insertion, Wilson line length $z/a = 4$ and boost $P_3 = 6\pi/L$. To the gauge links entering the insertion operator we apply multiple steps of 3-D stout smearing and in Fig. 5.10 we show constant fits performed to the data at 0 and 15 levels of smearing. As can be seen, the real and imaginary parts of the unrenormalized matrix elements are shifted towards larger absolute values and we find this effect to be momentum-independent. In fact,
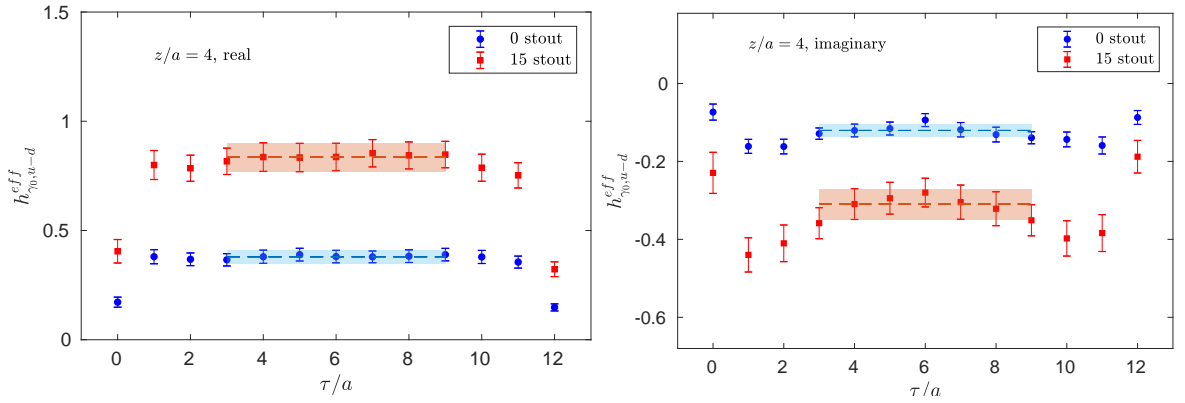
Figure 5.10 Effective unrenormalized matrix elements for Wilson line length $z/a = 4$, as a function of the insertion time τ/a and for γ_0 insertion. The data refer to 0 and 15 3-D steps of stout smearing and are extracted from a nucleon boosted with $P_3 = 6\pi/L$.

we observe the same qualitative behavior for other boosts. In Figs. 5.11 and 5.12 we report the results at nucleon momentum $P_3 = 8\pi/L$ and for the three classes of operators, corresponding to different quark distributions.

The use of link-smearing techniques is very advantageous in our calculation because it helps to reduce the ultra-violet divergences that are typical of non-local operators. As shown in Ref. [55], in lattice regularization long-link operators are power divergent with respect to the UV cutoff $1/a$ and the divergence increases exponentially as $e^{\delta m |z|/a}$, where $\delta m > 0$ is a dimensionless quantity characterizing the strength of the power divergence. From a practical point of view, the presence of a power-like divergence introduces a large noise to the data, especially at large values of the Wilson line length, that can however be mitigated by smearing the gauge links. In principle, any kind of smearing can be used and another choice has been so far also the HYP-smearing [148], applied for PDFs calculations in works [37, 39]. However, here we prefer to apply stout smearing for its analytic properties and because perturbative
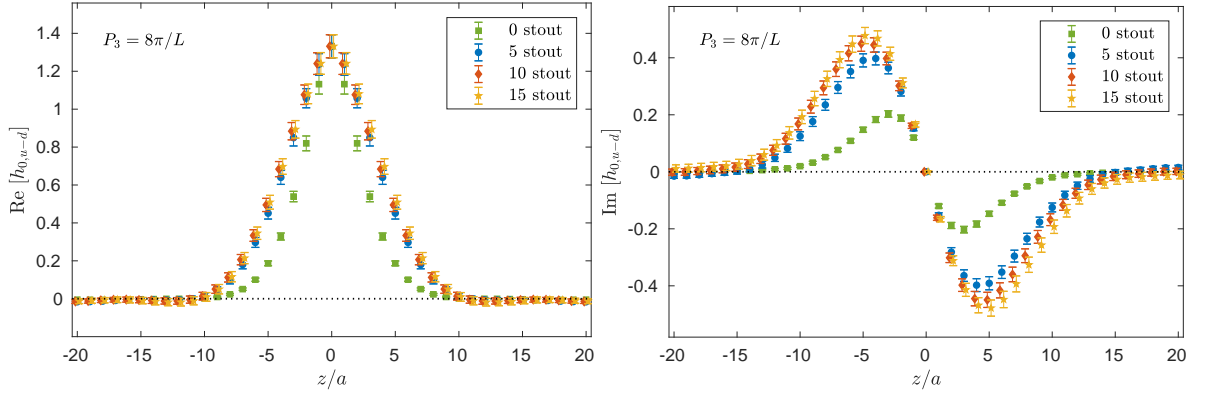
Figure 5.11 Unrenormalized matrix elements for γ_0 operator as a function of Wilson line length and boost $P_3 = 8\pi/L$. 0, 5, 10, 15 steps of stout smearing are compared (squares, circles, diamonds and pentagons respectively).
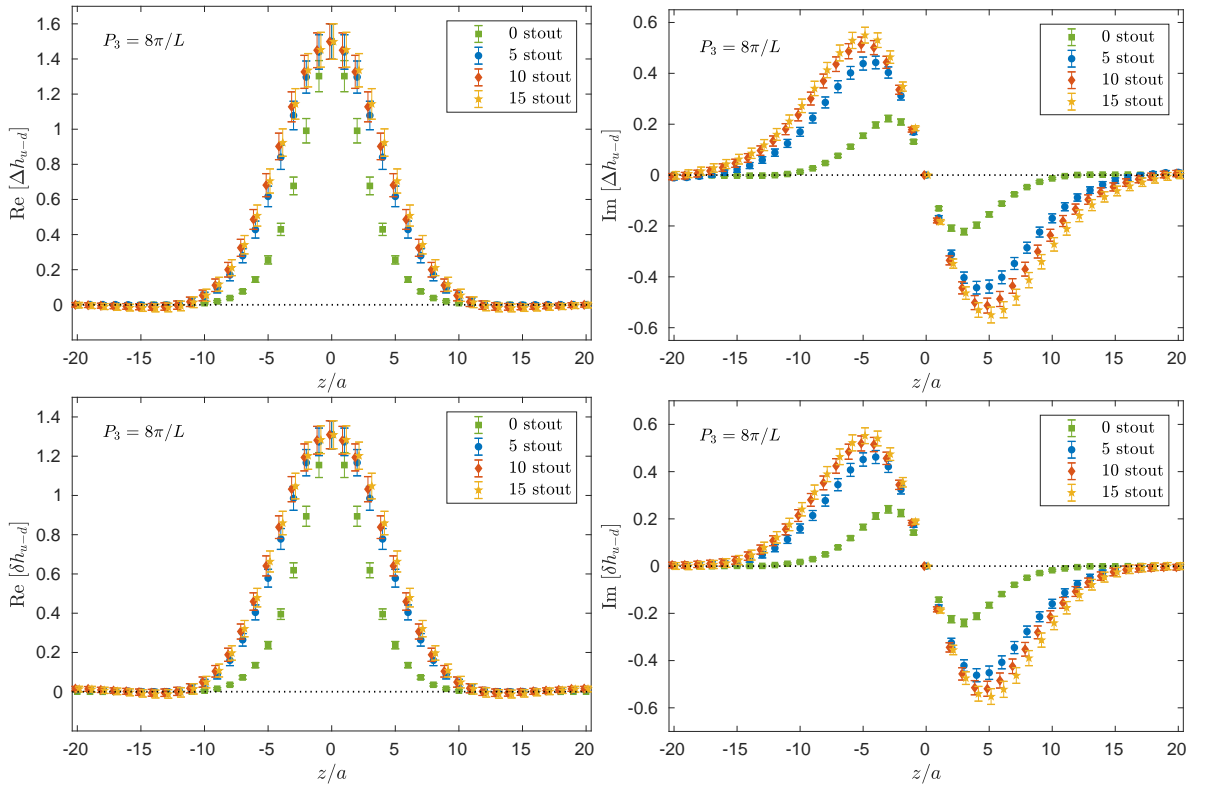
Figure 5.12 Unrenormalized matrix elements for polarized distributions, for different steps of stout smearing and boost $P_3 = 8\pi/L$. Top: axial operator ($\gamma_5\gamma_3$). Bottom: tensor operator (σ_{3j}). Same conventions of color and markers as in Fig. 5.11.

calculations on the renormalization functions are considerably simplified. The divergences of the lattice operators are discussed in detail in the next Chapter, which is dedicated to the description of our renormalization procedure of the lattice matrix elements and results for the renormalization functions are also presented.

Another important feature that is worth to mention is the symmetry property of the matrix elements under the exchange $z \to -z$. As we can see from Fig. 5.11 and Fig. 5.12, the real part is symmetric and the imaginary part is antisymmetric, as expected from the relation $h_\Gamma(P_3, +z) = h_\Gamma(P_3, -z)^\dagger$ derived in Eq. (5.8). This property has been applied to get

the results shown in Figs. 5.11 and 5.12 and, from now on, all results have to be intended properly symmetrized. We anticipate here that the relation $h_\Gamma(P_3, +z) = h_\Gamma(P_3, -z)^\dagger$ has the fundamental consequence of producing an asymmetry between quark and antiquarks distributions, as it will be clear in Chapter 7.

5.2.2 Momentum dependence

Within the quasi-PDF approach, parton distributions are expected to be reconstructed in the limit of very large momenta. Thus, our final goal is to study the momentum dependence of the lattice distributions, which at sufficiently large boosts should get closer to the light-cone PDFs. In this Section we start studying how the bare matrix elements depend on the value of the nucleon momentum. In Fig. 5.13, a comparison is shown for the matrix elements of the unpolarized PDF, obtained using γ_0 in the insertion operator. The statistics is indicated in Table 5.2.
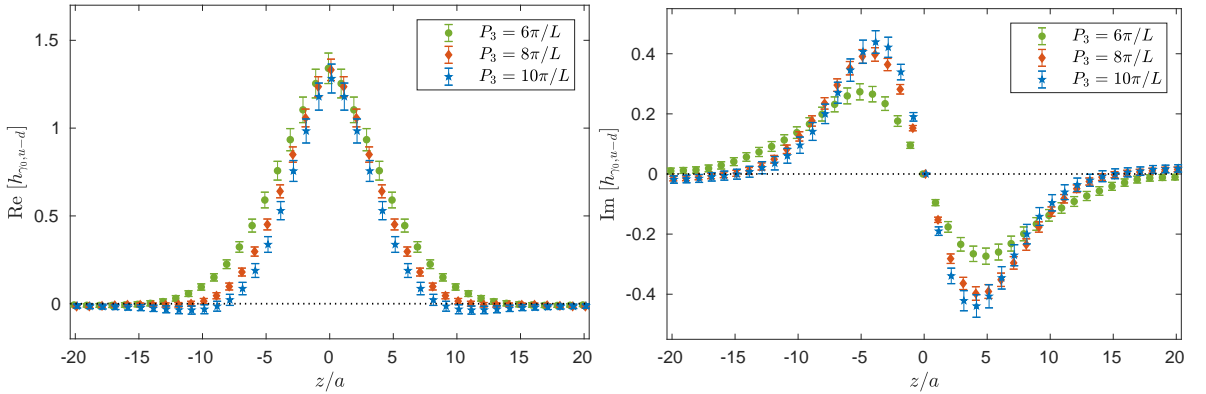
Figure 5.13 Momentum dependence of the unrenormalized matrix elements for unpolarized PDFs (γ_0 is used in the insertion operator), as a function of the displacement z/a. Left: real part. Right: imaginary part. The nucleon boosts are $P_3 = 6\pi/L$ (green diamonds), $P_3 = 8\pi/L$ (red circles) and $P_3 = 10\pi/L$ (blue pentagons).

As the momentum increases, one can see that the matrix elements decay to zero faster. This behavior can be qualitative interpreted as a contraction of the spatial correlation length of the nucleon valence distribution, which manifests along the direction of the boost. Therefore, this effect will be more evident as the value of the nucleon boost increases. Computations at larger momenta are highly desirable to make contact with the light-cone PDFs, but they require huge computational resources, especially for source-sink separations $t_s \gtrsim 1$ fm. Indeed we observe that, for γ_0-Dirac structure, it is necessary to increase the number of measurements of a factor around 8 and 15 with respect to $P_3 = 6\pi/L$ in order to extract meaningful results. Also, the worsening trend is expected to be exponential with time separation and boost, as shown for the two-point correlator in Fig. 5.8. For a detailed discussion about the consequence of a rapid deterioration of the signal we refer to the last Section of this Chapter, where we discuss the computational cost of our simulations, including also a "projected cost" for achieving 10% precision for a wide range of nucleon momenta.

On the other hand, even if computations at large momenta were feasible, the nucleon boost cannot be arbitrarily large, because cutoff effects become important if the condition

$aP_3 << 1$ is not satisfied. Finer lattice spacings would surely help to reach large momenta with reduced cutoff effects.

The polarized matrix elements show a similar momentum dependence as for the one of the unpolarized case, as can be seen in Fig. 5.14. The only difference is an increased gauge noise and more overlap between data at $P_3 = 8\pi/L$ and $P_3 = 10\pi/L$. Overall, we can say
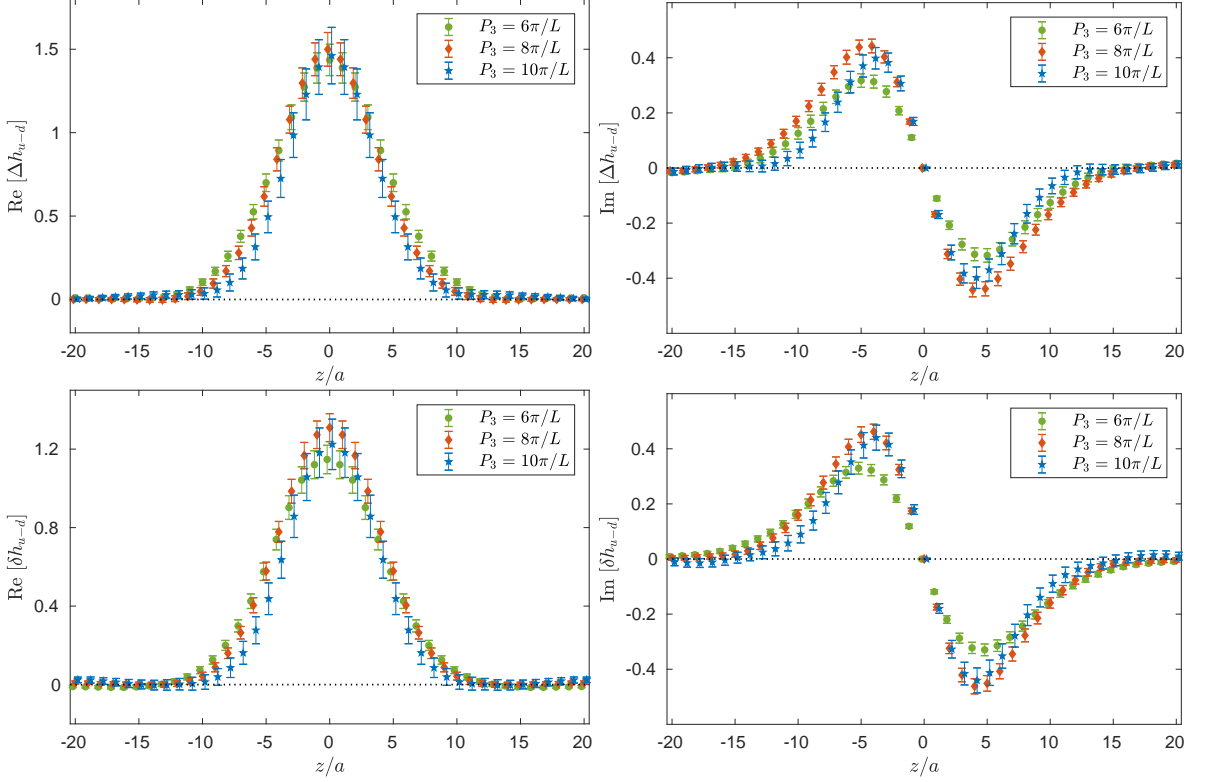
Figure 5.14 Momentum dependence of the unrenormalized matrix elements for helicity (top) and transversity (bottom) PDFs. Left: real part. Right: imaginary part. The nucleon boosts are: $P_3 = 6\pi/L$ (green diamonds), $P_3 = 8\pi/L$ (red circles) and $P_3 = 10\pi/L$ (blue pentagons).

that at the highest momentum the unrenormalized matrix elements are compatible with zero within $\sim 10\%$ errors for $z \geq 11a \approx 1.03$ fm.

5.2.3 Unpolarized matrix elements: choice of the Dirac structure

As regards the unpolarized distribution, so far we have only presented results for the matrix elements obtained by using γ_0 as Dirac matrix in the current insertion. The other explored choice for the Dirac structure is γ_3, where the index has to be intended parallel to the direction of the Wilson line and nucleon momentum. A comparison between the two Dirac structures is reported in Fig. 5.15 at momentum $P_3 = 8\pi/L$. As we can see, the data extracted from γ_3 suffer from an increased noise contamination, being the statistics the same as for γ_0. Therefore, γ_3 is not our preferable choice and from now will not be used in the discussion of our numerical results. The origin of this peculiar behavior can be traced back to the operator mixing of $\mathcal{O}_{\gamma_3}$ with the scalar operator

$$\mathcal{O}_I = \bar{\psi}(x)\mathcal{P}\,e^{-ig\int_0^z A_\mu(x+\xi\hat{\mu})\,d\xi}\,\psi(x+z\hat{\mu}) \quad, \tag{5.14}$$
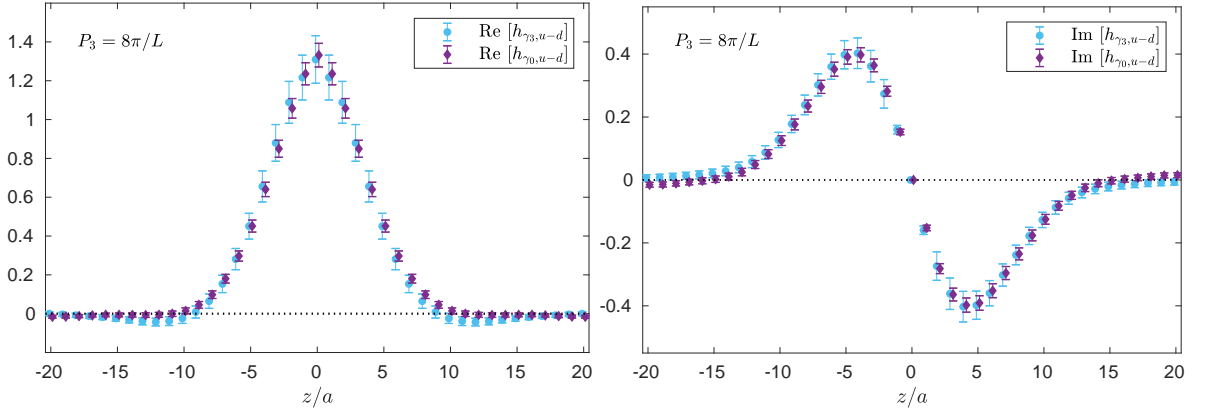
Figure 5.15 Comparison between results at $P_3 = 8\pi/L$, obtained with γ_0 (cyan circles) and γ_3 (violet diamonds) as Dirac structure in the current insertion. Both choices are possible for extracting unpolarized PDF.

discovered in the recent study [55]. The direct consequence of having an operator mixing between the vector (γ_3) and the scalar ($\mathbb{1}$) is that a mixing renormalization matrix must be computed [56] in order to evaluate the renormalized unpolarized distribution function. In other words, the renormalization of the operator $\mathcal{O}_{\gamma_3}$ is not simply multiplicative. From a practical point of view, larger statistical errors are unavoidable, since the accuracy and systematic uncertainties on the physical PDF will eventually depend on both matrix elements with $\Gamma = \gamma_3$ and $\Gamma = \mathbb{1}$, and also on the estimates of the renormalization functions. The logic can also be reversed, in the sense that also the bare results obtained with the vector (γ_3) are affected by a larger noise, due to the mixing with the scalar operator.

However, we note that the mixing between $\mathcal{O}_{\gamma_3}$ and $\mathcal{O}_I$ does not manifest in all lattice discretization schemes, but it does in the twisted mass formulation, as the chiral symmetry is explicitly broken by the twisted mass term. In the lattice formulations where chiral symmetry is instead preserved, $\mathcal{O}_{\gamma_3}$ and $\mathcal{O}_I$ would not mix, because these operators transform in a different way under chiral rotations, for which the action is instead invariant.

The perturbative calculation of Ref. [55] has also shed light on the possible Γ structures that guarantee a multiplicatively renormalization of operators for quasi-PDFs. Indeed, it was found that if the Wilson line is along μ-direction, then the Γ matrices for which $\{\Gamma, \gamma_\mu\} = 0$ do not suffer from operator mixing. Thus, one can in principle use any vector operator γ_ν with $\nu \neq \mu$. However, if the Wilson line and nucleon momentum are both taken in the 3-direction, γ_1 and γ_2 would give a vanishing contribution in the calculation; hence, we are left with only one possibility, γ_0, which also offers a faster convergence to the light-cone PDFs than γ_3, as demonstrated in Ref. [45].

Since the discovery of the operator mixing in Ref. [55], lattice calculations do not use anymore $\mathcal{O}_{\gamma_3}$, which was the first proposal for extracting the unpolarized PDF [33]. At the same time, we note that for our choices for the helicity ($\gamma_5\gamma_3$) and transversity (σ_{3j}) PDFs no mixing occurs, because the Dirac matrices have one index in the direction of the Wilson line. To conclude, from now on we will only focus on results extracted with O_{γ_0} as regards the unpolarized PDF and we expect the final results to be in agreement with the ones from $\mathcal{O}_{\gamma_3}$,

also in light of the comparison shown in Fig. 5.15 at the level of the unrenormalized matrix elements.

5.3 Lattice results for excited states analysis

The matrix elements showed so far are extracted at one single value of the source-sink separation, namely $t_s = 12a \simeq 1.13$ fm. To check to what extent they are contaminated by excited states, at our highest momentum $P_3 = 10\pi/L$ we perform measurements using other three values of the source-sink time separation: $t_s = [8, 9, 10]a \simeq [0.75, 0.84, 0.94]$ fm. The t_s values explored here are chosen such that we can achieve a statistical accuracy comparable to one obtained at $t_s = 12a$ and at moderate computational effort. Moreover, we focus only on the highest boost since we expect excited states contamination to be more severe at large momenta.

In general, the number of excited states increases not only with the nucleon boost but also going towards to the physical point; at fixed pion mass, it also increases with the lattice volume, since the spectrum becomes denser [159]. Predicting excited states contributions is impossible in lattice QCD, because that would require knowing the whole spectrum E_n that composes the two- and three-point functions, as well as the operator matrix elements $\langle n'|O|n \rangle$ and the overlap terms $Z_n = \langle \Omega|N|n \rangle$, where N is the nucleon interpolating field. Given the impossibility of extracting all this information, it is good practice employing more than one methodology for data analysis. In this way we can establish at which level of accuracy excited states are suppressed or hidden within statistical errors.

Before presenting our results we list the methods used to analyze our data, in order to examine the dominance of the ground state in the lattice matrix elements. These are the strategies applied in typical hadron structure calculations of the nucleon charges and form factors among others.

5.3.1 The method

As we have seen in Chapter 4, two- and three-point functions have the following spectral decomposition

$$C^{2pt}(P_3, t) = \sum_n \langle \Omega|N|n \rangle \langle n|\bar{N}|\Omega \rangle e^{-E_n t} , \tag{5.15}$$

$$C^{3pt}(P_3, t_s; \tau) = \sum_{n,n'} \langle \Omega|N|n' \rangle \langle n'|\mathcal{O}|n \rangle \langle n|\bar{N}|\Omega \rangle e^{-E_n \tau} e^{-E_{n'}(t_s - \tau)} , \tag{5.16}$$

where $N(\bar{N})$ is the nucleon interpolating field and $|n\rangle$, $|n'\rangle$ the eigenstates of the Hamiltonian ($|0\rangle$ - ground state, $|1\rangle$- first excited state, etc). For convenience the time-slice of the source is set to zero. From the expressions in Eq. (5.15) and (5.16) we can construct three analysis methods:

1. *Plateau method*

   This is the methodology with which the matrix elements in previous Sections have been obtained. The logic is to build the ratio of the three- over the two-point functions and individuate a region where it becomes constant, equal to the desired matrix element. Indeed, isolating the ground state contribution, the ratio of Eq. (5.9) reads

$$\frac{C^{3pt}(P_3, t_s; \tau)}{C^{2pt}(P_3, t_s)} = \frac{\langle 0|\mathcal{O}|0\rangle + f_{10}\langle 1|\mathcal{O}|0\rangle e^{-\Delta E(t_s-\tau)} + f_{10}^\dagger \langle 0|\mathcal{O}|1\rangle e^{-\Delta E\tau} + |f_{10}|^2 \langle 1|\mathcal{O}|1\rangle e^{-\Delta E t_s} + \ldots}{1 + |f_{10}|^2 e^{-\Delta E t_s} + \ldots},$$

$$(5.17)$$

   where $f_{10} = \langle \Omega|N|1\rangle / \langle \Omega|N|0\rangle$ and $\Delta E = E_1 - E_0$ is the energy gap between the first excited state and the ground state. Thus, in the limit of large Euclidean time separation we obtain

$$\frac{C^{3pt}(P_3, t_s; \tau)}{C^{2pt}(P_3, t_s)} \to \langle 0|\mathcal{O}|0\rangle + O(e^{-\Delta E\tau}) + O(e^{-\Delta E(t_s-\tau)}) + O(e^{-\Delta E t_s}) . \qquad (5.18)$$

   $\langle 0|\mathcal{O}|0\rangle$ can be extracted through a constant fit within the plateau region.

2. *Summation method*

   This approach, proposed in Ref. [160], involves summing the ratio of Eq. (5.17) over the insertion time τ of the operator. One can see that the terms τ-dependent give rise to geometric series, whereas the other terms grow linearly with the source-sink separation, yielding the relation

$$S(P_3, t_s) \equiv \sum_{\tau=a}^{t_s-a} \frac{C^{3pt}(P_3, t_s; \tau)}{C^{2pt}(P_3, t_s)} = const. + \langle 0|\mathcal{O}|0\rangle t_s + O(e^{-\Delta E t_s}) \quad . \qquad (5.19)$$

   Thus, we can extract the desired matrix element $\langle 0|\mathcal{O}|0\rangle$ from a linear two-parameter fit. This method has the advantage of suppressing the excited states contamination by a faster decaying factor, $e^{-\Delta E t_s}$, but the linear fit usually leads to results with larger uncertainties as compared to the ones obtained with the plateau method. This aspect negates some of the advantage of the summation method.

3. *Two-state fits*

   Within this method, we take into account terms involving the ground state and the first excited state, and perform many-parameter fit to the data extracted at three and four values of the source-sink time separation. To this aim, we use the following decompositions of the nucleon two- and three-point functions in terms of the overlap factors

$$C^{2pt}(P_3, t) = |Z_0|^2 e^{-E_0 t} \left(1 + |f_{10}|^2 e^{-\Delta E t}\right) , \qquad (5.20)$$

$$C^{3pt}(P_3, t_s; \tau) = |Z_0|^2 e^{-E_0 t_s} \left(\langle 0|\mathcal{O}|0\rangle + f_{10}\langle 1|\mathcal{O}|0\rangle \, e^{-\Delta E(t_s-\tau)} \right.$$
$$\left. + f_{10}^\dagger \langle 0|\mathcal{O}|1\rangle \, e^{-\Delta E\,\tau} + |f_{10}|^2 \langle 1|\mathcal{O}|1\rangle \, e^{-\Delta E t_s} \right) . \qquad (5.21)$$

The two-point function depends on four parameters, $|Z_0|^2$, E_0, $|f_{10}|^2$ and ΔE, while the three-point function depends in addition on the operator matrix elements and on the factors f_{10} and $f_{10}^\dagger$. We perform the analysis using two approaches:

(a) *sequential fit*, where we first carry out a four-parameter fit to the two-point correlators to extract $|Z_0|^2$, E_0, $|f_{10}|^2$ and ΔE; the values obtained are then used as inputs into the three-point functions fit. The latter depends on eight parameters, distinguishing between real and imaginary contributions: Re/Im $[\langle 0|\mathcal{O}|0\rangle]$, Re/Im $[f_{10}\langle 1|\mathcal{O}|0\rangle]$, Re/Im $[f_{10}^\dagger\langle 0|\mathcal{O}|1\rangle]$, Re/Im $[\langle 1|\mathcal{O}|1\rangle]$;

(b) *simultaneous fit*, where the desired matrix element is extracted from a simultaneous combined fit of Eq. (5.20) and Eq. (5.21).

When the three methodologies described above (plateau, summation method and two-state fit) give results which are consistent with each other, we consider contributions from excited states to be under control. This is the criterion used by us to ensure the ground state dominance at a certain level of accuracy.

5.3.2 Two-point function analysis

The simplest two-state fit that can be carried out is the one on the two-point correlator, using the relation in Eq. (5.20). The result of the fit to the data at boost $P_3 = 10\pi/L$ is shown in the left panel of Fig. 5.16, where the error band includes the covariance matrix of the fitting parameters computed via binning Jackknife analysis. The fitting range excludes the first few time-slices close to the source where higher excited states are predominant. We choose it to be $[3-16]a$, as including larger time separations leads to values of the fitting parameters which are compatible with each other within statistical errors. The nucleon ground state energy from the two-state fit is $aE_0^{2-state} = 0.773(18)$, in line with the value extracted from a constant fit in the plateau region to the effective energy, $aE_0^{1-state} = 0.788(9)$. The comparison of the nucleon ground state energies obtained with these two approaches is shown in the right panel of Fig. 5.16.
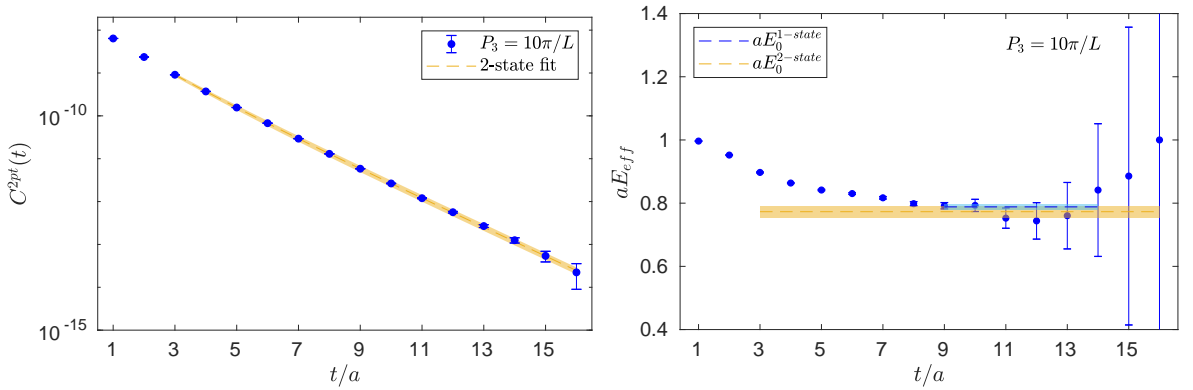

Figure 5.16 Left: Two-state fit to the two-point correlator and error band (orange); logarithmic scale is used in the y-axis for improving legibility. Right: Effective energy plotted together with the ground state energy, obtained from one-state (cyan band) and two-state fit (orange band). The nucleon boost is $P_3 = 10\pi/L$.

Moreover, to check whether the extracted nucleon energy at momentum $P_3 = 10\pi/L$ satisfies the energy dispersion relation, we complement our measurements and compute nucleon two-point correlators at zero momentum and at $P_3 = 2\pi/L \simeq 0.28$ GeV and $P_3 = 4\pi/L \simeq 0.55$ GeV, using momentum smearing. To derive the energy dispersion relation, we first compute the nucleon energy from one-single state fit at each value of the boost and then perform a two-parameter fit using the expression $aE = \sqrt{a^2 m_N^2 c^4 + a^2 P_3^2 c^2}$. In Fig. 5.17 we show the lattice data and the continuum dispersion relation, together with the error band and the values of the fitting parameters.
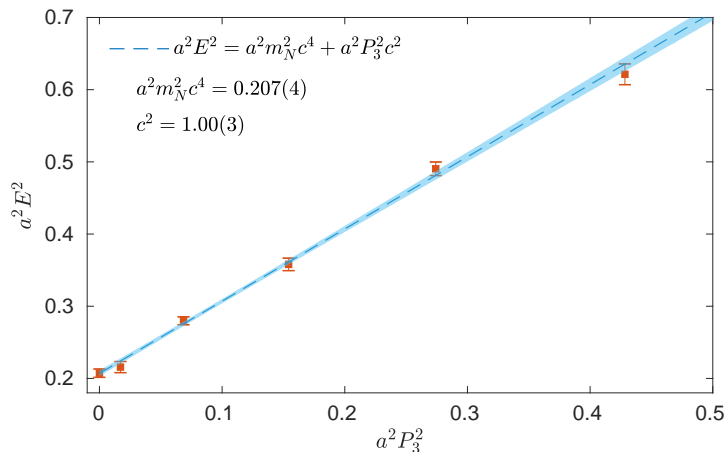
Figure 5.17 Energy of the nucleon as a function of the boost P_3 in lattice units. We fit the relativistic energy-momentum relation $E^2 = m_N^2 c^4 + P_3^2 c^2$ to the lattice data (red squares) obtained from one-state analysis. The values of the parameters extracted from the fit are shown in the Figure. The error band (cyan) includes the covariance matrix of the fitting parameters.

We observe that up to momentum $P_3 = 10\pi/L \simeq 1.38$ GeV there are no deviations from the continuum energy-momentum relation within the present statistical accuracy. In fact, at our highest momentum we have $10\pi/L \approx 0.65/a$, which is well below the lattice cutoff $1/a$ of our ensemble. Moreover, from the fit to the data we obtain $c^2 = 1.00(3)$ for the squared of the speed of light and $a^2 m_N^2 c^4 = 0.207(4)$ for the nucleon mass in lattice units, which is in line with the value $am_N = 0.4436(11)$ extracted at zero-momentum in Ref. [152]. Having discussed the analysis on the two-point functions, in the next Sections we show the results for the matrix elements at our highest boost and for the three Dirac structures in the inserted operator.

5.3.3 Matrix elements for the unpolarized PDFs

To study the influence of excited states for the unpolarized PDFs we explore four values of the source-sink time separation, namely $t_s/a = [8, 9, 10, 12]$ or in physical units $t_s \simeq [0.75, 0.84, 0.94, 1.13]$ fm. This analysis is carried out only at the highest momentum $P_3 = 10\pi/L$, because three-point functions evaluated at different nucleon boosts require separate sequential inversions, and the calculation becomes very computationally demanding when multiple source-sink separations have to be considered as well. Thus, we prefer to focus on the case in which excited states may be more influent, i.e on the highest momentum. The

statistics for the excited state analysis on the unpolarized PDF is reported in Table 5.3. For all values of the source-sink time separation we use the same CAA setup as for $t_s/a = 12$, i.e. 1 HP and 16 LP source positions from which high- and low-precision inversions are carried out respectively, as discussed in Section 5.1.4.

The first approach used is the plateau method, which involves a constant fit within the insertion time interval, as illustrated in Fig. 5.18 for $z/a = 1$ and source-sink separation $t_s/a = 8, 9$. Iterating the procedure for each t_s value, we get the results in Fig. 5.19. We

$P_3 = 10\pi/L$, Ins: γ_0	$t_s = 8a$	$t_s = 9a$	$t_s = 10a$	$t_s = 12a$
N_{conf}	48	98	100	811
N_{meas}	4320	8820	9000	72990

Table 5.3 Number of analyzed configurations and measurements at each source-sink separation, for the unpolarized case (γ_0) at $P_3 = 10\pi/L$.
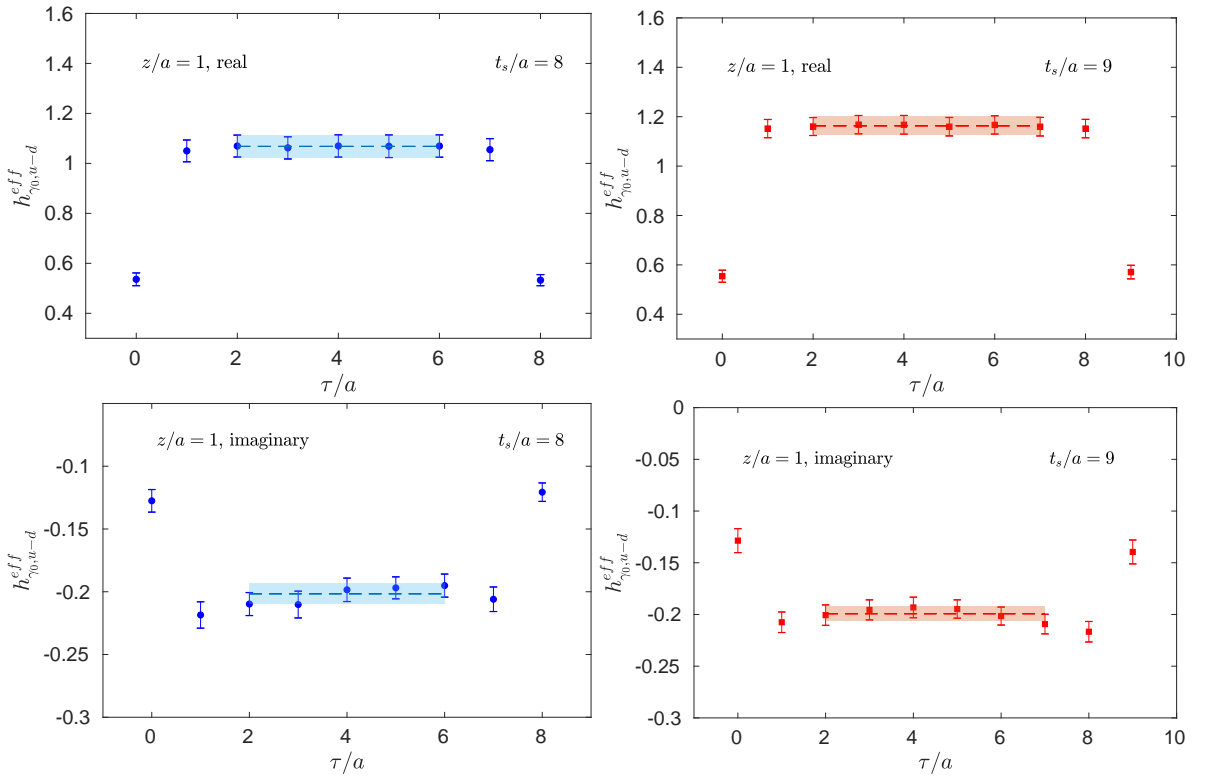
Figure 5.18 Plateau method for extracting the real and imaginary part of the matrix element at $t_s/a = 8$ (left panel) and $t_s/a = 9$ (right panel).

notice that for $t_s = 8a$, the real part of the matrix element is shifted towards smaller values at each z/a compared to larger t_s, while the effect in the imaginary part is less prominent.

We also analyze the data using the summation method, in which a linear fit with respect to t_s is performed, as indicated in Eq. (5.19). To this aim, we employ two ranges of t_s values: 1) $t_s/a = [8, 9, 10]$ and 2) $t_s/a = [8, 9, 10, 12]$. The results from these two sets are reported in Fig. 5.20. They are obtained summing over the whole range of τ ($\tau \in [a, t_s - a]$, contact terms
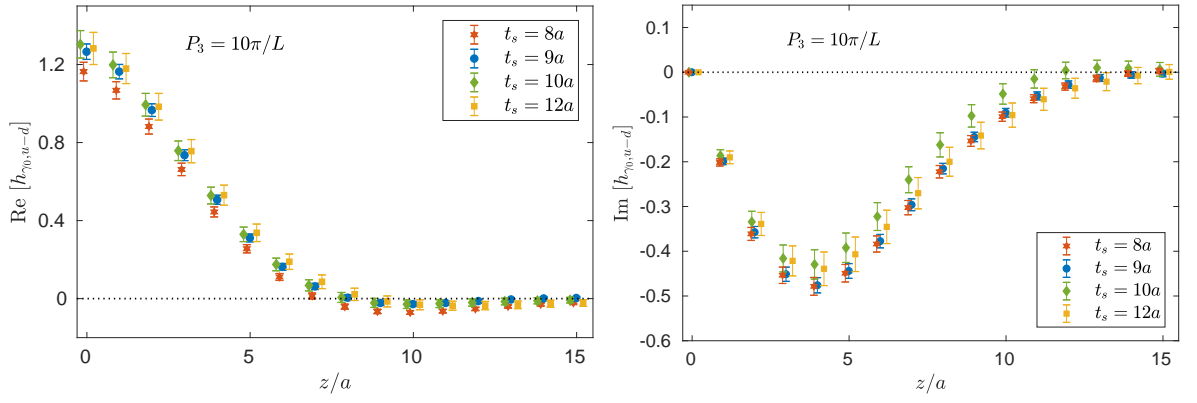
Figure 5.19 Real (left) and imaginary (right) part of the matrix elements for the unpolarized PDFs at $t_s = 8a$ (red stars), $t_s = 9a$ (blue circles), $t_s = 10a$ (green diamonds), $t_s = 12a$ (yellow squares). The nucleon boost is $P_3 = 10\pi/L$.
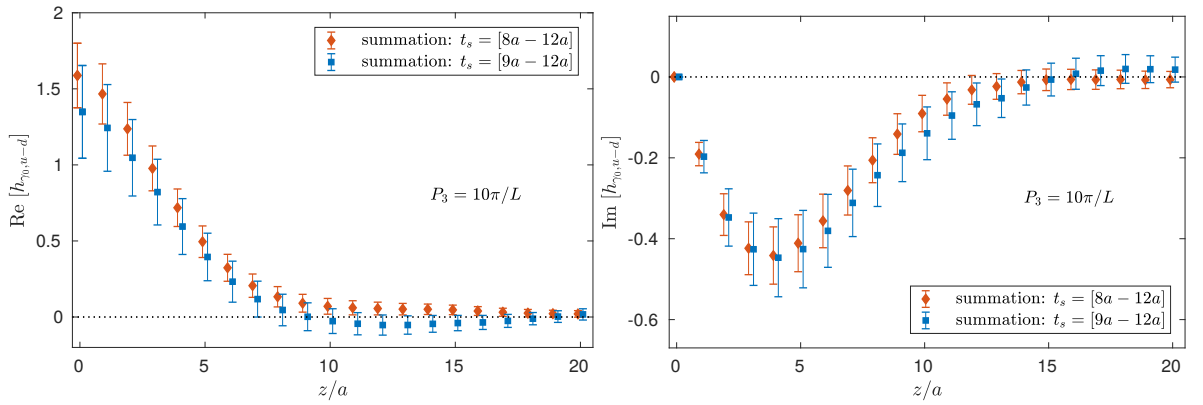
Figure 5.20 Summation method applied to the matrix elements for the unpolarized PDF. Left: real part. Right: imaginary part. Two sets of t_s values are compared, with the sum over τ extended from $\tau = a$ to $\tau = t_s - a$. The nucleon boost is $P_3 = 10\pi/L$.

excluded) and, as we can see, they are compatible with each other. However, $t_s = [8a - 12a]$ does not provide a good description of the data, since for $z/a \approx 10 - 15$ the linear fit has $\chi^2/\text{d.o.f} > 2$, see Fig. 5.21. We find that at $z/a = 12$, $\chi^2/\text{d.o.f.} \simeq 0.16$ when fitting in the range $t_s = [9a - 12a]$ and $\chi^2/\text{d.o.f.} \simeq 2.4$ for $t_s = [8a - 12a]$. The origin of this behavior is
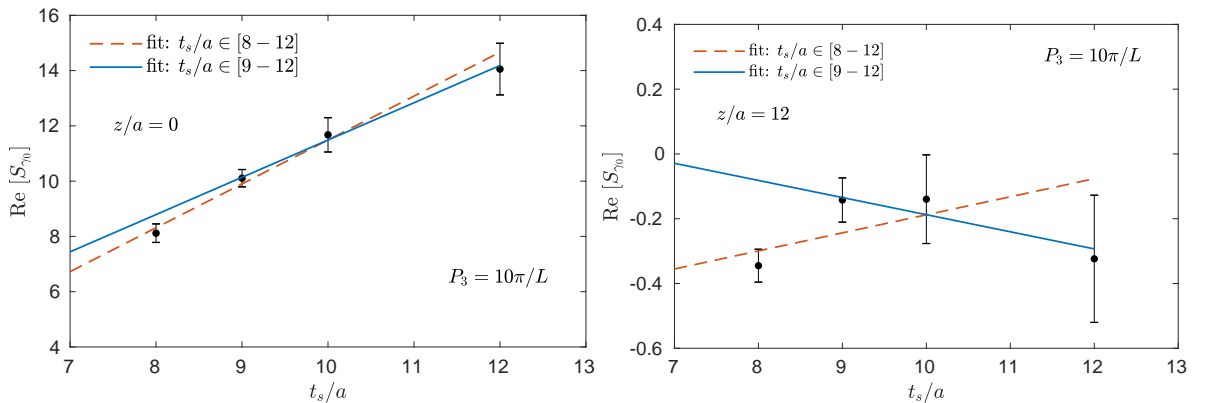
Figure 5.21 Quality of the linear fit in the summation method, shown for the real part of the matrix element for the unpolarized PDF. In both plots the dashed line (red) denotes the fits to all source-sink separations, while the solid line (blue) to the three largest separations. The error bands of the fits are not included.

due to the fact that the matrix element at $t_s = 8a$ (obtained from the ratio method) is well below the ones at larger separations, compromising the quality of the fit. Besides that, the fitting interval $t_s = [8a - 12a]$ also leads to an overestimation of the real part of the matrix elements. This can be deduced by looking at the value at $z/a = 0$, that we know has to be equal to the valence quark number of the proton (i.e. 1), upon renormalization. Applying the Z-factor $Z_V = 0.655$ estimated for $N_f = 2$ twisted mass fermions at $z/a = 0$ in Ref. [161], we find that the renormalized matrix element is $1.02(24)$ when fitting for $t_s = [9a - 12a]$ and $1.21(16)$ for $t_s = [8a - 12a]$. Therefore, as concerns the summation method we consider only the results from the fit to the largest source-sink separations. We also note that, varying the interval over which τ is summed, the quality of the fit is almost unchanged to the one showed in Fig. 5.21 and the statistical errors remain much larger than the ones obtained from the plateau method. Consequently, it is difficult to derive conclusions about the ground state dominance from the summation method.

We also perform two-state analysis and in Fig. 5.22 we compare the results from the sequential and simultaneous two-state fits. The central values and the errors of the matrix
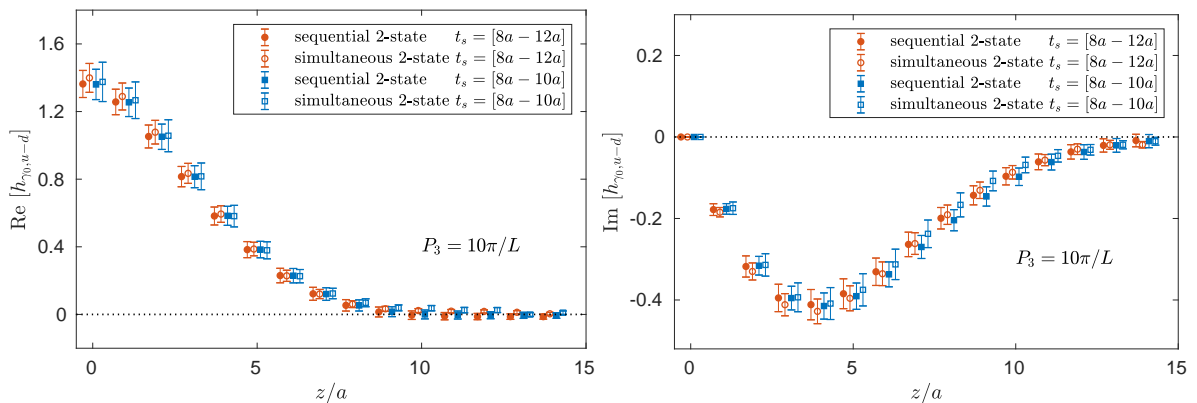
**Figure 5.22** Real (left) and imaginary (right) part of the matrix element for the unpolarized PDF from two-state fits, using source-sink separations $8a - 12a$ (circles) and $8a - 10a$ (squares). Sequential fit (filled symbols) is compared to simultaneous fit (open symbols). The nucleon is boosted with $10\pi/L \simeq 1.38$ GeV.

elements are very similar in both procedures and also when varying the fitting range as indicated in the Figure, demonstrating that the fits are quite robust. Given their equivalence, for comparison purpose we focus only on two cases, i.e. sequential fit in $t_s = [8a - 10a]$ and $t_s = [9a - 12a]$, and collect the results in Fig. 5.23.

Overall, we can see that excited states are clearly visible for $t_s = 8a$, especially in the real part. For the imaginary part we notice only a very small tension between $t_s = 8a, 9a$ from one side and $t_s = 12a$ and two-state fits from the other, but everything is within statistical errors. For better legibility, a comparison between different methods is illustrated in Fig. 5.24 for two selected values of the Wilson line length, $z/a = 5$ and $z/a = 10$.

Summarizing our analysis for the unpolarized operator, we observe that the values obtained at the higher separation $t_s = 12a$ are perfectly compatible with the ones from two-state fits at each length z/a of the Wilson line. This implies that at the level of accuracy of our results,
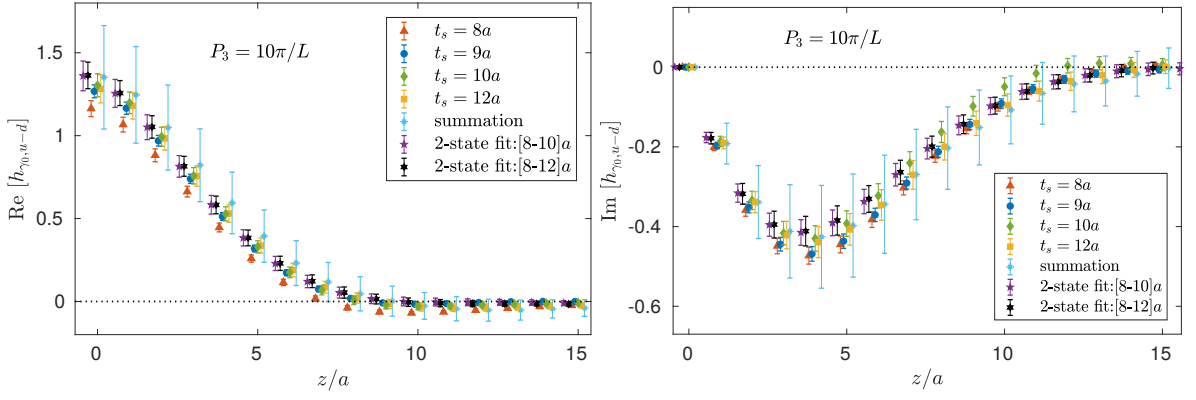
Figure 5.23 Real (left) and imaginary (right) part of the matrix element for the unpolarized PDF from plateau method (points labeled with appropriate t_s), summation method (for $t_s \geq 9a$), two-state sequential fits. The nucleon is boosted with $10\pi/L \simeq 1.38$ GeV.
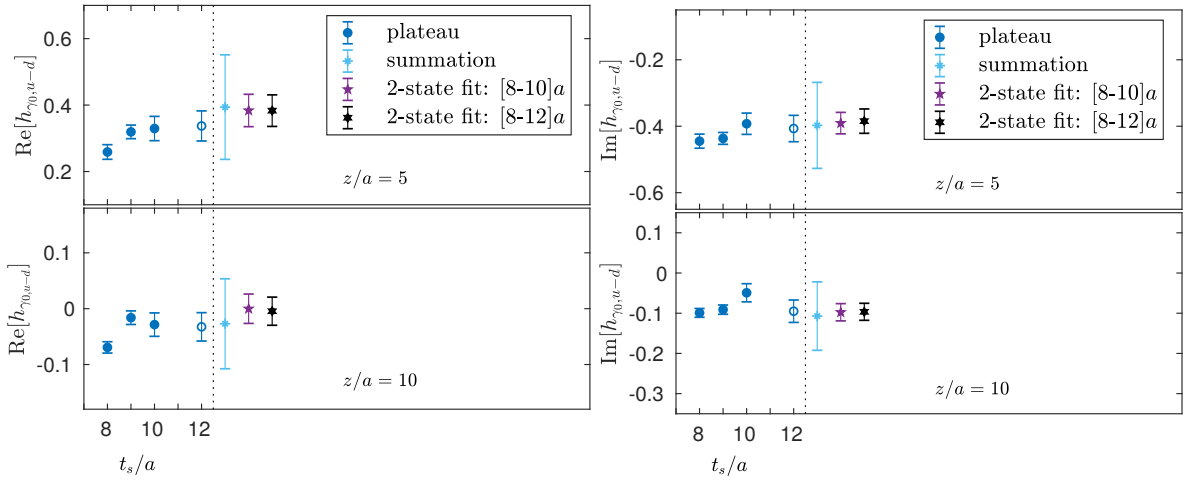
Figure 5.24 Real (left) and imaginary (right) part of the matrix element for the unpolarized PDF at $z/a = 5$ and $z/a = 10$. Different analysis procedures are compared to each other: plateau method (for $t_s/a = 8, 9, 10, 12$), summation method (for $t_s \geq 9a$) and two-state sequential fits. The nucleon is boosted with $10\pi/L \simeq 1.38$ GeV.

$\approx 10\%$, excited states are hidden within statistical errors up to the source-sink separations considered in this work. Thus, for all the momentum values, the results for the unpolarized PDFs will be given from now on at $t_s = 12a$ using the plateau method.

5.3.4 Matrix elements for the helicity PDFs

To study the contamination by excited states on the matrix elements for the helicity distribution, we use the same source-sink separations as for the unpolarized case, namely $t_s/a = [8, 9, 10, 12]$ or $t_s \simeq [0.75, 0.84, 0.94, 1.13]$ fm in physical units. The statistics is reported in Table 5.4.

In Fig. 5.25 we show the results obtained with the plateau method, applied for each t_s value. As can be seen, the imaginary part is amplified at lower separations and the values of the operator are not compatible with those at the highest t_s, meaning that they are strongly contaminated by excited states of the nucleon. The two-state fit analysis for both intervals $[8 - 12]a$ and $[9 - 12]a$ is reported in Fig. 5.26, where the results are shown up to $z/a = 13$

94

$P_3 = 10\pi/L$, Ins: $\gamma_5\gamma_3$	$t_s = 8a$	$t_s = 9a$	$t_s = 10a$	$t_s = 12a$
N_{conf}	36	50	88	811
N_{meas}	3240	4500	7920	72990

Table 5.4 Number of analyzed configurations and measurements for the excited states analysis for the helicity operator ($\gamma_5\gamma_3$) at $P_3 = 10\pi/L \simeq 1.38$ GeV.

Figure 5.25 Real (left) and imaginary (right) part of the matrix element for the helicity PDF. The data at $t_s = 8a$ (red triangles), $t_s = 9a$ (blue circles), $t_s = 10a$ (green diamonds), $t_s = 12a$ (yellow squares) are analyzed using the plateau method. The nucleon momentum is $10\pi/L \simeq 1.38$ GeV.

for better legibility. From the right panel of Fig. 5.26, we notice that the two-state fits using

Figure 5.26 Real (left) and imaginary (right) part of the matrix element for the helicity PDF. We compare the results from the plateau method at $t_s = 8a$ (red triangles), $t_s = 9a$ (blue circles), $t_s = 10a$ (green diamonds), $t_s = 12a$ (yellow squares) with the two-state fits data (violet and black pentagons) extracted from fitting ranges $[8-10]a$ and $[8-12]a$. The nucleon momentum is $10\pi/L \simeq 1.38$ GeV.

$t_s/a = 8, 9, 10$ are incompatible with the plateau values at $t_s = 10a$, suggesting that with only these three source-sink separations excited states are not yet under control. This is also illustrated in Fig. 5.27 for two selected values of z/a ($z/a = 5$ and $z/a = 10$) where summation method results are included as well. All this enforces the necessity of simulating at $t_s = 12a$ to check the consistency of results obtained with different analysis methodologies. Given that at $t_s = 12a$ compatibility is achieved between plateau method and two-state fits at the highest momentum, we take the data at $t_s = 12a$ as our final values for the nucleon helicity operators at all momenta considered in this work.

Figure 5.27 Comparison between plateau (for $t_s/a = 8, 9, 10, 12$), summation method and two-state sequential fits, for the helicity operator at Wilson line length $z/a = 5$ and $z/a = 10$. Left: real part. Right: imaginary part. The nucleon momentum is $10\pi/L \simeq 1.38$ GeV.

5.3.5 Matrix elements for the transversity PDFs

The investigation of the excited states effects for the tensor operator proceeds along the lines of the previous cases. Using the number of measurements listed in Table 5.5 we get the results shown in Fig. 5.28 when the plateau method is employed.

$P_3 = 10\pi/L$, Ins: σ_{3j}	$t_s = 8a$	$t_s = 9a$	$t_s = 10a$	$t_s = 12a$
N_{conf}	36	50	88	811
N_{meas}	3240	4500	7920	72990

Table 5.5 Number of analyzed configurations and measurements for the excited states analysis for the tensor operator (σ_{3j}), at boost $P_3 = 10\pi/L \simeq 1.38$ GeV.
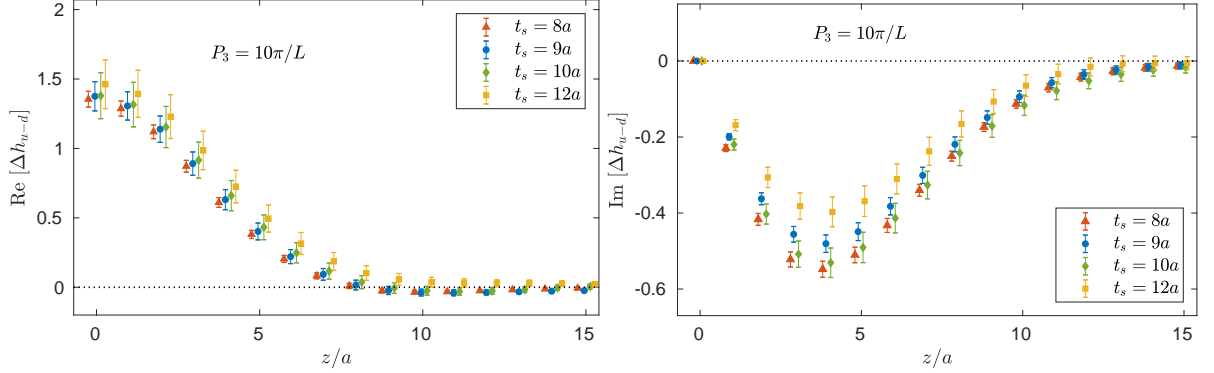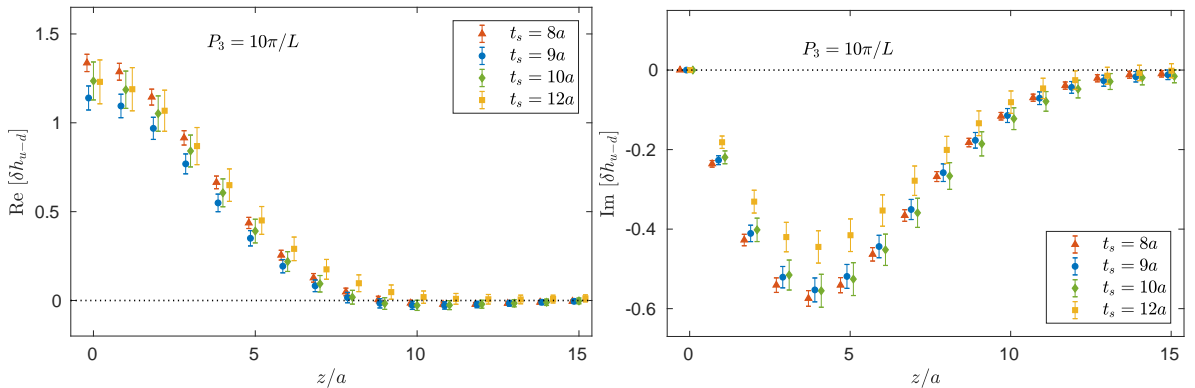

Figure 5.28 Real (left) and imaginary (right) part of the matrix element for the transversity PDF. The data at $t_s = 8a$ (red triangles), $t_s = 9a$ (blue circles), $t_s = 10a$ (green diamonds), $t_s = 12a$ (yellow squares) are analyzed using the plateau method. The nucleon momentum is $10\pi/L \simeq 1.38$ GeV.

As for the helicity matrix elements, the excited states effects manifest through an enhancement of the imaginary part for small source-sink separations. Moreover, at small lengths of the Wilson line ($z \leq 5a$) the two-state fits in the interval $t_s = [8 - 10]a$ do not give compatible

results with the plateau values at $t_s = 10a$. This is illustrated in Fig. 5.29 and Fig. 5.30, for two values of z/a. However, at a level of accuracy of around 10%, this incompatibility is not observed for the real part.
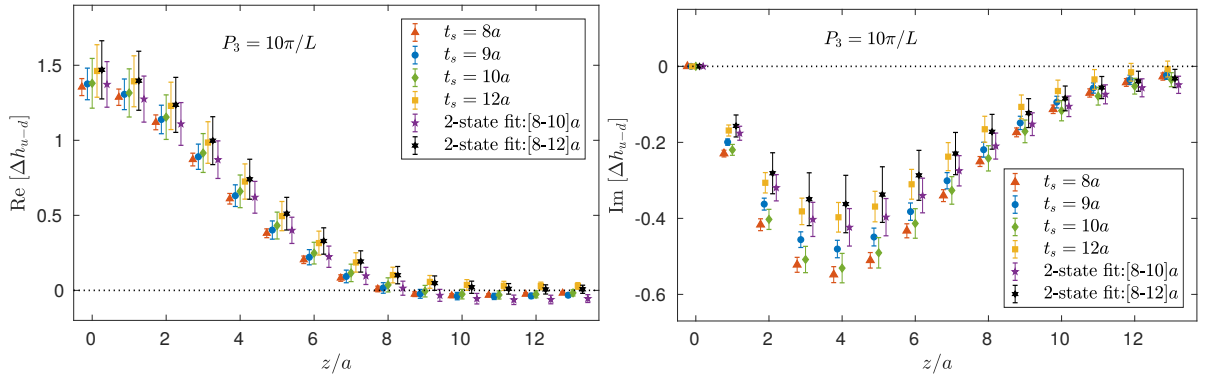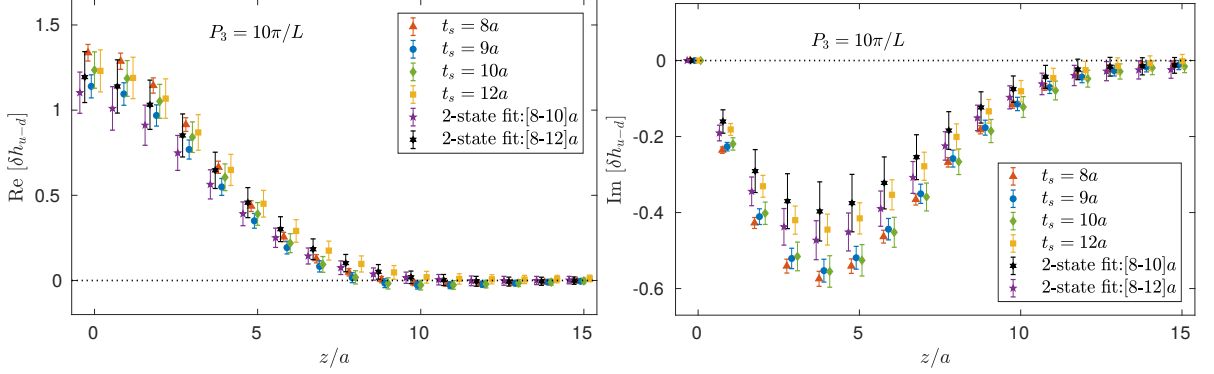

Figure 5.29 Real (left) and imaginary (right) part of the matrix element for the transversity PDF. We compare the results from the plateau method at $t_s = 8a$ (red triangles), $t_s = 9a$ (blue circles), $t_s = 10a$ (green diamonds), $t_s = 12a$ (yellow squares) with the two-state sequential fits data (violet and black pentagons) extracted from fitting ranges $[8 - 10]a$ and $[8 - 12]a$. The nucleon momentum is $10\pi/L \simeq 1.38$ GeV.
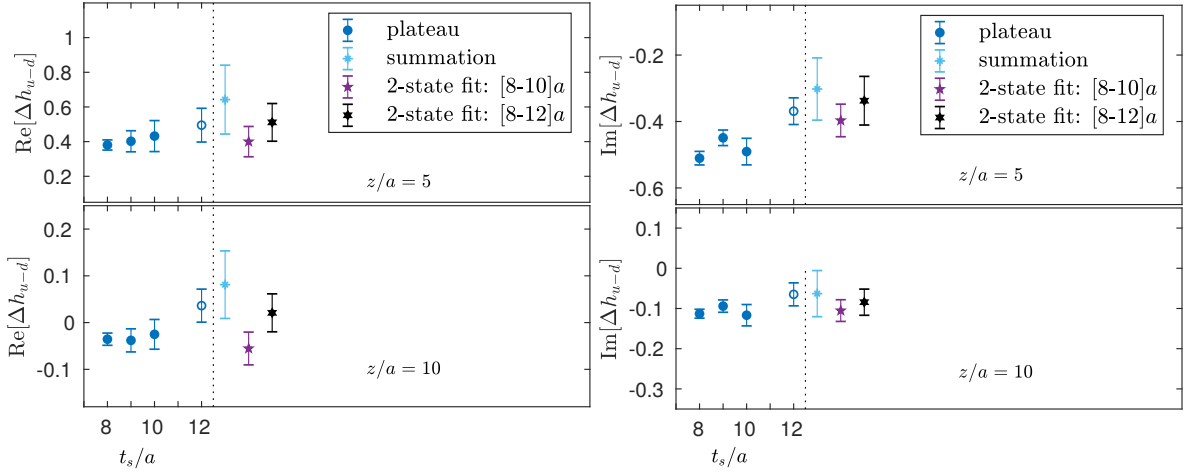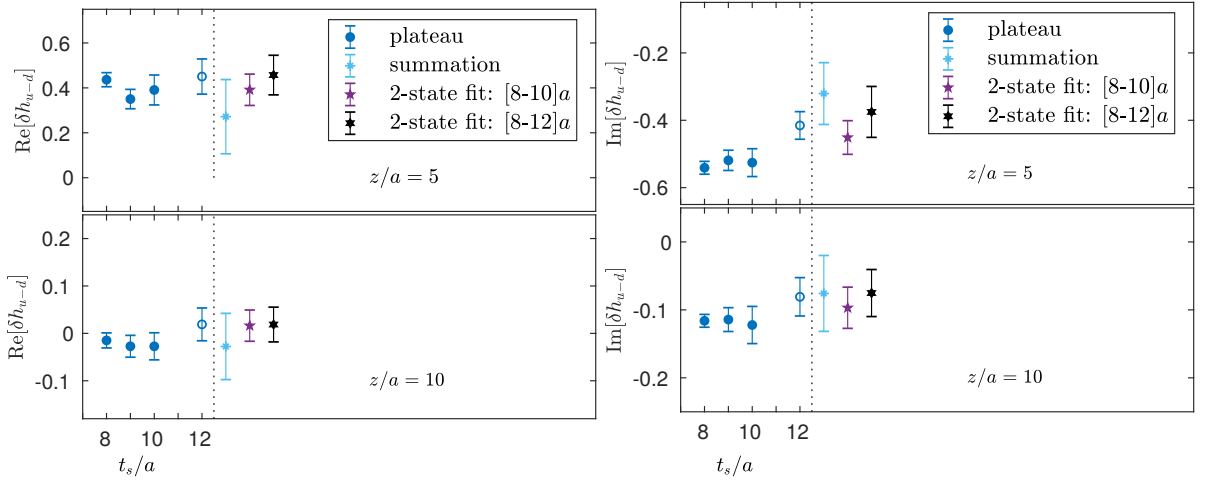

Figure 5.30 Comparison between plateau (for $t_s/a = 8, 9, 10, 12$), summation method and two-state sequential fits, for the tensor operator at Wilson line length $z/a = 5$ and $z/a = 10$. Left: real part. Right: imaginary part. The nucleon momentum is $10\pi/L \simeq 1.38$ GeV.

The results obtained reinforce the conclusion reached in the previous cases for the bare matrix elements for the unpolarized and helicity quasi-PDFs, namely that the tensions observed between results from source-sink separations below 1 fm are indeed manifestations of excited states contamination.

Since $t_s = 12a \simeq 1.13$ fm is the minimum value of the source-sink separation at which plateau values and two-state fits results are compatible with each other, we can conclude that ground state dominance is achieved only at $t_s = 12a$ in our setup, to around 10% statistical accuracy. Even if the plateau and two-state approaches are in agreement, we prefer to extract PDFs by taking the plateau values, as they are more precisely determined. We also note that the more severe excited states effects observed for the helicity and transversity

operators (as compared to the vector case) are in accordance with observations in lattice computations of the nucleon axial and tensor charges, extracted at zero-momentum (see for instance Refs. [157, 162]).

5.4 Computational cost of simulations

Natural questions that may arise at this point are: Why do we reach $P_3 \simeq 1.38$ GeV as maximal value of the nucleon boost and do not go beyond if very large momenta ($P_3 \gg \Lambda_{QCD}$) are crucial to make contact with light-cone PDFs? Or, why source-sink time separations larger than 1.13 fm are not employed if they suppress excited states by a larger factor?

These questions can be addressed with the help of Fig. 5.31 and Fig. 5.32. These are qualitative illustrations of what the computational cost would be if simulations are performed with larger momenta, up to 3 GeV to make an example, and aiming at 10% of accuracy for the unrenormalized matrix elements. Knowing how many measurements are needed for the boosts $\{0.83, 1.11, 1.38\}$ GeV at $t_s \simeq 1.13$ fm and the corresponding computational cost, we can perform an exponential fit to have an idea about the resources required to push the calculation forward. As can be seen from Fig. 5.31, we estimate that to reach a momentum of around 2 GeV one would need $\mathcal{O}(10) - \mathcal{O}(100)$ million core-hours for a 10% precision only, depending on the Dirac structure in the inserted operator. These estimates increase up $\mathcal{O}(10^4) - \mathcal{O}(10^6)$ million core-hours at 3 GeV, going clearly beyond what is currently available.
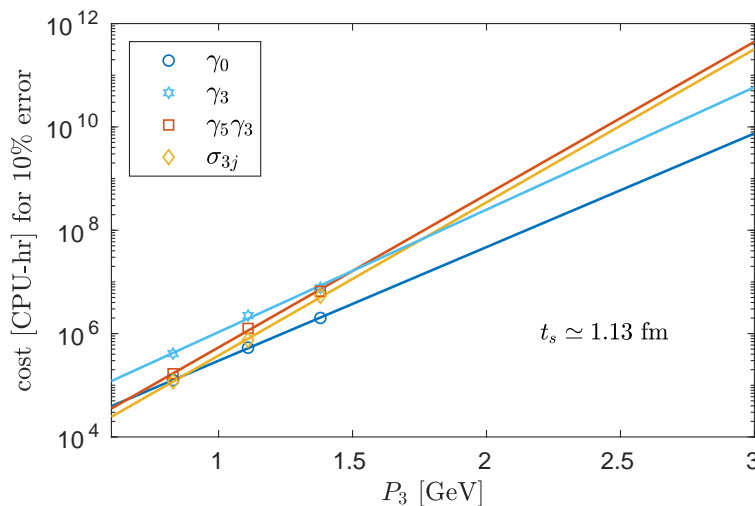
Figure 5.31 Projection of the computational cost for 10% of accuracy on the bare matrix elements of PDFs varying the nucleon momentum. We compare the unpolarized operators (γ_0-circles, γ_3-hexagons), helicity operator ($\gamma_5\gamma_3$-squares) and transversity operator (σ_{3j}-diamonds) at $t_s \simeq 1.13$ fm.

Thus, simulating at very large boosts and at $t_s \gtrsim 1$ fm is a computational challenge in lattice QCD. These cost requirements may be alleviated with further efficient algorithms and lattice techniques that might beat the exponential decreasing of the signal-to-noise ratio at large nucleon boosts and sufficiently large source-sink separations. On the other hand, in our PDF-

related work, additional help may come from theoretical side investigations that may allow a robust extraction of PDFs even at lower momenta. This aspect is discussed in Chapter 7.

From Fig. 5.31, it is also evident that computations at source-sink separations larger than $t_s \simeq 1.13$ fm are prohibitively demanding. Therefore, in quasi-PDF calculations a compromise is needed between the maximal value of the boost and source-sink time separation one is aiming at. This very stringent limit is less severe in lattice calculations of the nucleon charges (vector, axial and tensor), which are quantities that do not need a boosted frame in order to be extracted from the lattice. In those investigations, typical lattice calculations reach source-sink time separations of around $t_s \simeq 1.3$ fm and even larger (see e.g. Refs. [162, 163]).

In Fig. 5.32 we show the estimate of the computational cost when using a smaller source-sink separation, namely $t_s = 8a \simeq 0.75$ fm. As we can see, achieving high momenta is
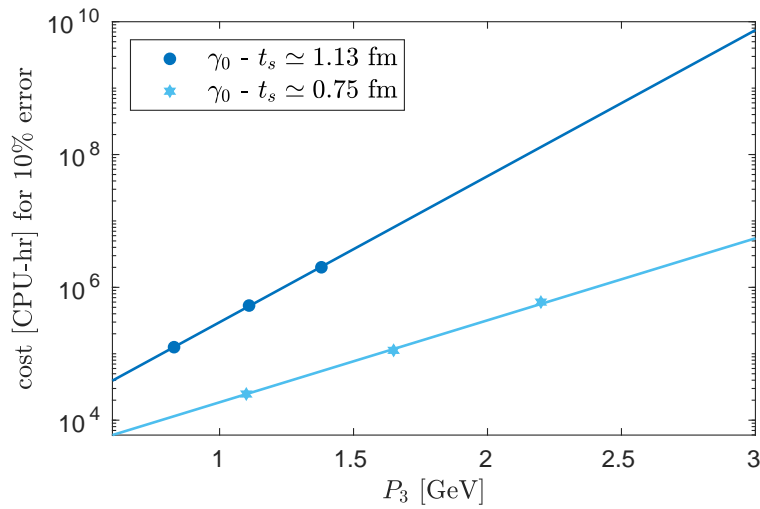
Figure 5.32 Projection of the computational cost for 10% of accuracy on the bare matrix elements of the unpolarized PDFs as a function of the nucleon momentum. The computational resources at $t_s \simeq 0.75$ fm are compared to those at $t_s \simeq 1.13$ fm.

perfectly feasible for this setup and does not require huge computational resources. Indeed, for the unpolarized operator, an order $\mathcal{O}(1)$ million of core-hours must be compared with $\mathcal{O}(10^4)$ millions of core-hours to reach a nucleon momentum of around 3 GeV at $t_s \simeq 1.13$ fm. Even if appealing, using very large boosts at $t_s < 1$ fm is not our choice. If too small source-sink separations are employed, physical results may be strongly dominated by excited states and two-state analysis might be in disagreement with the plateau method, as found for instance in Refs. [163, 164] for the nucleon scalar and tensor charges extracted on the same ensemble as the one used in this work. It is also crucial to observe that the nucleon momentum has to satisfy the condition $P_3 << 1/a$, to avoid huge cutoff effects.

Chapter 6

Renormalization of matrix elements

The renormalization of lattice operators is one of the main components of our parton distribution functions calculation, that is addressed in this work following a non-perturbative approach. Here we give an overview of the method employed to renormalize the matrix elements for quasi-distributions and show results for the renormalization functions, as well as for the renormalized matrix elements. Our method is based on the non-perturbative renormalization prescription presented in 2017 in Ref. [56], which in turn has received crucial inputs from the perturbative study of the renormalization properties of quasi-PDF operators of Ref. [55].

Compared to previous works in this field, our analysis also involves a number of improved elements and important checks described along this Chapter. We also refer to Ref. [59] for a detailed description of the analysis on the renormalization functions in our physical point setup.

6.1 The method

Renormalization is needed in order to relate the bare lattice QCD matrix elements to physical results, removing the divergences that prevent taking the continuum limit, $a \to 0$.

Apart from finite terms related to the lattice regularization and logarithmic divergences with respect to the regulator (i.e. $\log(a\mu_0)$), the bare matrix elements of quasi-PDFs have an additional power divergence, related to the Wilson line [55]. The divergent term assumes the form $e^{\delta m |z|/a}$, where z is the length of the Wilson line and $\delta m > 0$ represents the strength of the power divergence. Moreover, heavy quark effective theory arguments [165] suggest the dependence of the matrix elements on a dimensionful scale, c. For quasi-PDFs this extra term could be of the form $c|z|$. Consequently, from the bare matrix elements one necessarily needs to remove an overall exponential factor of the type $e^{\delta m |z|/a + c|z|}$. The perturbative one-loop calculation of Ref. [55] has demonstrated that δm depends only on the parameters of the gluon action and thus is expected to be operator independent. However, a proper determination of δm requires a non-perturbative approach, since higher orders than one-loop will dominate in the limit $a \to 0$.

In this work, we use the non-perturbative renormalization program developed in Ref. [56] for quasi-PDFs. The procedure consists in a generalization of the RI$'$-scheme [166] and is

appropriate for operators with Wilson line, i.e. well-suitable to eliminate all divergences of the matrix elements discussed above, power-like and logarithmic. In a nutshell, our procedure is composed of two main steps:

- Lattice calculation of appropriate *vertex functions*, from which renormalization functions (Z-factors) are extracted in a RI$'$-scheme at a scale μ_0. In the RI$'$-scheme, each operator $\mathcal{O}$ (associated to the vector, axial, tensor current) has a corresponding Z-factor, $Z_{\mathcal{O}}^{\text{RI}'}$ ($Z_{V_0}^{\text{RI}'}$, $Z_A^{\text{RI}'}$, $Z_T^{\text{RI}'}$).

- Renormalization functions $Z_{\mathcal{O}}^{\text{RI}'}$ are then converted to the traditional scheme (and scale) in which phenomenological results are presented, i.e. the $\overline{\text{MS}}$-scheme. The conversion from RI$'$ to $\overline{\text{MS}}$-scheme makes use of perturbation theory and brings each $Z_{\mathcal{O}}^{\text{RI}'}$ to the appropriate $Z_{\mathcal{O}}^{\overline{\text{MS}}}$, that are eventually applied to renormalize the lattice matrix elements.

In the following we outline the procedure to extract the Z-factors in the RI$'$-scheme, at a given energy scale μ_0. The general idea is the same as the one applied for the renormalization of ultra-local matrix elements and we refer to Refs. [161, 167] for a more detailed description. Defining an operator $\mathcal{O}$ of the type

$$\mathcal{O} = \bar{\psi}(x)\Gamma \mathcal{P}\, e^{-ig\int_0^z A(\xi)d\xi}\, \psi(x+z\hat{\mu})\,, \tag{6.1}$$

the renormalization functions of the operator and the quark field ($Z_{\mathcal{O}}$ and Z_q) are obtained by imposing the following conditions

$$\frac{Z_{\mathcal{O}}^{\text{RI}'}(z,\mu_0)}{Z_q^{\text{RI}'}(\mu_0)}\frac{1}{12}\text{Tr}\left[\mathcal{V}(z,p)\left(\mathcal{V}^{\text{Born}}(z,p)\right)^{-1}\right]\Big|_{p^2=\mu_0^2} = 1\,, \tag{6.2}$$

$$Z_q^{\text{RI}'}(\mu_0)\frac{1}{12}\text{Tr}\left[(S(p))^{-1}S^{\text{Born}}(p)\right]\Big|_{p^2=\mu_0^2} = 1\,. \tag{6.3}$$

Z_q, which renormalizes the quark field ($\psi^R = Z_q^{1/2}\psi$), is computed by taking the trace over the color and spin indices of the product between the fermion propagator $S(p)$ (up- and down-propagator) and its tree-level value S^{Born} in momentum space. In this work, we take S^{Born} to be [167, 168]

$$S^{\text{Born}} = \frac{-i\sum_{\rho}\gamma_{\rho}(p_{\rho})}{\sum_{\rho}\sin(p_{\rho})^2} \tag{6.4}$$

in Euclidean space. In Eq. (6.2), $\mathcal{V}(z,p)$ is the amputated vertex function of the operator $\mathcal{O}$ and $\mathcal{V}^{\text{Born}}(z,p)$ is its tree-level value, e.g. $\mathcal{V}^{\text{Born}}(z,p) = \gamma_0\, e^{ipz}$ for the unpolarized operator. The amputated vertex functions $\mathcal{V}(z,p)$ are extracted through lattice computation of the vertex functions $G(z,p)$. The corresponding expressions are

$$\mathcal{V}(z,p) = (S^u(p))^{-1}G(z,p)(S^d(p))^{-1}\,, \tag{6.5}$$

$$G(z,p) = \frac{a^{12}}{V}\sum_{x,x',z',y}e^{-ip(x-y)}\langle u(x)\bar{u}(x')\,\Gamma\,W(x',z')d(z')\bar{d}(y)\rangle\,, \tag{6.6}$$

where S^u (S^d) is the up (down) quark propagator, $z' = x' + z\hat{e}_\mu$ where z is the length of the Wilson line, W, and Γ is a Dirac structure. For the calculation of $G(z,p)$ we employ the momentum source method [161, 169], that has the advantage of yielding results of high statistical accuracy. This method requires separate inversions for each momentum used, but significant reduction in the gauge noise is observed, which by far outweighs the additional computational cost.

Within this framework, the amputated vertex functions $\mathcal{V}(z,p)$ contain the same power divergence as the nucleon matrix elements, as can be deduced from Eq. (6.5) and Eq. (6.6). Consequently, since $Z_\mathcal{O}$ is related to the inverse of $\mathcal{V}(z,p)$ from the first renormalization condition, one obtains the following relation

$$Z_\mathcal{O}(z,\mu_0) = \hat{Z}_\mathcal{O} \, e^{-\delta m|z|/a - c|z|} \,, \quad \text{with} \quad \delta m > 0 \,, \tag{6.7}$$

where $\hat{Z}_\mathcal{O}$ is the multiplicative Z-factor of the operator. Therefore, upon multiplication $Z_\mathcal{O} \cdot h_\Gamma^{\text{bare}}$, such a renormalization program ensures the elimination of all the divergences of the bare matrix elements, the power-like divergence included.

It is also important to notice that the renormalization conditions of Eqs. (6.2-6.3) are imposed for each length z of the Wilson line and therefore $Z_\mathcal{O}$ is a function of z. Moreover, both $Z_\mathcal{O}$ and Z_q depend on the RI$'$ renormalization scale μ_0, that in this work is chosen to be "democratic" in the spatial directions, that is

$$(a\mu_0) \equiv 2\pi \left(\frac{n_t}{L_t} + \frac{1}{2L_t}, \frac{n}{L_s}, \frac{n}{L_s}, \frac{n}{L_s} \right) \,, \tag{6.8}$$

being L_t (L_s) the temporal (spatial) extent of the lattice. Another possibility for the scale μ_0 is the so-called "parallel" choice, where the integer numbers are taken to be $(n_t, 0, 0, n)$, i.e. n is non-zero only along the direction of the Wilson line. However, this choice is found to produce enhanced lattice artifacts for the renormalization functions [56, 161] and therefore is not considered in this work.

The dependence of the renormalized results on the RI$'$-scale (6.8) is highly non-trivial, because of the complex nature of the Z-factors and the extra dependence on the Wilson line length, z. Thus, we explore several values for μ_0. We consider scales $(a\mu_0)^2 \geq 2$ for which perturbation theory is trustworthy and that minimize the following ratio

$$\hat{P} \equiv \frac{\sum_\rho \mu_{0_\rho}^4}{\left(\sum_\rho \mu_{0_\rho}^2 \right)^2} \,, \tag{6.9}$$

to avoid enhanced discretization effects [56, 161].

Before showing any results for Z-factors, we list in detail the steps carried out in this work to estimate the renormalization functions, eventually converted in the $\overline{\text{MS}}$-scheme:

1. at a given RI′-scale, we perform a chiral extrapolation using three ensembles $N_f = 2$ at different values of the pion mass but at the same lattice spacing. This is an important step because even if a RI-type scheme is mass-independent [166], the Z-factors show a residual dependence on the value m_π of the ensemble, that ideally has to be eliminated;

2. using two physical point ensembles $N_f = 2$ with $m_\pi \simeq 130$ MeV and different volumes, we check any finite size effects on the renormalization functions;

3. the chirally extrapolated Z-factors from point 1 are then converted from each scale μ_0 to $\overline{\text{MS}}$ scheme, using the one-loop conversion formulae derived in Ref. [55] in perturbation theory and in dimensional regularization;

4. the final Z-factors in $\overline{\text{MS}}$ are obtained performing a linear fit in $(a\mu_0)^2$, where always $(a\mu_0)^2 \geq 2$. We explore different fitting ranges and eventually take the one corresponding to a better $\chi^2/d.o.f$. This procedure allows us to eliminate the residual dependence on the initial choice of the RI′ scale μ_0. Such a dependence is in general interpreted as a truncation effect in the perturbative conversion and evolution from the intermediate RI′-scheme to $\overline{\text{MS}}$, that are currently performed using one-loop formulae [55]. For a discussion about systematic effects on the estimate of renormalization functions see [54, 56].

6.2   Lattice results for renormalization functions

The pion mass dependence of the renormalization functions is studied on three $N_f = 2$ twisted mass ensembles having the same value of the lattice spacing but different volumes, see Table 6.1.

$\beta = 2.10,$	$c_{\text{SW}} = 1.57751,$	$a = 0.0938(3)(2)$ fm	$m_\pi L$
$48^3 \times 96$	$a\mu = 0.0009$	$m_\pi = 130$ MeV	2.98
$24^3 \times 48$	$a\mu = 0.003$	$m_\pi = 235$ MeV	2.69
$24^3 \times 48$	$a\mu = 0.006$	$m_\pi = 340$ MeV	3.89

Table 6.1 Parameters of the ensembles used to chirally extrapolate the Z-factors in this work. For other details about the gauge ensembles see Ref. [152].

The chiral extrapolation is performed at each RI′ scale μ_0, after the renormalization conditions of Eqs. (6.2-6.3) are imposed at every value of the Wilson line length [59]. The data are expected to have a quadratic dependence on m_π and therefore they are fitted by the following function

$$Z_\mathcal{O}^{\text{RI}'}(z, \mu_0, m_\pi) = Z_{\mathcal{O},0}^{\text{RI}'}(z, \mu_0) + m_\pi^2 Z_{\mathcal{O},1}^{\text{RI}'}(z, \mu_0) \,, \tag{6.10}$$

where $Z_{\mathcal{O},0}^{\text{RI}'}(z, \mu_0)$ represents the extrapolated value. In Fig. 6.1, we show an example of chiral extrapolation for $z/a = 1$ and $z/a = 5$. The dashed lines and bands of different colors indicate

the chiral fits for the three operators. Z_{V_0}, Z_A and Z_T are the Z-factors of the unpolarized, helicity and transversity PDFs, obtained via the Dirac structures γ_0, $\gamma_5\gamma_3$ and σ_{3j} respectively. For small values of the Wilson line we find a very mild dependence on m_π^2 both for real and
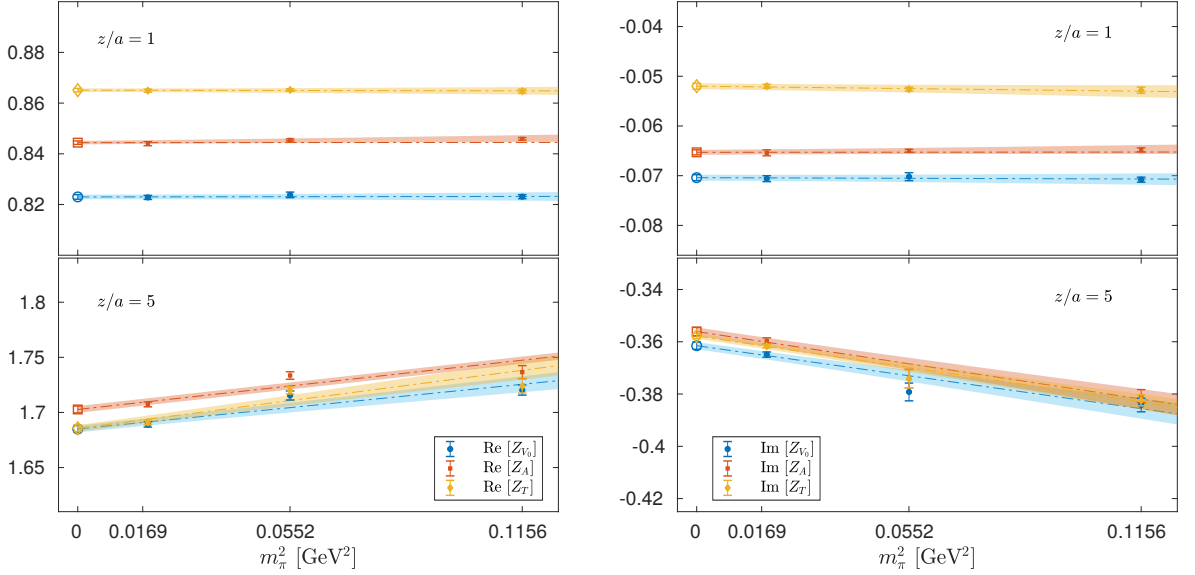
Figure 6.1 Chiral extrapolation of the Z-factors for the unpolarized (blue circles), axial (red squares), tensor (orange diamonds) operator at the RI$'$ scale $(a\mu_0)^2 = 2.5$. Left: real part. Right: imaginary part. The open symbols show the extrapolated values. The errors on the Z-factors are estimated by employing the Jackknife binning [133].

imaginary part of the Z-factors, as also observed for ultra-local operators [161]. For large values of z/a, the dependence is quadratic as expected.

To check possible finite-volume effects on the renormalization functions, we extract the RI$'$ Z-factors on another $N_f = 2$ twisted mass ensemble, simulated at the same value of the lattice spacing and pion mass of the one employed to compute the matrix elements for PDFs, i.e. $a = 0.0938(3)(1)$ fm and $m_\pi \simeq 130(2)$ MeV. The difference is in the lattice volume, that is $64^3 \times 128$, corresponding to $m_\pi L \simeq 3.97$ [130]. These parameters have to be compared with a volume $V = 48^3 \times 96$ and $m_\pi L \simeq 2.98$, see Table 5.1 in Chapter 5. To study finite volume effects, we monitor the ratios of the real and imaginary part of the Z-factors, obtained from the two ensembles:

$$\mathcal{R}_\mathcal{O}(z) \equiv \frac{\text{Re}[Z_{\mathcal{O},64}^{\text{RI}'}(z,\mu_0,m_\pi)]}{\text{Re}[Z_{\mathcal{O},48}^{\text{RI}'}(z,\mu_0,m_\pi)]}, \qquad \mathcal{I}_\mathcal{O}(z) \equiv \frac{\text{Im}[Z_{\mathcal{O},64}^{\text{RI}'}(z,\mu_0,m_\pi)]}{\text{Im}[Z_{\mathcal{O},48}^{\text{RI}'}(z,\mu_0,m_\pi)]} . \qquad (6.11)$$

A fair comparison between the two lattices has to be done at the same RI$'$ scale, because the results may be otherwise affected by lattice artifacts to a different extent. In Fig. 6.2 we show these ratios for $(a\mu_0)^2 = 2.5$. Both the real and imaginary parts do not show a significant dependence on the volume and this is observed for all RI$'$ scales considered in this work. In fact, the ratios take a maximum value of around 1.03 for z/a up to 15, which is well within the range of interest. Thus, to the estimates of the Z-factors we do not attribute any systematic error due to finite volume effects. This is also motivated by the fact that the bare matrix elements of quasi-PDFs go to zero for large values of the Wilson line (see e.g. Figs. 5.13,

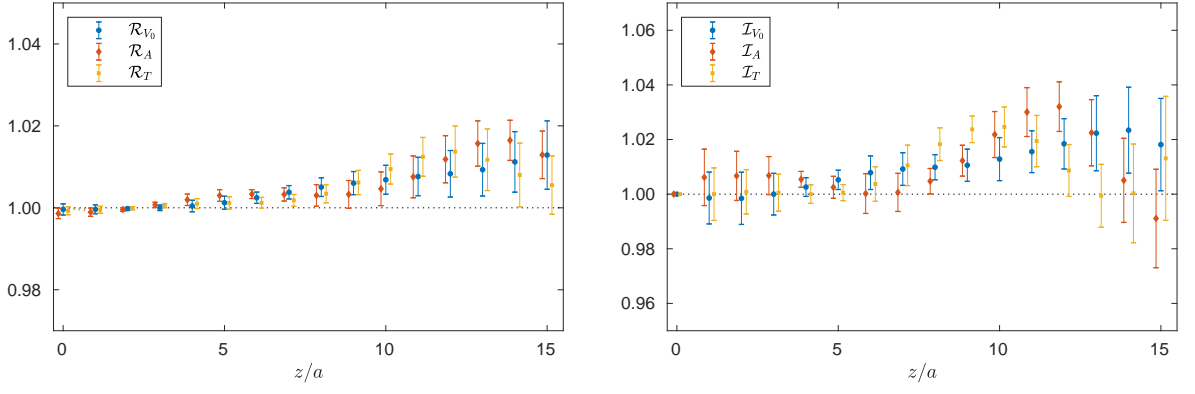**Figure 6.2** Study of volume effects on the RI′ Z-factors. The scale is $(a\mu_0)^2 = 2.5$. The ratios for the real (left) and imaginary (right) part are defined in Eq. (6.11) for the vector, axial and tensor operator.

5.14) and systematic errors on the renormalization functions in that region would be even more negligible.

It is important to remark that finite size effects should also be investigated at the level of the bare matrix elements, before quoting any credible estimates of the systematic uncertainties. Such a study requires significant computational resources and so far has not been performed yet for quasi-PDFs. However, due to the non-trivial volume dependence that non-local matrix elements may have [170], the computation at different physical volumes is among the future goals of collaborations studying *x*-dependent hadron structure.

After chiral extrapolation, the Z-factors are then converted from each RI′ scale μ_0 to $\overline{\text{MS}}$ scheme, using the conversion formulae of Ref. [55]. The remaining dependence on μ_0 is studied with a linear fit in $(a\mu_0)^2$ and is eventually eliminated by taking a fit of the form

$$Z_{\mathcal{O}}^{\overline{\text{MS}}}(z,\bar{\mu},\mu_0) = \mathcal{Z}_{\mathcal{O},0}^{\overline{\text{MS}}}(z,\bar{\mu}) + (a\mu_0)^2 \mathcal{Z}_{\mathcal{O},1}^{\overline{\text{MS}}}(z,\bar{\mu}) \,. \tag{6.12}$$

$Z_{\mathcal{O}}^{\overline{\text{MS}}}(z,\bar{\mu},\mu_0)$ denotes the chirally extrapolated Z-factor converted to the $\overline{\text{MS}}$ scheme at a scale $\bar{\mu}$ and $\mathcal{Z}_{\mathcal{O},0}^{\overline{\text{MS}}}(z,\bar{\mu})$ is the desired Z-factor. We note that the same form for the extrapolation in Eq. (6.12) has already been applied in previous works for ultra-local and non-local operators, see e.g. Refs. [56, 161].

Our renormalization program entails a new element, namely the use of a *modified* $\overline{\text{MS}}$ scheme (M$\overline{\text{MS}}$). The development of such a scheme was motivated by the fact that the existing matching formulae to the light-cone PDFs (see e.g. [171]) do not satisfy particle number conservation. The latter is computed through the integral of the unpolarized quasi- and physical PDF in the region of quark momentum fraction $x \in [-1,1]$. For details about the need and the extraction of a M$\overline{\text{MS}}$ scheme we refer to Ref. [59]. Here we just sketch our procedure, which in a nutshell includes an additional conversion factor to bring $\mathcal{Z}_{\mathcal{O},0}^{\overline{\text{MS}}}(z,\bar{\mu})$ to $\mathcal{Z}_{\mathcal{O},0}^{\text{M}\overline{\text{MS}}}(z,\bar{\mu})$ via

$$\mathcal{Z}_{\mathcal{O},0}^{\text{M}\overline{\text{MS}}}(z,\bar{\mu}) = \mathcal{Z}_{\mathcal{O},0}^{\overline{\text{MS}}}(z,\bar{\mu}) \mathcal{C}^{\overline{\text{MS}},\text{M}\overline{\text{MS}}}(z,\bar{\mu}) \,, \tag{6.13}$$

where $\mathcal{C}^{\overline{\text{MS}},\text{M}\overline{\text{MS}}}$ is operator-dependent, whose form has been derived in Ref. [59]. The M$\overline{\text{MS}}$ scheme allows us to compare our lattice results with the phenomenological ones, presented in the $\overline{\text{MS}}$ scheme.

Moreover, our approach contains another improved component, that is the subtraction of the $\mathcal{O}(g^2 a^\infty)$ terms from the quark renormalization functions Z_q, computed perturbatively in Ref. [161] on the same ensembles. The effect of subtraction of lattice artifacts to all orders of the lattice spacing is shown in Ref. [59], to which we refer for more details about the analysis of the renormalization functions for this work.

In Figs. 6.3, 6.4 and 6.5 we show the final Z-factors employed to renormalize the unpolarized, helicity and transversity PDFs in the M$\overline{\text{MS}}$ scheme.

Figure 6.3 Final values of the Z-factors in the M$\overline{\text{MS}}$ scheme for the vector operator (γ_0), upon chiral and $(a\mu_0)^2$ extrapolation. Real and imaginary parts are shown in the left and right panels, respectively. 5 levels of 3-D stout smearing are applied to the gauge links in the vertex functions.

Figure 6.4 Final values of the Z-factors in M$\overline{\text{MS}}$ scheme for the axial ($\gamma_5\gamma_3$) operator, upon chiral and $(a\mu_0)^2$ extrapolation. Left: real part. Right: imaginary part. 5 levels of 3-D stout smearing are applied to the gauge links in the vertex functions.

The results are obtained by applying 5 steps of 3-D stout smearing to the gauge links entering the vertex functions. The renormalization scale is set to $\bar{\mu} = 2$ GeV for the unpolarized and helicity operator and $\bar{\mu} = \sqrt{2}$ GeV for the tensor operator. With these choices, the lattice PDFs will be renormalized at the same scale at which the phenomenological results used for comparison purpose are presented (see next Chapter).

The Z-factors have two important properties: **i)** the real and imaginary parts are respectively symmetric and antisymmetric with respect to $z \to -z$, as for the bare matrix elements; **ii)** the imaginary part is around a factor 2 smaller than the real counterpart. However, as demonstrated in Ref. [55], the Z-factors should be real after conversion in $\overline{\text{MS}}$ scheme to
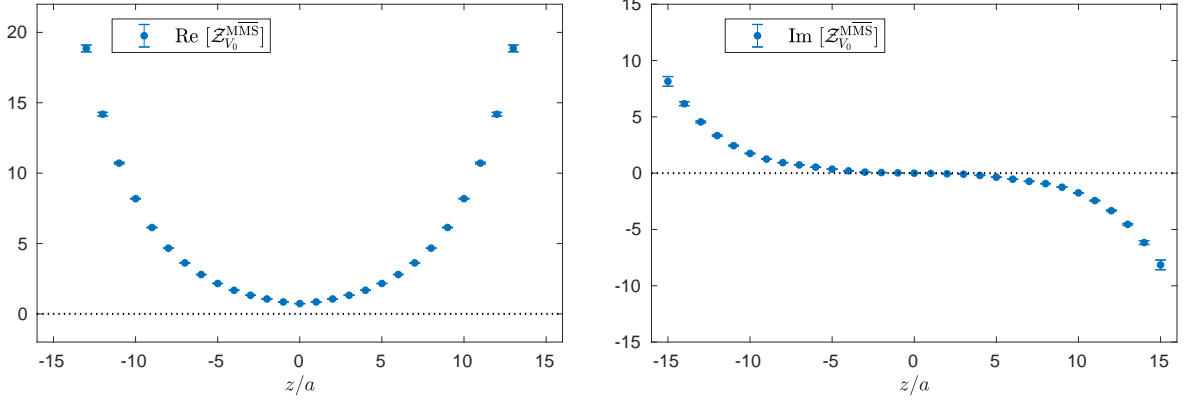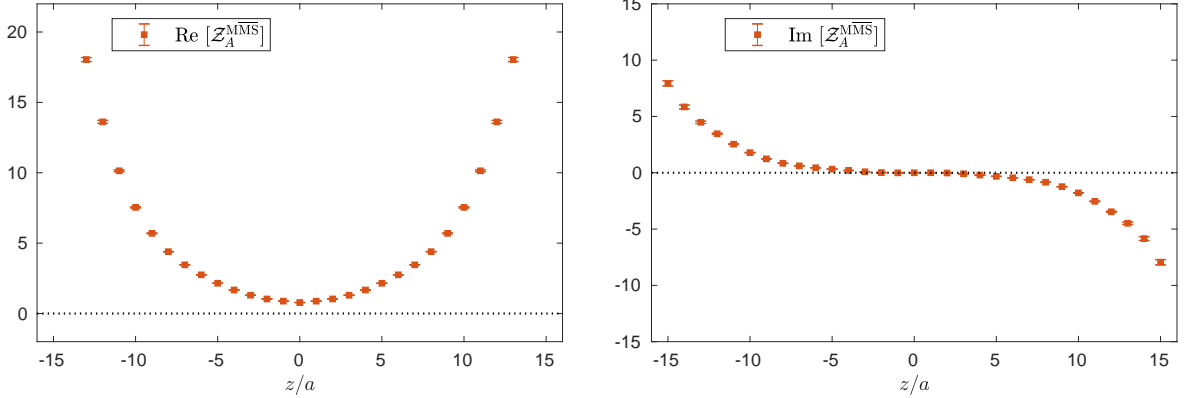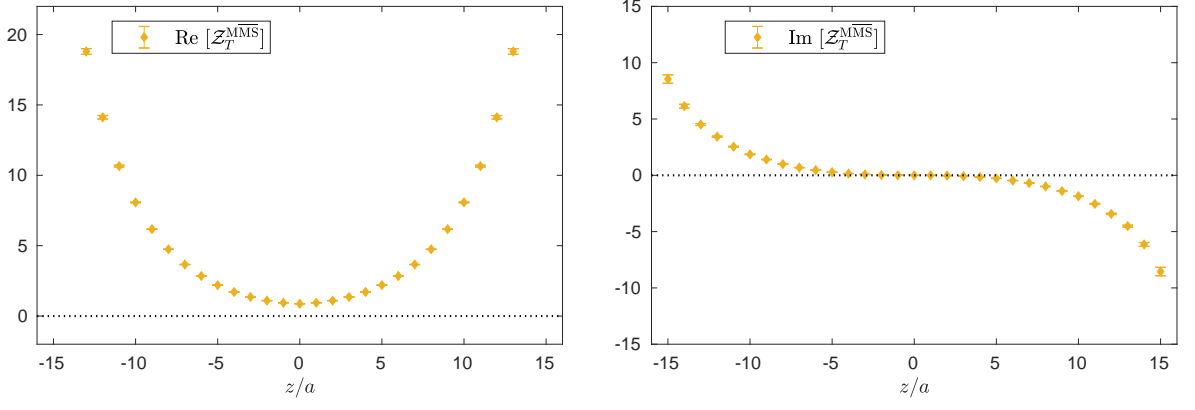
Figure 6.5 Final values of the Z-factors in the M$\overline{\text{MS}}$ scheme for the tensor (σ_{3j}) operator, upon chiral and $(a\mu_0)^2$ extrapolation. Left: real part. Right: imaginary part. 5 levels of 3-D stout smearing are applied to the gauge links in the vertex functions.

all orders in perturbation theory. Their complex nature observed here is an artifact due to truncation effects in the conversion and evolution from RI$'$ to $\overline{\text{MS}}$ scheme at a given scale, currently performed to one-loop order. For a discussion about systematic effects on the renormalization functions see [54, 56].

6.3 Renormalized matrix elements

Having computed the Z-factors, we can now renormalize the nucleon bare matrix elements (h_Γ^{bare}) in the M$\overline{\text{MS}}$ scheme by the complex multiplication

$$h_\Gamma^{\text{M}\overline{\text{MS}}}(P_3, z, \bar{\mu}) = h_\Gamma^{bare}(P_3, z) \cdot \mathcal{Z}_\Gamma^{\text{M}\overline{\text{MS}}}(z, \bar{\mu}) . \tag{6.14}$$

Therefore, the real and imaginary part of $h_\Gamma^{\text{M}\overline{\text{MS}}}$ are sums of two terms

$$\begin{aligned}
\text{Re}[h_\Gamma^{\text{M}\overline{\text{MS}}}] &= \text{Re}[\mathcal{Z}_\Gamma^{\text{M}\overline{\text{MS}}}]\,\text{Re}[h_\Gamma^{bare}] - \text{Im}[\mathcal{Z}_\Gamma^{\text{M}\overline{\text{MS}}}]\,\text{Im}[h_\Gamma^{\text{bare}}] , \\
\text{Im}[h_\Gamma^{\text{M}\overline{\text{MS}}}] &= \text{Re}[\mathcal{Z}_\Gamma^{\text{M}\overline{\text{MS}}}]\,\text{Im}[h_\Gamma^{bare}] + \text{Im}[\mathcal{Z}_\Gamma^{\text{M}\overline{\text{MS}}}]\,\text{Re}[h_\Gamma^{\text{bare}}] ,
\end{aligned} \tag{6.15}$$

where both $\text{Re}[\mathcal{Z}^{\text{M}\overline{\text{MS}}}]$ and $\text{Im}[\mathcal{Z}^{\text{M}\overline{\text{MS}}}]$ contribute. In Figs. 6.6, 6.7 and 6.8 we compare the bare and renormalized matrix elements for the vector, axial and tensor operator. Since the behavior after renormalization is similar to all values of momenta, here we discuss the general properties showing only one single case, corresponding to a nucleon boosted with $P_3 = 10\pi/L \simeq 1.38$ GeV. The results presented here are extracted by applying 5 levels of 3-D stout smearing, both to the Wilson line of the matrix elements and of the vertex functions. As can be seen, after renormalization, the real and imaginary part of the matrix elements are shifted towards larger values and decay to zero slower than the bare ones. The amplification of the bare matrix elements, more profound in the large z-region, is due to the large values of Z-factors and stems from the power divergence of non-local operators with Wilson line. We also observe that statistical errors are increased and this very large noise on the data will

Figure 6.6 Bare (filled symbols) and renormalized (opened symbols) matrix elements for unpolarized distributions ($\Gamma = \gamma_0$) in the M$\overline{\text{MS}}$ scheme at $\bar{\mu}$=2 GeV. Left: real part. Right: imaginary part. The nucleon boost is $P_3 = 10\pi/L \simeq 1.38$ GeV.
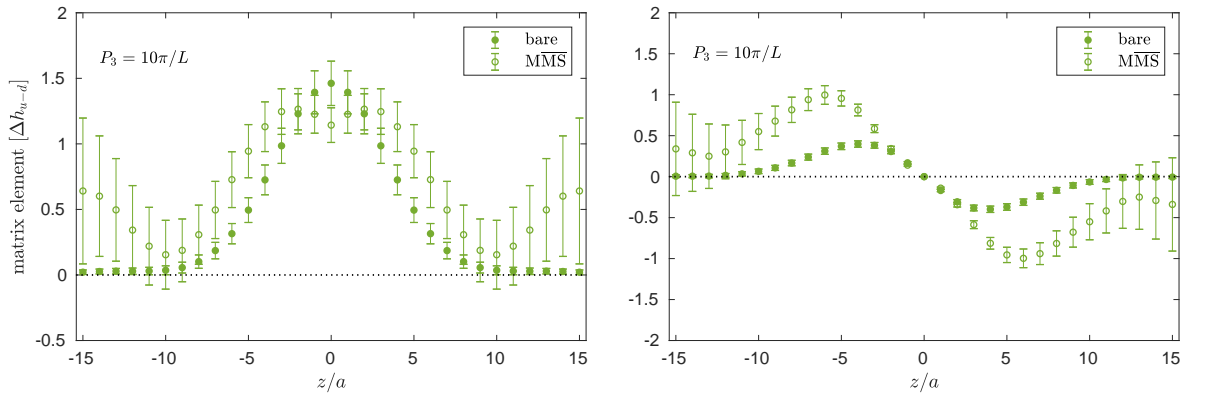
Figure 6.7 Bare (filled symbols) and renormalized (opened symbols) matrix elements for helicity distributions ($\Gamma = \gamma_5\gamma_3$) in the M$\overline{\text{MS}}$ scheme at $\bar{\mu}$=2 GeV. Left: real part. Right: imaginary part. The nucleon boost is $P_3 = 10\pi/L \simeq 1.38$ GeV.
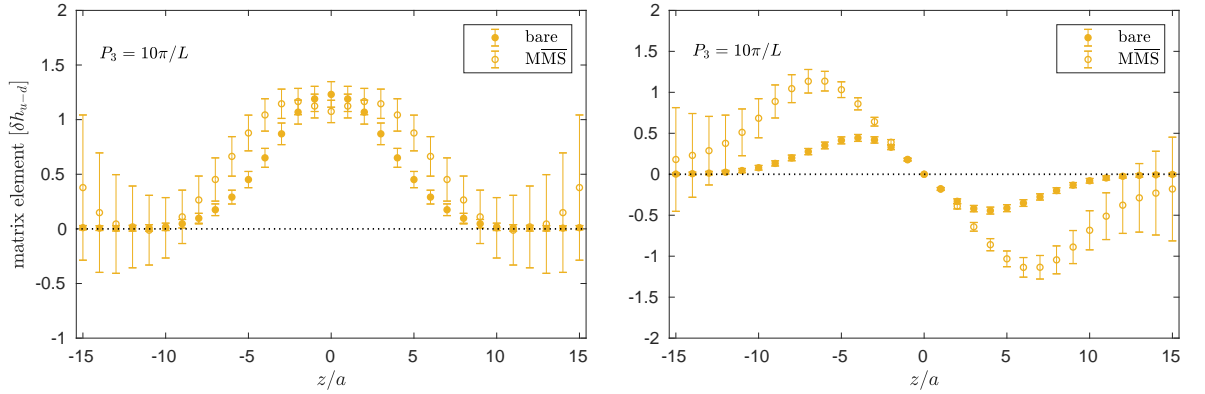
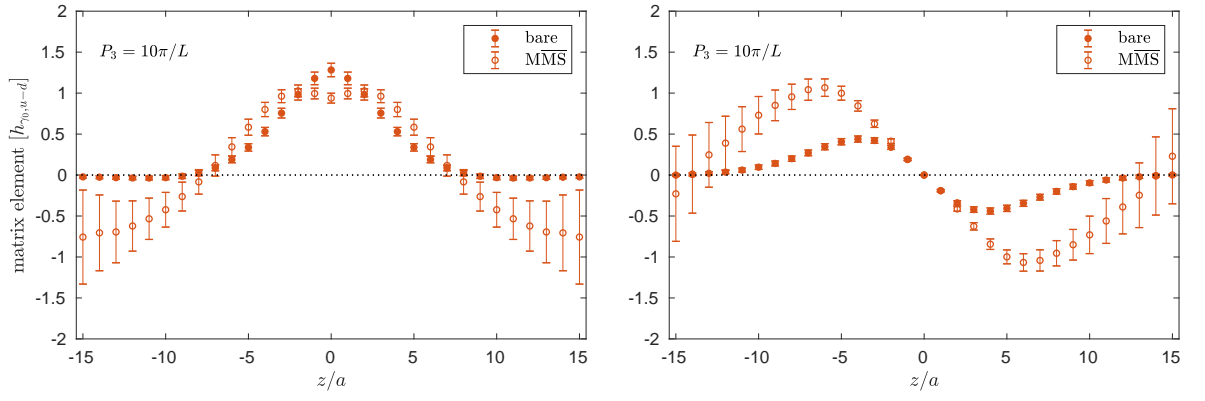**Figure 6.8** Bare (filled symbols) and renormalized (opened symbols) matrix elements for transversity distributions ($\Gamma = \sigma_{3j}$) in the M$\overline{\text{MS}}$ scheme at $\bar{\mu} = \sqrt{2}$ GeV. Left: real part. Right: imaginary part. The nucleon boost is $P_3 = 10\pi/L \simeq 1.38$ GeV.

propagate through the Fourier transform and matching to the final distributions, as described in Chapter 7.

6.4 Renormalized matrix elements with stout smearing

For a given operator (vector, axial, tensor), the renormalized matrix elements depend not only on the nucleon momentum but in principle on any technique employed in a lattice calculation, such as link-smearing that is used in this work. In Fig. 6.9 we show the Z-factors in the $M\overline{MS}$ scheme for the helicity operator, obtained by applying $0, 5, 10, 15$ levels of 3-D stout smearing to the gauge links in the vertex functions of Eq. (6.6). As one can see, smearing reduces both real and imaginary part of $\mathcal{Z}_A^{M\overline{MS}}$, shifting them towards their tree-level values and thus reducing the power-like divergence. This effect is significant for $z/a > 3$ and is stronger from $N_{st} = 0$ to $N_{st} = 5$ stout iterations than from 5 to 10. However, once applied the
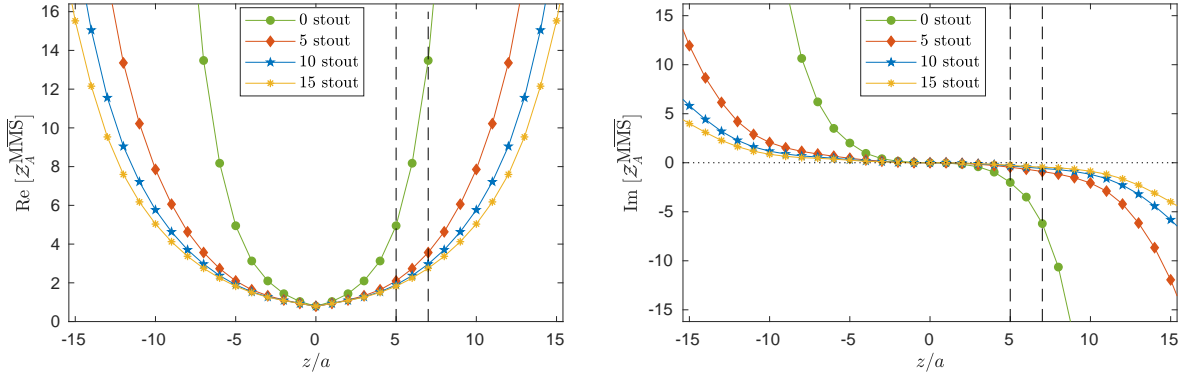
Figure 6.9 Real (left) and imaginary (right) part of the Z-factors in the $M\overline{MS}$ scheme at 2 GeV for the helicity operator, applying $0/5/10/15$ (green circles/red diamonds/ blue pentagons/orange stars) levels of stout smearing to the Wilson line in the vertex functions.

renormalization functions to the bare matrix elements (see Figs. 5.11 and 5.12) the smearing dependence almost vanishes, as shown in Fig. 6.10 for the axial operator, where the nucleon is boosted with $P_3 = 6\pi/L \simeq 0.83$ GeV. The difference when using different smearing iterations
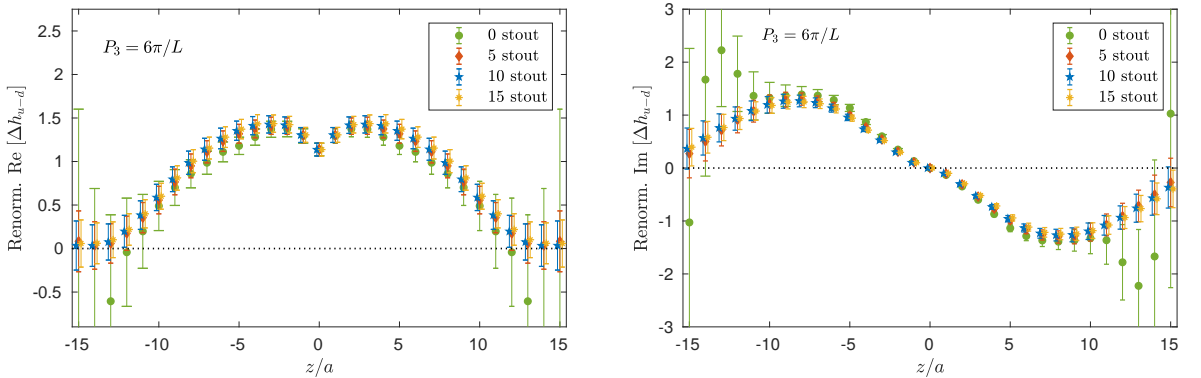
Figure 6.10 Real (left) and imaginary (right) part of renormalized matrix elements for the axial operator (helicity PDF) for momentum $6\pi/L \simeq 0.83$ GeV, as a function of the length of the Wilson line. They are obtained using the Z-factors shown in Fig. 6.9.

is mostly in the statistical errors, which are much larger in absence of link-smearing. To make an example, for the helicity operator shown here the error at $z/a = 9$ is around 18% on the real bare matrix element and 20% and 28% after renormalization, using five and zero levels of smearing respectively. Therefore, we can exploit the property that the results are almost

equivalent (see Fig. 6.10) to smear the gauge links in the inserted operator and reduce in this way the statistical uncertainties, which originate from an ultra-violet power divergence of the type $e^{\delta m |z|/a}$. Smearing independence is also observed for the renormalized unpolarized and transversity nucleon matrix elements, that share similar properties to the ones presented in Fig. 6.10 and therefore are not shown here.

From now on, all results will be understood as obtained applying 5 levels of 3-D stout smearing, both to the bare matrix elements and the vertex functions. However, we stress that any number of stout smearing iterations may be used in the renormalization process without changing the physical results, but it has to be kept fixed as the continuum limit is taken. The independence on the stout smearing step is an important check that indicates that the elimination of the power divergences is realized correctly.

Chapter 7

Physical Quark distributions

In this Chapter we present our final results for the renormalized unpolarized, helicity and transversity distribution functions within the nucleon, with focus on the flavor structure $u - d$. We describe the steps leading to the final PDFs, that involve the Fourier transform of the renormalized matrix elements, the implementation of the matching procedure and the nucleon mass corrections (NMCs). We also discuss the importance of having simulations at the physical value of quark masses, by comparing the results of this work with the ones of a previous computation [39] performed on a twisted mass $N_f = 2 + 1 + 1$ ensemble simulated at $m_\pi \simeq 372$ MeV [172].

7.1   Matching to light-cone PDFs

According to the quasi-PDF approach, to reconstruct parton distribution functions we need to compute quasi-distributions that are eventually related to the light-cone PDFs via a perturbative matching procedure [34, 134, 171, 173].

Having renormalized the nucleon matrix elements for the different operators, as described in the previous Chapter, we perform a Fourier transform to obtain the renormalized quasi-PDFs. They represent the would-be quark momentum distributions in a nucleon moving with a large but finite momentum along the z-direction

$$\tilde{q}(x, \bar{\mu}, P_3) = \int_{-\infty}^{+\infty} \frac{dz}{4\pi} e^{-izxP_3} \langle N | \bar{\psi}(0, z) \Gamma W(0, z) \psi(0, 0) | N \rangle^{\mathrm{M\overline{MS}}, \bar{\mu}} , \qquad (7.1)$$

where $\bar{\mu}$ is the renormalization scale in the modified $\overline{\mathrm{MS}}$ scheme (M$\overline{\mathrm{MS}}$), introduced in Section 6.1. On the lattice we use the discretized form of the Fourier transform

$$\tilde{q}(x, \bar{\mu}, P_3) = \frac{2P_3}{4\pi} \sum_{z=-z_{max}}^{+z_{max}} e^{-izxP_3} h_\Gamma^{\mathrm{M\overline{MS}}}(z, P_3) , \qquad (7.2)$$

where the factor $2P_3$ is needed to have the correct normalization for different momenta. At this stage there is some flexibility on the maximal value of the Wilson line length (z_{max}) to use for the Fourier transform. This issue originates from the fact that lattice provides data for a finite number of lengths z/a of the Wilson line; therefore, a truncation of the Fourier

transform is unavoidable. This represents a delicate issue within the quasi-PDF approach, that is numerically investigated in Section 7.1.1.

Once computed the M$\overline{\text{MS}}$ renormalized quasi-PDFs as in Eq. (7.2) for the unpolarized, helicity and transversity distributions, we apply a matching procedure in order to make contact with the physical PDFs. The matching procedure relies on perturbation theory and consists in computing corrections to the quark probability distribution of Eq. (7.1) in terms of the strong coupling. To one-loop order, the diagrams describe the process $q \to qg$, i.e. the gluon emission out of a quark, whose momentum $p_3 = yP_3$ is collinear to the nucleon boost. After gluon emission, the daughter quark will have a momentum $\xi p_3 = \xi y P_3$. The corrections entering this process are known as *self-energy* and *vertex* corrections, that together build the so-called *matching kernel* $\mathcal{C}$.

The matching formula we implement reads [59]

$$q^{\text{M}\overline{\text{MS}}}(x,\bar{\mu}) = \int_{-\infty}^{+\infty} \frac{dy}{|y|} \mathcal{C}^{\text{M}\overline{\text{MS}}}\left(\frac{x}{y}, \frac{\bar{\mu}}{p_3}\right) \tilde{q}^{\text{M}\overline{\text{MS}}}(y,\bar{\mu},P_3) + \mathcal{O}\left(\frac{\Lambda_{QCD}^2}{P_3^2}, \frac{m_N^2}{P_3^2}\right), \qquad (7.3)$$

where $\tilde{q}$ in the r.h.s. is the renormalized quasi-PDF, whereas q is the matched PDF, which is equal to the light-cone distribution in the limit $P_3 \to \infty$. Thus, for a finite-momentum frame, the lattice distributions differ from the light-cone PDFs by power corrections suppressed in Λ_{QCD}^2/P_3^2 and m_N^2/P_3^2, where m_N is the nucleon mass.

For the matching kernel $\mathcal{C}^{\text{M}\overline{\text{MS}}}$ we use the expression derived to one-loop order in Ref. [59], to which we refer for a complete derivation of the formulae. For the unpolarized and helicity distributions the matching kernel reads

$$C_{\gamma^0,\gamma^3\gamma^5}^{\text{M}\overline{\text{MS}}}\left(\xi, \frac{\bar{\mu}}{p_3}\right) = \delta(1-\xi) - \frac{\alpha_s C_F}{2\pi}$$

$$\times \begin{cases} \left(\frac{1+\xi^2}{1-\xi}\ln\left(\frac{-\xi}{1-\xi}\right) - 1 + \frac{3}{2\xi}\right)_{+(1)}, & \xi > 1, \\[2ex] \left(\frac{1+\xi^2}{1-\xi}\left[\ln\left(\frac{p_3^2}{\bar{\mu}^2}\right) + \ln(4\xi(1-\xi))\right] - \frac{\xi(1+\xi)}{1-\xi} + 2\iota(1-\xi)\right)_{+(1)}, & 0 < \xi < 1, \\[2ex] \left(-\frac{1+\xi^2}{1-\xi}\ln\left(\frac{-\xi}{1-\xi}\right) - 1 + \frac{3}{2(1-\xi)}\right)_{+(1)}, & \xi < 0, \end{cases}$$

$$(7.4)$$

where $\iota = 0$ for γ_0 (unpolarized) and $\iota = 1$ for $\gamma_3\gamma_5$ (helicity).

The matching kernel for the transversity PDF is given by [59]

$$
\begin{aligned}
C_{\gamma^3\gamma^j}^{\mathrm{M\overline{MS}}}\left(\xi,\frac{\bar{\mu}}{p_3}\right) &= \delta(1-\xi) - \frac{\alpha_s C_F}{2\pi} \\
&\times
\begin{cases}
\left[\dfrac{2\xi}{1-\xi}\ln\left(\dfrac{\xi}{\xi-1}\right)+\dfrac{2}{\xi}\right]_{+(1)}, & \xi > 1, \\[2ex]
\left[\dfrac{2\xi}{1-\xi}\left[\ln\left(\dfrac{p_3^2}{\bar{\mu}^2}\right)+\ln(4\xi(1-\xi))\right]-\dfrac{2\xi}{1-\xi}\right]_{+(1)}, & 0 < \xi < 1, \\[2ex]
\left(-\dfrac{2\xi}{1-\xi}\ln\left(\dfrac{\xi}{\xi-1}\right)+\dfrac{2}{1-\xi}\right)_{+(1)}, & \xi < 0.
\end{cases}
\end{aligned}
$$

(7.5)

In the equations above, $C_F = 4/3$ for SU(3) gauge theories. The subscript "+(1)" denotes the *plus prescription* at $\xi = +1$, which in a domain D acts in the following way

$$
\int_D \frac{d\xi}{|\xi|} C^{\mathrm{M\overline{MS}}}\left(\xi,\frac{\bar{\mu}}{p_3}\right)\tilde{q}\left(\frac{x}{\xi},\bar{\mu},P_3\right) = \int_D \frac{d\xi}{|\xi|} C^{\mathrm{M\overline{MS}}}\left(\xi,\frac{\bar{\mu}}{p_3}\right)\tilde{q}\left(\frac{x}{\xi},\bar{\mu},P_3\right)
$$
$$
- \tilde{q}(x,\bar{\mu},P_3)\int_D d\xi\, C^{\mathrm{M\overline{MS}}}\left(\xi,\frac{\bar{\mu}}{p_3}\right),
$$

(7.6)

where we have defined $x/y = \xi$. Therefore, for the three kinds of quark distributions the connection between quasi- and physical PDFs at one-loop order can be written in a compact way as

$$
q^{\mathrm{M\overline{MS}}}(x,\bar{\mu}) = \tilde{q}^{\mathrm{M\overline{MS}}}(x,\bar{\mu},P_3) - \tilde{q}^{\mathrm{M\overline{MS}}}(x,\bar{\mu},P_3)Z_F^{(1)}(\bar{\mu},P_3) - \tilde{q}^{(1),\mathrm{M\overline{MS}}}(x,\bar{\mu},P_3),
$$

(7.7)

where the integrations in Eq. (7.3) have been included in the terms $Z_F^{(1)}$ and $\tilde{q}^{(1),\mathrm{M\overline{MS}}}$. In the equation above, the first term represents the tree-level matching, the second one is the contribution of the self-energy corrections and the third one of the vertex corrections.

After matching, we apply further corrections known as *nucleon mass corrections* (NMCs), that result from a non-zero ratio of the nucleon mass to its momentum, as can be seen from Eq. (7.3). Unlike the corrections in Λ_{QCD}^2/P_3^2, the NMCs can be exactly computed to all orders and in this work we use the expressions derived in Ref. [38] for the unpolarized, helicity and transversity quark distributions. For the sake of completeness, the formulae of the NMCs are reported in Appendix A.4.

7.1.1 Truncation of the Fourier transform

Computing quasi-distributions represents the first step towards the matching to the light-cone PDFs. In this Section we describe in detail the procedure to extract quasi-PDFs and discuss delicate issues arising from such lattice calculations.

When computing quasi-PDFs one needs to choose the maximal value of the Wilson line length over which the Fourier transform is performed, that we call z_{max}/a. Ideally, it should be a value for which the matrix elements have decayed to zero and physical results should

not change when considering any value of z/a larger than z_{max}/a. For unrenormalized matrix elements the choice of such a value poses no problem, since the matrix elements for each operator are compatible with zero for $|z|/a > 15$ in our setup (see e.g. Figs. 5.13 and 5.14). In contrast, this choice is non-trivial for the renormalized matrix elements, unless one employs sufficiently large values of z_{max}/a beyond which both real and imaginary parts are compatible with zero. Moreover, as seen in Figs. 6.6-6.8, the renormalized matrix elements are amplified and go to zero slower than the bare ones. If the physical distance at which the matrix elements decay to zero is too large, the periodicity of the Fourier transform will induce non-physical oscillations in the quasi-PDFs, as shown in Fig. 7.1 for the unpolarized quasi-distributions at nucleon boost $P_3 = 10\pi/L \simeq 1.38$ GeV. In the left plot of Fig. 7.1 we compare the bare,
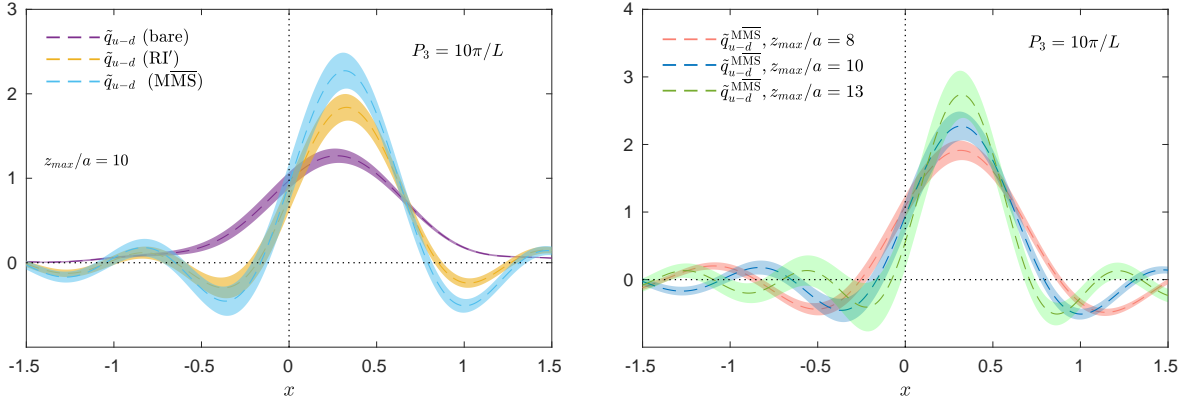
Figure 7.1 Left: Bare (violet), RI$'$ (yellow) and M$\overline{\text{MS}}$ (cyan) unpolarized quasi-PDFs. The RI$'$ scale is $a\mu_0 = 2\pi\left(\frac{6}{96} + \frac{1}{2\cdot96}, \frac{3}{48}, \frac{3}{48}, \frac{3}{48}\right)$. The Fourier transform is truncated at $z_{max}/a = 10$. Right: M$\overline{\text{MS}}$ unpolarized quasi-PDFs for $z_{max}/a = 8$ (red), $z_{max}/a = 10$ (cyan), $z_{max}/a = 13$ (green).

the RI$'$ and M$\overline{\text{MS}}$ quasi-PDFs (violet, orange and cyan bands respectively); the Fourier transform has been truncated at $z_{max}/a = 10$. As can be seen, oscillations manifest in the renormalized quantities and are more evident after conversion to the M$\overline{\text{MS}}$ scheme. This effect may originate from uncertainties related to the estimate of the renormalization functions and in particular from: **i)** lattice artifacts on the complex Z-factors; **ii)** truncation effect in the perturbative conversion between the intermediate RI$'$ scheme Z-factors and the M$\overline{\text{MS}}$ ones. In the right panel of Fig. 7.1, unpolarized quasi-distributions for three different cutoffs are compared. As we can see, the results are contaminated by a larger noise and stronger oscillations as z_{max}/a increases.

We remark that the selected values of z_{max}/a, for which results are presented in this Section, correspond to the smallest (largest) value of z/a where the real (imaginary) part of the renormalized matrix elements of each operator is compatible with zero (see Figs. 6.6, 6.7, 6.8).

After implementing the matching procedure of Eq. (7.3) with the kernel (7.4) and the nucleon mass corrections, we obtain the unpolarized quark distributions depicted in Fig. 7.2. First of all, we notice that the matching brings the support of the distributions into the range $x \in [-1, 1]$, where x represents the quark momentum fraction collinear to the moving hadron. At the level of quasi-PDF, x has no partonic interpretation. Moreover, due to the crossing relation $q(-x) = -\bar{q}(x)$ [174], the positive x-region in the Fig. 7.2 stands for the distribution

$u(x) - d(x)$, while the negative x-region can be interpreted as $\bar{d}(x) - \bar{u}(x)$. When comparing different values of the cutoff z_{max}/a, we can see that the matched PDFs are compatible with each other, but the statistical uncertainties are larger when choosing a larger cutoff.
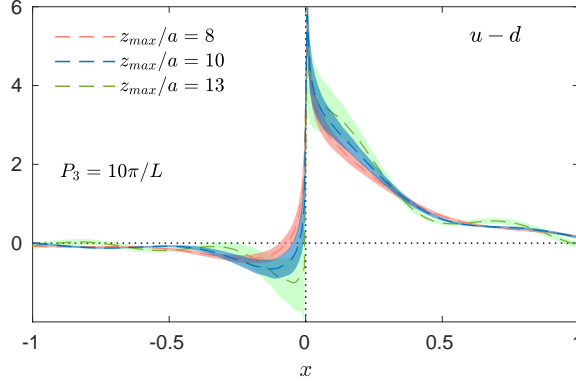
Figure 7.2 Matched unpolarized PDF in M$\overline{\text{MS}}$ scheme for different values of the cutoff in the Fourier transform: z_{max}/a (red), $z_{max}/a = 10$ (blue), $z_{max}/a = 13$ (green). The nucleon momentum is $P_3 = 10\pi/L \simeq 1.38$ GeV.

The analysis for the nucleon polarized distributions (helicity and transversity) leads to similar conclusions, shown in Fig. 7.3 for the matched PDFs. We notice that for the helicity (left plot) the crossing relation is $\Delta q(-x) = \Delta\bar{q}(x)$ [174], implying that we can extract $\Delta u(x) - \Delta d(x)$ for $x > 0$ and $\Delta\bar{u}(x) - \Delta\bar{d}(x)$ for $x < 0$. The transversity PDF (right plot in Fig. 7.3) shares the same crossing relation as the unpolarized distribution [174], and therefore the region $x > 0$ provides information about $\delta u(x) - \delta d(x)$, whereas $x < 0$ gives $\delta\bar{d}(x) - \delta\bar{u}(x)$. As can be seen in Fig. 7.3, for the selected values of z_{max}/a we do not observe a strong dependence on the cutoff, apart from increased statistical noise for larger values of z_{max}/a, as noticed before for the unpolarized case.
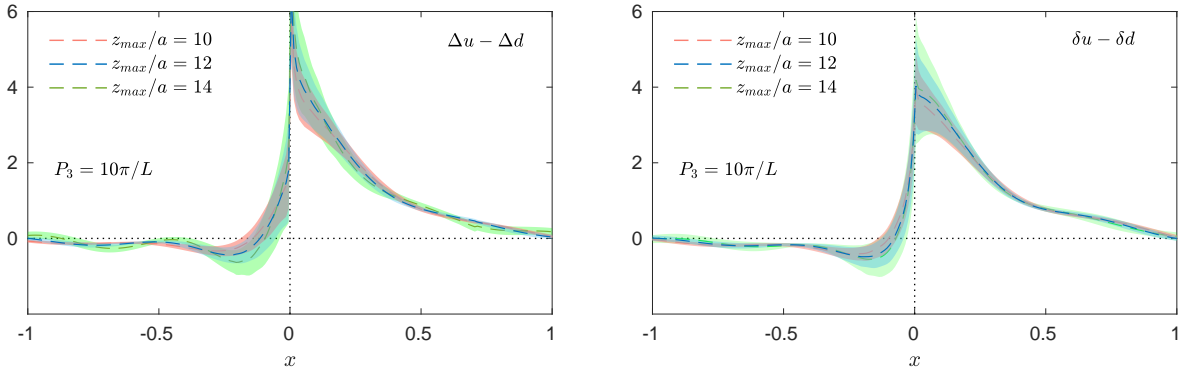
Figure 7.3 Matched helicity (left) and transversity (right) PDFs in the M$\overline{\text{MS}}$ scheme for cutoff values $z_{max}/a = 10$ (red), $z_{max}/a = 12$ (blue), $z_{max}/a = 14$ (green). The nucleon momentum is $P_3 = 10\pi/L \simeq 1.38$ GeV.

Therefore, to avoid a too large noise contamination that propagates through the Fourier transform and matching procedure to the final PDFs, we truncate the Fourier transform at some justified and middle values of z_{max}/a. We choose it to be: $z_{max}/a = \{10, 12, 12\}$ for unpolarized, helicity and transversity distributions respectively. We also keep the same cutoffs for the same distributions at smaller momenta.

At this point natural questions would be: Why does the periodicity of the Fourier transform cause oscillations at the level of quasi-PDFs, that propagate in a non-trivial way to the physical PDFs? What would be the natural solution to this problem? To understand the origin of this issue we decompose the Fourier transform in terms of cosine and sine functions as

$$\tilde{q}(x, P_3) \propto \sum_z \left(\cos(xzP_3)h_R(z, P_3) - \sin(xzP_3)h_I(z, P_3) \right) . \tag{7.8}$$

h_R, h_I are the real and imaginary parts of matrix elements and any numerical factors and dependence on the renormalization scale are neglected in the equation above, because irrelevant for the purpose of this discussion. As one can see, if the matrix elements do not decay to zero fast enough, the oscillations introduced by the cosine and sine functions lead to negative values for the quasi-PDFs, shown numerically in Fig. 7.1. Therefore, it is natural to expect that the oscillations become milder as the nucleon boost increases, as demonstrated for instance in Fig. 7.8. However, as argued in the recent work of Ref. [175], the problem of reconstructing a distribution from a limited data points is more general and mathematically ill-posed. Advanced reconstruction techniques applied to the lattice data might be necessary for solving this highly non-trivial aspect, that is among the sources of uncertainty of the whole quasi-PDF approach.

Another method to carry out the Fourier transform over the matrix elements was introduced in Ref. [176] and tested in this work. In this approach, one exploits the integration by part of the Fourier transform that yields the quasi-PDFs, namely

$$\tilde{q}(x, P_3) = h(z, P_3) \frac{e^{ixzP_3}}{2\pi ix} \Big|_{-z_{\max}}^{z_{\max}} - \int_{-z_{\max}}^{z_{\max}} \frac{dz}{2\pi} \frac{e^{ixzP_3}}{ix} \frac{\partial h(z)}{\partial z} , \tag{7.9}$$

and eventually one neglects the surface term. Thus, quasi-PDFs are computed through

$$\tilde{q}(x, P_3)_{deriv} = - \int_{-z_{\max}}^{z_{\max}} \frac{dz}{2\pi} \frac{e^{ixzP_3}}{ix} \frac{\partial h(z, P_3)}{\partial z} . \tag{7.10}$$

The comparison between the matched PDFs obtained by using this approach, that we refer to as "*derivative method*", and the previous one, that we call "*standard*", is shown in Fig. 7.4 for $P_3 = 10\pi/L$. Here we only show the unpolarized and helicity distributions at the highest momentum, but the same conclusions also hold for all the other cases that are not presented here. We notice that the matched PDFs are perfectly compatible in the intermediate and large x-region, but have a very different behavior for small values of x. The reason mostly relies on the presence of the factor $1/x$ in Eq. (7.10), that leads to uncontrolled effects for small values of x, where also the surface term has a large contribution but is being neglected. The additional discretization effects due to the use of a discretized form of $\partial h(x)\partial z$ lead us to employ the standard definition of quasi-PDFs and truncate the Fourier transform at some reasonable value of z_{max}/a, for which physical results are not altered.
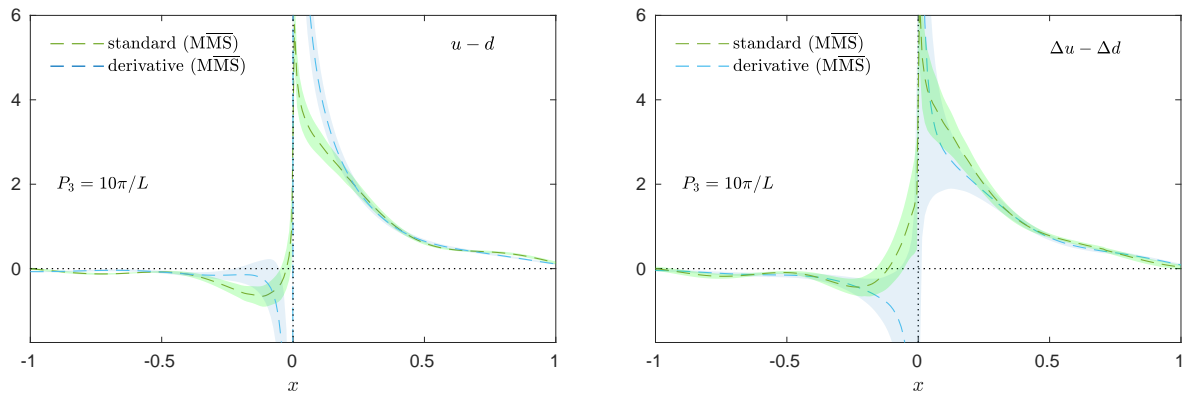
Figure 7.4 Comparison between two different approaches of performing the Fourier transform: standard (Eq. (7.2)-green band) and derivative (Eq. (7.10)-cyan band). Left: unpolarized PDF. Right: helicity PDF. The nucleon momentum is $P_3 = 10\pi/L \simeq 1.38$ GeV.

7.2   Dependence on the pion mass

Computing observables using ensembles simulated at the physical value of quark masses is crucial to make comparison with experiments. Lattice PDFs can be compared with results extracted from global QCD analyses. As stated in Chapter 2, global fits represent the traditional method to gain knowledge on quark distributions and rely on factorization of hard-scattering cross sections [22].

Here we investigate the pion mass dependence of quark distributions by comparing the results of this work, which uses a twisted mass $N_f = 2$ physical point ensemble, with the ones obtained in Ref. [39], where measurements are performed on a $N_f = 2 + 1 + 1$ twisted mass ensemble at $m_\pi \simeq 372$ MeV and volume $32^3 \times 64$ [177]. Fig. 7.5 shows the M$\overline{\text{MS}}$ renormalized unpolarized $u(x) - d(x)$ PDF at a value of the nucleon momentum which is very similar for both ensembles. The renormalization scale is $\bar{\mu} = 2$ GeV. We also include the phenomenological curve from NNLO analysis performed by the NNPDF collaboration [25]. As we can see, there is a clear pion mass dependence. This observation is compatible with the
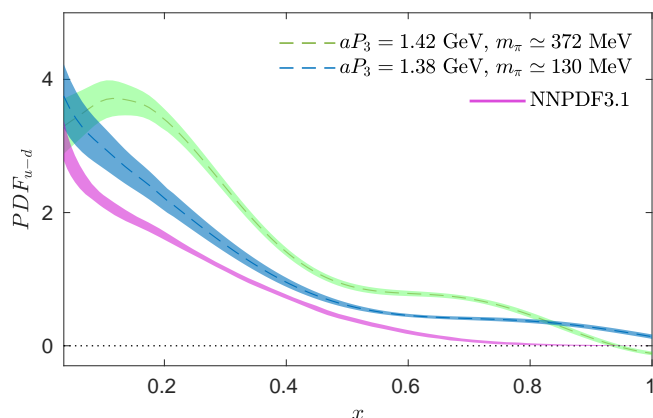
Figure 7.5 Unpolarized PDF using the ensemble of this work (blue) and a $N_f = 2 + 1 + 1$ ensemble at $m_\pi \simeq 372$ MeV (green). The nucleon momentum has a similar value for both PDFs. For comparison purpose we include phenomenological data from NNPDF3.1 analysis [25].

dependence observed for the momentum fraction in the nucleon $\langle x \rangle_{u-d}$, which in terms of

parton distribution functions is given by

$$\langle x \rangle_{u-d} = \int_0^1 dx \left\{ u(x) + \bar{u}(x) - d(x) - \bar{d}(x) \right\} , \qquad (7.11)$$

where $u(x)$, $\bar{u}(x)$, $d(x)$, $\bar{d}(x)$ stand for the unpolarized PDFs for the separate flavors of quarks and antiquarks. In Fig. 7.6 we show a selection of estimates for $\langle x \rangle_{u-d}$ as a function of the pion mass, obtained by different collaborations using different discretization schemes. The values
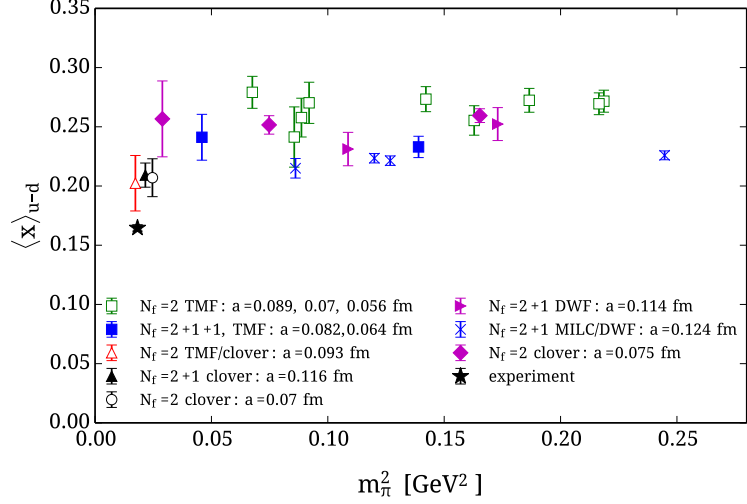
**Figure 7.6** Nucleon momentum fraction $\langle x \rangle_{u-d}$. Twisted mass fermion results are shown for $N_f = 2$ ensembles (open green squares), for two $N_f = 2 + 1 + 1$ ensembles (blue filled square) and for the $N_f = 2$ physical ensemble with a clover term (open red triangle), which is the one used in this work. Also shown are results from RBC-UKQCD using $N_f = 2 + 1$ DWF (magenta right pointing triangle) [178], from QCDSF/UKQCD using $N_f = 2$ clover fermions (filled magenta diamond) [179] and LHPC using DWF on $N_f = 2 + 1 + 1$ staggered sea (blue crosses) [133], $N_f = 2 + 1$ clover (filled black triangles) [180] and $N_f = 2$ clover [181]. All values are extracted using the plateau method and $t_s \sim (1 - 1.2)$ fm, except the result at the physical point extracted at $t_s \sim 1.3$ fm. The experimental value for $\langle x \rangle_{u-d}$ is taken from Ref [182]. The Figure is taken from Ref. [157].

in Fig. 7.6 are extracted from matrix elements involving the local operator $\mathcal{O} = \bar{\psi} \gamma^{\{\mu} D^{\nu\}} \tau_3 \psi$, where D^{ν} is the covariant derivative and $\{\ldots\}$ indicates index symmetrization. Lattice calculations show that the value of $\langle x \rangle_{u-d}$ is overestimated when simulations are performed at a pion mass larger than the physical one, and there is a clear decreasing trend going towards the physical point [157]. A smaller value for $\langle x \rangle_{u-d}$ corresponds to a shift of the quark distribution to smaller values of x, as indeed observed in Fig. 7.5 with our data.

7.3 Quark unpolarized distributions

In this Section we present our final results for the collinear unpolarized quark distributions corresponding to the flavor structure $u - d$. In Fig. 7.7 we show the quasi-PDFs, $\tilde{q}$, the matched PDFs, q, and the final PDFs that take into account the nucleon mass corrections (NMCs). These curves are depicted by green, orange and blue bands respectively. The nucleon boosts are: $P_3 = 6\pi/L \simeq 0.83$ GeV (top left), $P_3 = 8\pi/L \simeq 1.11$ GeV (top right) and $P_3 = 10\pi/L \simeq 1.38$ GeV (bottom). For the matching kernel we use Eq. (7.4), while for
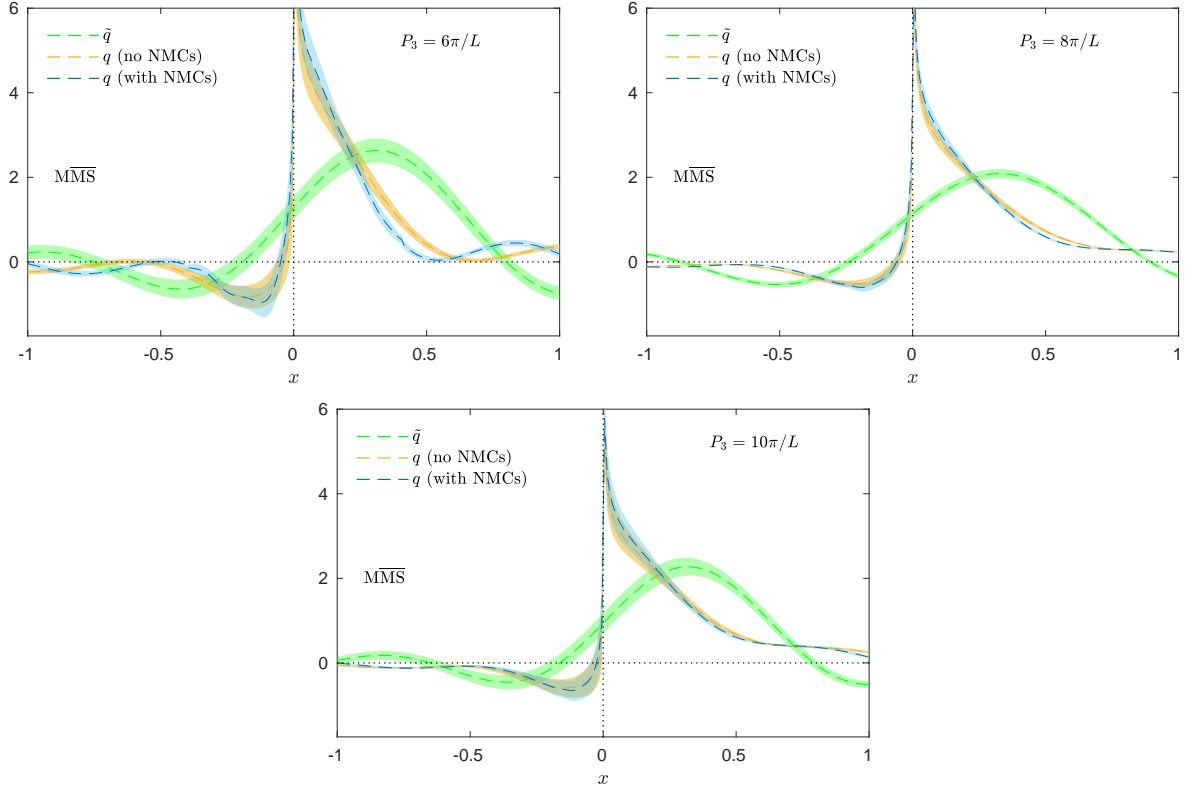
Figure 7.7 Unpolarized quasi-PDFs (green), matched PDFs (yellow) and final PDFs (blue) with NMCs included. The nucleon momentum is $P_3 = 6\pi/L \simeq 0.83$ GeV (top left), $P_3 = 8\pi/L \simeq 1.11$ GeV (top right) and $P_3 = 10\pi/L \simeq 1.38$ GeV (bottom).

the NMCs the expressions reported in Eq. (A.21). The latter are implemented up to m_N^4/P_3^4 order, since higher order corrections are found to be negligible. We remark that the errors are estimated using binning Jackknife procedure.

We note that the one-loop matching, connecting the quasi-PDFs $\tilde{q}$ to the light-cone PDFs, has a considerable effect. In fact, it alters completely the shape of the quasi-PDFs, giving to the distributions an asymmetric form with respect to $x \to -x$, regions that correspond to the momentum distribution $u(x) - d(x)$ and $\bar{d}(x) - \bar{u}(x)$ respectively. On the other hand, NMCs are found to be significantly smaller than the corrections from the matching. This is because the expansion parameter of the NMCs is $m_N^2/4P_3^2$ [38] and the NMCs are suppressed by powers of m_n^2/P_3^2, whereas the corrections from the matching are suppressed by $\mathcal{O}(\Lambda_{QCD}^2/P_3^2)$ terms. NMCs should be negligible in the limit of large momenta [46] and with our data we observe that already at $P_3 = 10\pi/L \simeq 1.38$ GeV they produce a very small effect.

In Fig. 7.8, we show how the physical PDFs (after matching procedure and NMCs) depend on the nucleon momentum. We observe a significant change of the PDF shape when increasing the momentum from $6\pi/L$ to $8\pi/L$, while the distributions for $8\pi/L$ and $10\pi/L$ are almost compatible over the whole x range, within the accuracy of our data. Moreover, the oscillatory behavior becomes milder as the momentum increases. As discussed in Section 7.1.1, unphysical oscillations result from the periodicity of the Fourier transform, which bounds the quasi-PDFs to be negative in certain x-regions.
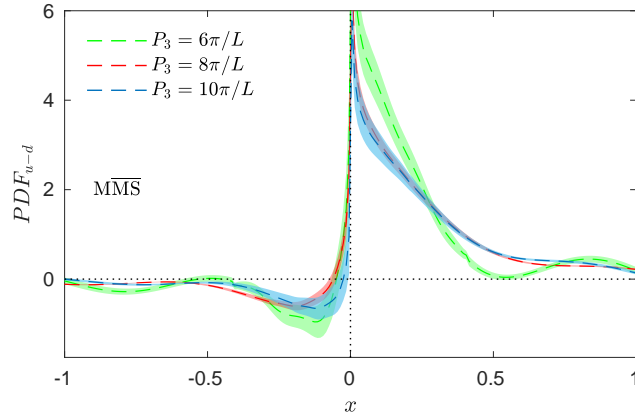
Figure 7.8 Momentum dependence for the unpolarized PDFs corresponding to the flavor structure $u - d$ (matching and NMCs are taken into account). The nucleon boosts are: $P_3 = 6\pi/L \simeq 0.83$ GeV (green), $P_3 = 8\pi/L \simeq 1.11$ GeV (red), $P_3 = 10\pi/L \simeq 1.38$ GeV (blue).

In Fig. 7.9 we compare the lattice distribution at the highest momentum with PDFs extracted from global fits to scattering data. In particular, for comparison purpose we consider PDFs from CJ15 [82], ABMP16 [28], NNPDF3.1 [25] sets. From Figs. 7.8 and 7.9 we observe
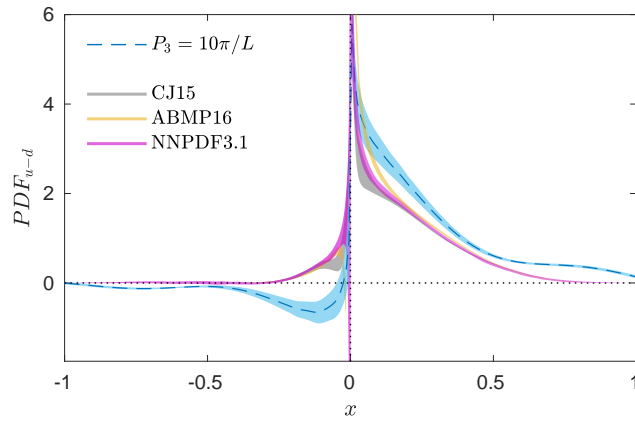
Figure 7.9 Final results for the isovector $u - d$ unpolarized PDF. The lattice data at nucleon boost $P_3 = 10\pi/L \simeq 1.38$ GeV are compared with phenomenological extracted PDFs from global analyses: CJ15 [82], ABMP16 [28], NNPDF3.1 [25].

that as the nucleon momentum increases the renormalized lattice PDFs move towards the phenomenological curves, as expected within the quasi-PDF approach. Achieving this result in lattice QCD is non-trivial, since on a Euclidean lattice we can only reconstruct PDFs from quark bilinear operators that are not on the light-cone, but separated by a space-like distance. We also note that the lattice PDF approaches zero in the large *x*-region. This is an expected result because in the infinite-momentum frame no constituents of the nucleon can carry more momentum of the nucleon as a whole. However, we can still notice small deviations from zero at $x = 1$ and a negative dip for $x \in [-0.4, 0]$, not observed in phenomenology. These effects may be due to a certain number of reasons and systematic effects that need to be addressed in the future. The first source of uncertainty is the value of the nucleon momentum, which might not be sufficiently large to make contact with light-cone PDFs. In fact, one can expect

a two-loop matching formula to have significant impact if the boost is not much larger than the nucleon mass.

7.4 Quark helicity distributions

Similarly to the computation of the unpolarized distribution we can obtain the helicity distribution, whose zeroth moment represents the number of quarks with helicity parallel and antiparallel to that of a longitudinally polarized nucleon.

At each nucleon boost we compute the quasi-PDFs by taking the Fourier transform of the renormalized matrix elements, as in Eq. (7.1), and we follow the procedure described in Section 7.1.1. The matching procedure is implemented by using the kernel of Eq. (7.4). As for the unpolarized case, the renormalization scale is $\bar{\mu} = 2$ GeV in the M$\overline{\text{MS}}$ scheme.

To account for a non-negligible nucleon mass as compared to the nucleon momenta, we apply the NMCs on the matched distributions. Since some small effect is visible when adding further corrections in m_n/P_3, we implement the NMCs up to $\mathcal{O}\left((m_N^2/P_3^2)^2\right)$ following the prescription of Ref. [38]. The expressions are in this case slightly more involved than for the unpolarized case, as they contain double integrals of the matched distributions, see Eq. (A.23).

The helicity quasi-distributions, $\Delta\tilde{q}$, are shown in Fig. 7.10 together with the matched distributions, Δq, with and without NMCs. As observed for the unpolarized PDF in the
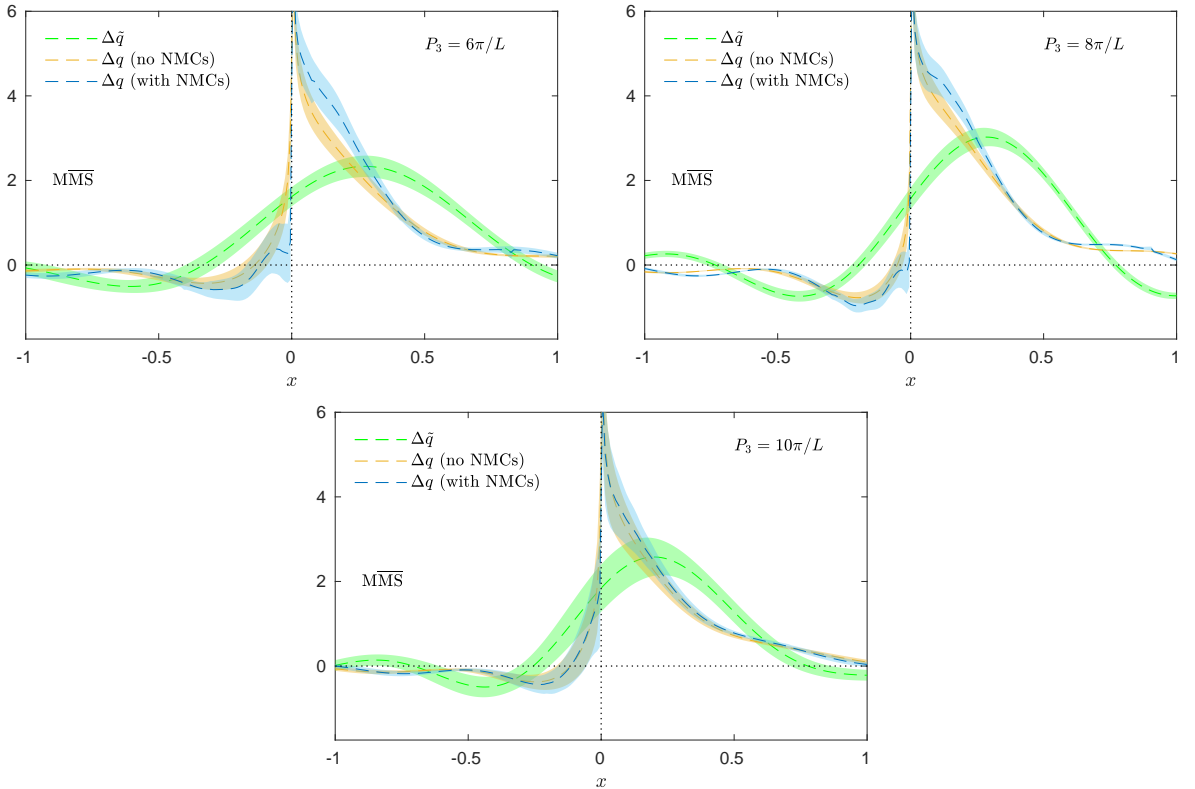

Figure 7.10 Helicity quasi-PDFs (green), matched PDFs (orange) and final PDFs (blue) with NMCs included. The nucleon momentum is $P_3 = 6\pi/L \simeq 0.83$ GeV (top left), $P_3 = 8\pi/L \simeq 1.11$ GeV (top right) and $P_3 = 10\pi/L \simeq 1.38$ GeV (bottom).

previous Section, the matching procedure modifies drastically the shape of the quasi-PDFs

moving the peak of the distributions around $x \approx 0$. The NMCs are not negligible for boosts $P_3 = 6\pi/L$ and $P_3 = 8\pi/L$ but they have a small effect at the highest momentum, as expected from the study of nucleon mass corrections in Ref. [46]. Collecting the results we can investigate the momentum dependence of the renormalized lattice PDFs, shown in Fig. 7.11. We observe that increasing the momentum from $6\pi/L$ to $8\pi/L$ has a very small effect and the
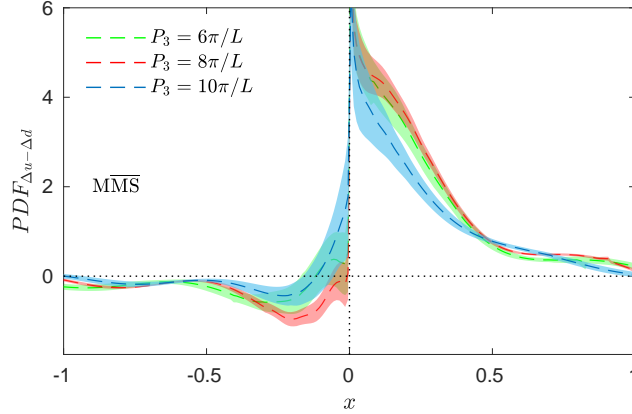
Figure 7.11 Momentum dependence of the quark helicity distributions for the flavor structure $u - d$. The nucleon boosts are: $P_3 = 6\pi/L \simeq 0.83$ GeV (green), $P_3 = 8\pi/L \simeq 1.11$ GeV (red), $P_3 = 10\pi/L \simeq 1.38$ GeV (blue). The renormalization scale is 2 GeV.

way the distributions are shifted towards small values of x seems to be non-monotonic, in both quark and antiquark sector. The appearance of a possible non-monotonic behavior was studied in Ref. [45] using models for quasi-distributions; in our work it can be a consequence of various systematics, among which truncation effects in the matching procedure, that may play an important role for momenta not much larger than the nucleon mass. Again, as observed previously for the unpolarized distributions, the oscillatory behavior is more pronounced in the antiquark sector ($x < 0$) and becomes less prominent as the nucleon momentum increases from $P_3 = 8\pi/L$ to $P_3 = 10\pi/L$.

In Fig. 7.12, our final result for the helicity distribution at the highest momentum is compared to three selected PDFs from global fits: NNPDF1.1pol [88], DDSV08 [183] and JAM17 [90]. A significant overlap is obtained with the phenomenological data for $0 \lesssim x \lesssim 0.4$ and for very small negative values of x, corresponding to $\Delta\bar{u} - \Delta\bar{d}$ distribution. In the large x-region ($0.5 < x < 1$) the slope of the lattice curve changes, possibly due to the oscillations mentioned above. The observed overlap for some regions of the quark momentum fraction seems to suggest a faster convergence of the quasi-PDF to the physical PDFs for the helicity case, but on the other hand it can also be the result of different systematic effects, with some of them possibly canceling out. However, from the momentum dependence shown in Fig. 7.11, one can expect a better agreement with phenomenological analyses as the nucleon momentum increases. The minimum value of the boost needed for this kind of calculations is not known and can be a few GeV [45]. Because of the oscillatory behavior for negative x values, at present we cannot address the question whether an asymmetry in the light sea-quark polarizations emerge from our calculations. Very recent results from global QCD analyses [184] seem to suggest a sizable difference between $\bar{u}$ and $\bar{d}$ quark helicity
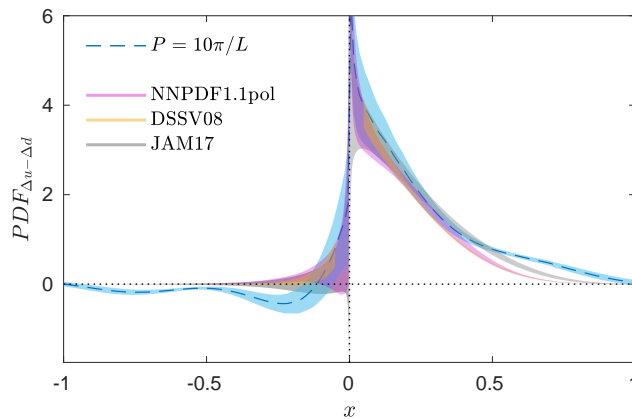
Figure 7.12 Final result for the isovector $u - d$ helicity distribution. The lattice data at $P_3 = 10\pi/L \simeq$ 1.38 are compared to the phenomenological PDFs: NNPDF1.1pol [88], DDSV08 [183], JAM17 [90].

distributions, with the consequence that the flavor asymmetry in the polarized quark sea might not be so small as previously thought.

7.5 Quark transversity distributions

In this Section we present the final results for the quark transversity distribution, often indicated with $h_1(x)$ or $\delta q(x)$. Transversity PDF gives information about the momentum decomposition of quarks with helicity aligned and anti-aligned to that of a transversely polarized hadron. As discussed in Chapter 2, it is the least known PDF among the three distributions studied, because it is chiral-odd, and totally inclusive processes cannot be used. Therefore, lattice QCD could be a powerful approach to complement our knowledge to what is already known from analysis of scattering data, mostly coming from e^+e^- annihilation into hadron pairs [96, 185, 186] and SIDIS data for single hadron production [187–189].

The general procedure to obtain the transversity PDFs proceeds along the lines of the unpolarized and helicity distributions. The difference relies on the use of a tensor structure σ_{3j} in the lattice matrix elements (where j-index is purely spatial), yielding different matching formulae. The effect of the matching and nucleon mass corrections on the quasi-PDFs, $\delta\tilde{q}$, is shown in Fig. 7.13 for all values of the momenta used in this work. Again, we start with the renormalized quasi-PDFs ($\delta\tilde{q}$), apply the matching given in Eq.(7.5) and finally include the NMCs [38], which lead to the final estimate of the distribution. The expressions of the NMCs are reported in Eq. (A.22). As can be seen, the application of the matching shifts the peak of the quasi-PDFs towards $x \approx 0$ and increases it, as expected. On the other hand, the NMCs affect mostly the positive x-region and become smaller as the value of the boost increases. Thus, we expect that the larger source of systematic effects comes from the matching procedure that, as highlighted previously, has been worked out to one-loop order in perturbation theory.

In Fig. 7.14 the dependence on the nucleon momentum of the final distributions is shown in the $\overline{\text{MMS}}$ scheme and at the scale of $\sqrt{2}$ GeV. For the nucleon boosts employed we notice that the momentum dependence is milder than for the unpolarized and helicity PDFs (see
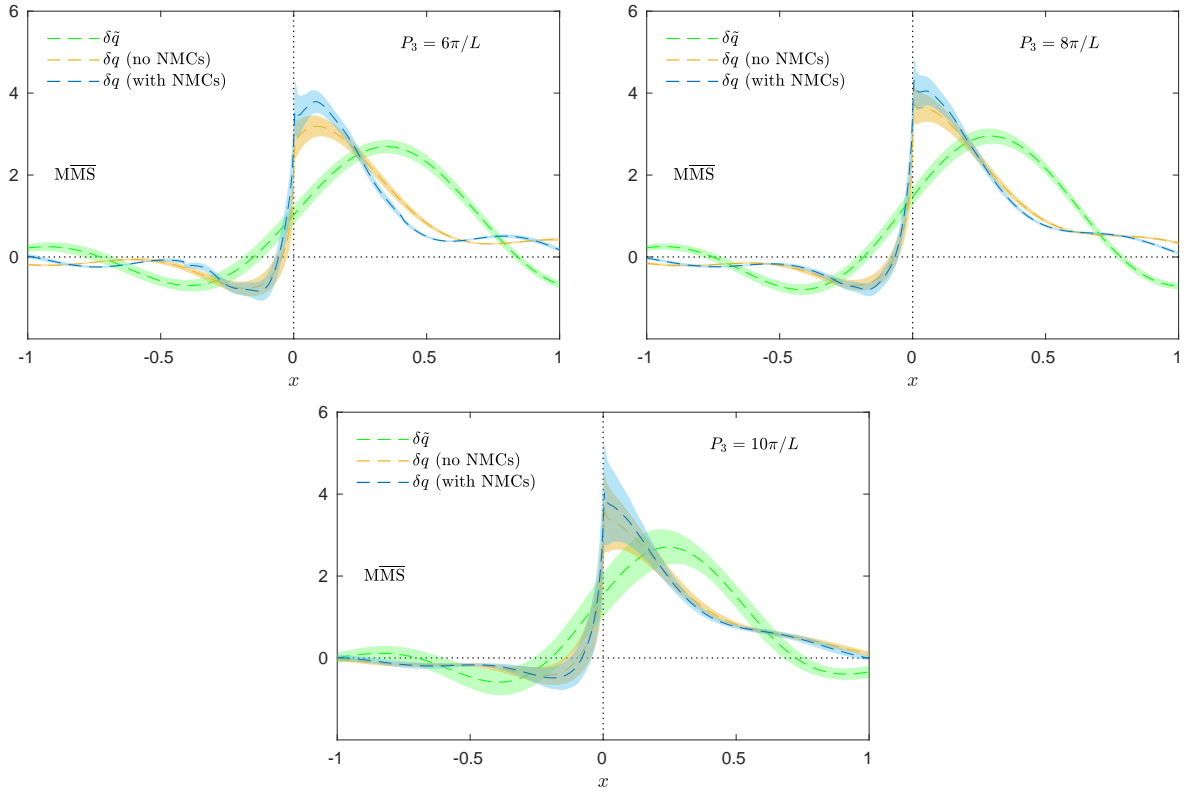
Figure 7.13 Transversity quasi-PDFs (green), matched PDFs (orange) and final PDFs (blue) with NMCs included. The nucleon momenta are: $P_3 = 6\pi/L \simeq 0.83$ GeV (top left), $P_3 = 8\pi/L \simeq 1.11$ GeV (top right) and $P_3 = 10\pi/L \simeq 1.38$ GeV (bottom). The renormalization scale is set to $\bar{\mu} = \sqrt{2}$ GeV in the M$\overline{\text{MS}}$ scheme.
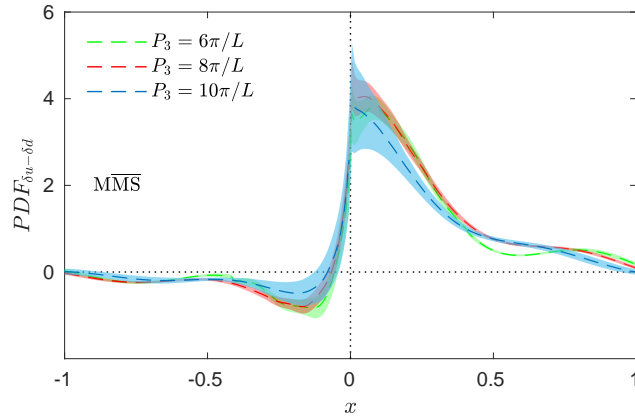
Figure 7.14 Momentum dependence of the lattice transversity PDFs for the flavor structure $u - d$. The nucleon boosts are: $P_3 = 6\pi/L \simeq 0.83$ GeV (green), $P_3 = 8\pi/L \simeq 1.11$ GeV (red) and $P_3 = 10\pi/L \simeq 1.38$ GeV (blue). The M$\overline{\text{MS}}$ renormalization scale is set to $\bar{\mu} = \sqrt{2}$ GeV.

Fig. 7.8 and Fig. 7.11 for comparison). The results using momentum $6\pi/L$ and $8\pi/L$ are indeed compatible over a wide range of x values, within statistical uncertainties. At the highest momentum the oscillatory behavior seems to be slightly milder, especially for $x < 0$. Reducing systematic effects can also help in this direction and must be strongly addressed in the future. We remark that, apart from finite volume and lattice discretization effects that can only be investigated performing simulations at different physical volumes and lattice spacings, improvements on a given gauge ensemble may come from: **i)** application of a

two-loop formula matching quasi- to physical PDFs, as mentioned previously; **ii**) improved estimates of the renormalization functions. As seen in Section 7.1.1, the renormalized RI$'$ quasi-PDFs has indeed reduced unphysical oscillations than the M$\overline{\text{MS}}$ counterpart, implying the presence of truncation effects on the perturbative conversion from RI$'$ scheme to M$\overline{\text{MS}}$ at the chosen reference scale.

In Fig. 7.15 we present our final result for the transversity PDF at the highest momentum, $P_3 = 10\pi/L$. We include two phenomenological determinations: one obtained from fits to only SIDIS data [97] and another one in which the tensor charge, computed in lattice QCD, is used as an additional constrain in the phenomenological analysis [97]. In Fig. 7.15 we refer to the latter as "SIDIS+$g_T^{lattice}$". Here g_T has to be intended as the zeroth moment of $\delta u(x) - \delta d(x)$. As can be seen, our result for the transversity PDF is in agreement with both phenomenological
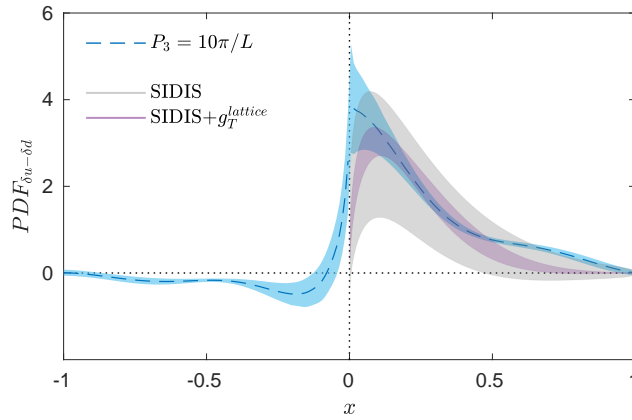
Figure 7.15 Final result for the isovector $u - d$ transversity distribution. The lattice data at $P_3 = 10\pi/L \simeq 1.38$ GeV (blue) are compared with phenomenological fits obtained using SIDIS data (grey) [97] and SIDIS data constrained using the tensor charge g_T computed within lattice QCD (violet) [97].

data for $x \lesssim 0.4 - 0.5$. An interesting feature is that the statistical errors of our results are strikingly smaller than the ones from phenomenological fits to the SIDIS data, underlining how the extraction of the transversity distribution is difficult from experiments. Moreover, the lattice distribution is significantly narrower, like the phenomenological determination that uses g_T as input.

A valuable check of our calculation is given by the value extracted for the tensor charge g_T^{u-d}. At the highest momentum, $P_3 = 10\pi/L$, we find $g_T^{u-d} = 1.07(10)$ from the value of the local matrix element with inserted current $\bar{\psi}\sigma_{3j}\psi$ and $g_T^{u-d} = 1.09(11)$ by integrating the distribution over x within the interval $[-1, 1]$. Both results are also compatible with the value of the tensor charge computed at zero nucleon momentum in Ref. [164] on the same physical point ensemble as the one used in this work. The observed agreement on the value of g_T^{u-d} obtained from two different approaches (via local matrix element and through integration) is non-trivial, because the steps leading to both values are different and involve different systematic effects.

Moreover, we note that in the antiquark sector ($x < 0$) no SIDIS data are available, whereas lattice QCD can potentially extract the sea quark distribution $\delta\bar{d} - \delta\bar{u}$ without any additional

difficulty. This is another element that favors the direct extraction of the transversity PDF from lattice QCD.

Chapter 8

Conclusions and Outlook

In this work we have presented state-of-the-art lattice calculations of the helicity-dependent and helicity-independent collinear parton distribution functions (PDFs) of the nucleon. The lattice QCD computation is performed on a twisted mass ensemble of two light degenerate quarks ($N_f = 2$) with masses tuned to their physical value.

Direct extractions of distribution functions require light-cone dynamics, which cannot be achieved within the Euclidean lattice QCD formulation. Such a computation was thought impossible a few years ago. The method proposed by X.Ji in 2013, known as *quasi-PDF approach*, has enabled such investigations, which proceed through extractions of quasi-distributions of non-local matrix elements between two nucleon states at finite momentum. The contact with light-cone PDFs is established through a perturbative matching procedure and nucleon mass corrections.

We have computed three collinear distributions: the *spin-averaged* (also called unpolarized), *helicity* and *transversity* distributions. The unpolarized PDFs give information about the momentum decomposition of quarks independently of their polarization, whilst the helicity and transversity PDFs describe the momentum decomposition of quarks with helicity aligned and anti-aligned to that of a longitudinally and transversely polarized nucleon. To simplify the lattice calculation, we have considered the isovector flavor structure $u - d$, as it receives contributions only by connected diagrams (up to cutoff effects). In this context, two- and three-point functions have been computed by boosting the nucleon with momentum 0.83 GeV, 1.11 GeV and 1.38 GeV, taken along spatial directions of the lattice. The all-to-all propagators are evaluated using sequential inversions through the sink. In total four source-sink time separations are tested to isolate the required ground state matrix element. Separate quark propagators are required for each momentum boost, source-sink time separation value and each kind of momentum distribution, since different parity projectors enter the construction of the nucleon sequential source. To improve the signal-to-noise ratio, we have implemented the momentum smearing method and optimized the smearing parameter for each value of the boost employed. For the three distributions studied in this work, we found that the ground state dominance is achieved only at our largest source-sink time separation, namely at $t_s = 12a \simeq 1.13$ fm. We check that a *two-state fit* analysis is in agreement with the *plateau* method at this value of

the source-sink time separation. Exploring larger t_s values is prohibitively costly, requiring computational resources that go beyond what is currently available to us.

The matrix elements are renormalized using a non-perturbative approach, which is a generalization of the RI$'$-scheme. This step has required the computation of appropriate vertex functions with the same divergences of the operators in the matrix elements. The renormalization functions are computed at different RI$'$ scales using three $N_f = 2$ twisted mass ensembles at different pion masses, that allow us to chirally extrapolate the results and eliminate the residual dependence on the pion mass. The final values are obtained after conversion and evolution to a *modified* $\overline{\text{MS}}$ scheme at the appropriate scale in which phenomenological distributions are presented. A fitting procedure is also applied to eliminate the residual dependence of the renormalization functions on the initial RI$'$ scale. Moreover, we have also applied three-dimensional stout smearing to the gauge links of the vertex functions and matrix elements of quasi-distributions, and studied the effect of the smearing on the renormalized matrix elements. We have found that, after renormalization, matrix elements with and without smearing are in agreement with each other, and the smeared matrix elements are affected by a reduced statistical noise. This is due to the fact that link-smearing brings the renormalization functions closer to their tree-level values, reducing the power divergences that are typical of operators with an extended Wilson line. Ultimately, we have used a maximal number of five smearing steps, to keep the iterations as fewer as possible.

The matching procedure on the quasi-distributions is carried out to one-loop order in perturbation theory and is followed by the nucleon mass corrections. As the momentum increases we have observed that the lattice distributions approach the phenomenological results, as shown in Figs. 7.8, 7.11 and 7.14. This is expected within the quasi-PDF approach, according to which light-cone distributions can be reconstructed in the limit of very large nucleon momenta. Our results at the largest boost show a similar behavior as the one of phenomenological distributions. As concerns the unpolarized PDF shown in Fig. 7.9, a complete agreement with the physical PDFs has not been reached yet, but the slope of the distribution is very similar to the one of global analyses. Unlike the unpolarized PDF, for the helicity case we have obtained a significant overlap with phenomenological analyses in the Bjorken region $0 \lesssim x \lesssim 0.5$ and at low negative x values, as can be seen in Fig. 7.12. Finally, the lattice determination of the nucleon transversity distribution is in agreement with the one obtained from semi-inclusive scattering processes (SIDIS) in the positive x-range, region for which SIDIS data currently allow a reconstruction of this distribution. As can be seen from Fig. 7.15, the lattice results have also strikingly smaller statistical errors than the ones extracted from SIDIS data only. This comparison favors the direct extraction of the transversity PDF using the quasi-PDF method, in terms of reliability and uncertainty.

The antiquark counterparts of the unpolarized, helicity and transversity PDFs (which can be read from the negative x values of the corresponding figures) are affected by oscillations that are not observed in the phenomenological analyses. Therefore, it is not possible to make any conclusive statement about asymmetries in the antiquark sector.

The great progress recently achieved in the *ab initio* calculation of PDFs is paving the way for further improvements. First of all, we note that the value of the pion mass is not

among the systematic uncertainties of the present calculation, since our extraction has been already carried out at the physical value of the quark masses and chiral extrapolation is not needed. Among systematics uncertainties are discretization effects and finite volume effects, which can be addressed and eliminated by computing distribution functions on additional gauge ensembles. Apart from the aforementioned systematics, there are also additional ones that are specific to the quasi-PDF approach. They include the unphysical oscillations of the distributions, that are due to the periodicity of the Fourier transform, and systematics related to the truncation of the conversion factor and the matching formula to one-loop level. In particular, having a matching formula to two-loops may lead to better convergence to light-cone PDFs at smaller nucleon momenta. On the other hand, new computer architectures can lead to the extraction of reliable estimates for PDFs using higher nucleon boosts, that would presently require huge computational resources to eliminate excited states contamination. Development of new techniques to tackle the exponential increase of the statistical noise with respect to the source-sink time separation and higher momenta will also be crucial for quasi-PDF calculations.

Despite these uncertainties, this work demonstrates the tremendous progress achieved in the last 3 years in the determination of parton distribution functions from first principles. The theoretical and technical aspects are now well understood and addressing the systematic uncertainties is the next step. A follow up of this research is the ongoing computation of the isovector $u - d$ nucleon PDFs on a twisted mass $N_f = 2 + 1 + 1$ ensemble, which includes a strange and charm quark in the sea, whose masses are tuned to their physical value. Another natural extension of this work is the extraction of distribution functions of the gluon and of the separate quark flavors, which necessarily require computations of disconnected diagrams. Other interesting directions would be the calculation of generalized parton distribution functions (GPDs) and transverse momentum-dependent parton distribution functions (TMDs).

Bibliography

[1] M. Gell-Mann, *A Schematic Model of Baryons and Mesons*, *Phys. Lett.* **8** (1964) 214.

[2] G. Zweig, *An SU(3) model for strong interaction symmetry and its breaking. Version 2*, in *DEVELOPMENTS IN THE QUARK THEORY OF HADRONS. VOL. 1. 1964 - 1978* (D. Lichtenberg and S. P. Rosen, eds.), pp. 22–101. 1964.

[3] M. Breidenbach, J. I. Friedman, H. W. Kendall, E. D. Bloom, D. H. Coward, H. C. DeStaebler et al., *Observed Behavior of Highly Inelastic electron-Proton Scattering*, *Phys. Rev. Lett.* **23** (1969) 935.

[4] E. D. Bloom et al., *High-Energy Inelastic e p Scattering at 6-Degrees and 10-Degrees*, *Phys. Rev. Lett.* **23** (1969) 930.

[5] J. D. Bjorken and E. A. Paschos, *Inelastic Electron Proton and gamma Proton Scattering, and the Structure of the Nucleon*, *Phys. Rev.* **185** (1969) 1975.

[6] R. P. Feynman, *Very high-energy collisions of hadrons*, *Phys. Rev. Lett.* **23** (1969) 1415.

[7] G. 't Hooft, *Renormalization of Massless Yang-Mills Fields*, *Nucl. Phys.* **B33** (1971) 173.

[8] D. J. Gross and F. Wilczek, *Ultraviolet Behavior of Nonabelian Gauge Theories*, *Phys. Rev. Lett.* **30** (1973) 1343.

[9] H. D. Politzer, *Reliable Perturbative Results for Strong Interactions?*, *Phys. Rev. Lett.* **30** (1973) 1346.

[10] H. Fritzsch, M. Gell-Mann and H. Leutwyler, *Advantages of the Color Octet Gluon Picture*, *Phys. Lett.* **47B** (1973) 365.

[11] PARTICLE DATA GROUP collaboration, M. Tanabashi et al., *Review of Particle Physics*, *Phys. Rev.* **D98** (2018) 030001.

[12] S. Aoki et al., *Review of lattice results concerning low-energy particle physics*, *Eur. Phys. J.* **C77** (2017) 112 [1607.00299].

[13] K. G. Wilson, *Confinement of Quarks*, *Phys. Rev.* **D10** (1974) 2445.

[14] X.-D. Ji, *Gauge-Invariant Decomposition of Nucleon Spin*, *Phys. Rev. Lett.* **78** (1997) 610 [hep-ph/9603249].

[15] A. V. Radyushkin, *Scaling limit of deeply virtual Compton scattering*, *Phys. Lett.* **B380** (1996) 417 [hep-ph/9604317].

[16] M. Diehl, *Generalized parton distributions*, *Phys. Rept.* **388** (2003) 41 [hep-ph/0307382].

[17] X. Ji, *Generalized parton distributions*, *Ann. Rev. Nucl. Part. Sci.* **54** (2004) 413.

[18] J. C. Collins and D. E. Soper, *Back-To-Back Jets in QCD*, *Nucl. Phys.* **B193** (1981) 381.

[19] J. C. Collins and D. E. Soper, *Parton Distribution and Decay Functions*, *Nucl. Phys.* **B194** (1982) 445.

[20] A. Accardi et al., *Electron Ion Collider: The Next QCD Frontier*, *Eur. Phys. J.* **A52** (2016) 268 [1212.1701].

[21] R. Angeles-Martinez et al., *Transverse Momentum Dependent (TMD) parton distribution functions: status and prospects*, *Acta Phys. Polon.* **B46** (2015) 2501 [1507.05267].

[22] H.-W. Lin et al., *Parton distributions and lattice QCD calculations: a community white paper*, *Prog. Part. Nucl. Phys.* **100** (2018) 107 [1711.07916].

[23] J. Gao, L. Harland-Lang and J. Rojo, *The Structure of the Proton in the LHC Precision Era*, *Phys. Rept.* **742** (2018) 1 [1709.04922].

[24] P. Jimenez-Delgado, W. Melnitchouk and J. F. Owens, *Parton momentum and helicity distributions in the nucleon*, *J. Phys.* **G40** (2013) 093102 [1306.6515].

[25] NNPDF collaboration, R. D. Ball et al., *Parton distributions from high-precision collider data*, *Eur. Phys. J.* **C77** (2017) 663 [1706.00428].

[26] L. A. Harland-Lang, A. D. Martin, P. Motylinski and R. S. Thorne, *Parton distributions in the LHC era: MMHT 2014 PDFs*, *Eur. Phys. J.* **C75** (2015) 204 [1412.3989].

[27] S. Dulat, T.-J. Hou, J. Gao, M. Guzzi, J. Huston, P. Nadolsky et al., *New parton distribution functions from a global analysis of quantum chromodynamics*, *Phys. Rev.* **D93** (2016) 033006 [1506.07443].

[28] S. Alekhin, J. Blümlein, S. Moch and R. Placakyte, *Parton distribution functions, α_s, and heavy-quark masses for LHC Run II*, *Phys. Rev.* **D96** (2017) 014011 [1701.05838].

[29] M. Constantinou, *Hadron Structure*, *PoS* **LATTICE2014** (2015) 001 [1411.0078].

[30] M. Constantinou, *Recent progress in hadron structure from Lattice QCD*, *PoS* **CD15** (2015) 009 [1511.00214].

[31] C. Alexandrou and K. Jansen, *Hadron structure from lattice QCD*, *Nucl. Part. Phys. Proc.* **261-262** (2015) 202.

[32] S. Syritsyn, *Review of Hadron Structure Calculations on a Lattice*, *PoS* **LATTICE2013** (2014) 009 [1403.4686].

[33] X. Ji, *Parton Physics on a Euclidean Lattice*, *Phys. Rev. Lett.* **110** (2013) 262002 [1305.1539].

[34] X. Ji, *Parton Physics from Large-Momentum Effective Field Theory*, *Sci. China Phys. Mech. Astron.* **57** (2014) 1407 [1404.6680].

[35] H.-W. Lin, J.-W. Chen, S. D. Cohen and X. Ji, *Flavor Structure of the Nucleon Sea from Lattice QCD*, *Phys. Rev.* **D91** (2015) 054510 [1402.1462].

[36] C. Alexandrou, K. Cichy, V. Drach, E. Garcia-Ramos, K. Hadjiyiannakou, K. Jansen et al., *First results with twisted mass fermions towards the computation of parton distribution functions on the lattice*, *PoS* **LATTICE2014** (2014) 135 [1411.0891].

[37] C. Alexandrou, K. Cichy, V. Drach, E. Garcia-Ramos, K. Hadjiyiannakou, K. Jansen et al., *Lattice calculation of parton distributions*, *Phys. Rev.* **D92** (2015) 014502 [1504.07455].

[38] J.-W. Chen, S. D. Cohen, X. Ji, H.-W. Lin and J.-H. Zhang, *Nucleon Helicity and Transversity Parton Distributions from Lattice QCD*, *Nucl. Phys.* **B911** (2016) 246 [1603.06664].

[39] C. Alexandrou, K. Cichy, M. Constantinou, K. Hadjiyiannakou, K. Jansen, F. Steffens et al., *Updated Lattice Results for Parton Distributions*, *Phys. Rev.* **D96** (2017) 014513 [1610.03689].

[40] K.-F. Liu and S.-J. Dong, *Origin of difference between anti-d and anti-u partons in the nucleon*, *Phys. Rev. Lett.* **72** (1994) 1790 [hep-ph/9306299].

[41] K. F. Liu, S. J. Dong, T. Draper, D. Leinweber, J. H. Sloan, W. Wilcox et al., *Valence QCD: Connecting QCD to the quark model*, *Phys. Rev.* **D59** (1999) 112001 [hep-ph/9806491].

[42] K.-F. Liu, *Parton degrees of freedom from the path integral formalism*, *Phys. Rev.* **D62** (2000) 074501 [hep-ph/9910306].

[43] Y.-Q. Ma and J.-W. Qiu, *Extracting Parton Distribution Functions from Lattice QCD Calculations*, *Phys. Rev.* **D98** (2018) 074021 [1404.6860].

[44] Y.-Q. Ma and J.-W. Qiu, *Exploring Partonic Structure of Hadrons Using ab initio Lattice QCD Calculations*, *Phys. Rev. Lett.* **120** (2018) 022003 [1709.03018].

[45] A. Radyushkin, *Nonperturbative Evolution of Parton Quasi-Distributions*, *Phys. Lett.* **B767** (2017) 314 [1612.05170].

[46] A. Radyushkin, *Target Mass Effects in Parton Quasi-Distributions*, *Phys. Lett.* **B770** (2017) 514 [1702.01726].

[47] A. V. Radyushkin, *Quasi-parton distribution functions, momentum distributions, and pseudo-parton distribution functions*, *Phys. Rev.* **D96** (2017) 034025 [1705.01488].

[48] A. V. Radyushkin, *Quark pseudodistributions at short distances*, *Phys. Lett.* **B781** (2018) 433 [1710.08813].

[49] J. Karpie, K. Orginos and S. Zafeiropoulos, *Moments of Ioffe time parton distribution functions from non-local matrix elements*, *JHEP* **11** (2018) 178 [1807.10933].

[50] J. Karpie, K. Orginos, A. Radyushkin and S. Zafeiropoulos, *Parton distribution functions on the lattice and in the continuum*, *EPJ Web Conf.* **175** (2018) 06032 [1710.08288].

[51] K. Orginos, A. Radyushkin, J. Karpie and S. Zafeiropoulos, *Lattice QCD exploration of parton pseudo-distribution functions*, *Phys. Rev.* **D96** (2017) 094503 [1706.05373].

[52] A. Radyushkin, *One-loop evolution of parton pseudo-distribution functions on the lattice*, *Phys. Rev.* **D98** (2018) 014019 [1801.02427].

[53] C. Monahan, *Recent Developments in x-dependent Structure Calculations*, *PoS* **LATTICE2018** (2018) 018 [1811.00678].

[54] K. Cichy and M. Constantinou, *A guide to light-cone PDFs from Lattice QCD: an overview of approaches, techniques and results*, 1811.07248.

[55] M. Constantinou and H. Panagopoulos, *Perturbative renormalization of quasi-parton distribution functions*, *Phys. Rev.* **D96** (2017) 054506 [1705.11193].

[56] C. Alexandrou, K. Cichy, M. Constantinou, K. Hadjiyiannakou, K. Jansen, H. Panagopoulos et al., *A complete non-perturbative renormalization prescription for quasi-PDFs*, *Nucl. Phys.* **B923** (2017) 394 [1706.00265].

[57] C. Alexandrou, K. Cichy, M. Constantinou, K. Jansen, A. Scapellato and F. Steffens, *Light-Cone Parton Distribution Functions from Lattice QCD*, *Phys. Rev. Lett.* **121** (2018) 112001 [1803.02685].

[58] C. Alexandrou, K. Cichy, M. Constantinou, K. Jansen, A. Scapellato and F. Steffens, *Transversity parton distribution functions from lattice QCD*, *Phys. Rev.* **D98** (2018) 091503 [1807.00232].

[59] C. Alexandrou, K. Cichy, M. Constantinou, K. Hadjiyiannakou, K. Jansen, A. Scapellato et al., *Systematic uncertainties in parton distribution functions from lattice QCD simulations at the physical point*, *Phys. Rev.* **D99** (2019) 114504 [1902.00587].

[60] M. E. Peskin and D. V. Schroeder, *An Introduction To Quantum Field Theory*. Addison-Wesley Publishing Company, 1995.

[61] M. D. Schwartz, *Quantum Field Theory and the Standard Model*. Cambridge University Press, 2013.

[62] M. N. Rosenbluth, *High Energy Elastic Scattering of Electrons on Protons*, *Phys. Rev.* **79** (1950) 615.

[63] E. Leader and E. Predazzi, *An Introduction to Gauge Theories and Modern Particle Physics*. Cambridge University Press, 1996.

[64] M. Born, *Quantenmechanik der Stoßvorgänge*, *Z. Phys.* **38** (1926) 803.

[65] R. Hofstadter and R. W. McAllister, *Electron Scattering From the Proton*, *Phys. Rev.* **98** (1955) 217.

[66] R. Devenish and A. Cooper-Sarkar, *Deep inelastic scattering*. 2004.

[67] X.-D. Ji, *Deeply virtual Compton scattering*, *Phys. Rev.* **D55** (1997) 7114 [hep-ph/9609381].

[68] J. Beringer et al., *(Particle Data Group)*, *Phys. Rev. D* **86, 010001** (2012) .

[69] T. Muta, *Foundation of Quantum Chromodynamics*. World Scientific Publishing Co. Pte. Ltd. (3rd Edition), 2010.

[70] J. Collins, *Foundations of Perturbative QCD*. Cambridge University Press, New York, 2011.

[71] J. C. Collins, D. E. Soper and G. F. Sterman, *Factorization of Hard Processes in QCD*, *Adv. Ser. Direct. High Energy Phys.* **5** (1989) 1 [hep-ph/0409313].

[72] G. Curci, W. Furmanski and R. Petronzio, *Evolution of Parton Densities Beyond Leading Order: The Nonsinglet Case*, *Nucl. Phys.* **B175** (1980) 27.

[73] L. Baulieu, E. G. Floratos and C. Kounnas, *Parton Model Interpretation of the Cut Vertex Formalism*, *Nucl. Phys.* **B166** (1980) 321.

[74] P. Cushman et al., *Working Group Report: WIMP Dark Matter Direct Detection*, in *Proceedings, 2013 Community Summer Study on the Future of U.S. Particle Physics: Snowmass on the Mississippi (CSS2013): Minneapolis, MN, USA, July 29-August 6, 2013*, 2013, 1310.8327, http://www.slac.stanford.edu/econf/C1307292/docs/CosmicFrontier/WIMPDirect-24.pdf.

[75] E. Perez and E. Rizvi, *The Quark and Gluon Structure of the Proton*, *Rept. Prog. Phys.* **76** (2013) 046201 [1208.1178].

[76] A. De Roeck and R. S. Thorne, *Structure Functions*, *Prog. Part. Nucl. Phys.* **66** (2011) 727 [1103.0555].

[77] S. Alekhin et al., *The PDF4LHC Working Group Interim Report*, 1101.0536.

[78] R. D. Ball et al., *Parton Distribution Benchmarking with LHC Data*, *JHEP* **04** (2013) 125 [1211.5142].

[79] A. Accardi et al., *A Critical Appraisal and Evaluation of Modern PDFs*, *Eur. Phys. J.* **C76** (2016) 471 [1603.08906].

[80] J. G. Morfin and W.-K. Tung, *Parton distributions from a global QCD analysis of deep inelastic scattering and lepton pair production*, *Z. Phys.* **C52** (1991) 13.

[81] S. Forte, L. Garrido, J. I. Latorre and A. Piccione, *Neural network parametrization of deep inelastic structure functions*, *JHEP* **05** (2002) 062 [hep-ph/0204232].

[82] A. Accardi, L. T. Brady, W. Melnitchouk, J. F. Owens and N. Sato, *Constraints on large-x parton distributions from new weak boson production and deep-inelastic scattering data*, *Phys. Rev.* **D93** (2016) 114017 [1602.03154].

[83] H1, ZEUS collaboration, H. Abramowicz et al., *Combination of measurements of inclusive deep inelastic $e^{\pm}p$ scattering cross sections and QCD analysis of HERA data*, *Eur. Phys. J.* **C75** (2015) 580 [1506.06042].

[84] J. Butterworth et al., *PDF4LHC recommendations for LHC Run II*, *J. Phys.* **G43** (2016) 023001 [1510.03865].

[85] Y. L. Dokshitzer, *Calculation of the Structure Functions for Deep Inelastic Scattering and e+ e- Annihilation by Perturbation Theory in Quantum Chromodynamics.*, *Sov. Phys. JETP* **46** (1977) 641.

[86] V. N. Gribov and L. N. Lipatov, *Deep inelastic e p scattering in perturbation theory*, *Sov. J. Nucl. Phys.* **15** (1972) 438.

[87] G. Altarelli and G. Parisi, *Asymptotic Freedom in Parton Language*, *Nucl. Phys.* **B126** (1977) 298.

[88] NNPDF collaboration, E. R. Nocera, R. D. Ball, S. Forte, G. Ridolfi and J. Rojo, *A first unbiased global determination of polarized PDFs and their uncertainties*, *Nucl. Phys.* **B887** (2014) 276 [1406.5539].

[89] G. Altarelli, S. Forte and G. Ridolfi, *On positivity of parton distributions*, *Nucl. Phys.* **B534** (1998) 277 [hep-ph/9806345].

[90] J. J. Ethier, N. Sato and W. Melnitchouk, *First simultaneous extraction of spin-dependent parton distributions and fragmentation functions from a global QCD analysis*, *Phys. Rev. Lett.* **119** (2017) 132001 [1705.05889].

[91] J. C. Collins, *Fragmentation of transversely polarized quarks probed in transverse momentum distributions*, *Nucl. Phys.* **B396** (1993) 161 [hep-ph/9208213].

[92] M. Anselmino, M. Boglione, U. D'Alesio, A. Kotzinian, F. Murgia, A. Prokudin et al., *Transversity and Collins functions from SIDIS and e+ e- data*, *Phys. Rev.* **D75** (2007) 054032 [hep-ph/0701006].

[93] M. Anselmino, M. Boglione, U. D'Alesio, A. Kotzinian, F. Murgia, A. Prokudin et al., *Update on transversity and Collins functions from SIDIS and e+ e- data*, *Nucl. Phys. Proc. Suppl.* **191** (2009) 98 [`0812.4366`].

[94] HERMES collaboration, A. Airapetian et al., *Single-spin asymmetries in semi-inclusive deep-inelastic scattering on a transversely polarized hydrogen target*, *Phys. Rev. Lett.* **94** (2005) 012002 [`hep-ex/0408013`].

[95] COMPASS collaboration, E. S. Ageev et al., *A New measurement of the Collins and Sivers asymmetries on a transversely polarised deuteron target*, *Nucl. Phys.* **B765** (2007) 31 [`hep-ex/0610068`].

[96] BELLE collaboration, K. Abe et al., *Measurement of azimuthal asymmetries in inclusive production of hadron pairs in e+ e- annihilation at Belle*, *Phys. Rev. Lett.* **96** (2006) 232002 [`hep-ex/0507063`].

[97] H.-W. Lin, W. Melnitchouk, A. Prokudin, N. Sato and H. Shows, *First Monte Carlo Global Analysis of Nucleon Transversity with Lattice QCD Constraints*, *Phys. Rev. Lett.* **120** (2018) 152502 [`1710.09858`].

[98] C. Gattringer and C. Lang, *Quantum Chromodynamics on the Lattice*. Springer, 2010.

[99] H. J. Rothe, *Lattice gauge theories: An Introduction*, *World Sci. Lect. Notes Phys.* **43** (1992) 1.

[100] C.-N. Yang and R. L. Mills, *Conservation of Isotopic Spin and Isotopic Gauge Invariance*, *Phys. Rev.* **96** (1954) 191.

[101] M. Creutz, *Monte Carlo Study of Quantized SU(2) Gauge Theory*, *Phys. Rev.* **D21** (1980) 2308.

[102] ALPHA collaboration, S. Schaefer, R. Sommer and F. Virotta, *Critical slowing down and error analysis in lattice QCD simulations*, *Nucl. Phys.* **B845** (2011) 93 [`1009.5228`].

[103] R. Gupta, *Introduction to lattice QCD: Course*, in *Probing the standard model of particle interactions. Proceedings, Summer School in Theoretical Physics, NATO Advanced Study Institute, 68th session, Les Houches, France, July 28-September 5, 1997. Pt. 1, 2*, pp. 83–219, 1997, `hep-lat/9807028`.

[104] J. Goldstone, A. Salam and S. Weinberg, *Broken Symmetries*, *Phys. Rev.* **127** (1962) 965.

[105] H. B. Nielsen and M. Ninomiya, *No Go Theorem for Regularizing Chiral Fermions*, *Phys. Lett.* **105B** (1981) 219.

[106] P. H. Ginsparg and K. G. Wilson, *A Remnant of Chiral Symmetry on the Lattice*, *Phys. Rev.* **D25** (1982) 2649.

[107] M. Luscher, *Exact chiral symmetry on the lattice and the Ginsparg-Wilson relation*, *Phys. Lett.* **B428** (1998) 342 [`hep-lat/9802011`].

[108] D. B. Kaplan, *A Method for simulating chiral fermions on the lattice*, *Phys. Lett.* **B288** (1992) 342 [`hep-lat/9206013`].

[109] H. Neuberger, *Exactly massless quarks on the lattice*, *Phys. Lett.* **B417** (1998) 141 [`hep-lat/9707022`].

[110] B. Sheikholeslami and R. Wohlert, *Improved Continuum Limit Lattice Action for QCD with Wilson Fermions*, *Nucl. Phys.* **B259** (1985) 572.

[111] K. Symanzik, *Continuum Limit and Improved Action in Lattice Theories. 1. Principles and phi**4 Theory*, *Nucl. Phys.* **B226** (1983) 187.

[112] K. Symanzik, *Continuum Limit and Improved Action in Lattice Theories. 2. O(N) Nonlinear Sigma Model in Perturbation Theory*, *Nucl. Phys.* **B226** (1983) 205.

[113] M. Luscher, *Advanced lattice QCD*, in *Probing the standard model of particle interactions. Proceedings, Summer School in Theoretical Physics, NATO Advanced Study Institute, 68th session, Les Houches, France, July 28-September 5, 1997. Pt. 1, 2*, pp. 229–280, 1998, `hep-lat/9802029`.

[114] M. Luscher, S. Sint, R. Sommer and P. Weisz, *Chiral symmetry and O(a) improvement in lattice QCD*, *Nucl. Phys.* **B478** (1996) 365 [`hep-lat/9605038`].

[115] M. Luscher, S. Sint, R. Sommer, P. Weisz and U. Wolff, *Nonperturbative O(a) improvement of lattice QCD*, *Nucl. Phys.* **B491** (1997) 323 [`hep-lat/9609035`].

[116] ALPHA collaboration, K. Jansen and R. Sommer, *O(a) improvement of lattice QCD with two flavors of Wilson quarks*, *Nucl. Phys.* **B530** (1998) 185 [`hep-lat/9803017`].

[117] JLQCD, CP-PACS collaboration, N. Yamada et al., *Non-perturbative O(a)-improvement of Wilson quark action in three-flavor QCD with plaquette gauge action*, *Phys. Rev.* **D71** (2005) 054505 [`hep-lat/0406028`].

[118] ALPHA collaboration, F. Tekin, R. Sommer and U. Wolff, *The Running coupling of QCD with four flavors*, *Nucl. Phys.* **B840** (2010) 114 [`1006.0672`].

[119] ALPHA collaboration, R. Frezzotti, P. A. Grassi, S. Sint and P. Weisz, *Lattice QCD with a chirally twisted mass term*, *JHEP* **08** (2001) 058 [`hep-lat/0101001`].

[120] R. Frezzotti and G. C. Rossi, *Twisted mass lattice QCD with mass nondegenerate quarks*, *Nucl. Phys. Proc. Suppl.* **128** (2004) 193 [`hep-lat/0311008`].

[121] C. Pena, S. Sint and A. Vladikas, *Twisted mass QCD and lattice approaches to the Delta I = 1/2 rule*, *JHEP* **09** (2004) 069 [`hep-lat/0405028`].

[122] A. Shindler, *Twisted mass lattice QCD*, *Phys. Rept.* **461** (2008) 37 [`0707.4093`].

[123] S. Sint, *Lattice QCD with a chiral twist*, in *Workshop on Perspectives in Lattice QCD Nara, Japan, October 31-November 11, 2005*, 2007, `hep-lat/0702008`, DOI.

[124] R. Frezzotti and G. C. Rossi, *Chirally improving Wilson fermions. 1. O(a) improvement*, *JHEP* **08** (2004) 007 [`hep-lat/0306014`].

[125] XLF collaboration, K. Jansen, M. Papinutto, A. Shindler, C. Urbach and I. Wetzorke, *Light quarks with twisted mass fermions*, *Phys. Lett.* **B619** (2005) 184 [`hep-lat/0503031`].

[126] R. Frezzotti, G. Martinelli, M. Papinutto and G. C. Rossi, *Reducing cutoff effects in maximally twisted lattice QCD close to the chiral limit*, *JHEP* **04** (2006) 038 [`hep-lat/0503034`].

[127] J. C. Ward, *An Identity in Quantum Electrodynamics*, *Phys. Rev.* **78** (1950) 182.

[128] Y. Takahashi, *On the generalized Ward identity*, *Nuovo Cim.* **6** (1957) 371.

[129] G. Herdoiza, K. Jansen, C. Michael, K. Ottnad and C. Urbach, *Determination of Low-Energy Constants of Wilson Chiral Perturbation Theory*, *JHEP* **05** (2013) 038 [`1303.3516`].

[130] ETM collaboration, A. Abdel-Rehim et al., *First physics results at the physical pion mass from $N_f = 2$ Wilson twisted mass fermions at maximal twist*, Phys. Rev. **D95** (2017) 094515 [1507.05068].

[131] C. Alexandrou et al., *Simulating twisted mass fermions at physical light, strange and charm quark masses*, Phys. Rev. **D98** (2018) 054518 [1807.00495].

[132] B. A. Berg, *Introduction to Markov chain Monte Carlo simulations and their statistical analysis*, cond-mat/0410490.

[133] LHPC collaboration, J. D. Bratt et al., *Nucleon structure from mixed action calculations using 2+1 flavors of asqtad sea and domain wall valence fermions*, Phys. Rev. **D82** (2010) 094502 [1001.3620].

[134] X. Xiong, X. Ji, J.-H. Zhang and Y. Zhao, *One-loop matching for parton distributions: Nonsinglet case*, Phys. Rev. **D90** (2014) 014051 [1310.7471].

[135] A. Frommer, K. Kahl, S. Krieg, B. Leder and M. Rottmann, *Adaptive Aggregation Based Domain Decomposition Multigrid for the Lattice Wilson Dirac Operator*, SIAM J. Sci. Comput. **36** (2014) A1581 [1303.1377].

[136] C. Alexandrou, S. Bacchio, J. Finkenrath, A. Frommer, K. Kahl and M. Rottmann, *Adaptive Aggregation-based Domain Decomposition Multigrid for Twisted Mass Fermions*, Phys. Rev. **D94** (2016) 114509 [1610.02370].

[137] M. Luscher, *Local coherence and deflation of the low quark modes in lattice QCD*, JHEP **07** (2007) 081 [0706.2298].

[138] J. Brannick, R. C. Brower, M. A. Clark, J. C. Osborn and C. Rebbi, *Adaptive Multigrid Algorithm for Lattice QCD*, Phys. Rev. Lett. **100** (2008) 041601 [0707.4018].

[139] M. A. Clark, J. Brannick, R. C. Brower, S. F. McCormick, T. A. Manteuffel, J. C. Osborn et al., *The Removal of critical slowing down*, PoS **LATTICE2008** (2008) 035 [0811.4331].

[140] S. Bernardson, P. McCarty and C. Thron, *Monte Carlo methods for estimating linear combinations of inverse matrix entries in lattice QCD*, Comput. Phys. Commun. **78** (1993) 256.

[141] S.-J. Dong and K.-F. Liu, *Stochastic estimation with Z(2) noise*, Phys. Lett. **B328** (1994) 130 [hep-lat/9308015].

[142] G. S. Bali, B. Lang, B. U. Musch and A. Schäfer, *Novel quark smearing for hadrons with high momenta in lattice QCD*, Phys. Rev. **D93** (2016) 094515 [1602.05525].

[143] G. Martinelli and C. T. Sachrajda, *A Lattice Study of Nucleon Structure*, Nucl. Phys. **B316** (1989) 355.

[144] S. Gusken, *A Study of smearing techniques for hadron correlation functions*, Nucl. Phys. Proc. Suppl. **17** (1990) 361.

[145] C. Alexandrou, S. Gusken, F. Jegerlehner, K. Schilling and R. Sommer, *The Static approximation of heavy - light quark systems: A Systematic lattice study*, Nucl. Phys. **B414** (1994) 815 [hep-lat/9211042].

[146] APE collaboration, M. Albanese et al., *Glueball Masses and String Tension in Lattice QCD*, Phys. Lett. **B192** (1987) 163.

[147] C. Morningstar and M. J. Peardon, *Analytic smearing of SU(3) link variables in lattice QCD*, Phys. Rev. **D69** (2004) 054501 [hep-lat/0311018].

[148] A. Hasenfratz and F. Knechtli, *Flavor symmetry and the static potential with hypercubic blocking*, *Phys. Rev.* **D64** (2001) 034504 [`hep-lat/0103029`].

[149] Y. Liang, K.-F. Liu, B.-A. Li, S. J. Dong and K. Ishikawa, *Lattice calculation of glueball matrix elements*, *Phys. Lett.* **B307** (1993) 375 [`hep-lat/9304011`].

[150] M. Della Morte, A. Shindler and R. Sommer, *On lattice actions for static quarks*, *JHEP* **08** (2005) 051 [`hep-lat/0506008`].

[151] S. Duane, A. D. Kennedy, B. J. Pendleton and D. Roweth, *Hybrid Monte Carlo*, *Phys. Lett.* **B195** (1987) 216.

[152] C. Alexandrou and C. Kallidonis, *Low-lying baryon masses using $N_f = 2$ twisted mass clover-improved fermions directly at the physical pion mass*, *Phys. Rev.* **D96** (2017) 034511 [`1704.02647`].

[153] P. Weisz, *Continuum Limit Improved Lattice Action for Pure Yang-Mills Theory. 1.*, *Nucl. Phys.* **B212** (1983) 1.

[154] Y. Iwasaki, *Renormalization Group Analysis of Lattice Theories and Improved Lattice Action: Two-Dimensional Nonlinear O(N) Sigma Model*, *Nucl. Phys.* **B258** (1985) 141.

[155] Y. Iwasaki, K. Kanaya, T. Kaneko and T. Yoshie, *Scaling in SU(3) pure gauge theory with a renormalization group improved action*, *Phys. Rev.* **D56** (1997) 151 [`hep-lat/9610023`].

[156] H.-n. Li, *Nondipolar Wilson links for quasiparton distribution functions*, *Phys. Rev.* **D94** (2016) 074036 [`1602.07575`].

[157] A. Abdel-Rehim et al., *Nucleon and pion structure with lattice QCD simulations at physical value of the pion mass*, *Phys. Rev.* **D92** (2015) 114513 [`1507.04936`].

[158] T. Blum, T. Izubuchi and E. Shintani, *New class of variance-reduction techniques using lattice symmetries*, *Phys. Rev.* **D88** (2013) 094503 [`1208.4349`].

[159] J. Green, *Systematics in nucleon matrix element calculations*, in *36th International Symposium on Lattice Field Theory (Lattice 2018) East Lansing, MI, United States, July 22-28, 2018*, 2018, `1812.10574`.

[160] L. Maiani, G. Martinelli, M. L. Paciello and B. Taglienti, *Scalar Densities and Baryon Mass Differences in Lattice QCD With Wilson Fermions*, *Nucl. Phys.* **B293** (1987) 420.

[161] ETM collaboration, C. Alexandrou, M. Constantinou and H. Panagopoulos, *Renormalization functions for Nf=2 and Nf=4 twisted mass fermions*, *Phys. Rev.* **D95** (2017) 034505 [`1509.00213`].

[162] T. Bhattacharya, V. Cirigliano, S. Cohen, R. Gupta, H.-W. Lin and B. Yoon, *Axial, Scalar and Tensor Charges of the Nucleon from 2+1+1-flavor Lattice QCD*, *Phys. Rev.* **D94** (2016) 054508 [`1606.07049`].

[163] C. Alexandrou, M. Constantinou, K. Hadjiyiannakou, K. Jansen, C. Kallidonis, G. Koutsou et al., *Nucleon axial form factors using $N_f = 2$ twisted mass fermions with a physical value of the pion mass*, *Phys. Rev.* **D96** (2017) 054507 [`1705.03399`].

[164] C. Alexandrou et al., *Nucleon scalar and tensor charges using lattice QCD simulations at the physical value of the pion mass*, *Phys. Rev.* **D95** (2017) 114514 [`1703.08788`].

[165] R. Sommer, *Non-perturbative Heavy Quark Effective Theory: Introduction and Status*, *Nucl. Part. Phys. Proc.* **261-262** (2015) 338 [`1501.03060`].

[166] G. Martinelli, C. Pittori, C. T. Sachrajda, M. Testa and A. Vladikas, *A General method for nonperturbative renormalization of lattice operators*, *Nucl. Phys.* **B445** (1995) 81 [hep-lat/9411010].

[167] C. Alexandrou, M. Constantinou, T. Korzec, H. Panagopoulos and F. Stylianou, *Renormalization constants for 2-twist operators in twisted mass QCD*, *Phys. Rev.* **D83** (2011) 014503 [1006.1920].

[168] ETM collaboration, M. Constantinou et al., *Non-perturbative renormalization of quark bilinear operators with $N_f = 2$ (tmQCD) Wilson fermions and the tree-level improved gauge action*, *JHEP* **08** (2010) 068 [1004.1115].

[169] M. Gockeler, R. Horsley, H. Oelrich, H. Perlt, D. Petters, P. E. L. Rakow et al., *Nonperturbative renormalization of composite operators in lattice QCD*, *Nucl. Phys.* **B544** (1999) 699 [hep-lat/9807044].

[170] R. A. Briceño, J. V. Guerrero, M. T. Hansen and C. J. Monahan, *Finite-volume effects due to spatially nonlocal operators*, *Phys. Rev.* **D98** (2018) 014511 [1805.01034].

[171] T. Izubuchi, X. Ji, L. Jin, I. W. Stewart and Y. Zhao, *Factorization Theorem Relating Euclidean and Light-Cone Parton Distributions*, *Phys. Rev.* **D98** (2018) 056004 [1801.03917].

[172] R. Baron et al., *Light hadrons from lattice QCD with light (u,d), strange and charm dynamical quarks*, *JHEP* **06** (2010) 111 [1004.5284].

[173] I. W. Stewart and Y. Zhao, *Matching the quasiparton distribution in a momentum subtraction scheme*, *Phys. Rev.* **D97** (2018) 054512 [1709.04933].

[174] W.-C. Chang and J.-C. Peng, *Flavor Structure of the Nucleon Sea*, *Prog. Part. Nucl. Phys.* **79** (2014) 95 [1406.1260].

[175] J. Karpie, K. Orginos, A. Rothkopf and S. Zafeiropoulos, *Reconstructing parton distribution functions from Ioffe time data: from Bayesian methods to Neural Networks*, *JHEP* **04** (2019) 057 [1901.05408].

[176] LP3 collaboration, H.-W. Lin, J.-W. Chen, T. Ishikawa and J.-H. Zhang, *Improved parton distribution functions at the physical pion mass*, *Phys. Rev.* **D98** (2018) 054504 [1708.05301].

[177] C. Alexandrou, V. Drach, K. Jansen, C. Kallidonis and G. Koutsou, *Baryon spectrum with $N_f = 2 + 1 + 1$ twisted mass fermions*, *Phys. Rev.* **D90** (2014) 074501 [1406.4310].

[178] Y. Aoki, T. Blum, H.-W. Lin, S. Ohta, S. Sasaki, R. Tweedie et al., *Nucleon isovector structure functions in (2+1)-flavor QCD with domain wall fermions*, *Phys. Rev.* **D82** (2010) 014501 [1003.3387].

[179] QCDSF/UKQCD collaboration, D. Pleiter et al., *Nucleon form factors and structure functions from N(f)=2 Clover fermions*, *PoS* **LATTICE2010** (2010) 153 [1101.2326].

[180] J. R. Green, M. Engelhardt, S. Krieg, J. W. Negele, A. V. Pochinsky and S. N. Syritsyn, *Nucleon Structure from Lattice QCD Using a Nearly Physical Pion Mass*, *Phys. Lett.* **B734** (2014) 290 [1209.1687].

[181] G. S. Bali, S. Collins, B. Gläßle, M. Göckeler, J. Najjar, R. H. Rödl et al., *The moment $\langle x \rangle_{u-d}$ of the nucleon from $N_f = 2$ lattice QCD down to nearly physical quark masses*, *Phys. Rev.* **D90** (2014) 074510 [1408.6850].

[182] S. Alekhin, J. Blumlein and S. Moch, *Parton Distribution Functions and Benchmark Cross Sections at NNLO*, *Phys. Rev.* **D86** (2012) 054009 [1202.2281].

[183] D. de Florian, R. Sassot, M. Stratmann and W. Vogelsang, *Extraction of Spin-Dependent Parton Densities and Their Uncertainties*, *Phys. Rev.* **D80** (2009) 034030 [0904.3821].

[184] STAR collaboration, J. Adam et al., *Measurement of the longitudinal spin asymmetries for weak boson production in proton-proton collisions at $\sqrt{510}$ GeV*, *Phys. Rev.* **D99** (2019) 051102 [1812.04817].

[185] BELLE collaboration, R. Seidl et al., *Measurement of Azimuthal Asymmetries in Inclusive Production of Hadron Pairs in e+e- Annihilation at s**(1/2) = 10.58-GeV*, *Phys. Rev.* **D78** (2008) 032011 [0805.2975].

[186] BABAR collaboration, I. Garzia, *Measurement of Collins asymmetries in inclusive production of pion pairs in e^+e^- collisions at BABAR*, *PoS* **ICHEP2012** (2013) 272 [1211.5293].

[187] HERMES collaboration, A. Airapetian et al., *Effects of transversity in deep-inelastic scattering by polarized protons*, *Phys. Lett.* **B693** (2010) 11 [1006.4221].

[188] COMPASS collaboration, M. Alekseev et al., *Collins and Sivers asymmetries for pions and kaons in muon-deuteron DIS*, *Phys. Lett.* **B673** (2009) 127 [0802.2160].

[189] COMPASS collaboration, C. Adolph et al., *Collins and Sivers asymmetries in muonproduction of pions and kaons off transversely polarised protons*, *Phys. Lett.* **B744** (2015) 250 [1408.4405].

[190] F. Steffens. Private communication.

Appendix A

A.1 Light-cone dominance

In this Section we show that, for deep inelastic scatterings in which $Q^2 \to \infty$ at Bjorken variable x fixed, the dominant contribution to the hadronic tensor

$$W_{\mu\nu} = \frac{1}{4\pi} \int d^4z \, e^{iq \cdot z} \langle N | [J_\mu(z), J_\nu(0)] | N \rangle \tag{A.1}$$

comes from the region where z^2 vanishes, i.e. from the light-cone. To this end we consider a scattering process in the laboratory frame, where the target particle has quadri-momentum $P = (M, 0, 0, 0)$ and the first component of the momentum transfer is $q^0 = P \cdot Q/M = \nu$. Denoting with r the component of $\vec{z}$ in the direction of $\vec{q}$, i.e.

$$r \equiv \frac{\vec{q} \cdot \vec{z}}{|\vec{q}|} \,, \tag{A.2}$$

the factor $q \cdot z$ can be written as

$$\begin{aligned} q \cdot z &= q^0 z^0 - \vec{q} \cdot \vec{z} = q^0 z^0 - |\vec{q}| r = q^0 z^0 - r\sqrt{q_0^2 - q^2} \\ &\overset{LAB}{=} \nu z^0 - r\sqrt{\nu^2 + Q^2} \approx \nu z^0 - r\nu(1 + Mx/\nu) = \nu(z^0 - r) - rMx \,, \end{aligned} \tag{A.3}$$

where $x = Q^2/(2P \cdot q)$ is the Bjorken variable, which is finite in the Bjorken limit, i.e. $Q \to \infty$ and $\nu \to \infty$. If $q \cdot z$ is large, the contribution to the integral (A.1) is suppressed by rapid oscillations and thus we are only interested in the region in which $|q \cdot z|$ is finite. To keep $|q \cdot z|$ finite in the Bjorken limit, we must have

$$|z^0 - r| \lesssim const./\nu \,, \quad \text{and} |r| \lesssim const./x \,, \tag{A.4}$$

which combined together give

$$z_0^2 \lesssim \left(r + \frac{const.}{\nu} \right)^2 \approx r^2 + const. \frac{r}{\nu} < |\vec{z}|^2 + \frac{const.}{x\nu} \,. \tag{A.5}$$

In the last step we have used the definition of r in Eq. (A.2). From this result, it follows that

$$z_0^2 = z^2 + |\vec{z}|^2 \lesssim |\vec{z}|^2 + \frac{const.}{x\nu} \Rightarrow \boxed{z^2 \lesssim \frac{const.}{Q^2}} \,. \tag{A.6}$$

Since the causality also imposes that the commutator in Eq. (A.1) must vanish for $z^2 < 0$, one can see that only the space-time region very close to the light-cone, $z^2 \sim 0$, contributes to the hadronic tensor and to the cross section in DIS processes.

A.2 Moments and matrix elements in the OPE

In Chapter 2 we have seen that the zeroth moment of the valence unpolarized distribution is related to the local vector matrix element by the expression (2.41), here rewritten

$$\int_0^1 dx\,[q_f(x) - q_{\bar{f}}(x)] = \frac{1}{2P^+} \langle N | \bar{\psi}_f(0) \gamma^+ \psi_f(0) | N \rangle , \tag{A.7}$$

where q_f ($q_{\bar{f}}$) denotes the unpolarized distribution of a quark (antiquark) with flavor f, $P^+ = (P^0 + P^3)/\sqrt{2}$ is the *plus* component of the nucleon momentum and $\gamma^+ = (\gamma^0 + \gamma^3)/\sqrt{2}$ the Dirac matrix in the light-cone frame. In this Section we want to generalize the expression above, showing that the n-th moment of the valence unpolarized distribution can be obtained through appropriate local matrix elements, which are exactly the ones arising from the operator product expansion (OPE). The derivation follows from [190] and makes use of the light-cone definition of the unpolarized distribution

$$q_f(x) = \frac{1}{4\pi} \int_{-\infty}^{+\infty} d\xi^- \, e^{-ixP^+\xi^-} h_f(\xi^-) , \tag{A.8}$$

$$h_f(\xi^-) = \langle N | \bar{\psi}_f(\xi^-) \gamma^+ e^{-ig_0 \int_0^{\xi^-} A^+(\xi')d\xi'} \psi_f(0) | N \rangle , \tag{A.9}$$

being $\xi^\pm = (\xi^0 \pm \xi^3)/\sqrt{2}$ the light-cone directions and $A^+ = (A^0 + A^3)/\sqrt{2}$ the *plus* component of the gluon field.

First of all, let us define the n-th moment, A_n, of the valence distribution of a quark f

$$A_n \equiv \int_{-1}^{+1} dx\, x^{n-1} q_f(x) = \int_0^1 dx\, x^{n-1} \left[q_f(x) + (-1)^n q_{\bar{f}}(x) \right] , \tag{A.10}$$

where the crossing relation $q_f(x) = -\bar{q}_f(-x)$ for the unpolarized distribution has been used. As can be seen, for $n = 1$ in Eq. (A.10), we obtain again the expression (A.7).

Since $q_f(x)$ vanishes for $|x| \geq 1$, the moment A_n can be written in the following way with the help of Eq. (A.8)

$$A_n = \int_{-1}^1 dx\, x^{n-1} q_f(x) = \int_{-\infty}^{+\infty} dx\, x^{n-1} q_f(x)$$

$$= \int_{-\infty}^{+\infty} dx \int \frac{d\xi^-}{4\pi} \frac{1}{(-iP^+)^{(n-1)}} \left(\partial^{+(n-1)} e^{-ixP^+\xi^-} \right) h(\xi^-) , \tag{A.11}$$

where $\partial^+ \equiv \partial/\partial\xi^-$. The integral over ξ^- can now be performed through integration by parts

$$\int d\xi^- \left(\partial^{+^{(n-1)}} e^{-ixP^+\xi^-}\right) h(\xi^-) = \left(\partial^{+^{(n-2)}} e^{-ixP^+\xi^-}\right) h(\xi^-)\Bigg|_{-\infty}^{+\infty}$$
$$- \int d\xi^- \left(\partial^{+^{(n-2)}} e^{-ixP^+\xi^-}\right) \partial^+ h(\xi^-), \qquad (A.12)$$

where the contribution at the border $\xi^- = \pm\infty$ can be neglected. Thus, iterating $(n-1)$ times the integration by parts (A.12), we get

$$\int d\xi^- \left(\partial^{+^{(n-1)}} e^{-ixP^+\xi^-}\right) h(\xi^-) = (-1)^{n-1} \int d\xi^- e^{-ixP^+\xi^-} \partial^{+^{(n-1)}} h(\xi^-). \qquad (A.13)$$

Replacing the result above in Eq. (A.11), we obtain

$$A_n = \int_{-1}^1 dx\, x^{n-1} q_f(x) = \frac{(-i)^{n-1}}{4\pi(P^+)^{(n-1)}} \int d\xi^- \left[\partial^{+^{(n-1)}} h(\xi^-)\right] \int_{-\infty}^{+\infty} dx\, e^{-ixP^+\xi^-}$$
$$= \frac{(-i)^{n-1}}{2(P^+)^n} \left[\partial^{+^{(n-1)}} h(\xi^-)\right]_{\xi^-=0}. \qquad (A.14)$$

We are now left with the derivatives of the matrix element $\partial^{+^{(n-1)}} h(\xi^-)$. Using the Eq. (A.9), the first derivative reads

$$\partial^+ h(\xi^-) = \frac{\partial}{\partial\xi^-} \langle N|\bar\psi(\xi^-)\gamma^+ e^{-ig_0 \int_0^{\xi^-} A^+(\xi')d\xi'} \psi(0)|N\rangle$$
$$= \langle N|\partial^+\bar\psi(\xi^-)\gamma^+ e^{-ig_0 \int_0^{\xi^-} A^+(\xi')d\xi'} \psi(0)|N\rangle$$
$$+ \langle N|\bar\psi(\xi^-)\gamma^+ (-ig_0 A^+(\xi^-)) e^{-ig_0 \int_0^{\xi^-} A^+(\xi')d\xi'} \psi(0)|N\rangle$$
$$= -\langle N|\bar\psi(\xi^-)\gamma^+ \left[\overleftarrow{\partial^+} + ig_0 A^+(\xi^-)\right] e^{-ig_0 \int_0^{\xi^-} A^+ d\xi'} \psi(0)|N\rangle, \qquad (A.15)$$

where the identity $[\partial^+\bar\psi(\xi^-)]\psi(0) = -\bar\psi(\xi^-)\overleftarrow{\partial^+}\psi(0)$ has been used in the last step. The derivative $\overleftarrow{\partial^+}$ acts on the fermion field on the left. From the result in Eq. (A.15), it turns out that each derivative $\partial^+ h$ of the matrix element will bring a covariant derivative, $D^+ = \partial^+ + ig_0 A^+$. Therefore, the n-th moment (A.14) of the unpolarized valence quark distribution becomes

$$A_n = \frac{i^{n-1}}{2(P^+)^n} \langle N| \left[\bar\psi(\xi^-)\gamma^+ \overleftarrow{D^+} \overleftarrow{D^+} \dots \overleftarrow{D^+}\right]_{\xi^-=0} \psi(0)|N\rangle, \qquad (A.16)$$

where the derivatives $D^+ = \partial^+ + ig_0 A^+$ are computed at $\xi^- = 0$. Eq. (A.16) is a generalization of the Eq. (A.7) for an integer moment of the distribution and has important implications. The moments of parton distributions are matrix elements of local operators, and therefore computable in Euclidean space. Unlike the moments, distribution functions are strictly Minkowski-space objects, light-cone dominated. As explained in Chapter 3, a direct implementation of the definition of parton distributions is impossible in Euclidean space. We also note that the result in Eq. (A.16) also applies for the helicity and transversity distributions replacing γ^+ with the appropriate Dirac structures.

A.3 Gamma Matrix Representation

In our lattice calculations we use the so-called chiral representation of γ-matrices. They obey to the anti-commutation relations

$$\{\gamma_\mu, \gamma_\nu\} = 2\delta_{\mu\nu}\mathbb{1}_4 \,, \tag{A.17}$$

where $\mathbb{1}_4$ is the 4×4 unit matrix. The γ-matrices are given by

$$\gamma_k = \begin{bmatrix} 0 & -i\sigma_k \\ i\sigma_k & 0 \end{bmatrix} \,, \quad \gamma_4 = \begin{bmatrix} 0 & \mathbb{1}_2 \\ \mathbb{1}_2 & 0 \end{bmatrix} \,, \tag{A.18}$$

where σ_k for $k = 1, 2, 3$ are the Pauli matrices and $\mathbb{1}_2$ is the 2×2 unit matrix. We also define the matrix γ_0 as $\gamma_0 = -\gamma_4$; it is redundant but practical in the applications. The chirality operator γ_5 is defined as

$$\gamma_5 = \gamma_1\gamma_2\gamma_3\gamma_4 \,, \quad \gamma_5 = \begin{bmatrix} \mathbb{1}_2 & 0 \\ 0 & -\mathbb{1}_2 \end{bmatrix} \tag{A.19}$$

and anti-commutes with all other γ-matrices, $\{\gamma_5, \gamma_\mu\} = 0$ for $\mu = 1, 2, 3, 4$.

A.4 Nucleon Mass Corrections

Here we report the formulae for the nucleon mass corrections (NMCs) used in this work in order to account for the non-zero ratio of the nucleon mass to its momentum. We follow the same formalism as in Ref. [38].

First of all we define the following factors

$$c = \frac{m_N^2}{4P_z^2}, \quad f_\pm = \sqrt{1+4c} \pm 1, \quad a = 1+4c, \quad b = \frac{f_+}{\sqrt{1+4c}}, \quad r = \frac{f_-}{f_+}, \qquad \text{(A.20)}$$

where m_N is the nucleon mass and P_z the nucleon momentum taken along the z-direction.

The NMCs for the unpolarized distribution functions read

$$q_{II}(x) = \sqrt{1+4c} \sum_{n=0}^{\infty} \frac{f_-^n}{f_+^{n+1}} \left[(1+(-1)^n)q_I\left(\frac{f_+^{n+1}x}{2f_-^n}\right) + (1-(-1)^n)q_I\left(\frac{-f_+^{n+1}x}{2f_-^n}\right) \right]$$

$$= \sqrt{1+4c} \sum_{n=0}^{\infty} \frac{(4c)^n}{f_+^{2n+1}} \left[(1+(-1)^n)q_I\left(\frac{f_+^{2n+1}x}{2(4c)^n}\right) + (1-(-1)^n)q_I\left(\frac{-f_+^{2n+1}x}{2(4c)^n}\right) \right],$$

$$\text{(A.21)}$$

where q_I denotes the matched unpolarized distribution, obtained after applying the matching kernel of Eq. (7.4) with $\iota = 0$. The final lattice distribution with NMCs subtracted is indicated via q_{II}.

The NMCs for the transversity distribution functions are the same as for the unpolarized case and read

$$\delta q_{II}(x) = \sqrt{1+4c} \sum_{n=0}^{\infty} \frac{f_-^n}{f_+^{n+1}} \left[(1+(-1)^n)\delta q_I\left(\frac{f_+^{n+1}x}{2f_-^n}\right) + (1-(-1)^n)\delta q_I\left(\frac{-f_+^{n+1}x}{2f_-^n}\right) \right]$$

$$= \sqrt{1+4c} \sum_{n=0}^{\infty} \frac{(4c)^n}{f_+^{2n+1}} \left[(1+(-1)^n)\delta q_I\left(\frac{f_+^{2n+1}x}{2(4c)^n}\right) + (1-(-1)^n)\delta q_I\left(\frac{-f_+^{2n+1}x}{2(4c)^n}\right) \right],$$

$$\text{(A.22)}$$

where δq_{II} is the final transversity distribution and δq_I the one obtained after matching procedure, given in Eq. (7.5).

The NMCs for the helicity distributions are given by

$$
\Delta q_{II}(x < 0) = \frac{2a}{f_+} \left\{ \Delta q_I \left(\frac{f_+}{2} x \right) - r \left[\Delta q_I \left(-\frac{f_+}{2} \frac{x}{r} \right) - \int_{-\infty}^{x} \frac{dy}{y} b \Delta(y) \right] \right.
$$
$$
+ r^2 \left[\Delta q_I \left(\frac{f_+}{2} \frac{x}{r^2} \right) - \int_{-\infty}^{x} \frac{dy}{y} b \Delta \left(-\frac{y}{r} \right) + \int_{-\infty}^{x} \frac{dy}{y} \int_{-\infty}^{y} \frac{dz}{z} b^2 \Delta(z) \right.
$$
$$
\left. \left. - \int_{-\infty}^{-\frac{x}{r}} \frac{dy}{y} b \Delta(y) + \int_{-\infty}^{x} \frac{dy}{y} \int_{-\infty}^{-\frac{y}{r}} \frac{dz}{z} b^2 \Delta(z) \right] \right\} + \mathcal{O}(r^3) \quad , \tag{A.23}
$$

where $\Delta(y)$ denotes the matched distribution computed as

$$
\Delta(y) = \Delta q_I \left(\frac{f_+}{2} y \right) + \Delta q_I \left(-\frac{f_+}{2} \frac{y}{r} \right). \tag{A.24}
$$

The matching kernel is given in Eq. (7.4) with $\iota = 1$. The final helicity distribution in the positive x-region is obtained via $\Delta q_I(x > 0) = \Delta q_I(x < 0)[-\infty \to \infty]$. In Eq. (A.23) we have reported only the corrections up to $\mathcal{O}(r^2)$, that have been implemented in this work. Higher order terms in r^3 can be found in Ref. [38].